Polyacrylonitrile-based porous polymer and carbon spheres for adsorption and catalysis

Dissertation

To obtain a doctor degree in natural science

- Dr. rer. nat. -

Presented by

Zhuo Gao

Born in Zouping, Shandong, China

Chair of Technical Chemistry II of

the Faculty of Chemistry

University of Duisburg-Essen

2022

This work was done during the period from October, 2017 to May, 2021 in the working group of Prof. Dr. Mathias Ulbricht at the Institute of Technical Chemistry II in University of Duisburg-Essen.

Supervisor:	Prof. Dr. Mathias Ulbricht
Second reviewer:	Prof. Dr. Corina Andronescu
Chairman:	Prof. Dr. Christian Mayer
Disputation:	16.01.2023

DOI: 10.17185/duepublico/77375
URN: urn:nbn:de:hbz:465-20230417-102909-4

Acknowledgement

First and foremost, I would like to thank my doctoral supervisor, Prof. Dr. Mathias Ulbricht. I feel honored that I can come into his working group. The topic of this dissertation is interesting and motivating. I am really grateful for the spiritual support and material help from professor.

I also thank Prof. Dr. Corina Andronescu for the friendly takeover of second reviewer and Prof. Dr. Christian Mayer as chairman of my disputation procedure.

For the preparation and characterization of samples by SEM, I would like to thank Mr. Dipl.-Ing. Smail Boukercha and Dr. Kateryna Loza. For the ORR characterizations of carbon samples, I would like to thank Dr. Ignacio Sanjuán Moltó from Technical Chemistry III. For the characterization of samples by XPS and Raman spectroscopy, I want to thank Dr. Ulrich Hagemann in NETZ. For the XRD characterization, I want to thank Dr. Oleg Prymak. As to TGA, DTA, and DSC measurements, I would like to thank Mr. Mateusz Olejnk. For the measurement of molecular weight, I want to thank Dr. Jackelyn Aragon-Gomez. For the elemental analysis, I want to thank Mr. Robin Meya. In addition, I also thank the kind cooperation from Technical Chemistry I (optical microscopy) and Inorganic Chemistry (AK Epple for IR spectroscopy).

For the current and former employees in Chair of Technical Chemistry II, I would like to thank you for the pleasant working atmosphere, good cooperation, and help. In particular, I want to thank Dr. Alexandra S. M. Wittmar, Mr. Duc Hoa Tran, Dr. Qirong Ke, and Dr. Jens Schumacher. Moreover, I also want to thank Mrs. Claudia Schenk, Mr. Tobias Kallweit, Mrs. Inge Danielzik, Mrs. Roswitha Nordmann, and Dr. Christina Kamp-Meltzer for the great support in technical and organizational matters. For the good cooperation and contribution to this work, I would like to thank my student, Miss Natalie Wolff.

I want to give special thanks to China Scholarship Council (CSC) and University of Duisburg-Essen for the financial support. Without this support, I can not come here and finish my doctoral degree.

At last, I would like to thank my family and relatives. Especially, I want to thank the two warrantors to this study abroad, Mr. Dazhi Ren and Mr. Liang Zhang. Without their financial guarantee, my study would not have been so smooth. I want to give my most precious thanks to my mother, who gives her unselfish love to me during these years and supports my original family firmly.

Figure list

Table list

Scheme list

Abbreviation

a.u.	arbitrary unit
AR	aspect ratio
ATR	attenuated total reflection
Ave.	average
BDDT	Brunauer, Deming, Deming, and Teller
BET	Brunauer-Emmett-Teller
BJH	Barrett-Joyner-Halenda
$CaCl_2$	calcium chloride
CCD	charge coupled device
CE	collection efficiency
CO_2	carbon dioxide gas
CV	cycle voltammetry
2D	two dimensional
DLS	dynamic light scattering
DMA	dynamic mechanical analysis
DMF	N, N-dimethylformamide
DMSO	dimethylsulfoxide
DOD	drop-on-demand
DSC	differential scanning calorimetry
DTA	differential thermal analysis
DTG	derivative thermo gravimetric
EA	elemental analysis
EDS	energy-dispersive X-ray spectroscopy
E_g	energy band gap or Raman active modes
e.g.	exempli gratia
EPMA	electron probe micro-analysis
ESCA	electron spectroscopy for chemical analysis
et al.	et alia
exo	exothermic
Fe_3O_4	ferroso ferric oxide
G’	storage modulus
G’’	loss modulus
H_2	hydrogen gas
HCl	hydrogen chloride
H_2O	water
H_2O_2 and HO_2^-	hydrogen peroxide and its anion
H_3PO_4	phosphoric acid
i.e.	id est
IOS	International Organization for Standardization
IR	infrared
IUPAC	International Union of Pure and Applied Chemistry

k	photocatalytic rate
K_2CO_3	potassium carbonate
$K_3[Fe(CN)_6]$	potassium ferricyanide
K-L	Koutecky-Levich
KOH	potassium hydroxide
L-PAN	polyacrylonitrile (M_w: 77 kg/mol)
LSV	linear sweep voltammetry
M	mol/L
MA	methyl acrylate
MB	methylene blue
MI	mean intensity diameter
min	minutes
min ()	minimum ()
MN	mean number diameter
M_n	number-weighted molecular weight
MO	methyl orange
MOF	metal organic framework
MV	mean volume diameter
M_w	weight-weighted molecular weight
N-5	pyrrolic N
N-6	pyridinic N
n	electron transfer number
N and N_2	nitrogen element and nitrogen gas
N/A	not applicable
NIPS	non-solvent induced phase separation
NP(s)	nanoparticle(s)
N-Q	quaternary N
N-X	pyridonic N
O_2	oxygen gas
OCP	open circuit potential
OH^- and $\cdot OH$	hydroxide and hydroxyl radical
ORR	oxygen reduction reaction
P25	a commercial name of titanium dioxide
P90 (315)	a commercial name of titanium dioxide
P90 (416)	a commercial name of titanium dioxide
P90	a commercial name of titanium dioxide
PAN 150	polyacrylonitrile (M_w: 150 kg/mol)
PAN 200	polyacrylonitrile (M_w: 200 kg/mol), i.e. H-PAN
PAN	polyacrylonitrile
PE	polyethylene
pH_{IEP}	isoelectric point
pH_{PZC}	point of zero charge
PMMA	polymethyl methacrylate
PP	polypropylene

X

PSS	Polymer Standards Service company
PTFE	polytetrafluoroethylene
PVC	polyvinylchloride
r	correlation coefficient
R^2	determination coefficient
RDE	rotating disk electrode
Rh B	rhodamine B
RHE	reversible hydrogen electrode
RRDE	rotating ring disk electrode
rpm	revolutions per minute
SA	sodium alginate
SEC	size exclusion chromatography
SEM	scanning electron spectroscopy
SOS	spin-orbit splitting
SSA	solid solute adsorption
T805	a commercial name of titanium dioxide
tan δ	loss factor
T_d	decomposition temperature
TiO_2	titanium dioxide
TGA	thermo gravimetric analysis
UV-Vis	ultraviolet visible
vs.	versus
WDS	wavelength-dispersive X-ray spectroscopy
X-PAN	polyacrylonitrile (M_w: 74 kg/mol)
XPS	X-ray photoelectron spectroscopy
XRD	X-ray diffraction
ζ	zeta potential

Abstract

This project describes the preparation of spherical and porous polymer and carbon materials. In terms of nanocomposite materials, nanoparticles of titanium dioxide are embedded in the porous matrix of polymer and carbon spheres.

Large polymer spheres and nanocomposites (both in millimeter-size) were prepared via syringe pump by droplet shaping *cum* phase separation. Polyacrylonitrile (i.e. PAN) was chosen as the shaping polymer. Nanoparticles of titanium dioxide (i.e. P90) were selected as model particles. The shape and inner structure of polymer spheres were investigated from the properties of polymer solution (such as viscosity and surface tension), the falling distance of polymer droplets, gelation rate, and gelation temperature.

Hydrogel spheres of micrometer-size were prepared via drop-on-demand (i.e. DOD) ink-jetting shaping *cum* crosslinking. Sodium alginate (i.e. SA) was chosen as the model polymer for feasibility study. The shape of SA hydrogel microspheres was studied from driving voltage and the properties of SA solution (e.g. viscosity and surface tension). PAN microspheres of micrometer-size were prepared via DOD ink-jetting shaping *cum* phase separation. The shape of PAN microspheres was studied from shaping parameters (such as driving voltage, shaping frequency, and shaping temperature), the direction and falling distance of microdroplets, gelation rate, and properties of PAN solution (e.g. molecular weight, viscosity, and surface tension).

Large polymer spheres and nanocomposites were carbonized to corresponding carbon spheres and nanocomposites. The carbonization process was divided into pre-oxidation and pyrolysis. In pre-oxidation, both oxidation temperature and retention time were studied. The oxidation temperature was influenced by the flow rate of air. In pyrolysis, pyrolysis and activation were done at the same time using carbon dioxide to reopen the surface pores of carbon samples. Important factors are pyrolysis temperature, retention time, and flow rate of atmosphere. Similarly, the pyrolysis temperature was also affected by the flow rate of atmosphere.

Large polymer and carbon spheres were applied in adsorption tests. The polymer spheres were used as polar adsorbents while carbon spheres were used as low polar adsorbents. The affinity between solutes (i.e. various phenols and dyes) and adsorbents was investigated by adsorption isotherms. Based on the properties of solutes and adsorbents, several adsorption mechanisms were proposed to explain the interaction between solutes and adsorbents. The adsorption capacity of different adsorbents to selected solutes was also compared in terms of the porous structure of adsorbents.

The photocatalytic performance of large polymer and carbon nanocomposites was also examined in terms of the content of nanoparticles. Compared with the photocatalytic rate of P90, both polymer and carbon nanocomposites had lower photocatalytic rates. In carbon nanocomposites, carbon matrix's absorption to UV light was responsible for the decrease of photocatalytic rates. In addition, the transformation of crystal form of P90 (i.e. anatase phase to rutile phase) was also found after carbonization. XPS results of carbon nanocomposites showed that there were no new bonds forming between nanoparticles and carbon matrix after carbonization.

Three carbon materials were inspected for the potential application in oxygen reduction

reaction (i.e. ORR). Active species, such as quaternary N (i.e. N-Q) and pyridinic N (i.e. N-6), were found in all three carbon materials. Carbon spheres of "1,000°C, 1 hour" showed the best ORR activity in all three carbon materials.

In conclusion, large polymer and carbon spheres were prepared and they showed distinct adsorption performance. Large polymer and carbon nanocomposites were also prepared, which showed quantitative photocatalytic activity towards model organic pollutant. Moreover, some carbon spheres showed promising properties for applications in ORR. Both PAN microspheres and SA hydrogel microspheres were successfully prepared by DOD ink-jetting shaping *cum* gelation. The preparation of PAN microspheres in this way has not ever been reported in literature.

Catalogue

1 Introduction

It is known that there is almost no serious problem of pollution in agricultural society. In industrial society, however, this problem becomes more and more challenging due to population explosion. With the advancement of industrialization and urbanization, vast pollutants from industry, households, and agriculture are poured into atmosphere, surface and underground water, soil, and ocean [1]. These pollutants are gathering and accumulating in these media and causing serious problems [2]. Due to the mobility of fluid, the treatment of large-area polluted air and water is rather tricky and troublesome. For small amount of pollutant in air and water, however, they can be diluted to harmless level by fast diffusion and convection.

The two main strategies of sewage treatment at a plant are separation and conversion. For separation strategy, it can be used for both undissolved pollutants (such as filtration, precipitation, centrifugation, and flotation) and dissolved pollutants (e.g. adsorption [3], ion exchange, membrane separation [4], and extraction). The conversion strategy is mainly divided into biological conversion and chemical conversion (such as acid-base neutralization, chemical precipitation, and redox process [5]).

As a part of the mainstream technologies, this project concentrates on the purification of contaminated water after preliminary treatment, which mainly contains dissolved pollutants. In this project, two principles of sewage processing are investigated, i.e. adsorption and redox process (i.e. photocatalysis).

Porous materials have superior adsorption performance due to its high porosity [6] and specific surface areas. Compared with porous monoliths [7], porous microspheres [8] in the range of micrometer allow a faster mass transfer in separation process due to their smaller size. An example of porous material is granular activated carbon [9], which is featured by high porosity and specific surface areas and used for the adsorption of pollutants from atmosphere and aqueous solution. Activated carbon can be produced by carbonizing natural materials or polymer precursors with preset pore structures. Polyacrylonitrile (i.e. PAN), which is famous in the fabrication of carbon fiber [10], can be readily carbonized into nitrogen-doped carbon materials. This nitrogen containing carbon material can also be used as electrode material in fuel cells [11].

Nanoscale inorganic particles, such as titanium dioxide, are popular in the fields of photocatalysis like water splitting [12] and pollutant degradation [13]. Nonetheless, due to their aggregation effects and ultra-small size, fixing them and increasing their operability and recoverability are vital issues for applications. Hence, a suitable carrier such as porous polymer or carbon spheres for nanoparticles (NPs) can overcome these problems to some extent. This composited material can not only adsorb pollutants but also decompose them.

In this work, spherical and porous polymer nanocomposites are composited by a simple blending method between nanoparticles and PAN matrix. Nanoparticles of titanium dioxide with photocatalytic activity are used as a model particle. After carbonization process, these polymer nanocomposites are converted to corresponding spherical and porous carbon nanocomposites. Porous polymer and carbon spheres are used as adsorbents to examine their adsorption performance while porous polymer and carbon nanocomposites are used as photocatalysts to evaluate their photocatalytic performance. Carbon materials as potential

ORR catalysts are also examined.

2 Theoretical foundations

In this chapter, the theoretical background and foundations of several concepts and technologies are introduced. They are porous materials, shaping methods, nanoparticles and photocatalysis, nanocomposites, carbonization, adsorption, and oxygen reduction reaction.

2.1 Porous materials

Porous materials are generally denoted as materials which have abundant pores and cavities. This structure renders porous materials low density, high specific surface areas, excellent adsorption property, and insulation performance. By these properties, porous materials are used in numerous areas, such as separation process [3, 4], carriers for catalyst or medicine [14, 15], and energy storage [11].

According to the classification of IUPAC with regard to pore diameter, pores can be divided into three categories [16]: micropores (less than 2 nm), mesopores (between 2 and 50 nm), and macropores (over 50 nm). Ordered porous materials have highly monodisperse pores while the pores of disordered ones are composed of micro-, meso-, and macropores with various ratios.

In terms of components, porous materials can be divided into organic porous materials (e.g. porous poly(styrene-co-divinylbenzene) resin), inorganic porous materials (such as zeolite, activated alumina, and silica gel), and organic-inorganic hybrid porous materials (e.g. metal organic framework, i.e. MOF).

Porous materials can be used in the form of spheres [8], two-dimensional membrane [4], and monolith [7]. In this work, spherical porous materials are preferred.

Polymer porous spheres with the diameter in the range of micrometer are called polymer porous microspheres. According to Fan and coworkers [16], polymer porous microspheres can be further classified by location and interconnectivity of pores as shown in Scheme 2.1.

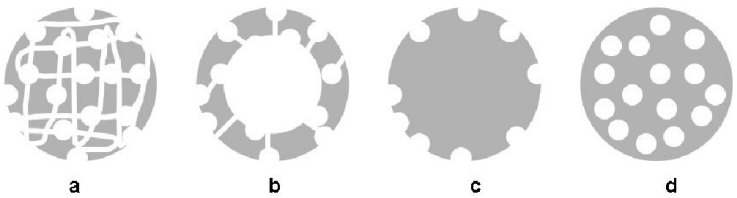

Scheme 2.1 The classification of polymer porous microspheres. a) a microsphere with “opened” pores; b) a microsphere with “opened” and hollow pores; c) a microsphere with “surface” pores; d) a microsphere with “closed” pores.

Porous microsphere “a” has inter-connective pores from surface to interior while the interior of microsphere “b” is hollow. Both “a” and “b” belong to “opened” porous microspheres. Microsphere “c” only has pores on its surface, which is called “surface” porous microsphere. Microsphere “d” only has pores in its interior and these pores are not inter-connective, which is called “closed” porous microsphere.

Polymer porous microspheres can be prepared by two methods. The first method is polymerization. Traditional polymerization method leads to polymer powders. The

introduction of porogen and cross-linking second monomer results in the formation of pores [8]. Most porogens are poor solvent or non-solvent to polymer. The importance of porogen to pore forming is higher than that of cross-linking second monomer [17, 18].
Both suspension and emulsion polymerization belong to heterogeneous polymerization [19, 20], which consists of monomer, cross-linking second monomer, porogen, water, and initiator. Stabilizer is used in suspension polymerization, which happens in the droplets of monomer, cross-linking second monomer, and porogen. Emulsifier is used in emulsion polymerization, which happens in the micelles of monomer, cross-linking second monomer, and porogen. Both dispersion and precipitation polymerization belong to homogeneous solution polymerization at the beginning [19, 20], which consists of monomer, cross-linking second monomer, porogen, solvent, and initiator. In dispersion polymerization, the early polymer nuclei can be swollen by monomer or solvent. Further polymerization happens in these nuclei. In precipitation polymerization, however, the early polymer nuclei can not be swollen by continuous phase. Further polymerization happens in continuous phase.
The modulation of size and porosity of porous microspheres by polymerization is complicated, which is related to many components and parameters. The purification of microspheres is also time-consuming.

2.2 Porous polymer spheres prepared from uncrosslinked polymers

2.2.1 Shaping polymer droplets

The second method of preparing polymer porous spheres is shaping, which has two steps: formation of droplets and solidification of droplets. Currently, there are three methods to shape droplets from polymer solution: dropping, spray, and dispersion. The solidification of droplets is mainly based on gelation (such as phase separation, sol-gel transition, salting out, and crosslinking reaction). Porous structure is formed during the gelation process, which will be discussed in detail in section 2.2.2. Examples of dropping method are shown in Scheme 2.2 [21].

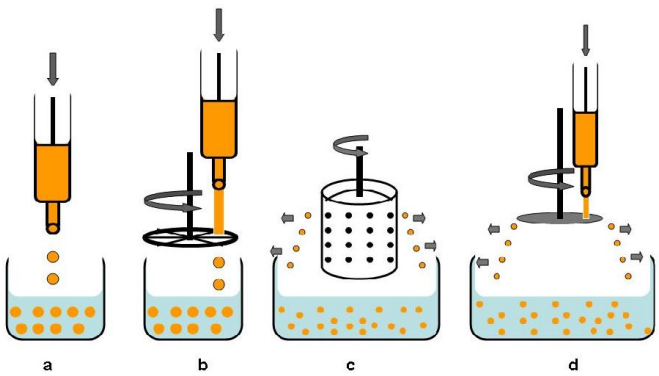

Scheme 2.2 Shaping droplets by dropping methods. a) by extrusion; b) by jet-cutting; c) by spinning cylinder; d) by spinning disk.

As shown in Scheme 2.2a, a spherical droplet is formed from an outlet, for example a syringe nozzle, by simply pressing. Droplets of polymer solution shaped by syringe pump are similar

to the formation of water droplets. The force analysis of a water droplet is shown in Scheme 2.3. Due to the low flow rate of water, water column can not be formed. With the increasing of volume of droplets attached on the tap, the droplets will form and fall down one by one if the gravity of droplets exceeds the additional pressure which is the total force (i.e. Δp) of surface tension.

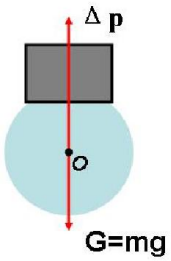

Scheme 2.3 Force analysis of an attached water droplet.

When the polymer solution is jetted at high speed from a nozzle, a thin continuous stream will form as shown in Scheme 2.2b. With a rotating knife, this thin jet will be cut into numerous discontinuous short jets. During the falling process, these short jets evolve into spherical droplets. In this technique, the size of droplets can be controlled by ejection speed, diameter of nozzle, and rotation speed of knife.

For large batch production, using "multithread" system is more favorable. In Scheme 2.2c, large numbers of droplets are formed in short time by rotary cylindrical vessel which is mapped with small holes. The size of droplets mainly depends on rotary speed, size of holes, and viscosity of solution. Instead by a disk, large numbers of droplets can also be thrown from the edge of disk as shown in Scheme 2.2d.

The spray method for large batch production is illustrated in Scheme 2.4.

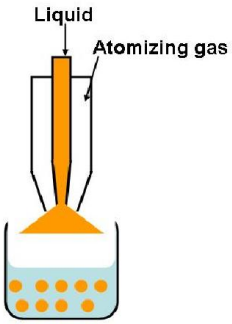

Scheme 2.4 Droplets shaped by spray method.

Large numbers of droplets can be shaped in short time. In this method, the liquid from inner pipe is scattered and dispersed into numerous droplets at the orifice by the high-pressure gas flowing from the outer pipe. It can be expected that the size of droplet is polydisperse and serious deformation of droplets can also happen. The size of droplets depends on many parameters, such as the pressure of atomizing gas, pumping pressure and viscosity of inner

liquid, and pressure difference between inner and outer pipe.
The dispersion method is demonstrated in Scheme 2.5 [21]. In this method, polymer solution is dispersed in another immiscible solvent of opposite polarity at high rotating speed. A large number of emulsion droplets are formed, which can be stabilized by surfactants. After gelation, these droplets are converted to spheres with the same size. The size of droplets depends on the amount and type of surfactant, stirring speed, ratio of "oil and water", and viscosity of both polymer solution and another liquid.

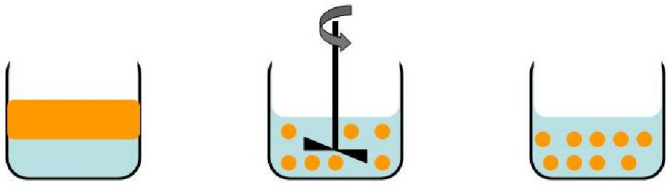

Scheme 2.5 Droplets shaped by dispersion method.

In this work, large droplets were prepared from a syringe pump (Scheme 2.2a) while microdroplets were prepared from an equipment as discussed in section 2.2.3.

2.2.2 Gelation of polymer
Non-solvent induced phase separation (NIPS)
Membrane filtration, as a booming technology which aims to separate, concentrate, refine, and purify substances from various processes, applies to vast fields, such as seawater desalination, industrial wastewater treatment, and pharmaceutical concentration. Combining the advantages of porous membrane (i.e. high flux) and dense membrane (i.e. high selectivity), the asymmetric membrane is mostly used in industrial processes. Most asymmetric membranes are made up of polymer. According to the materials used, asymmetric membranes are divided into phase separation membranes and composite membranes.
Several phase inversion methods can be used to prepare phase separation membranes, such as solvent evaporation and precipitation, non-solvent absorption and precipitation, thermo precipitation, and immersion precipitation (the Loeb-Sourirajan method [22, 23]).
In this work, phase inversion by immersion precipitation method was selected, which was used to transform droplets of polymer solution to porous polymer spheres. When the polymer droplets come into the coagulation bath of non-solvent, the non-solvent and solvent will diffuse mutually because of the chemical potential difference between them. In this case, the phase separation was initiated. Concentrated phase of polymer becomes the framework of polymer spheres while dilute phase of polymer becomes the pores and cavity. Based on the beginning time of phase separation upon immersion, phase separation can be classified as instantaneous demixing and delayed demixing. With isothermal and isobaric conditions, the phase diagram of a three-component system can be simplified to a composition triangle as shown in Scheme 2.6 [24].

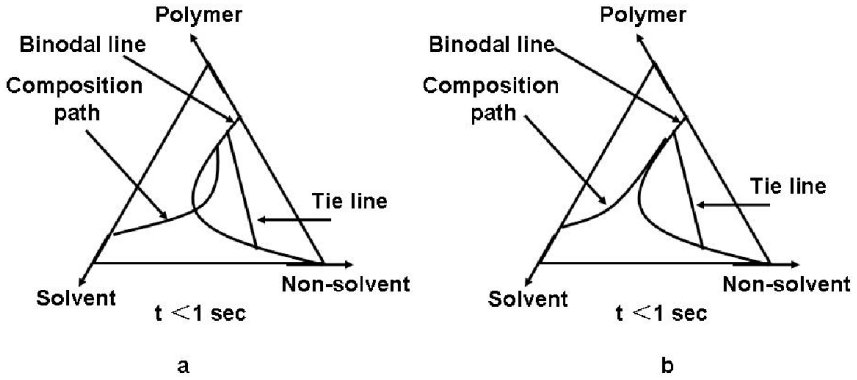

Scheme 2.6 Classification of non-solvent induced phase separation. a) instantaneous demixing; b) delayed demixing.

Instantaneous demixing is characterized by the intersection between composition path and binodal line immediately after immersion as shown in Scheme 2.6a. By contrast, delayed demixing (Scheme 2.6b) does not have this intersection at that time. Take an asymmetric membrane for example. Its skin layer is formed via delayed demixing (featured by sponge-like pores) while its supporting layer is formed via instantaneous demixing (featured by finger-like pores).
The principle of delayed demixing is to decrease the gelation rate of casting solution. This can be achieved by adding solvent into coagulation bath, which can decrease the chemical potential difference between the solvent of droplets and coagulant.

Crosslinking reaction
The feasibility of shaping by DOD ink-jetting was firstly studied with aqueous sodium alginate (SA) solutions. The polymer chains of sodium alginate connect with each other to form hydrogels via crosslinking reaction between Ca^{2+} (from $CaCl_2$ solution) and $-COO^-$ groups (from polymer chains).

2.2.3 Microdroplets shaped by drop-on-demand (DOD) method
Process description of DOD shaping
The qualitative description of shaping microdroplets by DOD is illustrated in Scheme 2.7. After being filled, the capillary tube is full of dispensing liquid. Under negative pressure, the gravity of droplet does not exceed the combination of air pressure and the total force of surface tension. As a result, the liquid can not form a droplet.
Take a shaping circulation for example [25]. When the shaping starts, the driver produces a series of driving signals (i.e. electrical pulses) which are accepted by the piezo-transducer. With these electrical pulses, the mechanical movement of piezo-transducer produces pressure pulses in the liquid. Then these pressure pulses propagate in the capillary tube. During this process, the liquid is accelerated and can reach a flow velocity as high as 10 m/s, which results in a small segment of liquid jet. This jet ejects from the nozzle. In the air, this liquid jet is quickly decelerated by pressure loss and air resistance with a typical terminal velocity of 2-3 m/s. As a result of interaction of gravity and surface tension, it forms a droplet. The rest

of the liquid retracts into the nozzle and oscillates until the frictional force makes the liquid rest. Owing to the capillary force in the nozzle, the vacancy of nozzle is refilled automatically from the liquid reservoir.

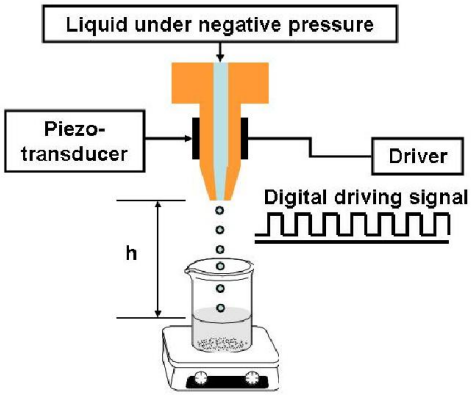

Scheme 2.7 Microdroplets shaped by DOD method. “h”: falling distance of liquid droplets.

The miniature high-speed camera system is an important supplementary system to observe the generation of droplets. With this system, both static photographs and dynamic videos of microdroplets can be captured. This system contains a strobe diode and a charge coupled device (i.e. CCD) camera. The strobe diode contains a light emitting diode, which generates short flashes synchronous to the driver electronics. As a result, the droplet generation is frozen optically and can be captured by the CCD camera. The delay between strobe light and the drive pulse is defined as “strobe delay”, which spans from 0 to 1,000 μs. This range makes the observation of most droplets formation possible.

Process analysis of DOD shaping

The formation of microdroplets by the DOD system can be divided into three stages: pipe flow of polymer solution with pressure, orifice flow, and jet breakup.

In capillary tube, due to the periodical movement and squeezing of piezo-transducer, the flow of polymer solution is a kind of flow with pressure. Because of the high viscosity and low flow rate (less than 10 m/s) of polymer solution, this pipe flow is also a laminar flow (i.e. flow in the form of layers) and one dimensional flow. Since the velocity gradient is perpendicular to the flow direction, this laminar flow is also a shear flow. Without heating and blocking, it is also a kind of isothermal flow and stable flow.

At the stage of orifice flow, continuous liquid column of polymer solution becomes a small segment of jet. Because the orifice is circular, this jet is a circular jet. There is no limitation to the flow of circular jet after coming out the orifice, so the circular jet is also a free jet. Since the polymer solution jet comes into a different medium (e.g. air), this circular jet is also an unsubmerged jet. After coming out of the nozzle, polymer solution still keeps the characters of laminar flow within short time. As the operation mode of shaping equipment is DOD, the circular jet is also a discontinuous jet and an impact jet.

At the stage of jet breakup of polymer solution, the main reason of jet breakup is the intermittent extrusion operation of piezo-transducer, i.e. the discontinuous jet. With the

interactions between surface tension and gravity, the cylindrical jet becomes a droplet.

2.2.4 Deformation and breakup of droplets

After coming out of the orifice, the spherical droplets of polymer solution fall down in the air and come into the coagulation bath. These droplets are transformed into polymer spheres by two steps: transient impact of droplets with coagulant surface and the following gelation process. The deformation and breakup of final spheres are related to these two steps. In addition, the deformation is also related to the properties of polymer solution.

The impact of general droplets on surface is a dynamic process within short time. During this process, the shape evolution of droplets is complex. According to the difference of surface, the impact of droplets can be divided into impact on a dry solid surface, impact on a wet solid surface, and impact on a liquid surface. In this section, the impact on a liquid surface is discussed in detail. The impact of droplets on a liquid surface is shown in Scheme 2.8. From the moment of impact to the vanishing of droplets (i.e. submerged in liquid reservoir), five typical behaviors of droplets can be summarized.

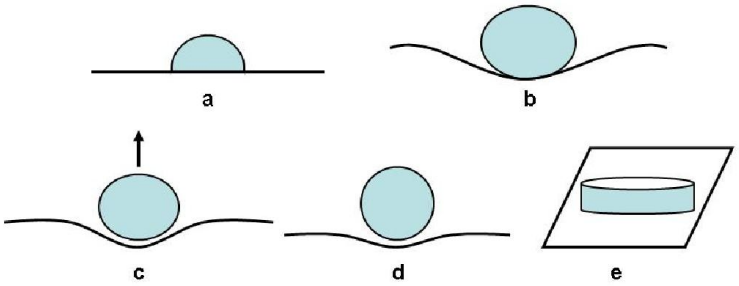

Scheme 2.8 Various situations of a droplet hitting on a liquid surface. a) “spreading”; b) “coalescence”; c) “bouncing”; d) “floating”; e) “splashing”.

- Behavior “a” is called deposition or spreading of droplets. This droplet remains attached to the liquid surface without breaking up. The impact of low-velocity droplets shows this behavior.
- Behavior “b” is called coalescence of droplets with liquid surface. If the droplet can rupture a thin film of gas and repel this gas film from the surface of liquid, this droplet can coalesce into the reservoir.
- Behavior “c” is called bouncing of droplet. If the liquid surface is perturbed, then bouncing of droplets can happen.
- Behavior “d” is called floating of droplets on liquid surface. With the help of gas cushion, droplets in this case can float for several seconds.
- Behavior “e” is called splashing of droplets on liquid surface. In this case, droplets with high impact velocity hit on the liquid surface. A crater is formed, which is surrounded by a liquid crown.

At the moment of impact, two parameters influence the deformation of droplets, which are impact velocity and rigidity of droplets. Impact velocity of droplets is a velocity at which the droplet hits the surface. Empirically, higher impact velocity leads to larger deformation of

droplets. Due to addition of polymer, droplets of polymer solution will not splash even impacting with high velocity. A critical impact velocity can be defined under specific conditions. Below this velocity, no deformation of droplets will happen. Above this velocity, the deformation of droplets will definitely occur. If the liquid reservoir is kept the same, higher rigidity of droplets results in smaller deformation of droplets. For droplets of polymer solution, rigidity can be described by viscosity or concentration of polymer solution.

At the stage of gelation, there are still two factors influencing the deformation of droplets, which are gelation rate of droplets and surface tension. Before complete gelation, high gelation rate of droplets is beneficial to spherical droplets and detrimental to deformed droplets. With enough coagulant and suitable speed of stirring, gelation rate is related to the ratio of N,N-dimethylformamide (i.e. DMF) in coagulant for droplets of polyacrylonitrile solution and related to concentration of Ca^{2+} in coagulant for droplets of sodium alginate solution. Higher DMF ratio leads to lower gelation rate while higher concentration of Ca^{2+} results in higher gelation rate.

If the droplets of polymer solution are in the state of "spreading" or "coalescence" as shown in Scheme 2.8a and 2.8b, the surface tension of droplets and coagulant will also count. The effect of surface tension can be demonstrated by Scheme 2.9 [26]. Droplet "1" is not miscible with liquid reservoir "2".

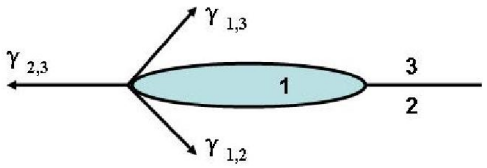

Scheme 2.9 Spreading analysis of a droplet on another kind of liquid. "1": droplet; "2": liquid reservoir; "3": gas; $\gamma_{1,3}$: interfacial tension between droplet and gas; $\gamma_{2,3}$: interfacial tension between liquid reservoir and gas; $\gamma_{1,2}$: interfacial tension between droplet and liquid reservoir.

According to Antonoff's rule [27], interfacial tension $\gamma_{1,2}$ can be calculated by Formula 2.1.

$$\gamma_{1,2} = |\gamma_1 - \gamma_2|$$

Formula 2.1

$\gamma_{1,2}$: interfacial tension between droplet and liquid reservoir;

γ_1: surface tension of droplet;

γ_2: surface tension of liquid reservoir.

Given that $\gamma_{1,3}$ equals the surface tension of this droplet and $\gamma_{2,3}$ is the surface tension of liquid reservoir, then droplet can spread on liquid reservoir if Formula 2.2 is satisfied [26]; otherwise, the droplet will try to keep spherical shape.

$$\gamma_{2,3} \geq \gamma_{1,3} + \gamma_{1,2}$$

Formula 2.2

Generally, liquid with low surface tension is easy to be spread on another liquid which has higher surface tension. Nonetheless, liquid with high surface tension is hard to be spread on another liquid which has lower surface tension.

2.3 Nanoparticles (NPs) and photocatalysis

Inorganic nanoparticles are denoted as aggregates of particles whose diameters are between 1 and 100 nm. This dimension belongs to mesoscopic range. Titanium dioxide (i.e. TiO_2) nanoparticles were used in this work and a short introduction of it is given below.

Titanium dioxide is a kind of n-type semiconductor, which can offer extra electrons compared to semiconductor silicon. There are three crystal forms of TiO_2 in nature, which are anatase phase, rutile phase, and brookite phase. Both anatase phase and rutile phase belong to tetragonal crystal system. Since they have different Bravais lattices, the X-ray diffraction spectra of them are different. In the XRD spectrum of anatase phase, the most intensive signal is at 25.5° while the most intensive signal of rutile phase is at 27.5° [28]. These two peaks can be used to calculate the ratio of anatase phase and rutile phase in a multiphase TiO_2 sample.

Both anatase phase lattice and rutile phase lattice can be described by a Ti-O tetrahedron. The main differences are the degree of distortion and connection style of this tetrahedron. The anatase phase lattice is composed of Ti-O_6 tetrahedron with common sides while the rutile phase lattice is composed of Ti-O_6 tetrahedron with common vertexes as shown in Scheme 2.10.

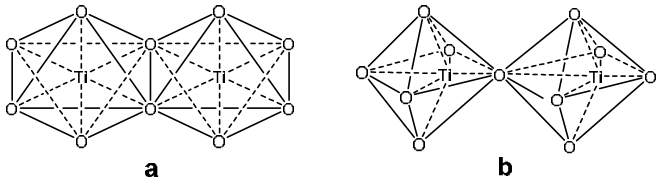

Scheme 2.10 Lattice structure of different phase of TiO_2. a) anatase phase; b) rutile phase.

The Ti-Ti distance in anatase phase is larger than that in rutile phase while the Ti-O distance of anatase phase is smaller than that of rutile phase. Actually, the anatase phase can be regarded as a tetrahedral structure while the rutile phase can be seen as an octahedral structure with a slightly distortion.

The rutile phase is the most stable and abundant in nature, generally used as pigments and absorber of ultraviolet light. Anatase phase is generally used as photocatalyst. The photocatalytic schematic of TiO_2 nanoparticles is shown in Scheme 2.11 [29].

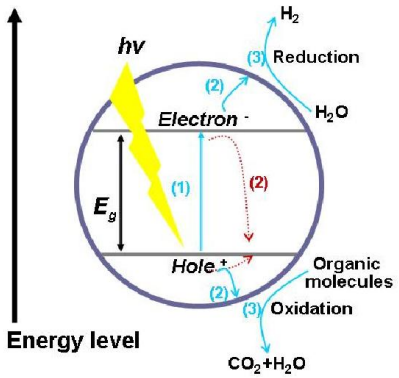

Scheme 2.11 Photocatalytic principle of TiO_2 nanoparticles.

The band gap of anatase phase is 3.2 eV while the band gap of rutile phase is 3.0 eV. When anatase phase is irradiated by light with a wavelength equal to or lower than 388 nm (414 nm for rutile phase), electrons are excited from valence band into conduction band. Therefore, the electron-hole couples form. These electron-hole couples can either recombine or react with the environment. The electrons can react with water as reducing agents and create hydrogen on the surface of nanoparticles. This process is called water splitting. The holes can react with water or OH^- as oxidizing agents and create hydroxyl radicals (i.e. $\cdot OH$). Organic pollutants will be mineralized or decomposed into water and carbon dioxide by contacting with these hydroxyl radicals. This process is called pollutant degradation. Some researches suggest that the photocatalytic activity of anatase phase is higher than that of rutile phase [30, 31].

The rutile phase is stable even at high temperature. Anatase phase will have an endothermic reaction when heated, becoming rutile phase at last. The phase transition from anatase to rutile is a non-equilibrium process, usually happening at 400-1,000°C. This transition temperature is related to impurities, the size and specific surface areas of particles, heating rate, and atmosphere of treatment. The anatase-rutile phase transition of TiO_2 nanoparticles can happen at low temperature. The smaller the size of TiO_2 nanoparticles is, the wider is the range of transition temperature.

The thermo instability of anatase phase restricts its application at high temperature; however, there are still methods to increase its thermo stability. An example is that with titanium dioxide particles coated with SiO_2, the anatase phase can be kept even at 1,050°C [32]. Doped with carbon or nitrogen, the band gap of anatase phase can be reduced, which will increase the range of absorption wavelength. However, there are no studies for the influence of doped carbon on the phase transition from anatase to rutile, but it is assumed that the phase transition to the rutile phase is supported by the carbon [33].

2.4 Nanocomposites

As mentioned in section 2.3, TiO_2 plays an important role in the field of catalysis like water splitting reaction or pollutant degradation. Due to the aggregation effect and ultra-small size of nanoparticles, increasing the recoverability and operability of them during application is a vital issue. Nanocomposite is a potential solution to these problems.

2.4.1 Introduction of composites

Given by International Organization for Standardization (IOS), the definition of composites is a multiphase solid material composed of two or more matters which are physically or chemically different. In composites, the continuous phase is called matrix while dispersed phase is called reinforcing material. The dispersed phase is distributed throughout the continuous phase as an independent phase and there are interfaces between continuous phase and dispersed phase. The dispersed phase can be in the form of fiber, particle, and dispersive state.

Nanocomposites consist of two or more solid materials. The nanocomposite itself or at least one component of it should be in the range of mesoscopic range. Typically, one dimension of dispersed phase is at least in the range between 1 and 100 nm. Based on nanocomposites, polymer-inorganic nanoparticles composite can be introduced. For nanocomposites composited by polymer and inorganic nanoparticles, two composite methods can be used. The first one is to composite them by strong covalent or coordinative bonds. This method often happens during the modification of nanoparticles either in their wet-chemical synthesis [7] or in the second stage of modification [34, 35] after production. Both methods are now well described. Nonetheless, the specific properties of nanoparticles, such as band gap, may be changed during surface modification. For this reason, organic polymer and inorganic nanoparticles are often composited by weak interactions, such as hydrogen bonds, Van der Waals' force, or electrostatic force [7].

As to synthetic methods, polymeric and inorganic nanocomposites can be prepared by blending, filling, intercalation, and sol-gel method. Blending method is to mix polymer (such as powder, solution, emulsion, or melt) and nanoparticles directly. This method is rather simple but it is hard to control the distribution of nanoparticles in polymer matrix. With the existence of nanoparticles, macromolecules are polymerized *in situ* from monomers. This method is called filling. By this method, the distribution of nanoparticles in polymer matrix is rather homogeneous. Intercalation nanocomposite is achieved by exfoliating materials into two dimensional nanosheets, which are then dispersed in polymer matrix. Monodisperse nanocomposites can be acquired by this method. In the preparation of nanocomposites by sol-gel method, nanoparticles are synthesized *in situ* in polymer matrix. Nanoparticles acquired by this method have higher monodispersity and distribute homogeneously in polymer matrix; however, this method is rather time-consuming and complex. This nanocomposite is called hybrid nanocomposite.

2.4.2 Spherical and porous nanocomposites

For adsorption and as carriers for catalyst, nanocomposites with high porosity and specific surface areas are necessary. Porous structure of nanocomposites can meet this requirement. In addition, compared with nanocomposites in the form of monoliths, spherical nanocomposites in the range of micrometer are preferred because they allow faster mass transfer. In this work, polyacrylonitrile (PAN) is used as continuous phase while TiO_2 powders are used as dispersed phase. They are composited directly and simply by blending TiO_2 powders with polymer solution. After carbonization, the polymer-based nanocomposites are converted to carbon-based nanocomposites as shown in Scheme 2.12.

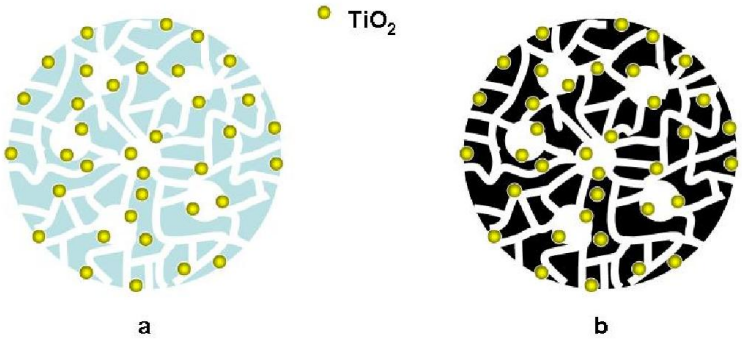

Scheme 2.12 Nanocomposites. a) polymer nanocomposites; b) carbon nanocomposites.

2.5 Carbonization

In order to convert polymer spheres and nanocomposites to corresponding carbon samples, carbonization of the polymer precursors is needed. For applications such as adsorption and catalysis, the carbon samples should be highly activated.

Activated carbon is characterized by high porosity and huge surface areas [3]. It is essentially a kind of amorphous carbon based on graphite microcrystals. The graphite microcrystals are hexagonal lattices with two dimensional orders. Activated carbon has various pores, such as capillary pores, ink-bottle pores, and slit. Activated carbon is currently used in many applications, such as the purification of gas, air, and water. Especially, it is the most common absorbent to remove dyes or organic pollutants from drinking water, groundwater, or wastewater through adsorption. Carbonaceous materials are used to prepare activated carbon, such as biomass, pitch, and coal.

2.5.1 General carbonization

The preparation of activated carbon needs two steps: carbonization and activation. Carbonization is essentially pyrolysis (i.e. thermal decomposition), which is done at inert atmosphere. The purpose of carbonization is to remove organic and volatile components, so this process is also called degassing or dry distillation [7]. During this process, reactions such as cyclization, aromatization, and polycondensation happen, which offers basic framework and strength to the final carbon materials.

Activation is essentially to etch carbon materials with activator [6]. With volatile products removed, new cavities form at the position of original carbon atoms. The first function of activation is to open closed pores, which are blocked by decomposed products, such as tar and amorphous carbon. The second function is to enlarge already existed pores with the help of activator. After activation, the internal channels are connected with each other.

There are two methods to activate carbon materials: physical activation and chemical activation [6]. The physical activation is to regard oxidative gas as activator, such as water steam and carbon dioxide (CO_2). The mechanism of CO_2 activation is shown in Formula 2.3.

$$C + CO_2 \rightarrow CO$$

The chemical activation uses activators such as KOH, H_3PO_4, and K_2CO_3. Compared with physical activation, this method is operationally complex though the activated products by this way usually have larger specific surface areas.

2.5.2 Carbonization of polyacrylonitrile (PAN)

Compared with biomass, pitch, and coal, the purity and composition of polyacrylonitrile prepared by polymerization is higher and more specific. When it is applied in carbonization, its behaviors of thermo decomposition will be easier to control. The reproducibility of results after carbonization is also good. It is known that mainstream carbon fibers are derived from polyacrylonitrile [10]. In addition, the existence of nitrogen can render final carbon materials additional advantages.

The carbonization of polyacrylonitrile in this work is divided into two steps: pre-oxidation and pyrolysis (with or without activation).

In literatures, there are mainly two reactions happened during the stabilization (i.e. pre-oxidation) process of PAN fiber, which are cyclization and dehydrogenation [10]. Both cyclization and dehydrogenation belong to thermal decomposition of PAN.

Cyclization is known to be the most important reaction in stabilization process [10]. In the cyclization reaction of linear PAN polymer, adjacent cyano groups firstly coalesced to form a six-membered ring. Then, a ladder structure formed, which is composed of a series of six-membered rings with common sides. This reaction is exothermic. Cyclization reaction can occur in both inert and oxidative atmosphere [10], i.e. oxygen is not involved in the reaction of cyclization.

By contrast, dehydrogenation is featured by the formation of double bonds in the chains of PAN [10]. This reaction can be divided into two steps: the oxidation of polymer chain and then the elimination of water. Due to the absence of oxygen, dehydrogenation reaction did not happen in inert atmosphere.

The intention of pre-oxidation is to crosslink the linear polymer chains and to generate a ladder structure to withstand following heat treatment [10]. This ladder structure can prevent the excessive removing of carbon element and thus improving the yield. The typical temperature for pre-oxidation is between 180 and 300°C. Factors related to this process are flow rate of air, heating rate, retention time, and oxidation temperature.

During pyrolysis, the aromatic growth and polymerization of the ladder polymer go further. Non-carbon elements are further removed and thermo stability and carbon content are further improved. Factors related to this process are flow rate of gas, heating rate, retention time, and pyrolysis temperature.

If the porosity and specific surface areas of final carbon materials are small, then activation is needed. In this work, CO_2 is selected as activator. In this case, pyrolysis and activation are done at the same time.

2.6 Adsorption

The schematic of gas-solid (or liquid-solid) adsorption system is shown in Scheme 2.13.

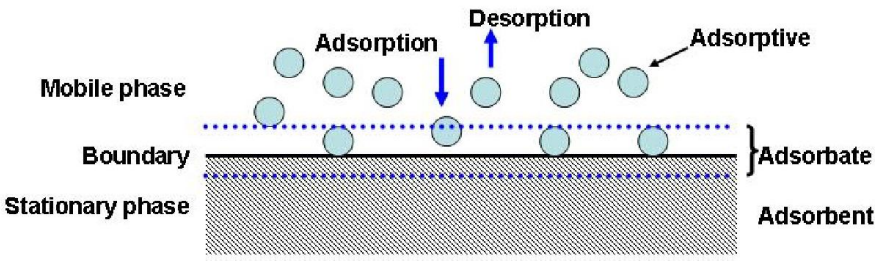

Scheme 2.13 Adsorption of fluid on solid.

This adsorption system basically contains two phases: mobile phase and stationary phase. The mobile phase is composed of gaseous or liquid substances while the stationary phase is generally solid.

When a molecule adheres to the surface of stationary phase, then an adsorption process of this molecule is finished. The substances adsorbed on the surface of stationary phase are called adsorbates whilst the stationary phase is called adsorbent. Being heated, for example, this molecule can also return back to the mobile phase. This process is called desorption.

According to the category of interaction between adsorbate and adsorbent, the adsorption process can be ascribed into chemical adsorption and physical adsorption. In chemical adsorption, new chemical bonds (such as covalent bonds) formed between adsorbates and adsorbents. This process is generally irreversible. With new bonds forming and old bonds broken, chemical adsorption is widely used in heterogeneous catalysis.

In physical adsorption, adsorbates are adsorbed on adsorbents by weak interactions, such as Van der Waals' force (such as dipole-dipole force and dispersion force), electrostatic force (between ions), and hydrogen bond. Due to these weak interactions, physical adsorption is generally reversible. Physical adsorption is widely used in separation process. This work focuses on physical adsorption.

2.6.1 Adsorption isotherms of gas-solid adsorption

In gas-solid adsorption, when the whole adsorption system reaches adsorption equilibrium, static adsorption capacity is defined by the Formula 2.4.

$$q_e = \frac{V_g}{m}$$

Formula 2.4

q_e: static equilibrium adsorption capacity;
V_g: volume of adsorbed gas;
m: mass of adsorbent.

For a specific gas-solid adsorption system, the adsorption capacity at adsorption equilibrium is related to temperature and pressure of the gas. This relation is described by Formula 2.5.

$$q_e = f(T, p)$$

Formula 2.5

q_e: adsorption capacity;
T: temperature at adsorption equilibrium;
p: pressure at adsorption equilibrium.

With the temperature of adsorption system constant, the experimental curves describing the relation between adsorption capacity and equilibrium pressure are called adsorption isotherms. Tens of thousands of adsorption isotherms were acquired from experiments. All of these isotherms can be classified into six categories as shown in Figure 2.1.

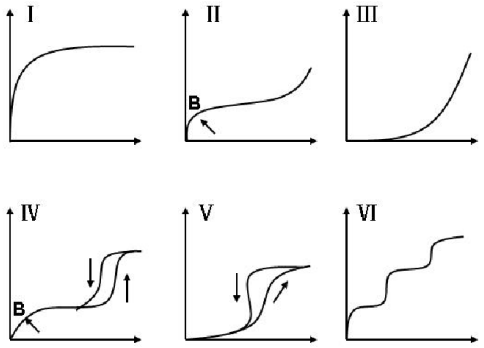

Figure 2.1 Classification of gas-solid adsorption isotherms. "B": B point, which implies the completion of monolayer adsorption of adsorbates.

This classification was firstly proposed by Brunauer, Deming, Deming, and Teller [36, 37], which is call BDDT classification.

Type I

In the scope of low pressure, the adsorption isotherm surges. It implies that strong adsorbate-adsorbent interaction exists in micropores. After a rapid increase, the adsorption capacity reaches saturated adsorption point, which means adsorption monolayer of adsorbate is finished. Materials featured by micropores always show this adsorptive behavior, such as zeolite and activated carbon.

Type II

In the scope of low pressure, the adsorption isotherm does not go up like the isotherm in Type I at the same pressure range. After that, the adsorption capacity increases linearly. In high pressure range, the adsorption capacity increases exponentially. Materials with micropores and macropores always show this adsorptive behavior and multilayer adsorption of adsorbates can happen.

Type III

In the whole pressure scope, the adsorption isotherm is convex to x axis. This adsorptive behavior demonstrates that the interaction between adsorbate and adsorbent is weak or the adsorbent is almost non-porous.

Type IV

This adsorption isotherm is similar to that of type II. There is hysteresis between adsorption isotherm and desorption isotherm. In adsorption isotherm, the pore filling (i.e. capillary condensation) starts from micropores, then mesopores, to macropores at last. In desorption isotherm, the order of pore draining is just reverse. The hysteretic isotherms can provide information about pore size and distribution of materials.

Type V

In the range of low pressure, isotherm of type V is similar to that of type III, which means the interaction between adsorbate and adsorbent is weak or the adsorbent is almost non-porous. At high pressure, the behavior of type V is similar to that of type IV. The hysteretic phenomenon of type V isotherm is also related to pore filling and pore draining.

Type VI

In the whole pressure range, the shape of this isotherm is similar to a ladder, which implies a step-by-step adsorption happens. This adsorption behavior is often observed in the adsorption process of fabrics with highly homogeneous surface.

2.6.2 Adsorption models of gas-solid adsorption

Gas adsorption is widely used to detect the porous structures of solid porous materials. Based on the adsorption isotherms from experiments, the porosity and specific surface areas of porous materials can be acquired. During this process, adsorption models are applied to explain the adsorption behavior of gas that various isotherms imply. In these adsorption models, both Brunauer-Emmett-Teller method (i.e. BET) [38] and Barrett-Joyner-Halenda method (i.e. BJH) [37, 39] demonstrate great superiority compared with other models.

BET method is known to estimate the surface areas of materials and its main hypotheses are as follows:

- The surface of adsorbent is homogeneous with all adsorption positions the same.
- There is no interaction between adsorbed molecules.
- The number of adsorbate layers varies from multilayers to infinite layers.

When adsorption and desorption of gas reach equilibrium, the total volume of adsorbed gas is the sum of the volume of each layer's adsorbed gas. The total volume of adsorbed gas is given by Formula 2.6.

$$V = V_{mono} \cdot \frac{C \cdot p}{(p_0 - p) \cdot \left[1 + (C-1)\frac{p}{p_0}\right]}$$

Formula 2.6

V: volume of adsorbed gas at specific relative pressure and temperature;

V_{mono}: volume of monolayer adsorbed gas;

C: a constant related to adsorption enthalpy change;

p: adsorption equilibrium pressure;

p_0: saturated vapor pressure of adsorptive.

Formula 2.6 is always used in its linear form as shown in Formula 2.7.

$$\frac{p}{V(p_0 - p)} = \frac{1}{V_{mono} \cdot C} + \frac{C-1}{V_{mono} \cdot C} \cdot \frac{p}{p_0}$$

Formula 2.7

With p/p_0 regarded as independent variable and $p/V/(p_0-p)$ as dependent variable, a regressive line can be acquired. Then C and V_{mono} can be determined from the slope and intercept of the regressive line. Generally, the relative pressure p/p_0 adopted by linear regression ranges from 0.05 to 0.2.

The most common gas adsorption instrument uses nitrogen as working medium. This physical adsorption instrument measures the adsorption isotherms at 77 K (i.e. -196°C), at which the saturated vapor pressure of liquid nitrogen is one atmospheric pressure. The surface areas of materials are given by Formula 2.8 [8].

$$S_{BET} = \frac{V_{mono} \cdot N_A \cdot A_M}{V_M}$$

Formula 2.8

S_{BET}: surface areas of adsorbent covered by nitrogen;
V_{mono}: volume of monolayer adsorbed nitrogen;
N_A: Avogadro's number, 6.022×10^{23} mol^{-1};
A_M: areas of a nitrogen molecule at 77 K, 0.162 nm^2;
V_M: molar volume, 22.414 L/mol.

The pore size distribution is determined according to BJH method [39], which is based on capillary condensation in the cylindrical pores. In this method, pore size in the range of 6-140 nm can be calculated based on the desorption isotherm. The pores of sample are firstly filled with nitrogen, and then pressure is gradually lowered. The adsorbed gas desorbs firstly from macropores, then mesopores, to micropores at last.

The radius of cylindrical pore (i.e. r_p) is composed of Kelvin radius (i.e. r_k) and the multilayer adsorption thickness (i.e. t) of nitrogen as shown in Formula 2.9.

$$r_p = r_k + t$$

Formula 2.9

r_p: radius of cylindrical pore;
r_k: Kelvin radius;
t: thickness of adsorbed layer.

The definitions of r_k and t are given in Formula 2.10 and 2.11, respectively.

$$r_k = \frac{2 \cdot \gamma \cdot V_M}{RT} \cdot \ln\left(\frac{p}{p_0}\right)$$

Formula 2.10

$$t = \sqrt{\frac{13.99}{\ln\left(\frac{p}{p_0}\right) + 0.034}}$$

Formula 2.11

r_p: radius of capillary pore;
r_k: Kelvin radius;
t: thickness of adsorbed layer;
γ: surface tension of adsorptive at boiling point;
R: universal gas constant (8.3145 J/mol/K);
T: temperature;
V_M: molar volume of adsorptive;
p: adsorption equilibrium pressure;
p_0: saturated vapor pressure of adsorptive.

2.6.3 Adsorption isotherms of solid solute adsorption

Different from binary gas-solid adsorption, solid solute adsorption (SSA) in dilute solution is related to solute, solvent, and adsorbent. Both solute and solvent can be regarded as adsorptive; therefore, there is possible competitive adsorption on adsorbent between solute and solvent.

In solid solute adsorption, the static adsorption capacity of adsorbent is given by Formula 2.12.

$$q_e = \frac{(C_0 - C_e) \cdot V_{sol}}{m}$$

Formula 2.12

q_e: static equilibrium adsorption capacity;
C_0: initial concentration of solute;
C_e: equilibrium concentration of solute;
V_{sol}: volume of solution;
m: mass of adsorbent.

This work concentrates on the adsorption of adsorbent in dilute solutions. With the adsorption temperature constant, the adsorption isotherms of SSA system can be classified into three categories (see Figure 2.2) according to the initial slopes of isotherms [40].

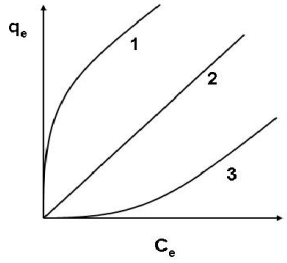

Figure 2.2 Classification of SSA adsorption isotherms. “1”: strong affinity; “2”: moderate affinity; “3”: weak affinity.

As shown in Figure 2.2, type 1 isotherm means there is strong affinity between solute and adsorbent while type 3 means the affinity between solute and adsorbent is very weak. Type 2 isotherm describes the case of adsorption with moderate affinity in dilute solution, adsorption with low coverage of adsorbates, or partition. It should be mentioned that Figure 2.2 mainly reflects the shape of isotherms within low equilibrium concentration section and this low concentration section varies for different adsorption systems. In addition, the affinities reflected by isotherms 1, 2, and 3 are only qualitative rather than quantitative.
In addition, Giles [41] proposed a more detailed classification of SSA isotherms according to the initial slopes of isotherms. There are four categories in this classification, which are S type, L (i.e. Langmuir) type, H (i.e. high affinity) type, and C (i.e. constant partition) type as shown in Figure 2.3.

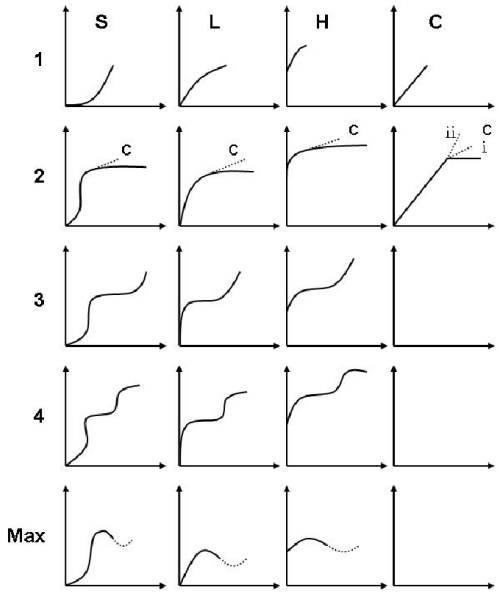

Figure 2.3 The classification of Giles’ adsorption isotherms. “S”: S type; “L”: Langmuir type; “H” high affinity type; “C”: constant partition type; “1”, “2”, “3”, and “4”: subgroups; “Max”: further adsorption; “c” in subgroup “2”: adsorption of micropores;

- Cases of S isotherm
  Adsorption in the system of non-polar adsorbents, polar solute, and non-polar solvent;

Adsorption in the system of polar adsorbents, non-polar solute, and polar solvent;

- Cases of L isotherm
  Adsorption in the system of non-polar adsorbents, non-polar solute, and polar solvent;
  Adsorption in the system of polar adsorbents, polar solute, and non-polar solvent;
- Cases of H isotherm
  This is a special case of L isotherm featured by extremely high affinity between solute and adsorbent.
- Cases of C isotherm
  This case is the same as that of type 2 isotherm. In C-2, the number of adsorption positions is constant before reaching saturated adsorption point.

It should be also mentioned that Figure 2.3 mainly reflects the shape of isotherms within low equilibrium concentration section and this low concentration section varies for different adsorption systems. In addition, the affinities reflected by isotherms S, L, H, and C are only qualitative rather than quantitative.

2.6.4 Adsorption models of solid solute adsorption

To describe adsorption behavior in dilute solutions, the basic adsorption models used in this work are Henry model, Langmuir model, and Freundlich model.

Henry model

In this model, the adsorption capacity is proportional to equilibrium concentration as shown in Formula 2.13. Type 2 isotherm can be finely described by Henry model [8].

$$q_e = K_H \cdot C_e$$

Formula 2.13

q_e: adsorption equilibrium capacity (mg/g);
C_e: adsorption equilibrium concentration (mg/L);
K_H: Henry partition coefficient (L/g).

Langmuir model

Langmuir model is classical for describing monolayer adsorption of adsorbates as shown in Formula 2.14 [8].

$$q_e = \frac{q_{mono} \cdot b \cdot C_e}{1 + b \cdot C_e}$$

Formula 2.14

q_e: adsorption equilibrium capacity (mg/g);
C_e: adsorption equilibrium concentration (mg/L);
q_{mono}: adsorption monolayer capacity (mg/g);
b: Langmuir adsorption factor (L/mg).

The basic hypotheses of this model are as follows:

- Both adsorption and desorption of adsorbates continue before reaching adsorption equilibrium.
- At equilibrium, adsorbates form a monolayer on the surface of adsorbent.
- The surface of adsorbents is homogeneous and there is no interaction between adsorbates.

The Langmuir model can be applied to analyze the affinities quantitatively reflected by adsorption isotherms. Two preconditions, however, should be met. The first one is that the type of all the isotherms should be type 1 (i.e. L or H type). The second one is that all the isotherms for comparison should have fine regression results from Langmuir model. For the concentration section to regress, low concentration section is preferred which meets the definition of isotherms' classification as discussed in section 2.6.3. The larger the *b* value is, the higher is the affinity of isotherm within selected concentration section.
The linear form (Formula 2.15) of Langmuir model can be used to determine the monolayer capacity by linear regression, with C_e as independent variable and C_e/q_e as dependent variable.

$$\frac{C_e}{q_e} = \frac{1}{q_{mono}} \cdot C_e + \frac{1}{b \cdot q_{mono}}$$

Formula 2.15

Freundlich model
For inhomogeneous surface of adsorbents, Freundlich model is preferred as shown in Formula 2.16 [8]. In this model, when the *n* equals to one, Freundlich model becomes Henry model, which can describe the isotherm of type 2. When the *n* is less than one, Freundlich model can describe the isotherm of type 3. If *n* is more than one, type 1 isotherm can be described by this model.

$$q_e = K_F \cdot C_e^{\frac{1}{n}}$$

Formula 2.16

q_e: adsorption equilibrium capacity (mg/g);
C_e: adsorption equilibrium concentration (mg/L);
K_F: indicator of adsorption affinity [(mg/g)(L/mg)$^{1/n}$];
1/n: Freundlich adsorption constant.

K_F is known to be related to adsorption affinity and adsorption capacity while *1/n* is only related to affinity between adsorbates and adsorbents. The larger the K_F value is, the higher is the affinity of isotherm within selected concentration section. Moreover, the smaller the *1/n* value is, the higher is the affinity of isotherm within selected concentration section.
The Freundlich model can be applied to analyze the affinities quantitatively reflected by adsorption isotherms. The affinities reflected by isotherms from different types can also be

compared by using Freundlich model. The only requirement is that all the isotherms for comparison should have fine regression results from Freundlich model. For the concentration section to regress, low concentration section is preferred which meets the definition of isotherms' classification as discussed in section 2.6.3.
The linear form (Formula 2.17) of Freundlich model can be used to determine K_F and $1/n$ by linear regression, with $lg(C_e)$ as independent variable and $lg(q_e)$ as dependent variable.

$$\lg(q_e) = \frac{1}{n} \cdot \lg(C_e) + \lg(K_F)$$

Formula 2.17

2.6.5 Adsorption mechanism of activated carbon
Van der Waals' force is a kind of attractive force and it only exists within several picometers. If the interaction between adsorbate and adsorbent is mainly Van der Waals' force (dipole-dipole force or dispersion force), the affinity between adsorptive and adsorbent will depend on the size of adsorptives and the diameter of pores in adsorbent. The following discussions are based on that Van der Waals' force offers the main affinity.
With the diameter of pores less than 2 nm, the surface areas of micropores are huge if the number of them is large enough. These pores offer the main adsorption positions for general adsorptives.
With the diameter of pores over 2 nm but less than 50 nm, mesopores are the main access for adsorptives. These pores can also provide some positions for large adsorptives.
With the diameter of pores over 50 nm, macropores are the entrance for adsorptives entering the interior of adsorbent. Generally, the ratio of surface areas from macropores in total surface areas is small if the number of macropores is small.
The detailed adsorption state of adsorbates on adsorbents is illustrated in Scheme 2.14 [6].

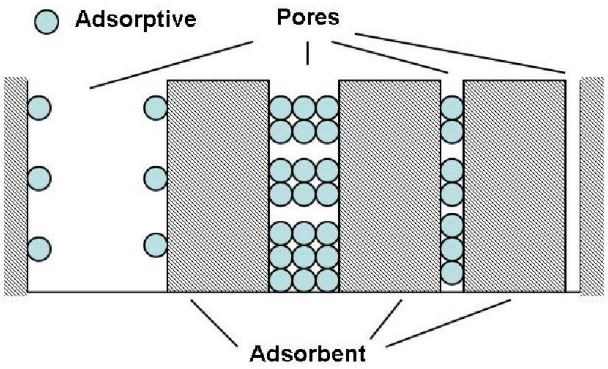

Scheme 2.14 Adsorption mechanism dominated by Van der Waals' force.

- With the diameter of adsorptive far less than that of pores, the adsorbates can easily desorb from adsorption positions. At low equilibrium concentration, the adsorption capacity is low.
- With the diameter of adsorptive less than that of pores, capillary condensation of

adsorptives happens in these pores. The adsorption capacity is large in this case.

- With the diameter of adsorptive close to that of pores, the affinity between adsorbent and adsorbate is the strongest. The adsorption capacity is huge even at low equilibrium concentration.
- With the diameter of adsorptive more than that of pores, no adsorption happens. All pores are closed for adsorptives.

Activated carbon is a kind of material with low polarity, which prefers to adsorb non-polar molecules. When it is used as adsorbent in solid solute adsorption, the affinity mainly comes from dispersion interaction between activated carbon and solute. For adsorptive with specific size, high adsorption capacity depends on two conditions.
The first condition is the affinity of adsorption site. With the diameter of pores more than that of specific adsorptive, higher affinity comes from those pores with diameter closer to the size of adsorptive.
The second one is the number of adsorption sites. The number of adsorption sites mainly depends on the surface areas and pore volumes of suitable pores, which cater for the first requirement.

2.7 Oxygen reduction reaction (ORR)

The generation, conversion, and storage of energy are a core problem from ancient times. Since electricity is clean, economic, and convenient, it constitutes the framework of modern society. Up to now, electrical energy is mainly and indirectly generated by mechanical energy conversion from fossil energy. Direct electrochemical conversions, such as metal-air batteries and fuel cells [11], are emerging, which have a core concern on the oxygen reduction reaction (ORR).
With fuel as energy, the equipment which can convert the chemical energy of fuel to electricity directly is called fuel cell. This equipment is an open system, which allows the continuous exchange of energy and substance between cell itself and external environment. Moreover, the energy conversion efficiency of fuel cell is not limited by the efficiency of heat engine of Carnot cycle.
A typical hydrogen-oxygen fuel cell is shown in Scheme 2.15 [26].

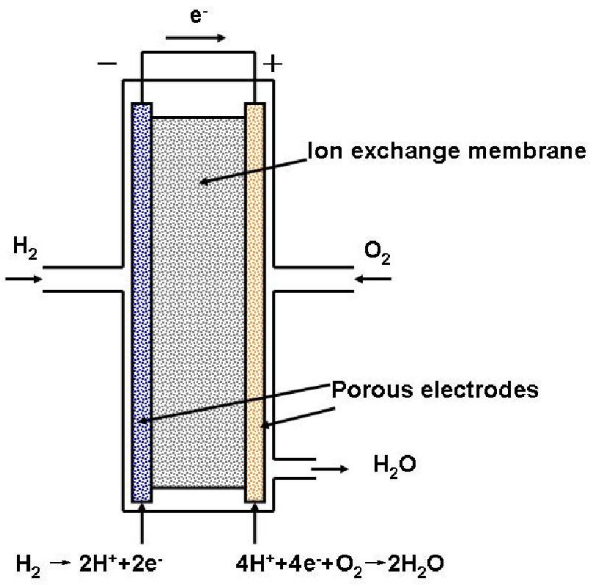

Scheme 2.15 Principle of a hydrogen-oxygen fuel cell using ion change membrane as separator in acid environment.

In order to convert chemical energy to electricity, the fuel should be firstly ionized. Since most fuels are organic compounds, the electrodes should be able to catalyze the conversion from electroneutral molecule to ions. In hydrogen-oxygen fuel cell, the exchange current of hydrogen anode is large enough while the exchange current of oxygen cathode is too small. In order to enhance the overall performance of fuel cell, materials (e.g. catalyst) that can catalyze the reduction reaction of oxygen are thought to be used in electrode materials. Traditionally, metal platinum can efficiently catalyze this conversion; however, high cost of platinum-based materials limits its wide application [11]. Therefore, alternative catalysts, such as non-noble metal or metal-free catalyst, are necessary. Among these alternative catalysts, nitrogen doped carbon materials are emerging.

There are two microscopic mechanisms of oxygen reduction in ORR [11]. The first one is that an oxygen molecule is directly reduced into four OH^- or two H_2O. This is a four-electron transfer process in one step. The electron transfer number (n) per oxygen molecule is four. The second mechanism can be described by two-electron transfer in two steps. The oxygen molecule is firstly reduced into H_2O_2 or $(HO_2)^-$. This is a two-electron transfer process and the n is two. These H_2O_2 or $(HO_2)^-$ can be further reduced into H_2O or OH^-, which is also a two-electron transfer process. When the n of an ORR is between two and four, it means that the reduction reaction is a mixed process of four-electron transfer and two-electron transfer.

The ORR activity of one catalyst can be readily evaluated by electrochemical characterization. Since ORR process is an electrochemical reaction on electrode, voltammetry is preferred to study this process [11, 42], which focuses on the relation between electrode potential and current. With the electrode potential ramping linearly and continuously, linear sweep voltammetry (LSV) is developed by measuring the response current simultaneously. The results (i.e. polarization curves) are presented in the form of voltammograms (i.e. current-potential curves). Unlike in LSV, the sweep of electrode potential in cycle voltammetry (CV) is bidirectional rather than unidirectional. At the same time, the cycles of

sweep can be repeated as many as needed in CV.
When there is relative motion between electrodes and electrolyte solution, the mass transfer of reactants and products in measuring system is strongly affected by convection. This method is called hydrodynamic method [42], which is also called forced convection technology. Rotating disk electrode (RDE) and rotating ring disk electrode (RRDE) are two representatives. When this method is introduced into LSV, it can increase the rate of mass transfer by diffusion and thus suppress or eliminate the effect of mass transfer by diffusion on electrochemical reactions. In this way, the importance of mass transfer by diffusion among all electrode reactions can be suppressed and steady state of electrode reactions can be reached promptly. In addition, forced convection technology can render the diffusion layer more homogeneous.
In terms of catalyst's structure-property relation, the ORR performance of nitrogen doped carbon materials can be analyzed from three aspects: porosity, conductivity, and catalytic activity.

- Porosity

In fuel cell, the electrode should be porous, which can provide much contact interface between fuel, electrolyte, and electrodes and accelerate the electrode reactions. In this way, higher output current can be generated. Nitrogen doped carbon materials with large specific surface areas and specific pore volumes undoubtedly promote the mass transfer happening on the electrodes.

- Conductivity

The conductivity of carbon materials can be analyzed from two aspects: the conductivity of carbon matrix and the effect of non-carbon elements doping on conductivity. Single crystal graphite is composed of multilayer graphene, which is linked by Van der Waals' force. Therefore, graphite is anisotropic. The conductivity of graphite varies as the conduction channel of electrons varies. The conductivity of graphite is high when the channel of electron conduction is parallel to the basal plane of graphite while the conductivity is low when the channel of electron conduction is vertical to the basal plane. Overall, the conductivity of graphite is higher than that of amorphous carbon.
Nitrogen atoms can be introduced into carbon materials as chemical nitrogen and structural nitrogen [43]. Both $-NH_x$ (x: 1-2) and $-NO_x$ (x: 1-3) can be attributed to chemical nitrogen while pyrrolic N, pyridinic N, and quaternary N belong to structural nitrogen as shown in Scheme 2.16.

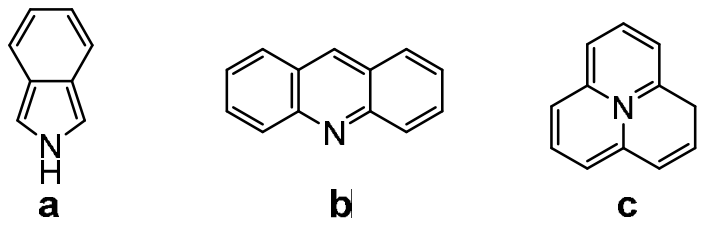

a b c

Scheme 2.16 Possible structural nitrogen in nitrogen doped carbon materials. a) pyrrolic nitrogen; b) pyridinic nitrogen; c) quaternary nitrogen.

Chemical nitrogen atoms do not engage in the conjugated π system of graphene and could be seen as defects in the carbon matrix. Theoretically, structural nitrogen at least does not damage the conjugated π system of graphene since the carbon atoms in graphene are replaced by nitrogen atoms and the p electrons of nitrogen are incorporated into the conjugated π system of graphene. Therefore, over doping of nitrogen (especially chemical nitrogen) can decrease the conductivity of carbon materials due to the nitrogen induced substitution defects. Apart from nitrogen species, another factor that affects the conductivity of carbon materials is the total content of nitrogen in carbon materials. In the work of Ismagilov and et al. [44], an optimum nitrogen concentration was found to be 3.1% by weight. When the nitrogen concentration increased up to 8.2%, the electrical conductivity of the carbon fibers decreased. The authors in research [43] found that the total amount of nitrogen within the carbon matrix is not the predominant main parameter to the electrical conductivity but the content of quaternary N counts.

- Catalytic activity

Generally, four species [45, 46] of nitrogen related to the ORR activity of nitrogen doped carbon materials could be recognized, which are quaternary N (i.e. N-Q), pyridinic N (i.e. N-6), pyrrolic N (i.e. N-5) and pyridonic N (i.e. N-X). In most articles, the active sites for ORR in nitrogen doped carbon can be attributed to quaternary N [47] or pyridinic N [48]. In research [48], the ORR active site is created by pyridinic N. More exactly, the ORR active sites in nitrogen doped carbon materials are carbon atoms with Lewis basicity next to pyridinic N.
One common phenomenon can be found in research [43, 45]. With the pyrolysis temperature increasing, the content of quaternary N increases whilst the contents of pyridinic N and pyrrolic N decrease.

In actual carbonization process, increasing the pyrolysis temperature can increase the degree of graphitization and remove the excessive nitrogen, both of which can increase the conductivity of carbon materials. Similarly, increasing the retention time of pyrolysis also has the same effect. Accompanied with effective activation, pyrolysis process can render carbon materials advanced porous structure. High conductivity and porosity of nitrogen doped carbon materials are undoubtedly beneficial to the ORR performance.

3 Goals and Concepts

This project aims to prepare spherical and porous polymer nanocomposites by compositing functional nanoparticles and polymer solution in a blending way. After carbonization process, polymer nanocomposites are converted to corresponding carbon nanocomposites. The merits of blending method are time-saving, simple, and scalable. The distribution of nanoparticles in polymer and carbon matrix should be as homogeneous as possible. Potential applications of these nanocomposites are adsorption and photocatalysis, such as removing organic pollutants from aqueous solution.

The preparation route of large (i.e. millimeter-sized) polymer nanocomposites is shown in Scheme 3.1.

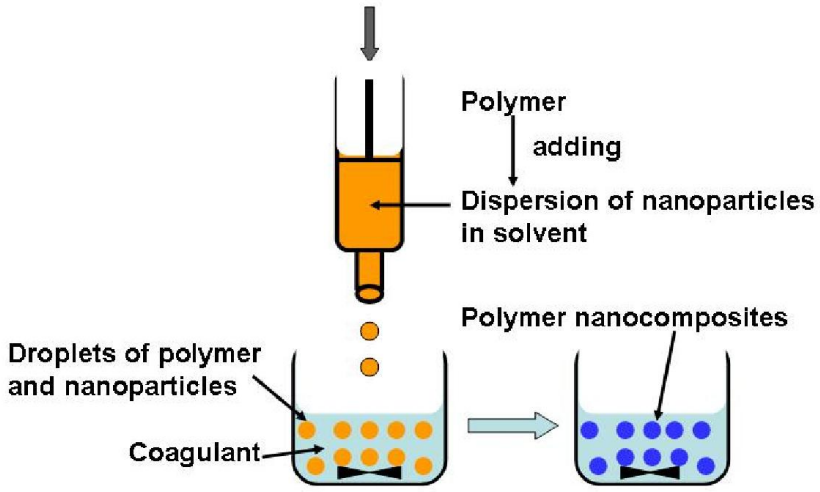

Scheme 3.1 Preparation of large polymer nanocomposites.

Nanoparticles are firstly dispersed in solvent by ultrasonic treatment. The size of nanoparticles in dispersion is examined by dynamic light scattering (DLS). Then polymer powders are dissolved in this dispersion to form solvent-nanoparticles-polymer ternary dispersion. And then, this ternary dispersion is shaped to spherical droplets by free falling from the tip of orifice. After that, these droplets gel and solidify in coagulation bath. The porous structure of polymer nanocomposites is formed due to phase separation of dispersion.

In the scope of this work, it is also necessary to study the formation and resulting structure of porous polymer-based spheres and their conversion of carbon materials. The detailed work arrangements of large polymer (and carbon) spheres and nanocomposites are shown in Scheme 3.2.

Polyacrylonitrile (PAN), a kind of linear and rigid polymer, is used, which can be carbonized to nitrogen-doped carbon materials. This polymer is dissolved in DMF, which shows the best dissolving capacity to PAN among a series of solvents. Before the preparation of polymer nanocomposites, the preparation conditions of large PAN spheres are firstly investigated. These preparation conditions focus on the shape and inner structure of large PAN spheres.

After carbonization, larger PAN spheres are converted to large carbon spheres. During carbonization process, the inner structure of large PAN spheres may change. Both large PAN

and carbon spheres are used in the following adsorption tests. Moreover, some carbon spheres are ground to powders and used in oxygen reduction reaction (ORR) tests.

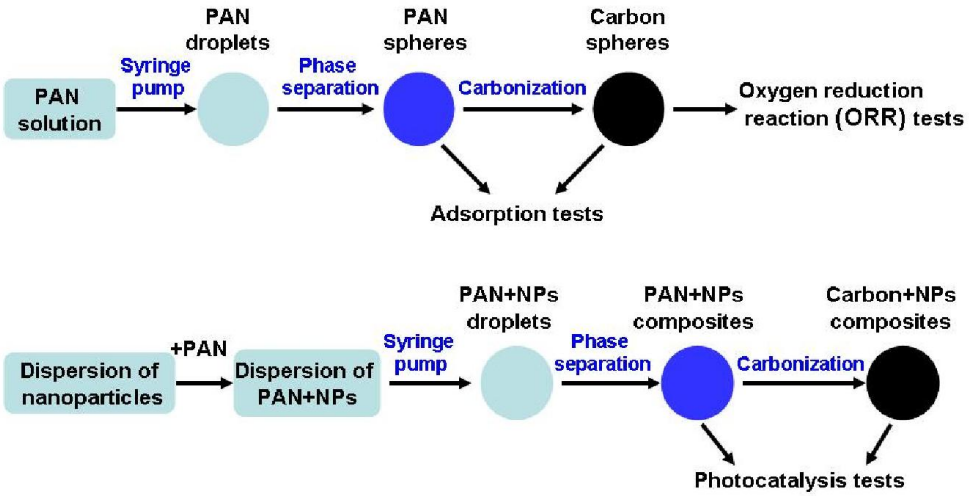

Scheme 3.2 Preparation routes and potential applications of large polymer (and carbon) spheres and nanocomposites.

The basic preparation process of larger polymer nanocomposites has been introduced. Based on the optimized preparation conditions of large PAN (and carbon) spheres, the preparation of large PAN (and carbon) nanocomposites will be finished. Then both polymer and carbon nanocomposites are used in the photocatalysis tests.
The detailed work arrangements of polymer microspheres (i.e. micrometer-sized) are shown in Scheme 3.3.

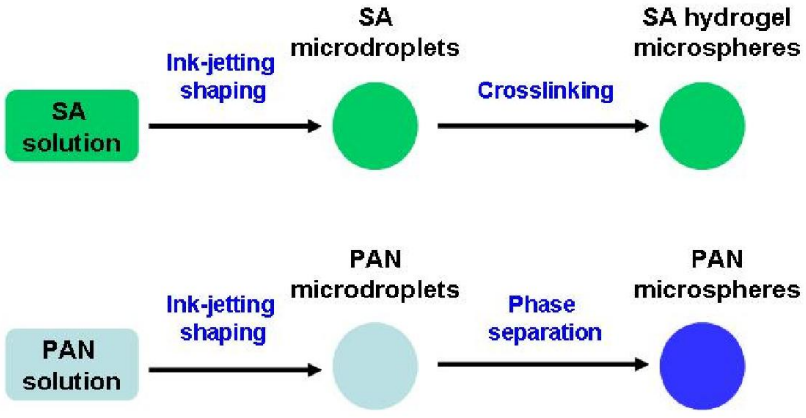

Scheme 3.3 Preparation of SA hydrogel microspheres and PAN microspheres.

This part aims to prepare spherical and porous PAN microspheres in the range of 10-100 µm with rather narrow size distribution by drop-on-demand (DOD) ink-jetting shaping *cum* phase separation, which is a new and not yet well established method.
The feasibility of ink-jetting shaping is firstly studied with aqueous sodium alginate (SA) solution. The SA microdroplets are converted to SA hydrogel microspheres by crosslinking

in the coagulation bath of $CaCl_2$ solution. The preparation conditions of SA hydrogel microspheres focus on their shape.

Based on the shaping conditions of large PAN droplets and SA microdroplets, the shaping of PAN microdroplets is done. At the same time, PAN microdroplets are converted to PAN microspheres based on the phase separation conditions of large PAN droplets. The preparation conditions of PAN microspheres focus on their shape and inner structure.

The morphology of samples is inspected by digital camera, optical microscope, and scanning electron microscopy (SEM).

The specific surface areas and pore size distribution of polymer (and carbon) spheres (and nanocomposites) are determined by measuring the adsorption isotherms of nitrogen (BET method and BJH model, respectively). The porosity of large PAN spheres is determined by the method of weight loss of water. The porosity of large carbon spheres is determined by the uptake of *n*-heptane.

The elemental compositions of polymer (and carbon) nanocomposites are determined by elemental analysis (EA), X-ray photoelectron spectroscopy (XPS), and energy-dispersive X-ray spectroscopy (EDS). The functional groups and phase structures of polymer (and carbon) nanocomposites are determined by infrared spectroscopy (IR), X-ray diffraction (XRD), and Raman spectroscopy.

The content of nanoparticles in nanocomposites is determined by thermo gravimetric analysis (TGA).

4 Experiments

In this chapter, basic methods and principles for the characterization of samples are firstly introduced. Then, the preparation (methods and procedures) of samples are given. In the end, potential applications of these samples are described. The chemicals used in this work are listed in appendix 8.1.

4.1 Methods and principles of characterization

In this section, several methods are used to characterize the samples, such as morphology analysis, pore analysis, elemental composition, and structural analysis. These characterizations are the most important that they are to be illustrated firstly. Other analytical methods, including thermal analysis of samples, molecular weight of polymer, properties of polymer solutions (such as viscosity and surface tension), and dispersion of nanoparticles, are also demonstrated.

4.1.1 Morphology analysis of samples

Images captured by the camera

A Samsung Landiao L730 camera was used to record the morphology of millimeter-sized samples. The size analysis of these samples was done with Image J.

Images captured by the optical microscope

An Olympus system BX53 with a digital camera was used to record the morphology of micrometer-sized samples. The size determination of these samples was done with Image J.

Images captured by a CCD camera

A CCD camera was used to observe the morphology of micrometer-sized droplets. The size determination of these microdroplets was done with Image J.

Images captured by electronic microscope

By means of scanning electron microscopy (SEM), with or without sample preparation, the observation of three-dimensional surface of samples is possible. With the interactions between electron beam (i.e. primary electrons) and the atoms of sample surface, various signals are generated, such as secondary electrons, backscattering electrons, and characteristic X-ray. This point-to-point emitted electrons are collected in a special detector. Similar to acquire the images of television photography, the SEM images are captured by modulating various physical signals mentioned above.

In this work, an ESEM QUANTA 400 FEG Environmental Scanning Electron Microscope was used. The measurement takes place in high vacuum. The samples to be measured must be electrically conductive; therefore, non-conductive sample must be coated with a conductive coating. To avoid accumulated charges, the polymer and carbon samples were also coated with gold/palladium.

Analysis of images

To determine the particle size distribution of samples, images of samples captured by camera, optical microscope, and SEM were analyzed with the aid of the image processing program Image J. Image J is a public domain Java image processing program inspired by NIH Image [49]. By converting the non-binary images into binary ones, the Image J program is able to detect and process the two dimensional (2D) images of samples. In terms of the shape of large polymer spheres, four description characters are used [50], which are major axis, minor axis, aspect ratio (AR), and circularity. The detailed definitions of these indexes are in appendix 8.2.

4.1.2 Porous structure of samples

Determination of adsorption isotherms

Nowadays, it is a popular method to analyze and determine the structure of porous materials by using gas adsorption. Surface areas and porosity analyzer based on physical adsorption of nitrogen is the most widely used. In this work, a Coulter SA 3100 of Beckman Coulter was used. The measuring range of pore diameter is 2-200 nm [8]. Therefore, it should be noted that the micropores (below 2 nm) can not be fully detected.

This kind of analyzer is designed based on static volumetric principle. The amount of condensed gas on the sample surface is determined by the pressure drop of gas. Samples are cooled with liquid nitrogen during the measurement; thus, temperature is kept at -196°C. At this temperature, the condensation of inert gas on the sample surface can be guaranteed.

With the adsorption isotherms acquired, the specific surface areas, pore size distribution, and specific pore volumes were determined by analyzing the isotherms according to different mathematical models. The specific pore volumes are estimated by single point adsorption method. The specific surface areas are calculated from Brunauer-Emmett-Teller (BET) method [38] while the pore size distribution is calculated from Barrett-Joyner-Halenda (BJH) model [39].

Determination of porosity

Pycnometer is widely used to calculate the relative density (i.e. specific gravity) of unknown liquid with water as the most common reference. Its basic principle is that at the same temperature, the ratio of gravity of two kinds of liquid with same volume equals the ratio of density of them. Besides this application, pycnometer can also be applied to determine of the density of powder, as well as the effective solid density [37] of materials with “opened” pores. The effective solid density is defined in Formula 4.1.

$$\text{Effective solid density} = \frac{\text{mass of solid}}{\text{volume of solid without "opened" pores}}$$

Formula 4.1

The porosity [37] of materials is defined in Formula 4.2.

$$\text{Porosity} = \frac{\text{volume of "opened" pores}}{\text{volume of materials including "opened" pores}} \times 100\%$$

4.1.3 Elemental analysis of samples

Elemental composition

The most common elemental analysis is based on the combustion of sample in oxidative atmosphere. Organic compounds containing carbon, hydrogen, nitrogen, and sulfur are oxidized into corresponding oxidation products. With the amount of these products determined, the contents of these elements in sample are acquired. The determination of oxygen content adopts a different method.

In this work, the measurements were carried out with the CHNS analyzer Euro EA Vector Instruments. Samples with 0.5-3.0 mg are weighed and put into a tin crucible. They are burned at 1,000°C within oxygen atmosphere. The resulting combustion products are separated and evaluated by a gas chromatographic separation column. In addition, this equipment can not distinguish organic oxygen element and inorganic oxygen element.

Chemical states of elements

X-ray photoelectron spectroscopy (XPS) was firstly applied in the field of chemistry; therefore, it is also called Electron Spectroscopy for Chemical Analysis (ESCA). The valance of an element reflects its chemical state, which is related to chemical environment. In a spectrum of XPS, the chemical shift (i.e. binding energy of inner-shell electrons) is influenced by chemical state. A specific chemical shift represents a specific element, which is the basis of qualitative analysis.

The basic principle of XPS is the photoelectric effect. With a beam of X-ray illuminating the surface of samples, the inner-shell electrons of samples are excited free and accepted by a detector. With the energy distribution of these photoelectrons determined, the chemical shifts of elements and thus elemental compositions of samples are known. Since these photoelectrons mainly come from the surface of samples with a depth of several layers of atoms (e.g. 1-10 nm), it is a useful technology for surface analysis. Both qualitative and quantitative analysis of surface elements can be accomplished by XPS.

In most cases, not only do people care about the chemical shift of an element, but also they are interested in the change of chemical shift of this element after some treatments. This change of chemical shift is related to the change of this element's chemical state, which results from the electronic interactions with other elements. This is because the valence electrons of an element influence the binding energy of its inner-shell electrons.

In this work, a PHI 500 Microfocus X-ray photoelectron spectrometer was used. XPS spectra are acquired at a chamber pressure in the range of 10^{-8} mbar. During data acquisition, samples are flooded with low energy electrons and Ar^{+} ions in order to neutralize the charging effects. The C 1s line at 284.5 eV is used as the binding energy standard [51]. Generally, there is more than one signal for a selected element in the XPS scanning of samples. The most intense signal, i.e. photoelectron line [51], of an element is selected for further scanning with narrower increment. XPS spectrum acquired by this way is called high-resolution XPS spectrum.

Distribution of elements in materials

In order to know the categories, contents, and distribution of elements in materials, Electron Probe Micro-Analysis (EPMA) is a useful tool to do this. This technology uses electron beams to illuminate the surface of samples and makes inner-shell electrons free. Then the inward transition of outer-shell electrons (near this inner-shell) generates characteristic X-rays. With the wavelength (Wavelength-Dispersive X-ray Spectroscopy, WDS) or energy (Energy-Dispersive X-ray Spectroscopy, EDS) of these characteristic X-rays determined, the category of this element is known. The relative contents of elements are also known by analyzing the intensity of characteristic X-rays. Similar to XPS, EPMA is also a technology of surface analysis. Besides the fixed point analysis, the linear analysis and surface analysis of EPMA also provide a profile of elemental distribution in materials.
Generally, the EPMA equipment comprises a SEM and an EDS (or WDS) accessory. In this work, the mapping of elements was done at an ESEM QUANTA 400 FEG Environmental Scanning Electron Microscope with an EDS attachment.

4.1.4 Structural analysis of samples

Functional groups

The infrared absorption of different organic samples is different; thus, the functional groups in these organic compounds can be inferred by infrared spectroscopy. Here, the sample is irradiated by a spectrum of continuous infrared light. During the irradiation, there are interactions between electromagnetic radiation and molecules of samples. If the energy of irradiated light corresponds to the energy difference between the vibration energy levels of groups, the light is absorbed and the molecule is excited to vibrate. Only those vibrations which cause a change of molecule's dipole moment are effective.
The principle of attenuated total reflection (ATR) was used in the ATR-IR equipment, which allows samples to be measured with only minimal amount. In ATR-IR spectroscopy, the sample contacts with the ATR crystal (e.g. zinc selenide). The infrared radiation travels through the crystal and interacts with the sample which contacts with the ATR crystal. Due to the differences in refractive indices between ATR crystal and samples, total internal reflection occurs. This reflection leads to the so-called "evanescent wave" which penetrates into the sample. In the sample, a small part of the infrared light is absorbed when the evanescent wave interacts with the sample. This is called attenuated total reflection. In this way, the reflected infrared light is weakened, which results in a similar effect to the absorption of infrared light during transmission process.
Different from the traditional IR spectrometer characterized by grating or prism, a Varian 3100 FT-IR (based on the principle of light's interference) Excalibur Series Spectrometer of Agilent Technologies was used in this work with an ATR attachment (i.e. diamond or zinc selenide crystal) of Pike Technologies.

Phase structure

Contrary to the structural analysis of organic compounds by IR spectroscopy, the phase analysis of inorganic samples, specifically crystalline substances, needs the help of X-ray diffraction (XRD). Crystalline substances are characterized by the long-range and ordered arrangement of their molecules or atoms. This periodic arrangement (i.e. repeated crystalline lattices) of molecules or atoms renders crystalline substances anisotropic.

With a beam of monochromatic and characteristic X-rays traveling through a piece of single crystalline, the diffraction (i.e. scattering) of X-rays will happen if the atomic distances within the lattice and wavelength of the X-rays are at the same order of magnitude. Due to the periodic arrangement of crystalline lattice, the interference of scattered X-rays will occur if the wavelengths of these X-rays are the same. The interaction of X-rays with same phase leads to constructive interference featured by maximum amplitude of superposing X-rays, while the interaction of X-rays with opposite phase results in destructive interference featured by minimum amplitude of superposing X-rays. As a result, the diffraction patterns of samples are formed. Two kinds of information are acquired from diffraction patterns: diffraction direction and diffraction intensity. The diffraction direction can be described by Bragg's Law [8] as show in Formula 4.3.

$$n \cdot \lambda = 2 \cdot d \cdot \sin\theta$$

Formula 4.3

n: order of reflection;
λ: wavelength of X-ray;
d: distance between two neighboring planes;
θ: angle of incidence of X-ray.

The diffraction of a beam of X-ray in crystalline lattice is illustrated in Scheme 4.1.

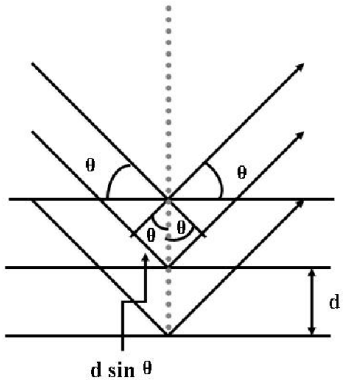

Scheme 4.1 Diffraction of a beam of X-ray in crystalline lattice.

Different crystals have different diffraction patterns; therefore, in qualitative process, the phase structure of monocrystalline substance can be inferred by its diffraction patterns. The diffraction patterns of polycrystalline powders are the mechanical superposition of those of monocrystalline substances. For the quantitative analysis of polycrystalline powders, direct comparison of different phases without introducing reference substance was used in this work.

For the main diffraction methods of polycrystalline powders, there are photographic method (e.g. Debye-Scherrer proceedings) and diffractometer. In this work, the XRD measurements were carried out on the device of D8 Advance with monochromatic Cu-K_α radiation from Bruker.

Vibrational modes

Apart from IR spectroscopy, Raman spectroscopy can also be applied for analyzing both functional groups and phase structure. When a sample is illuminated by a beam of monochromatic light, the scattered light at selected angles will be observed. In the spectrum of scattered light, there are various frequencies: some frequencies are higher than that of incident light (i.e. anti-Stokes bands); some frequencies are lower than that of incident light (i.e. Stokes bands); other frequencies are close to that of incident light (i.e. Rayleigh scattering). Both anti-Stokes bands and Stokes bands are attributed to the bands of Raman scattering. Generally, Raman spectra only show the Stokes bands. Structural analysis by Raman spectroscopy is based on that different samples have different Raman shifts (i.e. frequency difference between Stokes bands and incident light).

Both IR and Raman spectroscopy belong to vibrational spectroscopy in terms of the energy of absorbed light or scattered light. IR absorption needs the change of dipole moment of molecules whilst Raman scattering requires the change of polarization ratio of crystalline lattice or molecules. For some molecules with symmetry center, their IR spectrum and Raman spectrum are complementary to each other.

The intensity of Raman scattering is low. Because of this deficit, samples with large volume are needed. Thanks to emerging of intensive and monochromatic laser, laser Raman spectroscopy can overcome this shortcoming. In this work, an Invia 0113-20 Confocal Raman Microscope of Renishaw was used. It provides two exciting wavelengths for the samples, which are 532 nm and 633 nm. In this work, the wavelength of 633 nm was used.

4.1.5 Thermal analysis of samples

Thermo gravimetric analysis (TGA)

In this analysis, the mass change of a sample is measured as a function of temperature with a predetermined temperature program. Here, a sample is put in an inert crucible and weighed by a thermo balance during the heating process. Mass changes of samples indicate physical or chemical processes, which are dehydration, oxidation, reduction, evaporation, or decomposition. With the intention of analysis changing, various atmospheres can be used, such as air, oxygen, or argon [8]. In this work, a thermo gravimetric analyzer (NETZSCH STA 449 F3) was used.

Differential scanning calorimetry (DSC)

In this analysis, the heat needed to eliminate the temperature difference between the sample and the reference substance is defined as the compensatory heat. This compensatory heat is measured as a function of temperature with a predetermined temperature program.

DSC curves provide the starting temperature, peak temperature, and ending temperature of thermo incidents. Transition temperature in DSC curves indicates the categories of substances during heating process while integral areas of signals represent the magnitude of thermal effects during the measurement. The direction of (+/-) of signals means that the thermal effect is endothermic or exothermic. In this work, a differential scanning calorimeter (NETZSCH DSC 204) was used.

Differential thermal analysis (DTA)
In this analysis, the temperature difference between sample and reference substance is measured as a function of temperature with a predetermined temperature program. In terms of qualitative analysis, DTA is similar to DSC. DTA is rarely used in quantitative analysis. The sensitivity and resolution of DSC are much better than that of DTA; however, the operation temperature of DSC is much lower. In this work, a differential thermal analyzer (NETZSCH STA 449 F3) was used.

4.1.6 Determination of molecular weight of polymer

As a relative method of determining molecular weight, size exclusion chromatography (SEC) is widely used in both academia and industry. By virtue of this method, both number-weighted molecular weight (M_n) and weight-weighted molecular weight (M_w) can be acquired. In this work, M_w was used to characterize the molecular weight of various polymers.
When a polydisperse polymer is added into SEC, polymer fraction with monodisperse molecular weight will be separated from each other. The content of a specific polymer fraction is determined by the concentration of corresponding eluent. Then, the molecular weight of a specific polymer fraction is related to the volume of corresponding eluent and this relation can be described quantitatively by calibration curve. The calibration curve refers to dextran for water soluble polymer in this work, while this curve refers to polymethyl methacrylate (PMMA) for water insoluble polymer.
In this work, a SEC equipment from PSS (Polymer Standards Service) company was used. Two kinds of polymer were firstly used in this work. One is water soluble sodium alginate (SA) and the other one is water insoluble polyacrylonitrile (PAN). The commercial name of PAN from Dolan company is H-PAN, whose nominal molecular weight is 200 kg/mol. Based on the SEC results, the M_w of sodium alginate was calculated as 2095 g/mol. By contrast, the M_w of H-PAN was calculated as 229 kg/mol. From here, H-PAN is denoted as PAN 200.
According to the requirements of project, another three kinds of PAN polymer were introduced. The first one is X-PAN, which has a nominal molecular weight of 74 kg/mol. The second one is L-PAN with a nominal molecular weight of 77 kg/mol. The last one is PAN 150 with a nominal molecular weight of 150 kg/mol. The molecular structures of all polymers used are attached in appendix 8.3.

4.1.7 Viscosity of polymer solution

When fluids flow, molecules of this fluid show relative motion. At the same time, there are internal frictional forces accompanying this process. This flow resistance is defined as viscosity [52]. At constant temperature, for ideal viscous fluids (i.e. Newtonian fluids), the shear viscosity η equals the quotient of shear stress τ and shear rate $\dot{\gamma}$ (Formula 4.4). The curve that describes the relation between shear stress and shear rate is called flow curve.

$$\eta = \frac{\tau}{\dot{\gamma}}$$

Formula 4.4

τ: shear stress;

η: viscosity;

$\dot{\gamma}$: shear rate.

For non-Newtonian fluids, their shear viscosity is no longer constant and depends on the shear rate. Therefore, the viscosity curve is introduced to describe the relation between shear viscosity and shear rate. In a viscosity curve, the shear viscosity is also called apparent viscosity, which only represents the mobility of fluid. In order to describe the flow behavior of non-Newtonian fluids at low shear rate, zero-shear viscosity [52] is also introduced. The zero-shear viscosity is defined as a limiting value of shear rate-dependant viscosity curve at an "infinitely low" shear rate as shown in Formula 4.5.

$$\eta_0 = \lim_{\dot{\gamma}\to 0} \eta\left(\dot{\gamma}\right)$$

Formula 4.5

η_0: zero-shear viscosity;

$\dot{\gamma}$: shear rate.

In this work, a Physica MCR 301 rotary rheometer of Anton Paar was used. Two measuring systems were used in this work, which are cone-and-plate measuring system and parallel-plate measuring system as shown in Scheme 4.2.

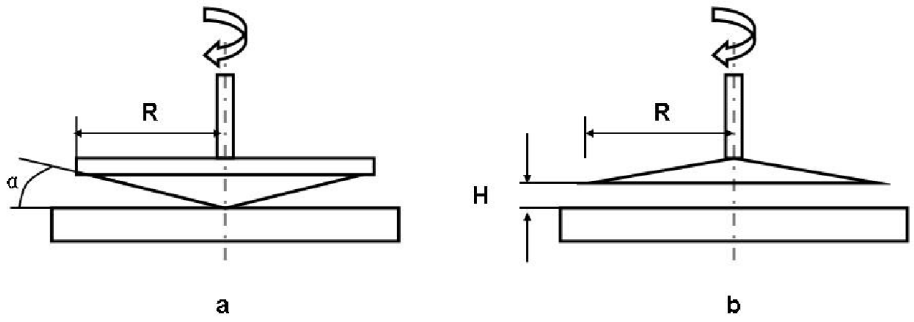

Scheme 4.2 Measuring system of MCR 301. a) cone-and-plate system; "R": radius of cone plate; "α": cone angle; b) parallel-plate system; "R": radius of plate; "H": distance between two parallel plates.

A few drops of liquid samples were dropped to the lower plate and the upper plate was driven downwards. During the measurement, the upper plate rotated while the lower plate did not move. There are two basic measuring modes: rotational tests and oscillatory tests, according to different pattern of movement of upper plate. Both viscosity curve and zero-shear viscosity are acquired from rotational tests while the dynamic mechanical analysis (DMA) of samples is characterized by oscillatory tests.

4.1.8 Surface tension of polymer solution

Surface tension is a kind of force which makes the surface of liquid shrink to minimum surface areas. It is a useful physical quantity to describe the surface or interfacial behavior of liquid. The surface tension is also called surface energy, which is defined as the non-expansion work needed to increase per unit area of liquid. Generally, the surface tension of a liquid can be estimated theoretically (i.e. indirect method) or measured directly (i.e. direct method). In this work, both these two methods were used.

Estimation of surface tension (indirect method)

When a droplet of liquid is dropped on a solid surface, it will wet or not wet the solid surface. The solid surface wetted by a kind of liquid is illustrated in Scheme 4.3.

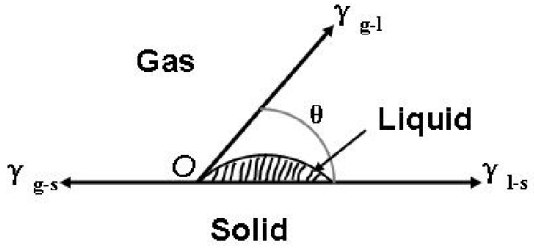

Scheme 4.3 Wetting of liquid on solid. "θ": the contact angle; "$\gamma_{g\text{-}s}$": gas-solid interfacial tension; "$\gamma_{g\text{-}l}$": gas-liquid interfacial tension; "$\gamma_{l\text{-}s}$": liquid-solid interfacial tension.

The shape of droplet on solid surface is dominated by interfacial tensions among gas, liquid, and solid. When the droplet stabilizes on solid surface, the state of this moment can be described by Young's equation [26], which is shown in Formula 4.6.

$$\gamma_{g-s} = \gamma_{g-l} \cdot \cos\theta + \gamma_{l-s}$$

Formula 4.6

θ: the angle between $\gamma_{g\text{-}l}$ and $\gamma_{l\text{-}s}$;
$\gamma_{g\text{-}s}$: gas-solid interfacial tension;
$\gamma_{g\text{-}l}$: gas-liquid interfacial tension;
$\gamma_{l\text{-}s}$: liquid-solid interfacial tension.

When the contact angle is smaller than 90°, the solid surface can be wetted by this liquid. The solid surface will not be wetted by this liquid if the contact angle is larger than 90°. Generally, there are two methods to measure the contact angle: one is the method of modified Wilhelmy plate, and the other one is the shape analysis of liquid meniscus. In this work, the observation of droplet's shape was done with the contact angle system OCA15 from Data physics. This equipment can capture the shape of static droplets via sessile drop method or pendant drop method. Sessile drop method was adopted in this work and the static contact angles are given automatically.

Given that $\gamma_{g\text{-}s}$ equals the surface tension of solid and $\gamma_{g\text{-}l}$ is the surface tension of liquid, it is impossible to know $\gamma_{g\text{-}l}$ according to Formula 4.6, since both $\gamma_{g\text{-}s}$ and $\gamma_{l\text{-}s}$ can not be measured directly. Then turning to other empirical models is needed.
The Owens & Wendt model [53] describes the relation of surface tension between solid and liquid as shown in Formulas 4.7-4.9.

$$(1+\cos\theta)\cdot\gamma_L = 2\cdot\sqrt{\gamma_S^d\cdot\gamma_L^d} + 2\cdot\sqrt{\gamma_S^p\cdot\gamma_L^p}$$

Formula 4.7

$$\gamma_L = \gamma_L^d + \gamma_L^p$$

Formula 4.8

$$\gamma_S = \gamma_S^d + \gamma_S^p$$

Formula 4.9

θ: contact angle;
γ_L: surface tension coefficient of liquid;
γ_L^d: dispersive component of surface tension coefficient of liquid;
γ_L^p: polar component of surface tension coefficient of liquid;
γ_S: surface tension coefficient of solid;
γ_S^d: dispersive component of surface tension coefficient of solid;
γ_S^p: polar component of surface tension coefficient of solid.

In this model, the surface tension of a solid can be calculated by measuring the contact angles of two different liquids on it. In turn, the surface tension of a liquid can be calculated by measuring the contact angles of two different solids under it. For the determination of surface tension coefficient of liquid, the solids used are polymers whose γ_S^d and γ_S^p are easy to be acquired in literatures.

Measurement of surface tension (direct method)
There are many methods to measure the surface tension coefficient of liquid, such as Du Noüy [54] ring method, capillary rise method, drop weight method, and maximum bubble pressure method. In this work, the ring method was used. The measuring method is illustrated in Scheme 4.4.

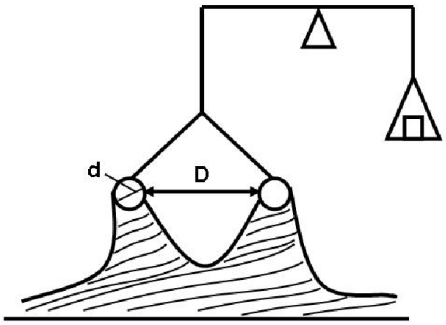

Scheme 4.4 Surface tension measured by ring method. “D”: diameter of platinum ring; “d”: diameter of platinum filament.

Firstly, the platinum ring is submerged into the liquid sample. When the ring is pulled out, the force needed to detach it from the liquid surface is measured. This force is related to the surface tension of liquid. Usually the correction for buoyancy must be introduced. The critical pulling force (W_t) needed to detach the ring is the sum of ring weight W_d and the surface tension multiplied by two, because the surface tension acts on two circumferences of the ring (i.e. inside and outside).

$$W_t = W_d + 2\pi(D + d)\gamma$$

Formula 4.10

W_t: critical pulling force;
W_d: weight of platinum ring;
D: inner diameter of ring;
d: diameter of platinum filament;
γ: surface tension coefficient.

Then the surface tension coefficient can be calculated from Formula 4.10. In this work, a tensiometer K6 of KRÜSS company was used, which is in essential a torsion balance. After a series of conversion, the surface tension coefficient can be read directly from the dial plate. Its measurement range spans from 0 to 90 mN/m.

4.1.9 Dispersion of nanoparticles

Ultrasonic treatment

The dispersion of particles in liquid is a commonly used method for the production of emulsion, dispersion, suspension, and colloid. Before treatment, individual particles aggregate or agglomerate mainly due to physical interactions, such as Van der Waals’ force and electrostatic interactions. In order to disperse particles in a liquid, these interactions must be overcome. This can be done via ultrasonic dispersing method.

With a sonotrode submerged in the liquid, the samples can be dispersed more rapidly and homogenously. The ultrasonic process can be divided into low pressure phase (relaxation) and high pressure phase (compression). During low pressure phase, the ultrasonic wave with high energy forms small bubbles in the liquid. If these cavities reach a certain volume and

they can not absorb more energy, they will burst during high pressure phase. This phenomenon is called ultrasonic cavitation. With this cavitation continuous, aggregates or agglomerates collapse and particles are separated from each other.
In this work, nanoparticles were dispersed in liquid with an ultrasonic homogenizer from Bandelin electronic, Sonoplus HD 2200 as sketched in Scheme 4.5.

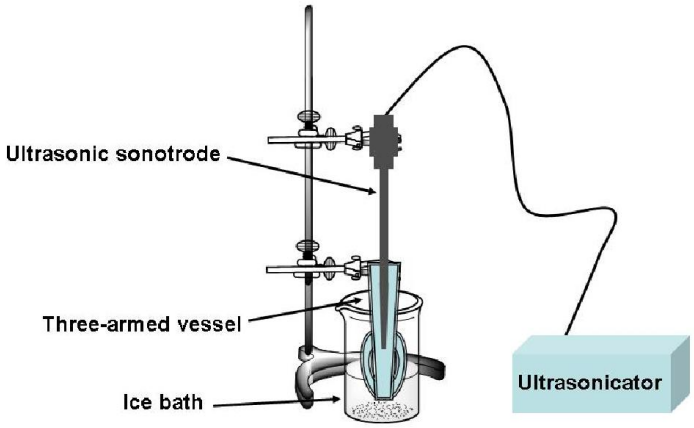

Scheme 4.5 Ultrasonic treatment of nanoparticles.

Three side arms of the dispersing vessel allow a better circulation of the dispersing liquid during the operation. Samples are cooled from the outside with an ice bath during the entire ultrasonic process.

DLS measurement
Dynamic light scattering (DLS, also called photon correlation spectroscopy or quasi-elastic light scattering) is an important technology in the field of nanotechnology. With the help of DLS, hydrodynamic radius, distribution width, and aggregation effect of nanoparticles can be determined.
With a beam of selected monochromic light illuminating the solution or dispersion of samples, the molecules or particles will not absorb but scatter the incident light. The frequency of the scattered light is the same as that of incident light. This is called static light scattering.
If the particles or molecules move at a specific velocity, such as Brownian movement, the frequency of scattered light will change. This phenomenon is called Doppler shift. The frequency difference between incident light and scattered light is related to the velocity of particles. Based on this velocity, the hydrodynamic radius of particles can be determined.
In this work, all of DLS measurements were carried out with Nano-flex 180° of Microtrac. The DLS measurement was performed immediately after the dispersion of nanoparticles by ultrasonic treatment.

4.2 Preparation of polymer spheres

Detailed methods and procedures for the preparation of various polymeric samples are given

in this section. The formation of two typical polymer spheres, i.e. large spheres in the range of millimeter and microspheres in the range of micrometer, are shown here. In addition, the preparation of hydrogel microspheres is also demonstrated.

4.2.1 Properties of polymer solution

Rotational tests of PAN and SA solution

The measurement principle of shear viscosity has been described in 4.1.7. In order to acquire the viscosity curve of polymer solution at 25°C, the cone-and-plate measuring system was selected. The upper cone plate has a cone angle of 0.986°, which can provide homogenous shear condition thus the shear rate is constant in the entire conical gap. Polyacrylonitrile was dissolved in DMF while sodium alginate was dissolved in water. A series of polymer solutions (PAN 200, X-PAN, L-PAN, PAN 150, and SA) with various concentrations were used. The measurement of each of the viscosity curves was repeated for three times. Then zero-shear viscosity of a selected polymer solution at specific concentration was acquired.
For temperature-dependant flow behaviors of polymer solution, the parallel-plate measuring system was chosen. The shear rate was set at 5 s^{-1}. The temperature range varied from 25 to 80°C and the heating rate was set at 5 K/min. Two kinds of polymer solutions (PAN 200 and SA) with various concentrations were used.

Oscillation tests of PAN 200 solution

Without extremely high pressure, most Newtonian liquids, such as water and solvent of small molecules, are regarded as incompressible, which means these fluids have no elasticity. This is due to the extremely low isothermal compression coefficient of these fluids and thus their densities are constant. The isothermal compression coefficient is defined in Formula 4.11 [55]. It represents the relative increasing ratio of liquid's density when pressure is increased by one unit at a specific temperature.

$$\gamma_T = \frac{1}{\rho}\left(\frac{\partial \rho}{\partial p}\right)_T$$

Formula 4.11

γ_T: isothermal compression coefficient;
ρ: density of the liquid;
p: applied pressure;
T: temperature.

If a macromolecule can be seen as a random coil, then this macromolecule will have elasticity and compressibility, which is like a woolen ball. When macromolecules are dissolved into Newtonian solvent, the average distances between solvent molecules increase. Then the whole polymer solution has some elasticity [56] and compressibility. This elasticity is essentially rubber elasticity, which derives from the rotation within a single bond and conformation change of the chain segments in polymer.
The higher the concentration of polymer solution is, the larger are the elasticity and compressibility of polymer solution. With the increasing of concentration of polymer in

solution, the isothermal compression coefficient of polymer solution increases. Even though the applied pressure is not high, the polymer solution can not be simply seen as incompressible any more.

Generally, the polymer solution can be divided into dilute solution and concentrated solution. Semidilute solution belongs to concentrated solution. Dilute polymer solution can be seen as Newtonian liquid approximately in specific cases, such as using Ubbelohde viscometer to measure the intrinsic viscosity of polymer solution. Apart from dilute polymer solution, the elasticity of other polymer solutions can not be ignored. All the PAN solutions used in this work are not dilute solution.

The simultaneous viscous flow and elastic behavior of matter are called viscoelasticity [52]. The investigation of matter's viscoelasticity can be done from three aspects: the form of applied stress or strain, time of duration, and temperature. According to the different forms of stress or strain, the study of viscoelasticity can be further divided as static viscoelasticity and dynamic viscoelasticity. Creep tests and relaxation tests are used to characterize the static viscoelasticity, while oscillatory tests are preferred to investigate the dynamic viscoelasticity featured by the high-frequency stress or strain applied.

In this work, since the flow of polymer solution in capillary tube is pressure-driven flow by applying high-frequency pressure pulse, oscillatory tests are needed. Three PAN 200 solutions were prepared, which are 1%, 3%, and 5%. In oscillatory tests, shear strain amplitude sweeps are used to study the sheared behavior of materials. Frequency sweeps are used to investigate the time-dependent shear behavior of materials since period is the inverse value of frequency. At last, temperature sweeps are applied to show the temperature-dependent shear behavior of materials.

Estimation of surface tension coefficient of PAN 200 solution

Theoretically, only two polymers are needed to calculate the surface tension coefficient of polymer solution according to Formula 4.7. In order to increase the reliability of results, three polymers were selected from the laboratory, which are polyethylene (PE), polypropylene (PP), and polytetrafluoroethylene (PTFE). The information of their surface tension coefficients is listed in Table 4.1 [57].

Table 4.1 Information of polymers used in the estimation of surface tension coefficient. γ_S: surface tension coefficient of solid; γ_S^d: dispersive component of surface tension coefficient of solid; γ_S^p: polar component of surface tension coefficient of solid.

Polymer	γ_S (mJ/m^2)	γ_S^d (mJ/m^2)	γ_S^p (mJ/m^2)
polyethylene (PE)	33.0	33.0	0.0
polypropylene (PP)	25.7	25.7	0.0
polytetrafluoroethylene (PTFE)	17.9	17.9	0.0

The γ_S^p values of PE, PP, and PTFE are all zero. During the process of calculation, one requirement is that γ_S^p values of two polymers should not be zero at the same time. Therefore, another polymer whose γ_S^p is not zero is required. After much selection and consideration, polyvinylchloride (i.e. PVC) was introduced without knowing its surface tension coefficient. Fortunately, the Formula 4.7 can be used again to calculate the surface tension coefficient of

this polymer.
In this work, three kinds of liquid were used to calculate the surface tension coefficient of PVC, which are water, glycerol, and dimethylsulfoxide (DMSO). The information of their surface tension coefficients is listed in Table 4.2 [57].

Table 4.2 Information of liquid used in the calculation of PVC's surface tension coefficient. γ_L: surface tension coefficient of liquid; γ_L^d: dispersive component of surface tension coefficient of liquid; γ_L^p: polar component of surface tension coefficient of liquid.

Liquid	γ_L (mJ/m^2)	γ_L^d (mJ/m^2)	γ_L^p (mJ/m^2)
water	72.8	21.8	51.0
glycerol	64.0	34.0	30.0
dimethylsulfoxide (DMSO)	44.0	36.0	8.0

After linear regression, the surface tension coefficient (i.e. γ_S) of PVC is 34.7 mJ/m^2. Its dispersive component (i.e. γ_S^d) is 10.4 mJ/m^2 while its polar component (i.e. γ_S^p) is 24.3 mJ/m^2.
A series of solutions (5%, 7.5%, 10%, 12.5%, and 15%) of PAN 200 were prepared to determine their surface tension coefficients. According to the combination of various polymers (PE, PP, or PTFE with PVC), three sets of surface tension coefficients of PAN 200 solution can be acquired.

Measurement of surface tension coefficient of PAN 200 and SA solution
The measurement principle of surface tension coefficient has been introduced in section 4.1.8 (direct method). During the measurement, both the density of polymer solution and temperature influence the surface tension coefficient of polymer solution. The fluctuation of these two factors has subtle effects on the final results; therefore, the surface tension coefficient read directly from the dial plate needs to be calibrated. According to the instruction of K6 [58], the first correction factor α is the ratio of surface tension coefficient's actual value (of water) and standard value (of water) at same temperature. The second correction factor β is related to the density difference between sample solution and air.
The final value of surface tension coefficient is the product of actual value, α, and β:

$$\gamma_{final} = \gamma_{actual} \cdot \alpha \cdot \beta$$

Formula 4.12

γ_{final}: final value of surface tension coefficient;
γ_{actual}: actual value of surface tension coefficient;
α: the first correction factor;
β: the second correction factor.

The γ_{actual} is a mean value of three times' measurements.
For the surface tension coefficient of PAN 200 solutions, a series of concentrations were prepared, which were 0%, 5%, 7.5%, 8%, 8.5%, 9%, 9.5%, and 10%. The measurement temperature was 22°C.

For the surface tension of SA solutions, a series of concentrations were prepared, which were 0%, 0.1%, 0.5%, 1%, 1.5%, 1.6%, 1.7%, 1.8%, and 2%. The measurement temperature was 20°C.

4.2.2 Shaping large polymer spheres by syringe pump

Shaping polymer droplets by syringe pump is similar to the case of water drops falling down from a tap. The sketch of shaping large polymer spheres is shown in Scheme 4.6. The extrusion of polymer solution is continuous while the formation of droplets is intermittent. For simplicity, other non-important components are omitted.

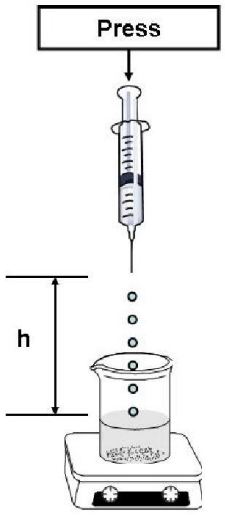

Scheme 4.6 Shaping large polymer spheres by syringe pump. "h": falling distance.

Polymer solution was firstly sucked into a syringe, which was then installed on the syringe pump. The diameter of the needle used is 0.4 mm, 1.2 mm, or 1.36 mm. The injection rate of polymer solution is set at 1 droplet per second. The falling distance of droplets between the tip of the needle and coagulant surface is an important factor that was controlled precisely. The coagulant was put in the beaker, which can be stirred and heated by the stirrer under the beaker.

Morphological modulation of large polymer spheres

In this section, three factors were investigated from various levels, which are concentration of PAN 200 solution, falling distance, and gelation rate.

For the concentration of PAN 200 solution, a series of polymer solutions were used, which are 5%, 7.5%, 8%, 8.5%, 9%, 9.5%, and 10%. The coagulant was pure water, which was set at 20°C. The falling distance of droplets was kept at 5 cm.

The falling distance of droplets was studied in detail. Both wet spheres and their dry counterparts were compared. The diameter of the needle used was 0.4 mm and 1.2 mm, respectively. The falling distance varied from 5 cm to 30 cm. The concentration of PAN 200 solution was 8% and the coagulant was pure water, which was set at 20°C.

For the study of gelation rate, a series of coagulants composed of DMF and water were

adopted. The volume fractions of DMF in water-DMF mixture were 0%, 5%, 10%, 15%, 20%, 25%, 30%, 35%, 40%, 45%, 50%, 55%, 60%, 65%, 70%, and 75%. The temperature of these coagulants was 20°C. The concentration of PAN 200 solution was 8% and the falling distance of polymer droplets was 5 cm.
For the shape characterization of polymer spheres by Image J, at least 100 polymer spheres prepared from 0.4 mm needle were analyzed. For polymer spheres prepared from 1.2 mm needle, at least 50 spheres were analyzed. The reference scale was introduced.

Investigation of polymer spheres' inner structure
For the inner structure of polymer spheres, composition of coagulant was selected as the most important factor. The coagulant was a mixture of DMF-water and the volume fractions of DMF were 0%, 25%, 50%, and 65%. The falling distance of polymer droplets was set at 5 cm. Gelation temperature was 20°C and the concentration of PAN 200 solution was 8%.
Another two factors, i.e. the concentration of polymer solution and gelation temperature, were also studied by orthogonal tests [59]. The factors and corresponding levels are shown in Table 4.3. Based on these factors and levels, the orthogonal test was designed in the form of orthogonal array as shown in Table 4.4. The falling distance of polymer droplets was set at 5 cm.

Table 4.3 Factors and corresponding levels of orthogonal tests of PAN 200 solution.

Levels	Concentration (A)	Coagulation bath	
		Gelation temperature (B)	Volume fractions of DMF (C)
1	5%	20°C	0%
2	8%	60°C	35%

Table 4.4 Orthogonal design of $L_8(2^7)$. Columns of A*B, A*C, and B*C: interactions between two factors; blank: column of error; factor A: concentration of PAN 200 solution; factor B: gelation temperature; factor C: volume fractions of DMF.

Order	A	B	A*B	C	A*C	B*C	Blank
1	1	1	1	1	1	1	1
2	1	1	1	2	2	2	2
3	1	2	2	1	1	2	2
4	1	2	2	2	2	1	1
5	2	1	2	1	2	1	2
6	2	1	2	2	1	2	1
7	2	2	1	1	2	2	1
8	2	2	1	2	1	1	2

The intention of orthogonal tests was to determine whether there was interaction between gelation rate, concentration of PAN 200 solution, and gelation temperature.

Drying of samples
After phase separation, the samples were rinsed with pure water for three times. Then drying of polymer spheres was done with Freeze Dryer Alpha 1-2 of Christ. The samples were kept

in glass vials.

Porosity of polymer spheres

The porosity of solid materials has been defined in 4.1.2. On the basis of this concept, the porosity of large polymer spheres is given in Formula 4.13. The volume of dry spheres is calculated by dividing the mass of dry spheres with the density of PAN 200 powder.

$$P_{sphere} = \frac{V_1}{V_1 + V_2} \times 100\%$$

Formula 4.13

P_{sphere}: porosity of large polymer spheres;

V_1: volume of water losing from the wet spheres;

V_2: volume of dry spheres.

4.2.3 Shaping microspheres by DOD ink-jetting system

Introduction of the equipment

The shaping of microdroplets was achieved by microdrop dosing system MD-E-3011-130 from Microdrop Technologies, as shown in Figure 4.1. This dispensing system mainly contains two components: the control electronics (driver) and the shaping head (type: MD-K-140-320).

Figure 4.1 Microdrop dosing system MD-E-3011-130 [22].

This system is based on the piezo-driven ink-jetting printing. The shaping head can form single droplet with volume from 20 pL to 380 pL via non-contact dispensing. The viscosity range of liquid that can be dispensed by this system is 0.4 to 10,000 mPa·s. The diameter of nozzle is 100 μm. Driving pulses are composed of driving voltage and pulse width. The driving voltage ranges from -250 V to 250 V and the pulse width spans from 0 to 200 μs. The maximum shaping frequency is 6,000 Hz. Both the shaping head and liquid delivery pipeline can be heated to as high as 130°C.

4.2.3.1 Preparation of sodium alginate (SA) hydrogel microspheres

In order to decrease the risk of blocking the shaping head, water soluble SA was used as a model polymer to investigate the droplet formation firstly. Shaping SA microdroplets was

firstly investigated and then SA hydrogel microspheres were prepared via DOD shaping *cum* ionic crosslinking in water.

Part one: screening suitable SA microdroplets

Considering the most general situation of droplet formation by DOD mode, there are five stages [60]. Stage one is the ejecting and stretching of liquid. Then, the liquid thread pinches off from the nozzle exit. The third one is the contraction of liquid thread. After that, the liquid thread disintegrates into primary drop and satellites. At last, some of the satellites recombine with the primary drop. After coming out of the nozzle outlet, four morphologies of droplets exist [61], which are single primary droplet, primary drop with satellites, random spray, and just wetting of the nozzle.

Since the phenomenon of orifice flow (i.e. discontinuous jet by DOD shaping) of liquid is dynamic and complex, several requirements are proposed to screen droplets jetted from the nozzle in short time.

The first requirement is the monodispersion of droplets, which means that all droplets have the same size. The most ideal situation is that only single primary droplet exists after ejection. Even though two or more droplets coexist, they are acceptable only if their sizes are similar to each other. Primary droplet with satellites is also acceptable if the satellites can recombine with primary droplet.

The second requirement is the stability of droplet ejection. The analysis of trajectories of droplets is restricted by the flight distance of droplets which can be captured by CCD camera. Over far flight distance of droplets which can not be captured by CCD camera is beyond the scope of analysis. The most ideal situation is that the primary droplets almost have the same trajectory after ejection. In this case, droplets in flight seem to fix at the same position at a selected strobe delay time. During the flight of droplets, droplets from stable ejection do not fly randomly and their trajectories are straight within a finite distance. Stable droplets do not break up or have a large deformation. Droplets with similar size do not merge, which also belong to stable ejection. In brief, the stability of droplet ejection is the capability of keeping this ejection state.

The third requirement is the reproducibility of droplet formation. The most ideal situation is that given the same polymer solution and shaping conditions, the droplets jetted from the nozzle are the same whenever shaping is done. Moreover, this requirement is not absolute and should be understood and applied statistically.

In this work, the temperature of shaping SA solution was 25°C while shaping frequency was set at 10 Hz. Voltage ranging from 0 to 250 V was used with a screening increment of 5 V. Pulse width between 0 and 200 μs was used with a screening increment of 5 μs. The shaping conditions of droplets meeting monodispersion, stability, and reproducibility were plotted in a contour. This contour describes the relation between droplet size of SA solution and driving voltage, pulse width. A series of aqueous SA solutions were investigated and their contours were plotted, which are 0.1%, 0.5%, 0.8%, 1%, 1.5%, 1.6%, 1.7%, and 1.8%.

In order to calculate the size of microdroplets by Image J, a scale was needed. Fortunately, the diameter of shaping head's orifice can be used, which is 100 μm as shown in Figure 4.2. For simplicity, the scale of "600 μm" was used in practice, which was calculated according to proportion between inner and outer diameter of the orifice.

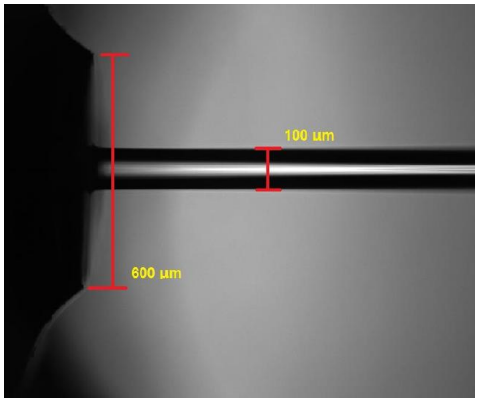

Figure 4.2 Scales used for the calculation of the size of microdroplets.

For the calculation of mean size of SA microdroplets, at least 5 of them were analyzed. In Image J, the photographs of SA microdroplets were fitted to an ellipse. The minor axis of a fitted ellipse represents the size of a SA microdroplet.

Part two: preparing SA hydrogel microspheres

In order to acquire large numbers of SA hydrogel microspheres, the shaping operation needs some durability. Given monodisperse, stable, and reproducible ejection, the duration of keeping this ejection state is defined as durability; however, for different polymer solutions with various shaping conditions, the fluctuation of this duration is large. The state of nozzle exit changes continuously in a shaping process and a typical example of non-durability is the accumulation of residual polymer. In order to meet this requirement, artificial interference is necessary to keep this durability.

In this work, three SA solutions were used, which are 0.5%, 1%, and 1.5%. Aqueous $CaCl_2$ solution with a concentration of 0.5 M was used. The shaping frequency was 400 Hz and the falling distance of SA microdroplets was 5 cm. The temperature of shaping head was 25°C. The temperature of gelation bath was 20°C. The default direction of shaping head is vertical to the surface of coagulant.

For the calculation of mean size of hydrogel microspheres, at least 100 of them were analyzed. In Image J, the photographs of hydrogel microspheres were fitted to an ellipse. In the calculation, the reference scale was introduced from the optical microscope. The minor axis of a fitted ellipse represents the size of a hydrogel microsphere.

4.2.3.2 Preparation of polyacrylonitrile (PAN) microspheres

According to the actual demand of work, four kinds of polymer were used in this section, which are X-PAN (M_w: 74 kg/mol), L-PAN (M_w: 77 kg/mol), PAN 150 (M_w: 150 kg/mol) and PAN 200 (M_w: 200 kg/mol). A selected polymer was dissolved in DMF to prepare PAN solution with various concentrations.

The driving voltage used here ranged from 0 to 250 V. The temperature range of shaping head was between 0 and 130°C. The pulse width was fixed at 25 µs. The maximum shaping frequency used in this section was 400 Hz and the falling distance of PAN microdroplets was between 0 and 30 cm. The default direction of shaping head is vertical to the surface of

coagulant.
For the phase separation of droplets of PAN solution, both water and DMF/water mixture were used. The temperature of coagulation bath was 20°C.
For the calculation of mean size of PAN microspheres, at least 100 of them were analyzed. In Image J, the photographs of PAN microspheres were fitted to an ellipse. In the calculation, the reference scale was introduced from the optical microscope. The minor axis of a fitted ellipse represents the size of a microsphere.

4.3 Carbonization of large polymer spheres

In this section, it will be shown how the polymeric samples were transformed into various carbon samples. The transformation refers to two stages, which are pre-oxidation and pyrolysis.
Four flow rates of gas were defined in this work, which are zero rate (i.e. static), low flow rate, moderate flow rate, and high flow rate. These four flow rates are distinguished by the different bubble formation rates in waste gas absorption bottle, which is linked to the pyrolysis quartz tube. This classification of flow rate is based on qualitative observation.
Two heating modes were used in this work, which are "one-step" heating mode and "stepwise" heating mode. For "one-step" heating mode, the desired temperature is set directly. By contrast, the desired temperature is increased by an increment of 50°C every time with "stepwise" heating mode.

4.3.1 Thermo analysis of PAN 200

Since large polymer spheres were made of PAN 200, the thermo property of PAN 200 should be known before carbonization. The basic principles and functions of TGA, DTA, and DSC have been introduced in 4.1.5. Thermo analysis conditions of PAN 200 are given in this section.
TGA measurements focus on the mass change of samples due to various thermo behaviors. With the existence of oxygen, the weight loss of PAN 200 in pre-oxidation stage was investigated. The derivative thermo gravimetric (DTG) curve derived from TGA curve shows the rate of weight loss. The heating rate was 5 K/min and temperature range varied from 25 to 800°C. Considering the actual oxidation process, the weight loss of PAN 200 in argon atmosphere was also analyzed. The measuring conditions of non-oxidative TGA were same to that of oxidative TGA.
In terms of temperature difference, DTA measurements investigate the categories and magnitude of thermo effects. With the existence of oxygen, the thermo effects of PAN 200 in pre-oxidation stage were investigated. The heating rate was 5 K/min and temperature range varied from 25 to 800°C. Considering the actual oxidation process, the thermo effects of PAN 200 in argon atmosphere was also analyzed. The measuring conditions of non-oxidative DTA were same to that of oxidative DTA.
In terms of enthalpy, DSC measurements investigate the categories and magnitude of thermo effects with higher sensitivity and resolution. The DSC measurement of PAN 200 was done in argon atmosphere. The heating rate was 5 K/min and temperature range varied from 20 to 600°C.

4.3.2 Pre-oxidation

Preliminary exploration

Large polymer spheres were used as precursors. Pre-oxidation was done in a quartz tube furnace from Heraeus company. Polymer spheres were put in a ceramic boat, which was pushed into the central part of quartz tube. Four pre-oxidation temperatures were used, which are 240°C, 270°C, 300°C, and 330°C. Similarly, four kinds of retention time were adopted, which are 1 hour, 1.5 hours, 2 hours, and 2.5 hours. For each of the test combination conditions of retention time and oxidation temperature, it was repeated for three times. During the pre-oxidation process, the polymer spheres contacted static air. The heating mode was "one-step".

Mean size of carbon spheres after pre-oxidation

For the calculation of mean size of carbon spheres, at least 100 of them were analyzed. In Image J, the photographs of carbon spheres were fitted to an ellipse. In the calculation, the reference scale was introduced. The minor axis of a fitted ellipse represents the size of a carbon sphere.

The effect of flow rate of air and heating mode

Another two factors which is related to the pre-oxidation process are the flow rate of air and heating mode. In this section, large polymer spheres were used. The pre-oxidation temperature was 300°C with a retention time of 2 hours. Three flow rates of air were used, which are zero rate, low flow rate (i.e. 1 bubble per second), and high flow rate. Both "one-step" and "stepwise" heating modes were adopted.

Determination of pre-oxidation temperature and time

Large polymer spheres were used. On the basis of preliminary exploration of oxidation, two oxidation temperatures were used in this section, which are 270°C and 300°C. Similarly, two kinds of retention time were used, which are 1 hour and 2 hours. During the pre-oxidation process, the polymer spheres contacted static air. The heating mode was "one-step".

4.3.3 Pyrolysis without activation

The second step of carbonization process is pyrolysis, which contains two modes. The first mode is pyrolysis without activation, which is shown in this section. The second mode is pyrolysis with activation, which is shown in 4.3.5.

Preliminary exploration

Carbon spheres after pre-oxidation were used as precursors. Four pyrolysis temperatures were used, which are 500°C, 550°C, 600°C, and 650°C. Similarly, four kinds of retention time were adopted, which are 23 min (i.e. minutes), 45 min, 68 min, and 90 min. For each of the test combination conditions of retention time and pyrolysis temperature, it was repeated for three times. During the pyrolysis process, the flow rate of nitrogen was low (i.e. 1 bubble per second). The heating mode was "stepwise".

Mean size of carbon spheres after pyrolysis

For the calculation of mean size of carbon spheres, at least 100 of them were analyzed. In Image J, the photographs of carbon spheres were fitted to an ellipse. In the calculation, the reference scale was introduced. The minor axis of a fitted ellipse represents the size of a carbon sphere.

4.3.4 Porosity of carbon spheres

The definitions of effective solid density and porosity have been interpreted in 4.1.2. The calculation of porosity of carbon spheres was divided into two steps. Firstly, the effective solid density of carbon spheres was calculated. Then the porosity of carbon spheres was acquired. Carbon spheres were from preliminary exploration of both pre-oxidation and pyrolysis.

Calculation of effective solid density

In this section, a pycnometer was used. Water was used as reference liquid, whose density was 0.99799 g/cm^3 at 21°C. Normal heptane (i.e. *n*-heptane) was adopted as working medium to calculate the effective solid density of carbon spheres.

At 21°C, the density of *n*-heptane was calculated by Formula 4.14.

$$\rho_{hep} = \frac{m_1 - m_0}{m_2 - m_0} \cdot \rho_{water}$$

Formula 4.14

ρ_{water}: density of water;

ρ_{hep}: density of *n*-heptane;

m_0: mass of pycnometer;

m_1: mass of pycnometer and *n*-heptane;

m_2: mass of pycnometer and water.

Still at 21°C, the effective solid density of carbon spheres is given by Formula 4.15.

$$\rho_{\text{carbon}} = \frac{m_3 - m_0}{(m_1 - m_0) - (m_4 - m_3)} \cdot \rho_{hep}$$

Formula 4.15

ρ_{carbon}: effective solid density of carbon spheres;

ρ_{hep}: density of *n*-heptane;

m_3: mass of pycnometer and carbon spheres;

m_4: mass of pycnometer and carbon spheres and *n*-heptane.

Calculation of porosity

In this section, a culture dish was used and weighed. Carbon spheres were put in the culture dish and weighed again. Then carbon spheres were soaked in *n*-heptane to saturation by dropping *n*-heptane to the dish. After removing redundant *n*-heptane, the dish was weighed

again. All the operations were done at 21°C. The porosity of carbon spheres is given by Formula 4.16.

$$P_{carbon} = \frac{\frac{m_7 - m_6}{\rho_{hep}}}{\frac{m_7 - m_6}{\rho_{hep}} + \frac{m_6 - m_5}{\rho_{carbon}}} \times 100\%$$

Formula 4.16

P_{carbon}: porosity of carbon spheres;
ρ_{hep}: density of *n*-heptane;
ρ_{carbon}: effective solid density of carbon spheres;
m_5: mass of culture dish;
m_6: mass of culture dish and carbon spheres.
m_7: mass of culture dish and carbon spheres and *n*-heptane.

4.3.5 Pyrolysis with activation

This section shows the second mode of pyrolysis, which is pyrolysis with activation.
In this section, main factors related to the structures of carbon spheres are activation, retention time, pyrolysis temperature, and flow rate of gas. The heating mode was "stepwise". Four pyrolysis temperatures were selected, which are 600°C, 800°C, 900°C, and 1,000°C. Three retention times were chosen, which are 0.5 hour, 1 hour, and 2 hours.
For gases with low flow rate, there were nitrogen (i.e. 1 bubble per second), nitrogen + carbon dioxide (i.e. 1+1 bubbles per second), and carbon dioxide (i.e. 1 bubble per second).
For gases with moderate flow rate, there were carbon dioxide (i.e. 5 bubbles per second), carbon dioxide (larger than 5 bubbles per second), and nitrogen (5 bubbles per second).
For gases with high flow rate, there were nitrogen and carbon dioxide.

4.4 Preparation of polymer and carbon nanocomposites

Screening appropriate nanoparticles
Several kinds of titanium dioxide nanoparticles were firstly used in this section, which are P90 (416), P25, P90 (315), T805, and pure anatase. The basic properties of these nanoparticles have been introduced in section 2.3.
The dosage of TiO_2 was 10 mg. Rhodamine B solution of 0.05 mmol/L was used with a volume of 30 mL. The inspection wavelength of rhodamine B solution was 555 nm in UviLine 9400 UV-Vis spectrometer. A controlled trial was also arranged without adding any TiO_2.
The photocatalytic tests were done in an UV irradiation system (TLC CN-15 viewing cabinet) from Vilber Lourmat GmbH, as shown in Scheme 4.7. The optical source is composed of two 15 W lamps with an emission wavelength of 365 nm.

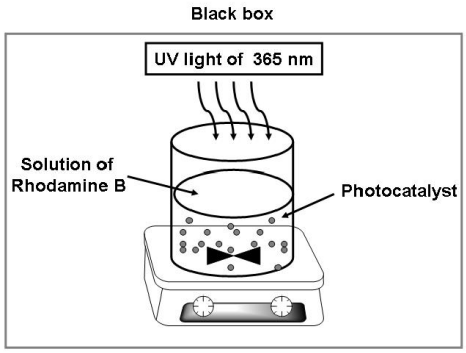

Scheme 4.7 Photocatalytic tests.

After photocatalytic tests started, the absorbance of rhodamine B solution was measured every 15 min. The conversion relation between absorbance and concentration of solution is shown in Formula 4.17 [62].

$$\frac{C_t}{C_0} = \frac{A_t}{A_0}$$

Formula 4.17

A_0: absorbance of rhodamine B solution at 0 times;
C_0: concentration of rhodamine B solution at 0 times;
A_t: absorbance of rhodamine B solution at *t* times;
C_t: concentration of rhodamine B solution at *t* times.

Preparation of solvent-nanoparticles-polymer ternary dispersion
P90 was firstly dispersed in DMF. The mass fractions of P90 in DMF were targeted at 0.5%, 0.75%, and 1%. The mixture of P90 and DMF were put in a three-armed dispersing vessel. After that, the tip of ultrasonic sonotrode (i.e. KE = 76) submerged in the mixture with a depth of two centimeters. The vessel was cooled from the outside with an ice bath. The ultrasonic power was set at 50% and the ultrasonic time was set for 30 min.
After sonication, the DLS measurement of dispersion was done immediately. The measurement started after a series of setting up of parameters. With three times' measurements finished, the DLS equipment gave the size distribution of nanoparticles automatically. The mean diameter of P90 dispersion was in the form of mean intensity diameter (i.e. MI), mean number diameter (i.e. MN), and mean volume diameter (i.e. MV). Because of the existence of occasional large nanoparticles, the MN diameter was preferred.
The solvent-nanoparticles-polymer ternary dispersion was made by adding PAN 200 powder into the P90 dispersion. The mass fraction of PAN 200 powder in DMF was 5%, so the mass fractions of P90 in PAN 200 powder were 10%, 15%, and 20%.

Preparation of polymer nanocomposites by droplets shaping *cum* phase separation
The shaping of spherical nanocomposites was the same as that of large polymer spheres. Droplets were shaped by a syringe pump. The diameter of the needle was 1.2 mm. The falling distance was 5 cm. The coagulant was made up of DMF and water with a volumetric ratio of

65 to 35. The temperature of coagulation bath was 20°C. The acquired polymer nanocomposites were named as “10% PAN+P90”, “15% PAN+P90”, and “20% PAN+P90”. As reference, PAN 200 solution of 5% was also shaped into spheres with the same methods and conditions. These spheres were denoted as “5% PAN spheres”.
The dosage of photocatalyst is shown in Table 4.5.

Table 4.5 The dosage of polymer nanocomposites used in photocatalytic tests.

Type of composites	P90 (mg)	Dry nanocomposites (g)	Wet nanocomposites (g)
10% PAN+P90	10	0.1	1.35
15% PAN+P90	10	0.067	0.90
20% PAN+P90	10	0.05	0.625

One requirement is that the dosage of P90 in both dry and wet nanocomposites should be 0.01 g. The dosage of dry nanocomposites was calculated based on the nominal content of P90 in polymer nanocomposites. The dosage of wet nanocomposites was calculated based on the mass fractions of nanocomposites in wet nanocomposites.

Carbonization of spherical nanocomposites
After drying of the nanocomposites, they were firstly pre-oxidized at 270°C for 1 hour. After that, the acquired oxidation nanocomposites were further pyrolyzed and activated at 900°C for 30 min. The atmosphere was CO_2, whose flow rate was 5 bubbles per second. The final nanocomposites used in photocatalytic tests were denoted as “10% Carbon+P90”, “15% Carbon+P90”, and “20% Carbon+P90”. As reference, “5% PAN spheres” were carbonized into “5% carbon spheres” with same methods and conditions.
As shown in Table 4.5, carbon nanocomposites were acquired by carbonizing corresponding dry polymer nanocomposites: “10% PAN+P90” (0.1 g), “15% PAN+P90” (0.067 g), and “20% PAN+P90” (0.05 g).

The content of P90 in nanocomposites
The content of nanoparticles in polymer and carbon nanocomposites was determined by TGA analysis. With the existence of oxygen atmosphere, the weight loss of nanocomposites was recorded. The heating rate was 10 K/min and temperature varied from 20 or 25 to 800°C. For polymer-based nanocomposites, the content of P90 was measured for three times.

4.5 Applications of various spheres and nanocomposites

In this section, three potential applications of spheres and nanocomposites are shown. The adsorption and photocatalytic degradation of organic molecules are given firstly. Carbon materials as reductive catalyst used in oxygen reduction reaction (ORR) is also shown here.

4.5.1 Adsorption tests and adsorption isotherms

In this section, standard curves of various organic molecules in aqueous solutions were plotted firstly. The measurement of absorbance was done by UviLine 9400 UV-Vis spectrometer from Schott Instruments. The standard curves of phenols and dyes are given in

appendix 8.4.

The plotting of standard curves

Solution of phenol

A series of standard solutions were prepared, which are 50, 100, 200, 300, 400, and 500 mg/L. The absorption wavelength of phenol solution used was 250 nm. With concentrated HCl solution as regulator, the pH of all standard solutions was two. This standard curve was used in the adsorption tests with both polymer and carbon spheres as adsorbents.

Used in the adsorption tests of polymer spheres, a series of standard solutions were prepared, which are 20, 40, 60, 80, and 100 mg/L. The absorption wavelength of phenol solution used was 270 nm. With 0.1 M HCl solution as regulator, the pH of all standard solutions was two.

Solution of *p*-chlorophenol

Used in the adsorption tests of polymer spheres, a series of standard solutions were prepared, which are 50, 100, 200, 300, 400, and 500 mg/L. The absorption wavelength of *p*-chlorophenol solution used was 250 nm. With 0.1 M HCl solution as regulator, the pH of all standard solutions was two.

Used in the adsorption tests of carbon spheres, a series of standard solutions were prepared, which are 50, 100, 200, 300, 400, and 500 mg/L. The absorption wavelength of *p*-chlorophenol solution used was 250 nm. With concentrated HCl solution as regulator, the pH of all standard solutions was two.

Solution of *p*-nitrophenol

Used in the adsorption tests of polymer spheres, a series of standard solutions were prepared, which are 100, 200, 300, 400, and 500 mg/L. The absorption wavelength of *p*-nitrophenol solution used was 402 nm. With 0.1 M HCl solution as regulator, the pH of all standard solutions was two.

Used in the adsorption tests of carbon spheres, a series of standard solutions were prepared, which are 100, 200, 300, 400, and 500 mg/L. The absorption wavelength of *p*-nitrophenol solution used was 402 nm. With concentrated HCl solution as regulator, the pH of all standard solutions was two.

Solution of methylene blue (MB)

A series of standard solutions were prepared, which are 10, 20, 30, 40, 50, and 60 mg/L. The absorption wavelength of MB solution used was 247 nm. This standard curve was used in the adsorption tests with both polymer and carbon spheres as adsorbents.

Solution of methyl orange (MO)

A series of standard solutions were prepared, which are 20, 40, 60, 80, 100, and 120 mg/L. The absorption wavelength of MO solution used was 272 nm. This standard curve was used in the adsorption tests with carbon spheres as adsorbents.

Solution of rhodamine B (Rh B)

A series of standard solutions were prepared, which are 20, 40, 80, 120, 160, and 200 mg/L.

The absorption wavelength of Rh B solution used was 354 nm. This standard curve was used in the adsorption tests with both polymer and carbon spheres as adsorbents.

Adsorption tests

The adsorption tests were designed according to the standard curves. All the adsorption tests were done on a shaker and happened in aqueous solution. Each of the adsorption tests was repeated for three times.

Two kinds of large polymer (i.e. PAN 200) spheres were used in this section, which are "8%, 0/100" and "8%, 65/35".

Two kinds of carbon spheres were used in adsorption tests, which are denoted as "1,000°C, 30 min" and "1,000°C, 1 hour".

Adsorption of phenol on polymer spheres

Two kinds of polymer spheres were used as adsorbents. The volume of phenol solution was 25 mL, with a concentration ranging from 100 to 500 mg/L. The mass of adsorbent varied from 100 to 500 mg, correspondingly. The pH of phenol solution was two and adsorption temperature was 20°C. After 48 hours' contact, the adsorption equilibrium was reached.

Two kinds of polymer spheres were used as adsorbents. The volume of phenol solution was 25 mL, with a concentration ranging from 20 to 100 mg/L. The mass of adsorbent varied from 20 to 100 mg, correspondingly. The pH of phenol solution was two and adsorption temperature was 20°C. After 48 hours' contact, the adsorption equilibrium was reached.

Adsorption of *p*-chlorophenol on polymer spheres

Two kinds of polymer spheres were used as adsorbents. The volume of *p*-chlorophenol solution was 25 mL, with a concentration ranging from 100 to 500 mg/L. The mass of adsorbent varied from 100 to 500 mg, correspondingly. The pH of *p*-chlorophenol solution was two and adsorption temperature was 20°C. After 48 hours' contact, the adsorption equilibrium was reached.

Adsorption of *p*-nitrophenol on polymer spheres

Two kinds of polymer spheres were used as adsorbents. The volume of *p*-nitrophenol solution was 25 mL, with a concentration ranging from 100 to 500 mg/L. The mass of adsorbent varied from 100 to 500 mg, correspondingly. The pH of *p*-nitrophenol solution was two and adsorption temperature was 20°C. After 48 hours' contact, the adsorption equilibrium was reached.

Adsorption of MB on polymer spheres

Two kinds of polymer spheres were used as adsorbents. The volume of MB solution was 25 mL, with a concentration ranging from 20 to 60 mg/L. The mass of adsorbent was 25 mg. The adsorption temperature was 20°C. After 48 hours' contact, the adsorption equilibrium was reached.

Adsorption of Rh B on polymer spheres

Two kinds of polymer spheres were used as adsorbents. The volume of Rh B solution was 25

mL, with a concentration ranging from 40 to 200 mg/L. The mass of adsorbent was 25 mg. The adsorption temperature was 20°C. After 48 hours' contact, the adsorption equilibrium was reached.

Adsorption of phenol on carbon spheres
Two kinds of carbon spheres were used as adsorbents. The volume of phenol solution was 25 mL, with a concentration ranging from 100 to 500 mg/L. The mass of adsorbent was 20 mg. The pH of phenol solution was two and adsorption temperature was 20°C. After two weeks' contact, the adsorption equilibrium was reached.

Adsorption of *p*-chlorophenol on carbon spheres
Two kinds of carbon spheres were used as adsorbents. The volume of *p*-chlorophenol solution was 25 or 30 mL, with a concentration ranging from 100 to 500 mg/L. The mass of adsorbent was 20 or 10 mg. The pH of *p*-chlorophenol solution was two and adsorption temperature was 20°C. After two weeks' contact, the adsorption equilibrium was reached.

Adsorption of *p*-nitrophenol on carbon spheres
Two kinds of carbon spheres were used as adsorbents. The volume of *p*-nitrophenol solution was 30 or 50 mL, with a concentration ranging from 100 to 500 mg/L. The mass of adsorbent was 10 mg. The pH of *p*-nitrophenol solution was two and adsorption temperature was 20°C. After two weeks' contact, the adsorption equilibrium was reached.

Adsorption of MB on carbon spheres
Two kinds of carbon spheres were used as adsorbents. The volume of MB solution was 50 mL, with a concentration ranging from 20 to 60 mg/L. The mass of adsorbent was 10 mg. The adsorption temperature was 20°C. After two weeks' contact, the adsorption equilibrium was reached.

Adsorption of MO on carbon spheres
Two kinds of carbon spheres were used as adsorbents. The volume of MO solution was 30 or 50 mL, with a concentration ranging from 40 to 120 mg/L. The mass of adsorbent was 10 mg. The adsorption temperature was 20°C. After two weeks' contact, the adsorption equilibrium was reached.

Adsorption of Rh B on carbon spheres
Two kinds of carbon spheres were used as adsorbents. The volume of Rh B solution was 30 or 50 mL, with a concentration ranging from 40 to 200 mg/L. The mass of adsorbent was 10 mg. The adsorption temperature was 20°C. After two weeks' contact, the adsorption equilibrium was reached.

4.5.2 Photocatalytic tests
Generally, the adsorption of solute on adsorbent will take long time to reach equilibrium adsorption. To decrease the effect of adsorption on photocatalysis as much as possible, a pre-treatment of adsorption without UV irradiation is needed before the photocatalytic

process.

Photocatalytic tests of polymer nanocomposites

The photocatalytic tests were done in an UV irradiation system (TLC CN-15 viewing cabinet), as shown in Scheme 4.7. The optical source is composed of two 15 W lamps with an emission wavelength of 365 nm. Rhodamine B solution of 0.05 mmol/L was used with a volume of 30 mL. The inspection wavelength of rhodamine B solution was 555 nm in UviLine 9400 UV-Vis spectrometer.

A controlled trial was also done with the same conditions except for no UV light. Before photocatalytic tests, a 24 hours' adsorption in dark environment was needed. After photocatalytic tests started, the absorbance of rhodamine B solution was measured every 20 min.

Photocatalytic tests of carbon nanocomposites

The photocatalytic tests were done in an UV irradiation system (TLC CN-15 viewing cabinet), as shown in Scheme 4.7. The optical source is composed of two 15 W lamps with an emission wavelength of 365 nm. Rhodamine B solution of 0.05 mmol/L was used with a volume of 30 mL. The inspection wavelength of rhodamine B solution was 555 nm in UviLine 9400 UV-Vis spectrometer.

A controlled trial was also done with the same conditions except for no UV light. Before photocatalytic tests, a 24 hours' adsorption in dark environment was needed. After photocatalytic tests started, the absorbance of rhodamine B solution was measured every 20 min.

4.5.3 Oxygen reduction reaction tests

Three kinds of carbon spheres, i.e. "5% carbon spheres", "1,000°C, 30 min" spheres, and "1,000°C, 1hour" spheres, were used in oxygen reduction reaction. These carbon spheres were ground to powders before tests. For better comparison, "5% carbon spheres" was used in the name of "900°C, 30 min".

Preparation of working electrodes

The carbon catalyst (5 mg) was put in a mixture, which contains 490 μL ethanol (absolute), 490 μL ultra-pure water, and 20 μL Nafion dispersion (5 % in weight). The mixture was sonicated for 30 min to obtain a fine dispersion.

The glassy carbon disk in a Teflon sheath was firstly polished by polishing paper with different size of abrasive particles (3 μm, 1 μm, and 0.3 μm). Absolute ethanol was used as lubricant. Then, the glassy carbon was polished by a suspension of alumina slurry (0.05 μm) for 5 min. After that, the glassy carbon was sonicated in a mixture of ultra-pure water and absolute ethanol to remove the remaining alumina and dried by a nitrogen stream.

In RDE tests, the working electrode was prepared by dropping the catalytic ink on the surface of glassy carbon to create a homogeneous film. The catalyst loading is from 0.2 to 0.4 mg/cm^2. The areas of disk electrode are 0.1134 cm^2.

The preparation of working electrode in RRDE tests was same to that in RDE tests. Especially, the casting of catalyst film should not be beyond the boundary of disk electrode.

The catalyst loading is always 0.2 mg/cm^2. The areas of disk electrode are 0.1963 cm^2.

Tests of rotating disk electrode (RDE)

The RDE tests were performed with a potentiostat/galvanostat (Autolab PGSTAT302N) from Metrohm company. A three-electrode cell setup was used, with a glassy carbon electrode as the working electrode, a platinum mesh as the counter electrode, and an Ag/AgCl (3 M KCl) electrode as the reference electrode. The rotating disk electrode (i.e. glassy carbon electrode) is an Autolab RDE-2 rotator, which is driven by motor controller. The counter electrode was separated from the working electrode by a glass frit to avoid possible contamination during measurements.

A KOH solution of 0.1 M was used as electrolyte. The open circuit potential (OCP) was measured in 60 seconds. Then electrochemical impedance spectroscopy (EIS) was used to determine the resistance (R) of solution at the open circuit potential. The frequency ranged from 50 kHz to 10 Hz with the alternating current amplitude of 10 mV. Before the measurement of polarization curve, a conditioning step was done by 15 cyclic voltammetry (CV) sweeps without rotation from 0 to -0.5 V vs. Ag/AgCl (3 M KCl) with a scan rate of 100 mV/s.

The polarization curve was captured by linear sweep voltammetry (LSV). The potential window was 0 to -1 V vs. Ag/AgCl (3 M KCl) with a scan rate of 5 mV/s. The revolutions per minute (rpm) ranged from 100 to 2,000 rpm. The electrolyte solution was firstly purged by argon or oxygen for 25 min. The background currents were acquired by recording polarization curves in argon saturated solution. After that, the working electrode was rinsed by water and immersed in oxygen saturated solution to record the corresponding polarization curves. During the measurement, a stream of argon or oxygen was maintained on the surface of solution.

All potentials were converted to the reversible hydrogen electrode (RHE) scale (see Formula 4.18) and corrected for the potential drop over the electrolyte. The pH value of electrolyte solution was 13.5.

$$E_{RHE} = E_{Ag\,/\,AgCl\,/\,3M\ KCl} + 0.21 + 0.059 \cdot pH - i_D R$$

Formula 4.18

E_{RHE}: electrode potential vs. RHE;

$E_{Ag/AgCl/3\ M\ KCl}$: measured electrode potential;

i_D: disk current;

R: resistance of solution.

The final disk current was acquired by deducting the disk current within argon atmosphere from the disk current within oxygen atmosphere. The polarization curves were presented in the form of current density against potential. Based on polarization curves and Koutecky-Levich (K-L) equations (see Formula 4.19) [11], the electron transfer number (n) can be estimated (see Formula 4.20).

$$\frac{1}{j} = \frac{1}{j_K} + \frac{1}{j_L} = \frac{1}{j_K} + \frac{1}{B \cdot \omega^{1/2}}$$

Formula 4.19

$$B = 0.62 \cdot n \cdot F \cdot C_0 \cdot (D_0)^{2/3} \cdot \upsilon^{-1/6}$$

Formula 4.20

j: measured current density (mA/cm^2);
j_K: kinetic current density (mA/cm^2);
j_L: diffusion-limiting current density (mA/cm^2);
B: the Levich constant;
ω: angular velocity of the disk (rad/s);
n: electron transfer number per oxygen molecule;
F: the Faraday constant (96485 C/mol);
C_0: bulk concentration of oxygen (1.2×10^{-6} mol/cm^3);
D_0: diffusion coefficient of oxygen (1.9×10^{-5} cm^2/s) in 0.1 M KOH electrolyte;
υ: the kinetic viscosity of electrolyte (0.01 cm^2/s).

Tests of rotating ring disk electrode (RRDE)

The RRDE tests were also performed on Autolab PGSTAT302N from Metrohm company by a bipotentiostat mode. A four-electrode cell setup was used, with a glassy carbon electrode as the working electrode (with platinum ring), a platinum mesh as the counter electrode, and an Ag/AgCl (3 M KCl) electrode as the reference electrode. The rotating ring disk electrode is an Autolab rotator, which is driven by motor controller.

A KOH solution of 0.1 M was used as electrolyte. The open circuit potential (OCP) was measured in 60 seconds. Prior to the measurement of polarization curve, a conditioning step was done by 15 cyclic voltammetry (CV) sweeps without rotation from 0 to -0.5 V vs. Ag/AgCl (3 M KCl) with a scan rate of 100 mV/s. Electrochemical impedance spectroscopy (EIS) was used to determine the resistance (*R*) of solution at the open circuit potential. The frequency ranged from 50 kHz to 10 Hz with the alternating current amplitude of 10 mV.

The polarization curve was also captured by linear sweep voltammetry (LSV). The potential window was 0 to -1 V vs. Ag/AgCl (3 M KCl) with a scan rate of 5 mV/s. The rotating speed of working electrode was set at 1,600 rpm. The potential of platinum ring was set at 0.4 V vs. Ag/AgCl (3 M KCl) for all measurements. The electrolyte solution was firstly purged by argon or oxygen for 25 min. The background currents were acquired by recording polarization curves in argon saturated solution. After that, the working electrode was rinsed by water and immersed in oxygen saturated solution to record the corresponding polarization curves. During the measurement, a stream of argon or oxygen was maintained on the surface of solution.

All potentials were converted to the reversible hydrogen electrode (RHE) scale (see Formula 4.18).The final disk current was acquired by deducting the disk current within argon atmosphere from the disk current within oxygen atmosphere. The polarization curves were presented in the form of current density against potential.

The collection efficiency (CE) was calculated by using the redox process of Fe^{3+}/Fe^{2+} in

KOH solution (0.1 M) with the concentration of $K_3[Fe(CN)_6]$ being 0.5 mmol/L. Before the measurement, the testing solution was purged by argon for 25 min. During the measurement, a stream of argon was maintained on the surface of solution. The potential of platinum ring was set at 0.4 V vs. Ag/AgCl (3 M KCl). The polarization curve was captured by LSV with a scan rate of 5 mV/s and rotating speed of 1,600 rpm. The CE is given by Formula 4.21.

$$CE = \frac{-\left[i_R - \min\left(i_R\right)\right]}{i_D} \cdot 100\%$$

Formula 4.21

CE: collection efficiency;
i_D: disk current;
i_R: ring current.

The electron transfer number (n) is given by Formula 4.22.

$$n = \frac{4 \cdot i_D}{i_D + i_R / CE}$$

Formula 4.22

n: electron transfer number;
i_D: disk current;
i_R: ring current;
CE: collection efficiency.

The yield of H_2O_2 was calculated by Formula 4.23.

$$H_2O_2(\%) = 200 \cdot \frac{i_R / CE}{i_R / CE + i_D}$$

Formula 4.23

H_2O_2(%): yield of hydrogen peroxide;
i_D: disk current;
i_R: ring current;
CE: collection efficiency.

5 Results and Discussion

5.1 Large polymer spheres shaped by syringe pump

5.1.1 Rheological characterization of PAN solutions

The rheological characterization of PAN 200 solutions is shown in Figure 5.1.

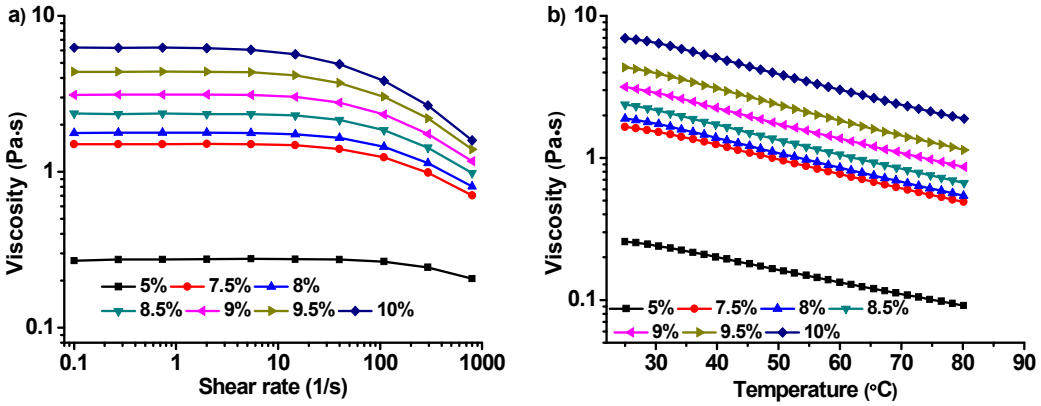

Figure 5.1 Rheological characterizations of PAN 200 solutions. a) viscosity curves of PAN 200 solutions, temperature: 25°C; b) temperature-dependent flow behaviors of PAN 200 solutions, shear rate: 5 s^{-1}.

With the increasing of shear rate, the apparent viscosity of PAN 200 solutions in Figure 5.1a decreases, which indicates a character of shear thinning. With the existence of shear force, the orientation and disentanglement of polymer chains result in the behavior of shear thinning [63]. At a specific shear rate, the viscosity of PAN 200 solutions increases as the concentration of PAN 200 solutions increases. Higher concentration of solution leads to higher degree of entanglement of polymer chains, which results in higher viscosity of the solution.

With the increasing of temperature, the movements of polymer segments and solvent molecules increase and the entanglement between polymer chains decreases; then the viscosity of PAN 200 solutions decreases as shown in Figure 5.2b. At a selected temperature, the viscosity of PAN 200 solutions increases as the concentration of PAN 200 solutions increases. In conclusion, both increasing shear rate and increasing temperature can improve the mobility of PAN 200 solutions.

The shaping of large polymer spheres was investigated from two aspects: morphology and inner structure. Morphology of polymer spheres was firstly studied and suitable shaping conditions were acquired. After that, the inner structure of polymer spheres was further investigated.

5.1.2 Morphology of large polymer spheres

The effect of concentration of polymer solution on the shape of polymer spheres is shown in Figure 5.2. In Figure 5.2a and 5.2b, because of the low concentration (5%) of PAN 200 solution, the rigidity of droplets to resist deformation due to collision with other droplets is finite. Some of the droplets deformed and adhered to each other when droplets fell into water. Due to the larger diameter of needle, the deformation and agglomeration of polymer spheres

in Figure 5.2b is more serious. The reason is that larger polymer droplets need more time to finish gelation via phase separation.

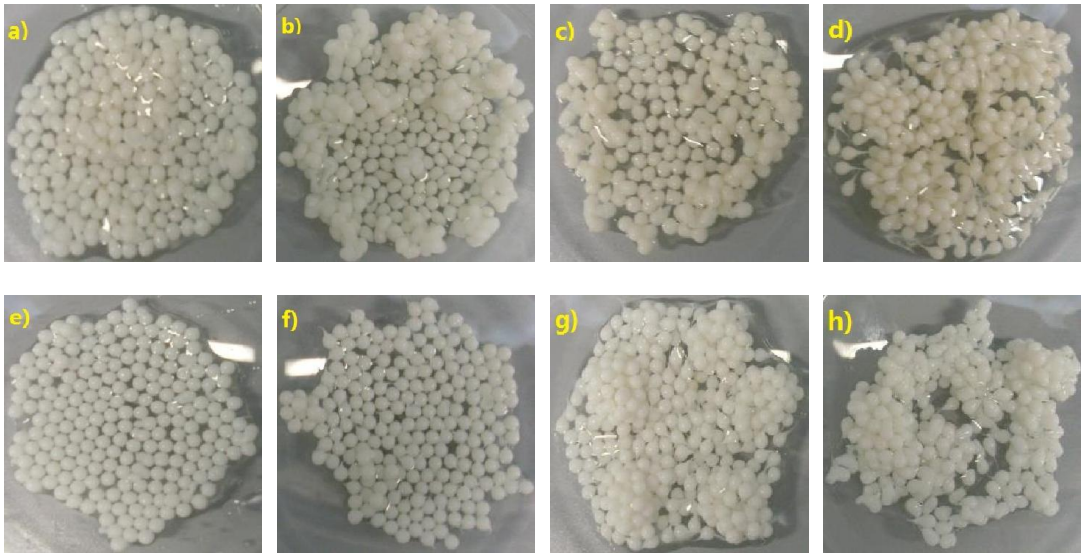

Figure 5.2 Effect of polymer concentration on the shape of polymer spheres. gelation conditions: pure water as coagulant at 20°C; falling distance: 5 cm; a), c-h): polymer spheres prepared from 5%, 7.5%, 10%, 8%, 8.5%, 9%, and 9.5% PAN 200 solutions with a needle of 1.2 mm; b) polymer spheres prepared from 5% PAN 200 solution with a needle of 1.36 mm.

In order to avoid deformation and agglomeration of droplets, further increasing the concentration is necessary. Polymer spheres in Figure 5.2c were shaped with a concentration of 7.5% and deformation and agglomeration of spheres can also be observed. Polymer spheres in Figure 5.2d were shaped with a concentration of 10%, and the deformation and agglomeration disappear. In addition, spheres in Figure 5.2d have long tails. These spheres look like a bunch of grapes because of the entanglement of tails. The existence of long tails is firstly due to the higher concentration of polymer solution, i.e. higher viscosity. Secondly, droplets shaped from polymer solution with higher concentration need a longer falling distance to transform their "tear-like" shape to spherical shape with the help of surface tension [21].

With the falling distance of droplets constant (i.e. 5 cm), decreasing the concentration of solution suppresses the formation of tails as shown in Figure 5.2e-h. In the end, PAN 200 solution of 8% was chosen for further preparation of spheres.

The effect of gelation rate on the shape of polymer spheres is demonstrated in Figure 5.3. The gelation rate of polymer droplets in coagulant was controlled by changing the volume fractions of DMF in water. Five typical samples were selected and presented here. With the volume fractions of DMF increasing from 0% to 50%, the morphology of polymer spheres does not change. Polymer spheres in Figure 5.3d and 5.4e are like tadpoles. In this case, polymer droplets gelled in a coagulant with 70% and 75% DMF, respectively. Over high factions of DMF decreases the gelation rate of polymer droplets, which deformed in coagulation bath due to stirring and collision with other droplets or spheres.

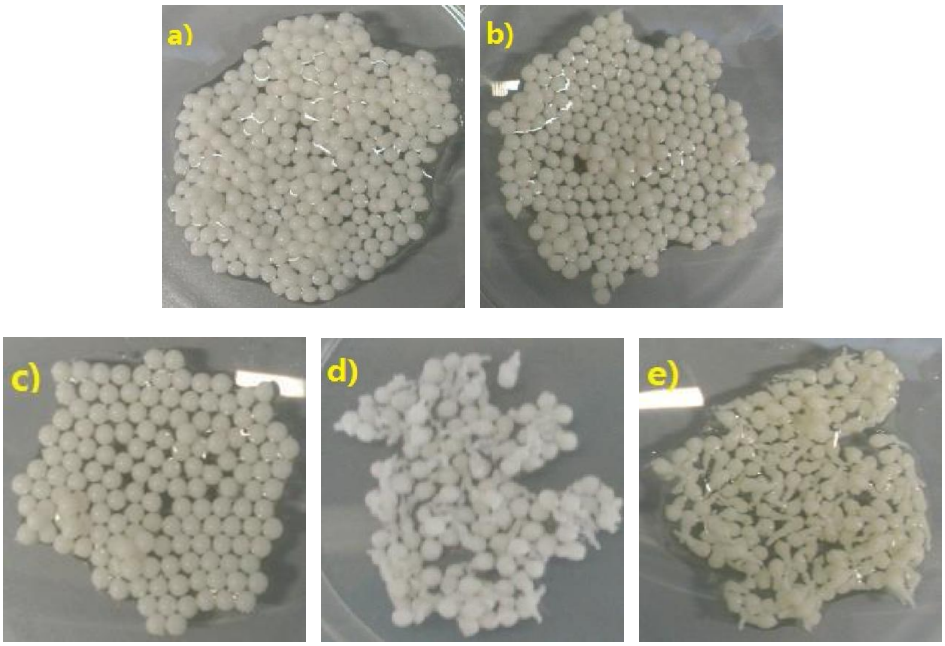

Figure 5.3 Effect of gelation rate on the shape of polymer spheres. 8% PAN 200 solution; gelation temperature: 20°C; falling distance: 5 cm; a-e): polymer spheres gelled in coagulant with various volume factions of DMF: 0%, 25%, 50%, 70%, and 75%.

The effect of falling distance on the aspect ratio of polymer spheres is indicated in Figure 5.4.

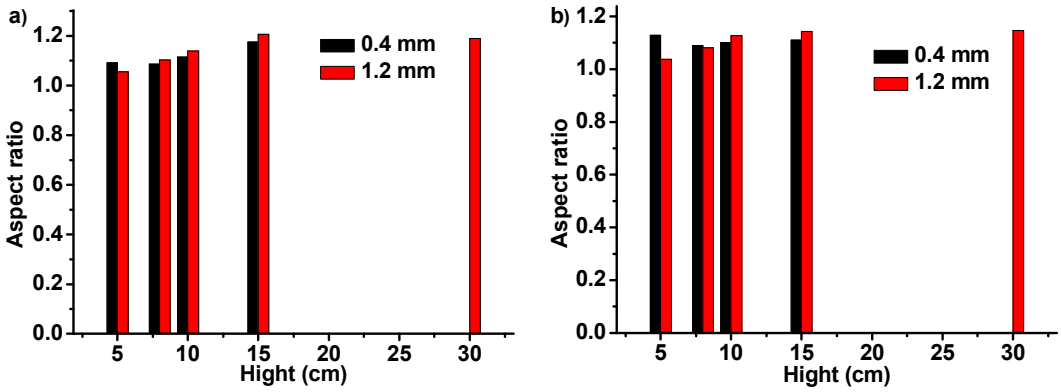

Figure 5.4 Effect of falling distance on the aspect ratio of polymer spheres. 8% PAN 200 solution; water as coagulant at 20°C; a) wet polymer spheres; b) dry polymer spheres.

Aspect ratio is a simple descriptor for near-rounded shapes. The shape of spheres was firstly fitted to ellipse by Image J, which gave the lengths of both major axis and minor axis. For the calculation of aspect ratio, the mean values of both major axis and minor axis were acquired by Gaussian fit [64]. For a perfect circle, its aspect ratio is definitely one. The aspect ratios of two kinds of wet spheres (0.4 mm and 1.2 mm, Figure 5.4a) are more than one, which implies these spheres are more close to ellipse. With the increasing of falling distance, the aspect ratios increase slightly. With the same falling distance (over 8 cm), spheres extruded from 0.4 mm needle have smaller aspect ratios than those of spheres extruded from 1.2 mm needle.

The deformation of polymer spheres derived from the impact of droplets with coagulant surface.

When polymer droplets started to fall from the tip of the needle, their initial velocity was close to 0 m/s. During the falling, the principle aerodynamic force of air to droplets is Strokes drag [65], which is proportional to the first power of the velocity of droplets. According to the force analysis of droplets, only when the velocity of droplets were accelerated to specific values did the influencing of aerodynamic drag become obvious. Due to the large mass of millimeter-sized droplets (i.e. large inertia and gravity), the actual decelerating effect of aerodynamic drag was finite. With the increasing of falling distance, the deformation of droplets upon impact with liquid surface increases. In conclusion, the smaller the mass of droplets are, the more obvious is the decelerating effect of aerodynamic drag.

The aspect ratio of two kinds of dry spheres is shown in Figure 5.4b, which is still over one. With the increasing of falling distance, the deformation of dry spheres extruded from 1.2 mm needle increases while that of dry spheres extruded from 0.4 mm needle does not change much.

The effect of falling distance on the circularity of polymer spheres is indicated in Figure 5.5.

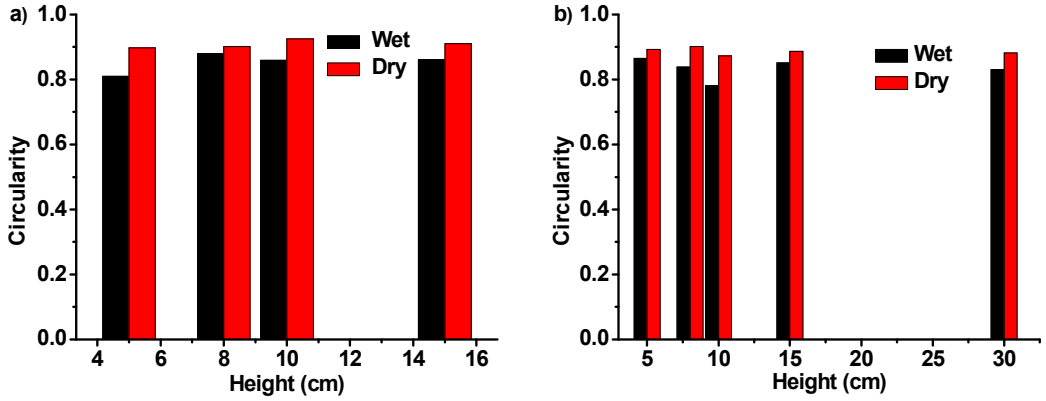

Figure 5.5 Effect of falling distance on the circularity of polymer spheres. 8% PAN 200 solution; water as coagulant at 20°C; a) 0.4 mm needle; b) 1.2 mm needle.

Circularity can be used to describe any shapes, especially for complex ones which can not be described simply by aspect ratio. For a perfect circle, its aspect ratio is also one. Since the calculation of circularity refers to areas and perimeters of a shape, the relation between deformation of droplets and circularity is less intuitive. The circularity of wet and dry spheres extruded from 0.4 mm needle (Figure 5.5a) and 1.2 mm needle (Figure 5.5b) is less than one. The circularity of dry spheres is larger compared with that of wet spheres.

The surface tension coefficient of PAN 200 solutions is shown in Figure 5.6. Surface tension coefficient calculated by using PTFE (Figure 5.6a) is the most close to the measured surface tension coefficient as shown in Figure 5.6b. Although the concentration of PAN 200 solution increases, the surface tension coefficient of corresponding solution almost keeps the same within the range of concentration presented. In addition, it can be estimated that the surface tension coefficient of DMF/water mixture (volume fractions of DMF: 0-75%) is between 35 mJ/m^2 (for DMF) and 73 mJ/m^2 (for water).

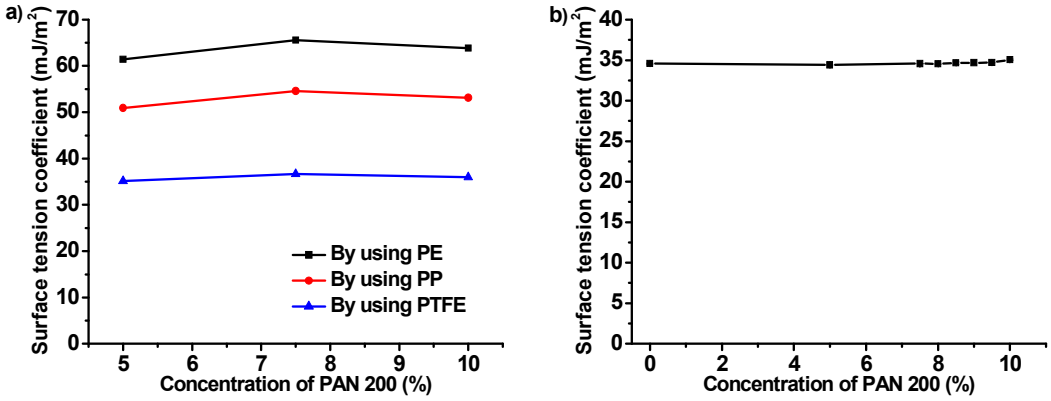

Figure 5.6 Surface tension coefficients of PAN 200 solutions. a) by calculation of using three kinds of polymer: PE, PP, and PTFE; b) by measurement; temperature: 22°C.

The effect of surface tension on the deformation of polymer droplets happens mainly during the stage of droplets' gelation. Since the solvent (i.e. DMF) of PAN 200 solution is miscible with water or water/DMF mixture, Formula 2.1 can not be used to calculate the interfacial tension between polymer droplets and coagulant. Therefore, the spreading of PAN 200 droplets on the surface of water/DMF mixture can not be analyzed according to Formula 2.2. With the accomplishment of gelation at PAN 200 droplets' surface, polymer curst on the surface suppresses the further deformation of PAN 200 droplets. This process of surface gelation is rather fast; in this case, it is pointless to take the surface tension into account.
Whether calculation or measurement, what can be acquired is the surface tension coefficient of polymer solutions. From surface tension coefficient to surface tension or interfacial tension, the areas of droplets should be known. These areas are hard to be known obviously.

5.1.3 Inner structure of large polymer spheres

The effect of gelation rate on the inner structure of large PAN 200 spheres is shown in Figure 5.7. Polymer spheres in Figure 5.7a-c show large numbers of finger-like pores, which results from instantaneous demixing. With the increasing of volume fractions of DMF in coagulant, the gelation rate of polymer droplets decreases. In this case, the phase separation of droplets tends to show more characters of delayed demixing. The inner pores evolve from large and finger-like pores to small and sponge-like pores as shown in Figure 5.7a and 5.7d, respectively. The mean diameter of inner pores decreases while the number of inner pores increases especially in the central part of polymer spheres.

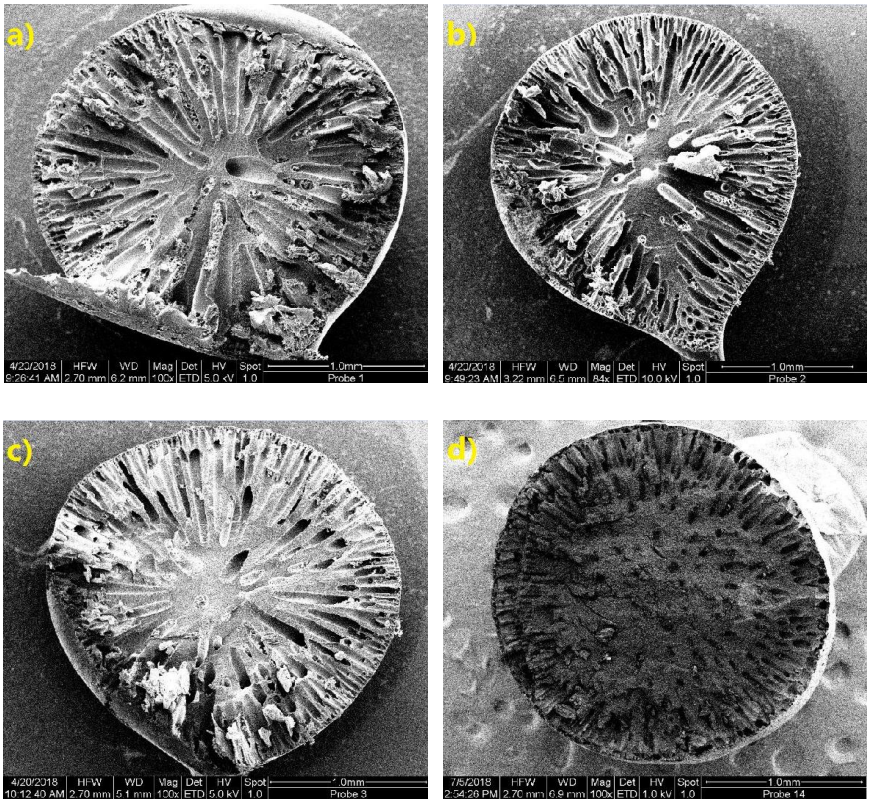

Figure 5.7 Cross sections of large polymer spheres. 8% PAN 200 solution; gelation temperature: 20°C; falling distance: 5 cm; polymer spheres gelled in DMF/water mixture with volume fractions of DMF: a) 0%, b) 25%, c) 50%, and d) 65%.

The specific surface areas and specific pore volumes of PAN 200 spheres can also prove this trend, which are shown in Figure 5.8.

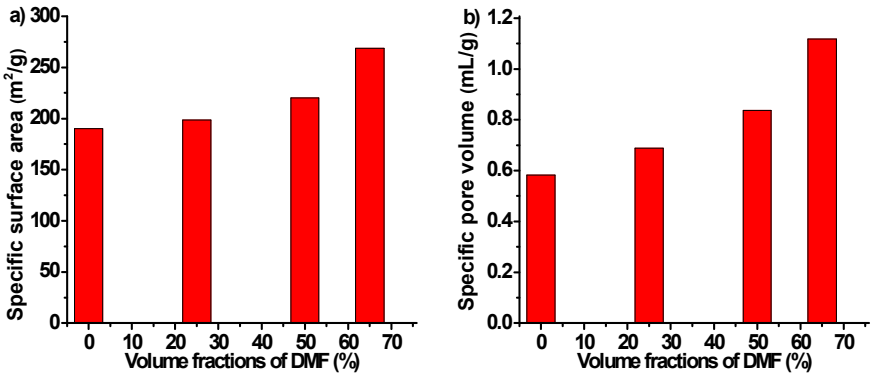

Figure 5.8 Pore characterizations of large polymer spheres. 8% PAN 200 solution; gelation temperature: 20°C; a) specific surface area; b) specific pore volume.

As the volume fractions of DMF in coagulant increases, both specific surface areas and specific pore volumes increase. In conclusion, the inner porous structure of PAN 200 spheres becomes denser and denser with the increasing volume fractions of DMF.

The porosity of polymer spheres is shown in Figure 5.9. With the increasing of volume

fractions of DMF, the porosity of polymer spheres almost keeps the same. In conclusion, there is no effect of volume fractions of DMF on the porosity of PAN 200 spheres.

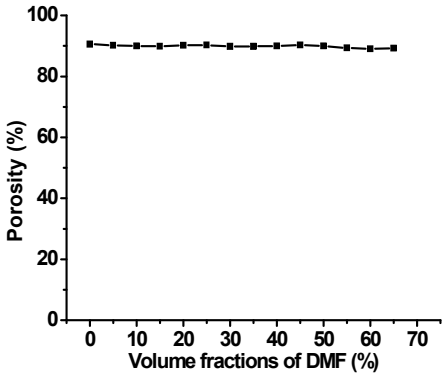

Figure 5.9 Porosity of large polymer spheres. 8% PAN 200 solution; gelation and measurement temperature: 20°C; density of water: 0.99777 g/cm^3; density of polyacrylonitrile: 1.013 g/cm^3.

The effect of gelation rate on skin-layer structure of PAN 200 spheres is shown in Figure 5.10. The formation of dense skin layers in Figure 5.10a-d was due to delayed demixing. Below the skin layer, the inner structure featured by finger-like pores can be observed.

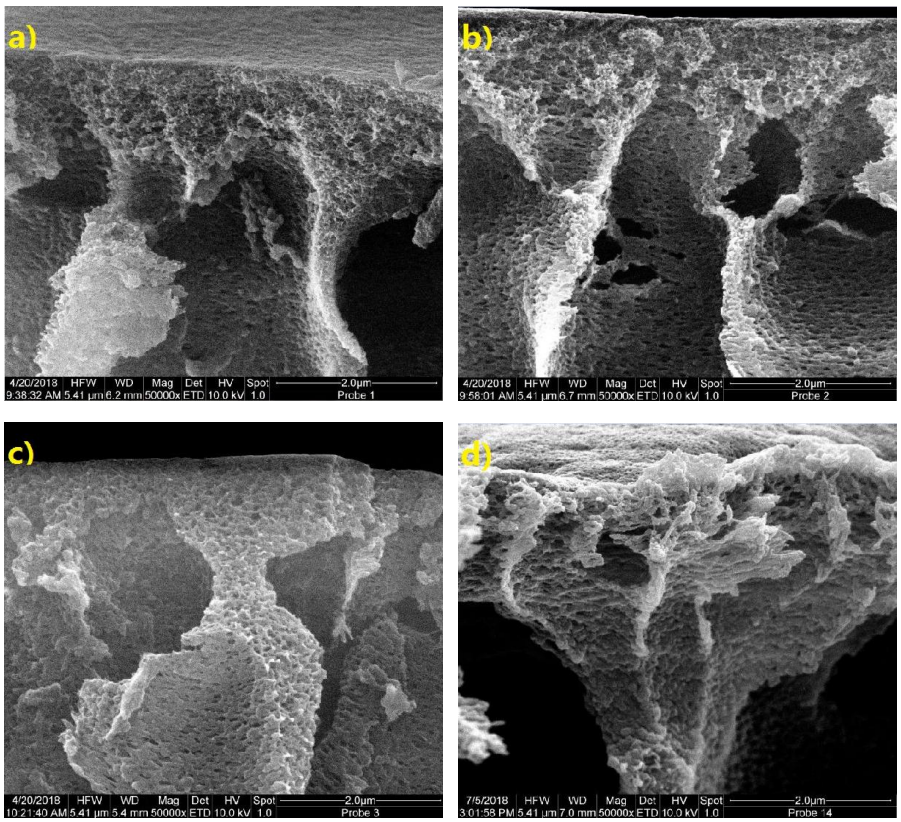

Figure 5.10 Skin layers of large polymer spheres. 8% PAN 200 solution; gelation temperature: 20°C; falling distance: 5 cm; polymer spheres gelled in DMF/water mixture with volume fractions of DMF: a) 0%, b) 25%, c) 50%, and d) 65%.

The effect of gelation rate on the surface morphology of PAN 200 spheres is shown in Figure 5.11.

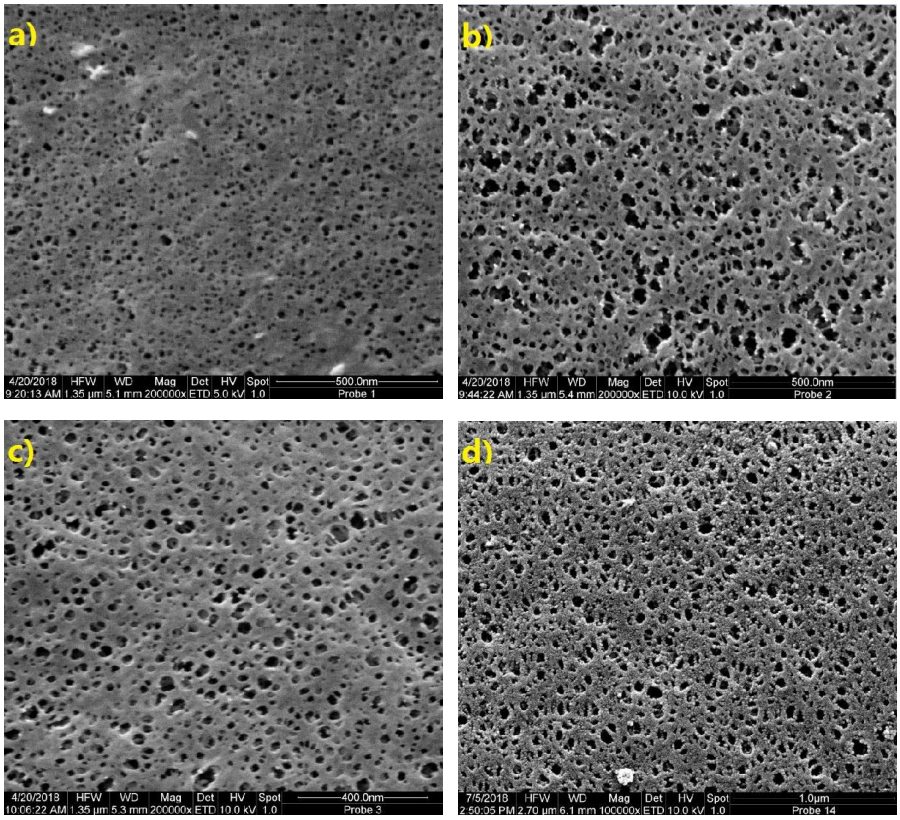

Figure 5.11 Surface morphologies of large polymer spheres. 8% PAN 200 solution; gelation temperature: 20°C; falling distance: 5 cm; polymer spheres gelled in DMF/water mixture with volume fractions of DMF: a) 0%, b) 25%, c) 50%, and d) 65%.

The surface of all polymer spheres is porous. With the increasing of volume fractions of DMF, many small and independent surface pores integrate into one or several larger pores.
The effect of polymer concentration (A) and gelation temperature (B) on the porous structure of PAN 200 spheres is discussed here. Moreover, the factor of gelation rate (C, i.e. volume fractions of DMF) is also added in the discussion. The indexes weighing the porous structure of PAN 200 spheres are specific surface areas, specific pore volumes, and porosity. The results of orthogonal tests were analyzed by intuitive analysis [59]. The range values of intuitive analysis for specific surface areas of PAN 200 spheres are shown in Table 5.1. The process of intuitive analysis for specific surface areas is shown in appendix 8.5.

Table 5.1 Range values of intuitive analysis for specific surface areas. A: concentration of PAN 200 solution; B: gelation temperature; C: gelation rate.

Factors	A	B	A*B	C	A*C	B*C	Blank
Range (m^2/g)	20.82	51.45	4.09	23.86	3.19	2.58	2.73

When the levels of a factor change, the range value of this factor indicates how the index is affected by this factor. Higher range value of a factor means larger influencing of this factor

on the index.

As shown in Table 5.1, the range values of A*B, A*C, and B*C are close to that of blank column. The range values of A, B, and C are far higher than that of blank column. This implies that compared with factors A, B, and C, there is no interaction between any two factors and the effect of interactions on specific surface areas is not significant. This point can also be demonstrated by Figure 5.12, which shows the combinations of two factors with corresponding two levels. In each of the figures, the two segments are approximately parallel, which indicates there is no interaction between these two factors within the scope of variable.

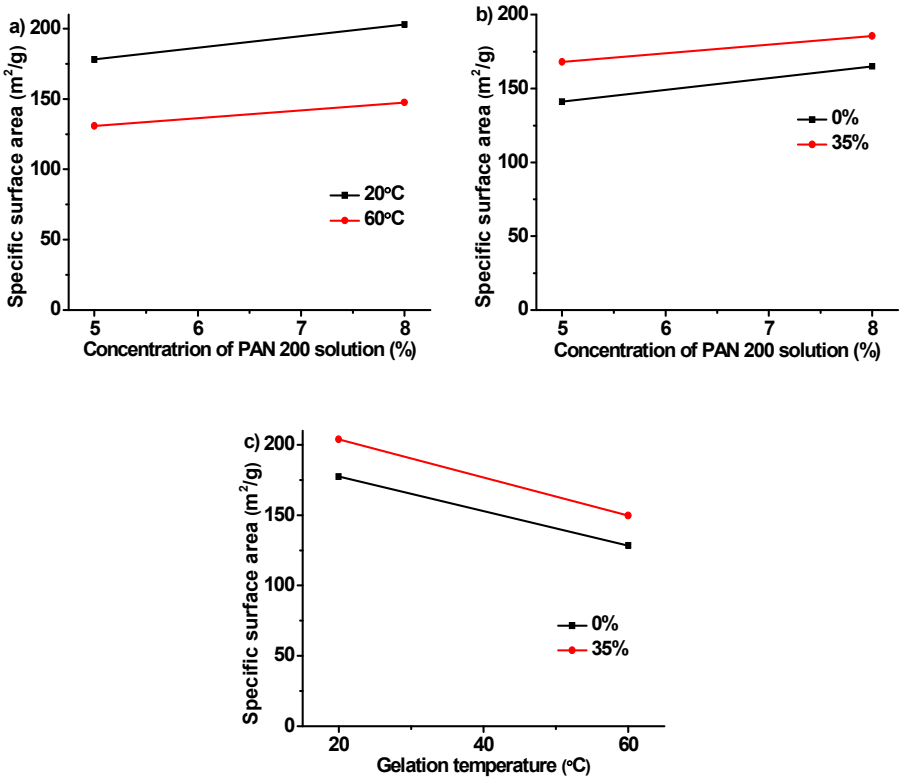

Figure 5.12 Specific surface areas of PAN 200 spheres. a) polymer concentration and gelation temperature; b) polymer concentration and gelation rate; c) gelation temperature and rate.

With the increasing of concentration, the specific surface areas of PAN 200 spheres also increase as shown in Figure 5.12a. For PAN 200 droplets with the same volume, droplets from solution with higher concentration can provide more porous frameworks in the final dry spheres. More porous frameworks can offer more surface areas to dry spheres.

Also in Figure 5.12a and 5.12c, as the gelation temperature increases, the specific surface areas of PAN 200 spheres decrease. Higher gelation temperature means higher gelation rate of the PAN 200 droplets, which render the final PAN 200 spheres more characters of instantaneous demixing. Compared with spheres from delayed demixing process, spheres from instantaneous demixing process have less but larger pores.

The range values of intuitive analysis for specific pore volumes of PAN 200 spheres are shown in Table 5.2. The process of intuitive analysis for specific pore volumes is shown in appendix 8.5.

Table 5.2 Range values of intuitive analysis for specific pore volumes. A: concentration of PAN 200 solution; B: gelation temperature; C: gelation rate.

Factors	A	B	A*B	C	A*C	B*C	Blank
Range (mL/g)	0.110	0.127	0.012	0.149	0.012	0.037	0.005

As shown in Table 5.2, the range values of A*B, A*C, and B*C are close to that of blank column. The range values of A, B, and C are far higher than that of blank column. This implies that compared with factors A, B, and C, there is no interaction between any two factors and the effect of interactions on specific pore volumes is not significant. This point can also be demonstrated by Figure 5.13, which shows the combinations of two factors with corresponding two levels. In each of the figures, the two segments are approximately parallel, which indicates there is no interaction between these two factors within the scope of variable.

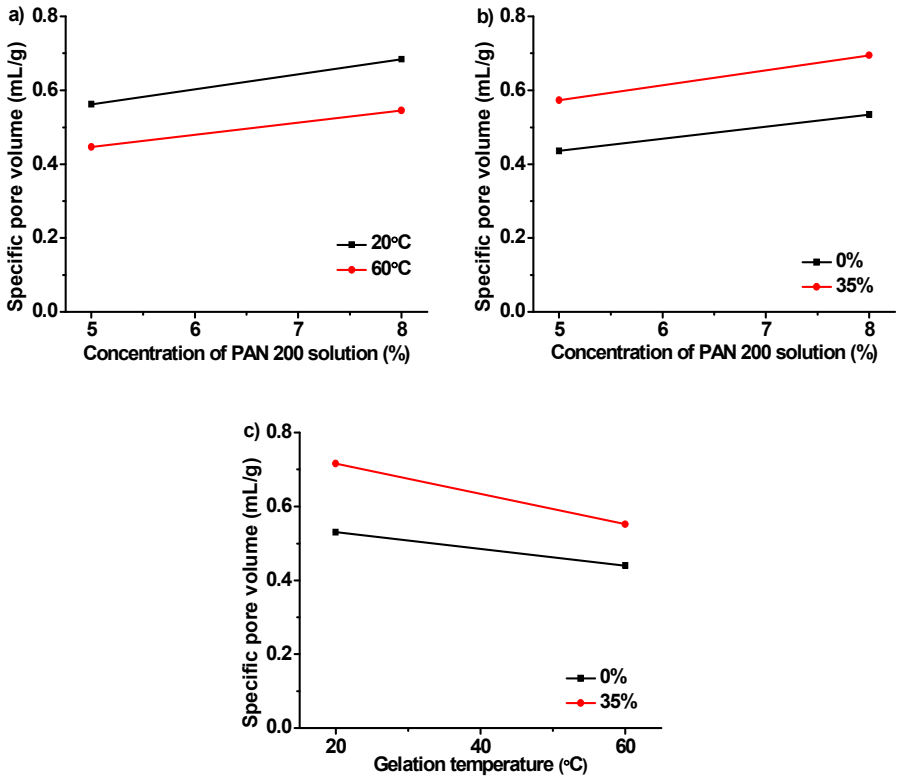

Figure 5.13 Specific pore volumes of PAN 200 spheres. a) polymer concentration and gelation temperature; b) polymer concentration and gelation rate; c) gelation temperature and rate.

With the increasing of concentration, the specific pore volumes of PAN 200 spheres also increase as shown in Figure 5.13a. For PAN 200 droplets with the same volume, droplets from solution with higher concentration can provide more porous frameworks in the final dry spheres. More porous frameworks can offer more pore volumes to dry spheres.

Also in Figure 5.13a and 5.13c, as the gelation temperature increases, the specific pore volumes of PAN 200 spheres decrease. Higher gelation temperature means higher gelation rate of the PAN 200 droplets, which render the final PAN 200 spheres more characters of

instantaneous demixing. Compared with spheres from delayed demixing process, spheres from instantaneous demixing process have less but larger pores.
The range values of intuitive analysis for porosity of PAN 200 spheres are shown in Table 5.3. The process of intuitive analysis for porosity is shown in appendix 8.5.

Table 5.3 Range values of intuitive analysis for porosity. A: concentration of PAN 200 solution; B: gelation temperature; C: gelation rate.

Factors	A	B	A*B	C	A*C	B*C	Blank
Range	0.043	0.005	0.004	0.007	0.001	0.001	0.001

As shown in Table 5.3, only the range value of factor A is far higher than that of blank column. The range values of other factors and interactions are close to that of blank column. This implies that compared with factor A, there is no interaction between any two factors and the effect of interactions on porosity is not significant. This point can also be demonstrated by Figure 5.14, which shows the combinations of two factors with corresponding two levels. In each of the figures, the two segments are approximately parallel, which indicates there is no interaction between these two factors within the scope of variable.

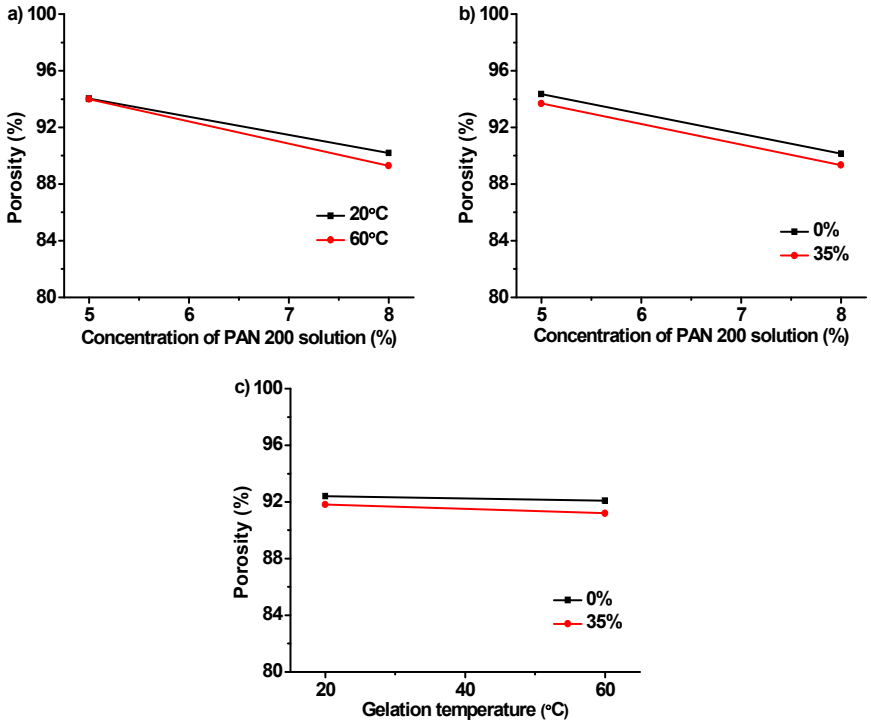

Figure 5.14 Porosity of PAN 200 spheres. a) polymer concentration and gelation temperature; b) polymer concentration and gelation rate; c) gelation temperature and rate.

With the increasing of concentration, the porosity of polymer spheres decreases as shown in Figure 5.14a. For PAN 200 droplets with the same volume, droplets from solution with higher concentration were occupied by more polymers. As a result, dry spheres derived from droplets with higher concentration had lower porosity.
Also in Figure 5.14a and 5.14c, as the gelation temperature increases, the porosity almost

keeps the same. With the increasing of volume fractions of DMF, the porosity of PAN 200 spheres almost keeps the same as shown Figure 5.14b and 5.14c. The conclusion reflected by Figure 5.9 repeats itself here.

5.2 Hydrogel microspheres shaped by DOD ink-jetting

5.2.1 Rheological characterization of SA solutions

The rheological characterization of SA solutions is shown in Figure 5.15.

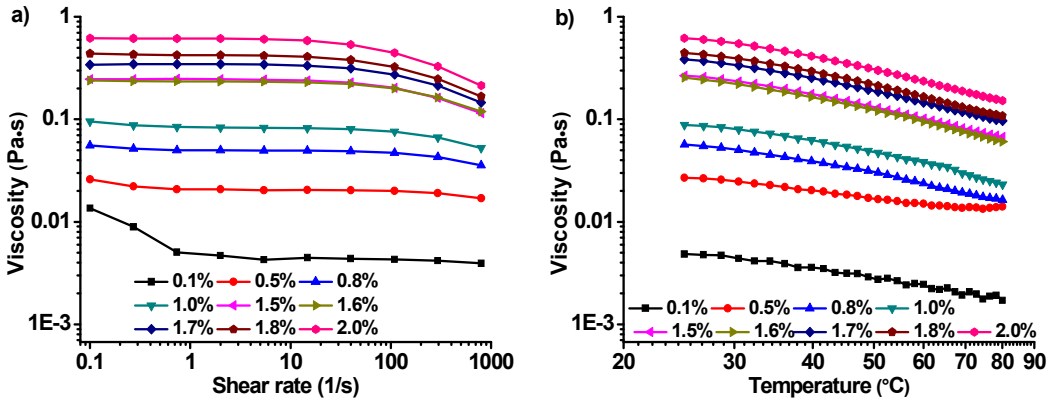

Figure 5.15 Rheological characterizations of SA solutions. a) viscosity curves of SA solutions; temperature: 25°C; b) temperature-dependent flow behaviors of SA solutions; shear rate: 5 s^{-1}.

With the increasing of shear rate, the apparent viscosity of SA solutions in Figure 5.15a decreases, which indicates a character of shear thinning. With the existence of shear force, the orientation and disentanglement of polymer chains result in the behavior of shear thinning [63]. At a specific shear rate, the viscosity of SA solutions increases as the concentration of SA solutions increases. Higher concentration of solution leads to higher degree of entanglement of polymer chains, which results in higher viscosity of the solution.

With the increasing of temperature, the movement of polymer segments and solvent molecules increase and the entanglement between polymer chains decreases. The viscosity of SA solutions decreases as shown in Figure 5.15b. At a selected temperature, the viscosity of SA solutions increases as the concentration of SA solutions increases. In conclusion, both increasing shear rate and increasing temperature can improve the mobility of SA solutions.

5.2.2 Screening suitable conditions to shape SA microdroplets

For a specific SA solution, SA microdroplets can be shaped from the shaping head if specific shaping conditions were met at room temperature, such as driving voltage, pulse width, and shaping frequency. The jetting moment of microdroplets from 0.5% SA solution was captured in Figure 5.16.

Figure 5.16 A photograph capturing the formation of a microdroplet. 0.5% SA solution; shaping conditions: 105 V, 25 µs, and 400 Hz; temperature of shaping head: 25°C.

Although SA solution is essentially a kind of non-Newtonian fluid, the jetting behavior of dilute SA solution approximated that of a Newtonian fluid. No filament of SA solution followed primary droplet, which indicates that the viscoelasticity of dilute SA solution is not obvious. Moreover, the stability of droplet ejection was also improved due to addition of SA [66], compared with the stability of droplet ejection from Newtonian fluid such as water.
When taking 0.5% SA solution for example, the combined conditions of voltage and pulse width to shape SA microdroplets are shown in Figure 5.17 [67], which meets the requirements of monodispersity, stability, and reproducibility for microdroplets as mentioned in section 4.2.3.

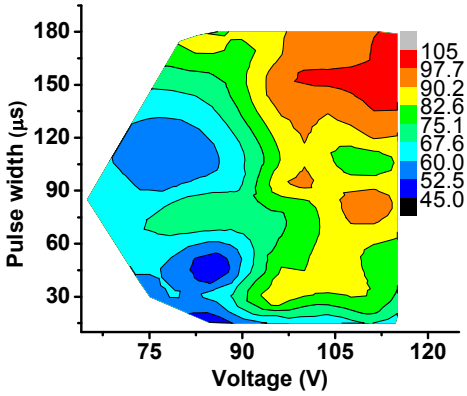

Figure 5.17 Combined shaping conditions of 0.5% SA solution. meeting the requirements of monodispersity, stability, and reproducibility; temperature and shaping frequency of the shaping head: 25°C and 10 Hz; unit of droplet size: µm.

The limitations of this contour should be claimed here. This contour was based on water-SA solution system and the shaping conditions can not be simply transferred to other polymer solution system. These combined shaping conditions were acquired by trial and error. In addition, these conditions are not totally complete and some other combinations which are not in the contour can also meet three requirements too. Moreover, it is highly possible to acquire microdroplets by using the conditions in the contour, which meet the three requirements; nevertheless, it is not guaranteed that satisfied microdroplets can be acquired in every practice. In conclusion, this contour can only be understood and applied statistically.

The combined shaping conditions for other concentrations of SA solutions are shown in appendix 8.6. The dismantled shaping conditions of 0.5% SA solution are shown in Figure 5.18.

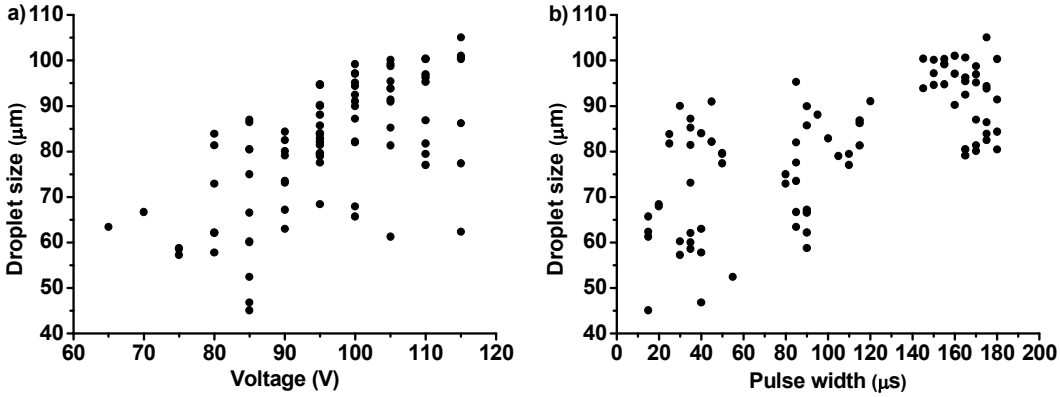

Figure 5.18 Dismantled shaping conditions of shaping 0.5% SA solution. temperature and shaping frequency of shaping head: 25°C and 10 Hz; a) voltage and droplet size; b) pulse width and droplet size.

With the increasing the driving voltage, the mean size of the maximum droplet also increases as shown in Figure 5.18a. The higher the driving voltage is, the larger is the volume change of capillary tube. Larger volume change of capillary tube can extrude larger microdroplets. This phenomenon has been reported by many research results [67, 68]. The various sizes of microdroplets at a selected voltage were due to various pulse widths. In Figure 5.17, with the pulse width constant, the mean size of microdroplets increases when the voltage increases; though this increasing is not monotonous within the range of voltage presented.

In the actual shaping of SA microdroplets, they always came out of the orifice if the driving voltage was larger than a specific value. It can be inferred that for each specific polymer solution, a threshold value of voltage exists to form microdroplets.

The relation between pulse width and mean droplet size is more complex as shown in Figure 5.18b. With the increasing the pulse width, the mean size of the maximum droplet also increases though this relation is more discrete than that between voltage and droplet size. The wider the pulse width is, the larger is the volume change of capillary tube. Larger volume change of capillary tube can extrude larger microdroplets. This phenomenon can also be found in other researchers' work [67, 68]. The various sizes of microdroplets at a selected pulse width were due to various driving voltages. In Figure 5.17, with the driving voltage constant, the mean size of microdroplets increases when the pulse width increases; though this increasing is not monotonous within the range of pulse width presented.

Three different regions of pulse width exist in Figure 5.18b, which are 10-60 μs, 80-130 μs, and 150-180 μs. Preliminary durability tests indicated that the durability of shaping was short when the numerical value of pulse width was larger than that of driving voltage. Shaping conditions with close numerical values of voltage and pulse width also had this problem. Narrow pulse width range (e.g. 20-50 μs) was the best for high-frequency and long time shaping without blocking. Therefore, a narrow pulse width of 25 μs was chosen for the next durability tests.

5.2.3 Preparation of SA hydrogel microspheres

The shaping durability of DOD system was investigated by preparing large numbers of microdroplets continuously. The method used was qualitative observation. Since the areas of shaping orifice is small (diameter of 100 μm), the solvent of SA solution evaporated easily and the concentration of SA solution at the orifice was not constant. With the ongoing of shaping process, the concentration of SA solution at the orifice tended to increase. The higher the concentration of SA solution was (i.e. higher viscosity), the higher was the evaporation rate of solvent. With the ongoing of shaping process, the rate of concentration increasing was higher for SA solution with higher concentration. When the concentration of SA solution reached at a specific value, the orifice of shaping head was blocked. With the shaping head blocked, cleaning of the shaping orifice is needed. For a fixed period of shaping, the higher the frequency of cleaning was, the shorter was the time of continuous shaping. In conclusion, higher concentration of polymer solution leads to shorter shaping durability [69].

The photographs of microdroplets and hydrogel microspheres from 1% SA solution are shown in Figure 5.19.

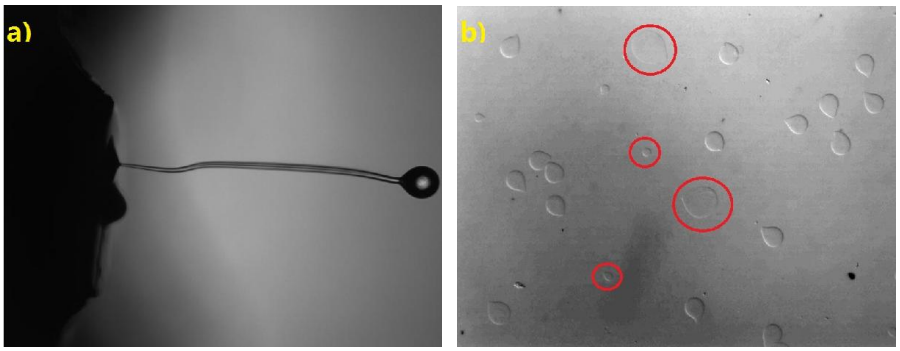

Figure 5.19 Photographs of a microdroplet and hydrogel microspheres. 1% SA solution; shaping conditions: 140 V, 25 μs, 400 Hz; temperature of shaping head: 25°C; a) the formation of a microdroplet captured by a CCD camera; b) the states (top view) of hydrogel microspheres on a glass slide by optical microscope; falling distance: 5 cm; gelation conditions: 0.5 M $CaCl_2$ solution at 20°C.

When the concentration of SA solution increased from 0.5% to 1%, a filament follows the primary droplet as shown in Figure 5.19a. With moderate concentration of polymer solution or molecular weight of polymer used, this liquid filament will merge with the primary droplet. Nonetheless, if the molecular weight of polymer or the concentration of polymer solution is too high, the filament will not break up or even draws the main drop back to the nozzle [70-72].

If the time of forming a microdroplet is larger than 1,000 μs, the formation process of this microdroplet can not be fully documented by this CCD camera. This is a disadvantage for the analysis of droplet size.

The photograph of hydrogel microspheres is shown in Figure 5.19b. This photograph captured the top view of these hydrogel microspheres. Except for some oversize (in red circles) and super small microspheres (in red circles), the rest hydrogel microspheres are almost “tear-like”. It is possible that oversize hydrogel microspheres were derived from oversize microdroplets. Nevertheless, this inference is less convictive. The shape of oversize

hydrogel microspheres is like a “disk”, which is due to the breakup of microdroplets when hitting the surface of coagulant. The formation of super small hydrogel microspheres was due to super small microdroplets.
The states of “tear-like” hydrogel microspheres in coagulation bath are simulated in Scheme 5.1.

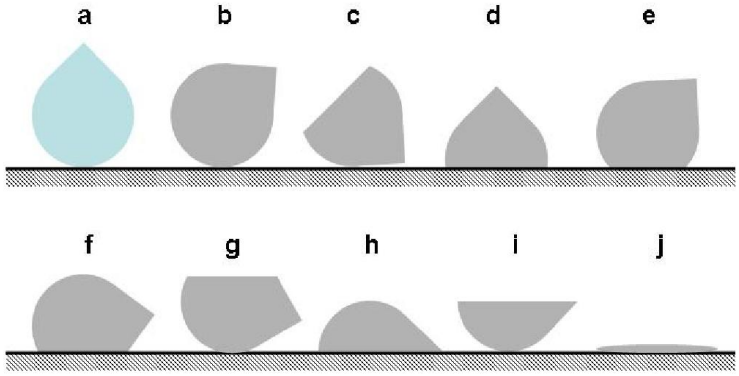

Scheme 5.1 Schematic states of “tear-like” SA microdroplets and hydrogel microspheres from front view. a) a “tear-like” microdroplet; b) the state of a “tear-like” hydrogel microsphere; c-d): states of deformed hydrogel microspheres with flattening tops due to impact; e-g): states of hydrogel microspheres with partial body deformation due to impact; h-i): states of hydrogel microspheres with large body deformation due to impact; j) the state of a broken hydrogel microsphere.

The shape of undeformed “tear-like” hydrogel microsphere is shown in Scheme 5.1b, which is a copy of a “tear-like” microdroplet “a”. During the shaping process, the axis of shaping head was perpendicular to the surface of coagulant. In this case, the direction of microdroplets’ initial velocity was also perpendicular to the surface of coagulant.
In the cases of “c” and “d”, the direction of microdroplets’ terminal velocity is hypothesized to be vertical to the coagulant surface. The higher driving voltage and shaping frequency the microdroplets were shaped by, the higher initial velocity did the microdroplets have. With the combined shaping conditions of low falling distance (5 cm), driving voltage (140 V), and shaping frequency (400 Hz), the tip of microdroplets from 1% SA solution may be flat due to impact as shown in Scheme 5.1c and 5.1d. Nonetheless, hydrogel microspheres with flat top were not found in all the photographs with the same shaping conditions. This implies that the rigidity of 1% SA solution is high enough to resist deformation due to impact and the schematic states of “c” and “d” are not reasonable.
In the cases of “e-i”, the direction of microdroplets’ terminal velocity is hypothesized to be not perpendicular to the coagulant surface. The top views of these five hydrogel microspheres are all “tear-like”. Theoretically, the formation probability of cases “e-i” is lower than that of cases “c” and “d”. For the cases of “e”, “f”, and “h”, the deformation of hydrogel microspheres aggravates. With the deformation further aggravating, oversize hydrogel microspheres were got. Since hydrogel microspheres with the shapes of “c” and “d” were not found, almost all hydrogel microspheres with “tear-like” shape from top view were in the shape of “b” rather than “e-i” from front view. In the case of “j”, the hydrogel microsphere is broken, which looks like a disk. The existence of tail was due to the low falling distance

which can not offer enough time to transform the shape of microdroplets from “tear-like” to spherical.
In order to exclude the possible influencing of cover glass on the shape of hydrogel microspheres, two more photographs are presented as shown in Figure 5.20.

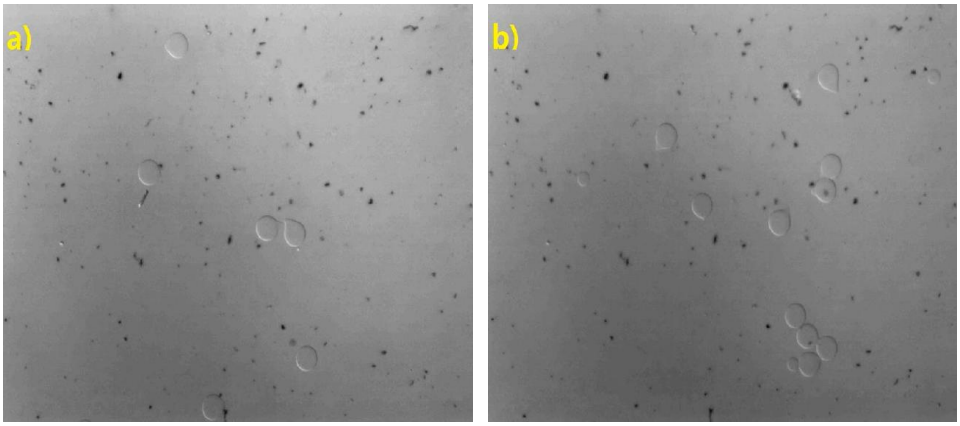

Figure 5.20 Photographs of hydrogel microspheres from 1% SA solution. shaping conditions: 160 V, 25 μs, 400 Hz; temperature of shaping head: 25°C; falling distance: 5 cm; gelation conditions: 0.5 M $CaCl_2$ solution at 20°C; a) states (top view) of hydrogel microspheres on a glass slide with a cover glass; b) states (top view) of hydrogel microspheres on a glass slide without a cover glass.

The shape of hydrogel microspheres with a cover glass (a) is the same as that of hydrogel microsphere without a cover glass (b). Both spherical and “tear-like” hydrogel microspheres can be seen in these two photographs.
The analysis of spherical hydrogel microspheres is shown in Scheme 5.2. The shape of spherical hydrogel microspheres is shown in Scheme 5.2b, which is a copy of a spherical microdroplet “a”. The top views of hydrogel microspheres “b-g” except for “d” are all round and the only difference between them is the areas of the circle. The shape of “tear-like” hydrogel microspheres has been analyzed. The oversize top-view areas of “tear-like” hydrogel microspheres indicate that deformation or breakup of hydrogel microspheres happened. Similarly, oversize top-view areas of spherical hydrogel microspheres also mean that deformation or breakup of hydrogel microspheres happened, such as the cases of “e”, “f”, and “g”. In Figure 5.20, the top-view areas of hydrogel microspheres whose top views are round are close to those of “tear-like” hydrogel microspheres. Therefore, these “spherical” hydrogel microspheres are not in the cases of “e”, “f”, and “g”. The states of hydrogel microspheres whose top views are round are in the cases of “b” or “c”. Since case “d” was not found in the photograph, hydrogel microspheres whose top views are round are more likely in the state of “b”, i.e. spherical hydrogel microspheres.

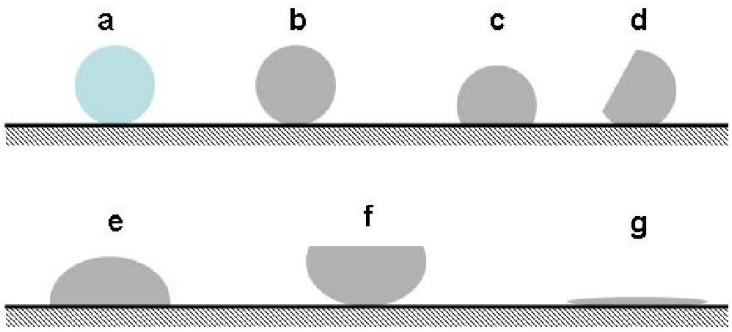

Scheme 5.2 Schematic states of spherical SA microdroplets and hydrogel microspheres from front view. a) a spherical microdroplet; b) the state of a spherical hydrogel microsphere; c-d): states of hydrogel microspheres with small deformation due to impact; e-f): states of hydrogel microspheres with large deformation due to impact; g) the state of a "disk-like" and broken hydrogel microsphere.

The surface tension coefficient of SA solutions is shown in Figure 5.21.

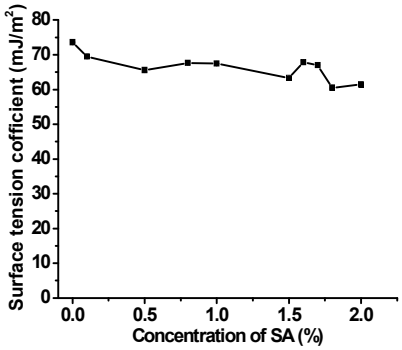

Figure 5.21 Surface tension coefficients of SA solutions. Temperature: 20°C.

As the concentration of SA solution increases, the surface tension coefficient of corresponding solution slightly decreases. By contrast, the surface tension coefficient of $CaCl_2$ solution is larger than that of pure water at same temperature [26].
The effect of surface tension on the deformation of SA microdroplets happens mainly during the stage of droplets' gelation. Since the solvent of SA solution, i.e. water, is miscible with $CaCl_2$ solution, Formula 2.1 can not be used to calculate the interfacial tension between SA microdroplets and $CaCl_2$ solution. Therefore, the spreading of SA microdroplets on the surface of $CaCl_2$ solution can not be analyzed according to Formula 2.2. With the accomplishment of gelation at SA microdroplets' surface, SA curst on the surface of SA microdroplets suppresses the further deformation of SA microdroplets. This process of surface gelation is rather fast; in this case, it is pointless to take the surface tension into account.
From surface tension coefficient to surface tension or interfacial tension, the areas of droplets should be known. These areas are hard to be known obviously.
The mean size of SA microdroplets and hydrogel microspheres, which meet the requirement

of long durability of shaping, is shown in Figure 5.22.

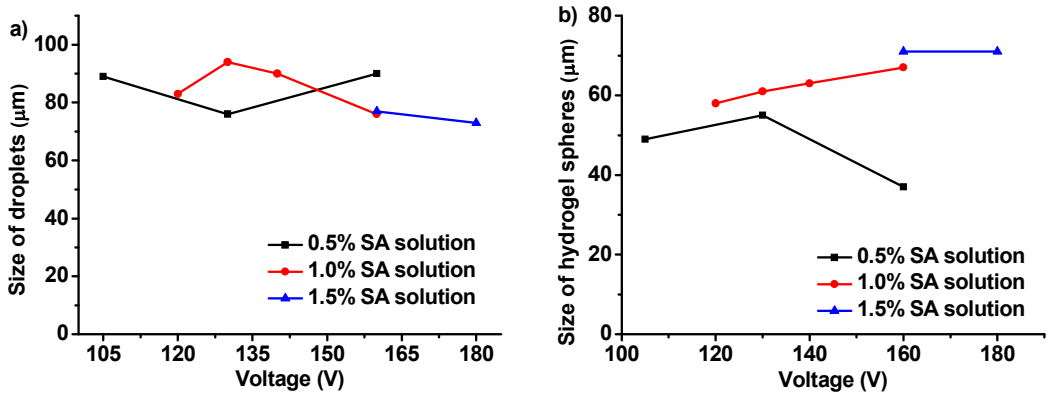

Figure 5.22 Mean sizes of SA microdroplets and hydrogel microspheres. shaping conditions: 25 μs, 400 Hz; temperature of shaping head: 25°C; falling distance: 5 cm; gelation conditions: 0.5 M $CaCl_2$ solution at 20°C; a) mean size of SA microdroplets; b) mean size of SA hydrogel microspheres.

First of all, the mean size of microdroplet is larger than that of corresponding hydrogel microspheres from the same solution. This indicates that SA microdroplets contracted after gelation. In Figure 5.22a, with the increasing of voltage, the mean size of microdroplets from 0.5% solution firstly decreases and then increases. The reason of size decreasing is that the photograph of microdroplets captured by CCD camera was not the final shape of microdroplets, which had a long tail when captured. If the volume of the tail had been added into the primary droplet, the mean size of final microdroplet would have been larger. With the driving voltage increasing from 120 to 130 V, the mean size of microdroplets from 1% solution increases. The mean size of 1% SA microdroplet decreases when the voltage increases further from 130 to 160 V. The reason for this size decreasing is also the incomplete photographing. The microdroplets (i.e. two blue triangles) in Figure 5.22a from 1.5% solution have the same problem.

With the increasing of concentration of SA solutions, the initial shaping voltage also increases from 105 V (0.5% SA solution), then 120 V (1% SA solution), to 160 V (1.5% SA solution). This indicates that with the increasing of concentration of polymer solution, the shaping capacity of solution decreases [70-72].

The relation between mean size of hydrogel microspheres and voltage is shown in Figure 5.22b. With the increasing of driving voltage, the mean size of hydrogel microspheres from the same SA solution also increases or at least keeps the same. There is one exception for hydrogel microspheres from 0.5% solution. As the driving voltage increases from 130 to 160 V, the mean size of hydrogel microspheres decreases from 55 to 38 μm. This is because the microdroplet split into two sub-microdroplets before entering the coagulant as shown in Figure 5.23. With the same shaping conditions, the mean size of hydrogel microspheres increases as the concentration of solution increases, such as at 130 V (0.5% to 1%) and 160 V (1% to 1.5%).

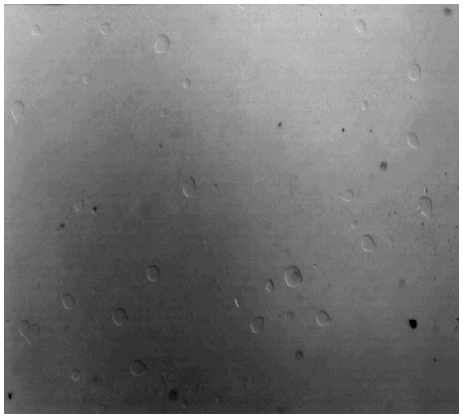

Figure 5.23 A photograph of hydrogel microspheres from 0.5% SA solution. shaping conditions: 160 V, 25 μs, 400 Hz; temperature of shaping head: 25°C; falling distance: 5 cm; gelation conditions: 0.5 M $CaCl_2$ solution at 20°C.

The linear regression of mean size of hydrogel microspheres from 1% solution is shown in Figure 5.24. The determination coefficient (i.e. R^2) between driving voltage and mean size of hydrogel microspheres is close to 0.99, which indicates a strong dependence of the mean size of hydrogel microspheres on driving voltage.

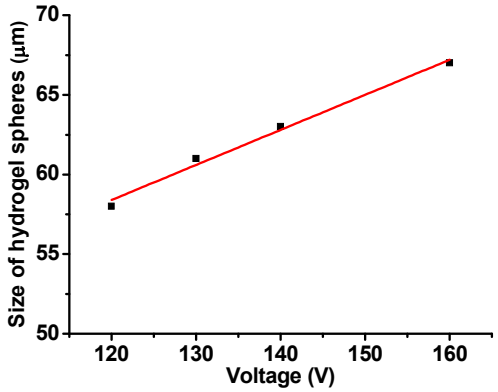

Figure 5.24 Linear regression of the mean size of SA hydrogel microspheres. 1% solution; shaping conditions: 25 μs, 400 Hz; temperature of shaping head: 25°C; falling distance: 5 cm; gelation conditions: 0.5 M $CaCl_2$ solution at 20°C.

5.3 Polymer microspheres shaped by DOD ink-jetting

5.3.1 Rheological characterization of PAN solutions

Before introducing the results of shaping PAN microspheres, the rheological study of PAN solutions is firstly discussed. The viscosity curves of X-PAN, L-PAN, PAN 150, and PAN 200 solutions are shown in Figure 5.25.

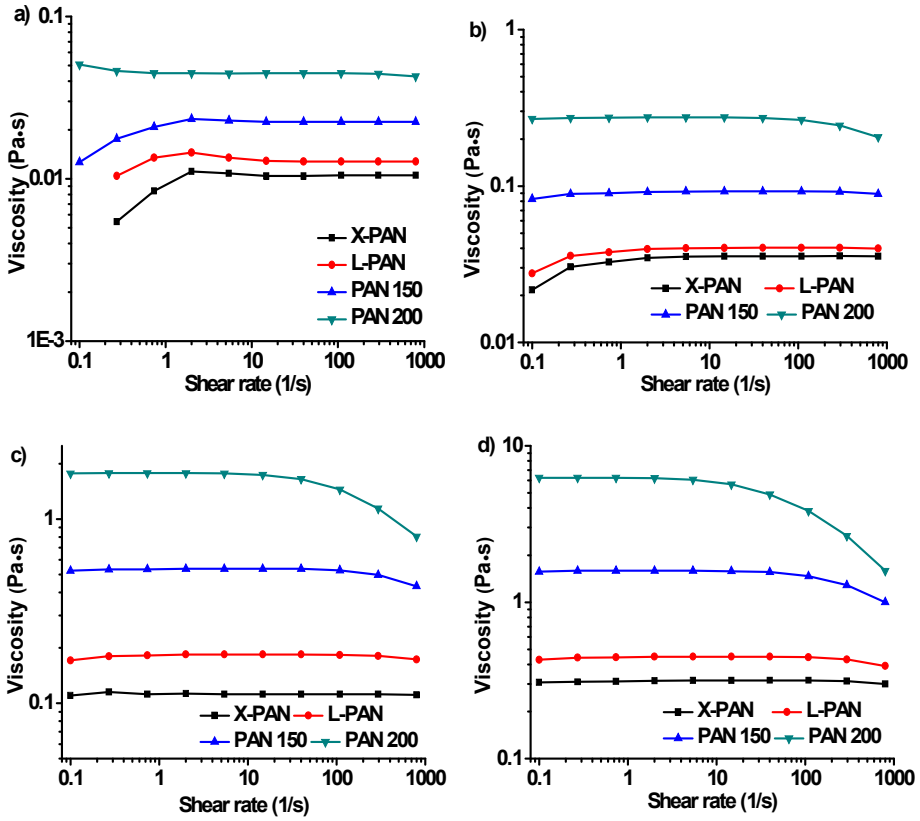

Figure 5.25 Viscosity curves of various PAN solutions. temperature: 25°C; concentration: a) 3%; b) 5%; c) 8%; d) 10%.

At a specific shear rate, the apparent viscosity of PAN solutions in Figure 5.25a increases as the molecular weight of PAN increases. This trend can also be seen in Figure 5.25b-d. Higher molecular weight of polymer leads to higher degree of entanglement of polymer chains, which results in higher viscosity of the polymer solution [63].

PAN solutions in Figure 5.25d show obvious shear thinning behaviors as the shear rate increases. With the same concentration of PAN solutions, the shear thinning behaviors of PAN solutions enhance as the molecular weight of PAN increases. This is because polymer chains with higher molecule weight suffer from larger degree of disentanglement at the same shear rate [63]. With the same polymer, the shear thinning behaviors of PAN solutions enhance as the concentration of PAN solutions increases. The reason is that polymer solutions with higher concentration suffer from larger degree of disentanglement at the same shear rate.

In conclusion, the smaller the molecular weight of polymer is, the better is the mobility of polymer solution [73]. Decreasing the concentration of polymer solutions also has this effect as discussed in Figure 5.1 and 5.15.

Based on the viscosity curves shown in Figure 5.25, the zero-shear viscosities of X-PAN, L-PAN, PAN 150, and PAN 200 solutions are summarized in Table 5.4. With the same polymer, the zero-shear viscosity of PAN solutions increases as the concentration of PAN solutions increases. Similarly, with the same concentration of polymer solutions, the zero-shear viscosity of PAN solutions increases as the molecular weight of polymer increases. The smaller the zero-shear viscosity of polymer solution is, the better is the mobility of

polymer solution. The zero-shear viscosity is directly influenced by molecular weight and concentration of polymer solution [74, 75].

Table 5.4 Zero-shear viscosity (η_0) of various PAN solutions. temperature: 25°C.

η_0 (mPa·s)	Concentration			
Solutions	3%	5%	8%	10%
X-PAN	5.44	21.7	110	307
L-PAN	10.4	27.7	171	429
PAN 150	12.7	82.7	524	1570
PAN 200	50.7	269	1770	6260

The high-frequency shear flow of polymer solutions in capillary tube driven by high-frequency pulse was investigated by oscillatory tests. The shear strain amplitude sweeps of PAN 200 solutions are shown in Figure 5.26.

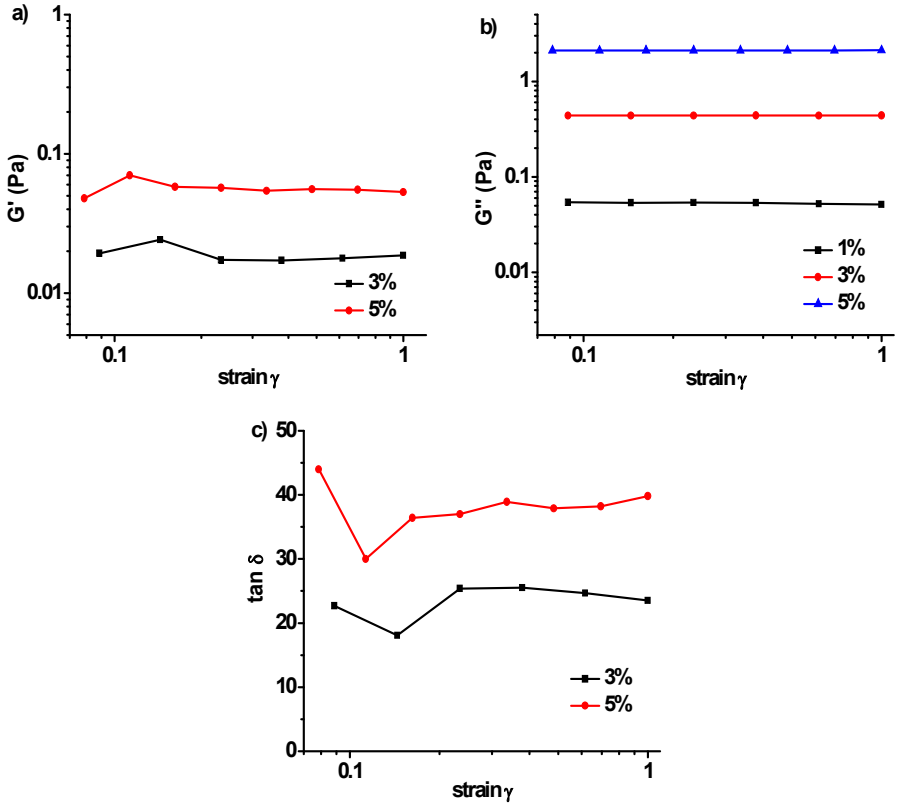

Figure 5.26 Shear strain amplitude sweeps of PAN 200 solutions. angular frequency: 10 rad/s; temperature: 25°C; a) storage modulus (G') and strain; b) loss modulus (G'') and strain; c) loss factor (tan δ) and strain.

In oscillatory tests, the storage modulus (G') of ideal viscous liquid (i.e. Newtonian liquid) is zero while the loss modulus (G'') of ideal elastic solid is zero. Due to the extreme low concentration of 1% solution, its G' values in amplitude sweeps are almost zero (not shown here). Only G'' of 1% solution was detected as shown in Figure 5.26b.

Both G' values and G'' values of 3% and 5% solutions are not zero within the strain presented, which implies that these two solutions are neither ideal viscous liquid nor ideal

elastic solid. Moreover, the loss factors (tan δ) of these two solutions are more than one and less than positive infinity (Figure 5.26c), which indicates that these solutions are viscoelastic liquid [52].

In the capillary tube of shaping head, higher driving voltage leads to larger deformation of capillary tube and stronger impetus to form a microdroplet. Increasing the pulse width also has the same effect. Larger deformation of capillary tube results in larger shear strain of the polymer solution. Both G' and G'' values of PAN 200 solutions are almost constant within the strain presented. The G' values of 5% solution are larger than that of solution of 3%, which indicates solution of 5% has higher capacity of storing energy of deformation (i.e. foreign work) when deformation of this solution happens. In Figure 5.26b, the higher the concentration of solution is, the higher is the capacity of solution dissipating energy of deformation. The composite effect of energy storing and dissipating in PAN 200 solution is shown in Figure 5.26c. With the decreasing of concentration of solution, the loss factor of solution also decreases within the strain presented. Even though the actual shear strain in the capillary tube is not known, decreasing the concentration of PAN solution can decrease the energy dissipated by internal friction and thus increase the initial kinetic energy of microdroplets. In addition, the loss factors of 3% and 5% solutions tend to be constant with the increasing of shear strain.

The frequency sweeps of PAN 200 solutions are shown in Figure 5.27.

In frequency sweeps, the short-term behavior of materials is investigated by applying high shear frequency [76] while the long-term behavior is estimated by applying low shear frequency. Due to the same reason as explained in strain amplitude sweeps, the G' values of 1% solution are not shown here.

In the capillary tube of shaping head, the higher the shaping frequency is, the larger is the deformation rate of capillary tube. Larger deformation rate of capillary tube results in larger shear rate of the polymer solution. Both G' and G'' values of PAN 200 solutions increase as the angular frequency increases within the section presented, which means both energy storing and dissipating in solution increase. At a specific angular frequency, G' values and G'' values increase as the concentration of solution increases as shown in Figure 5.27a and 5.27b, respectively.

The composite effect of energy storing and dissipating on PAN 200 solution is shown in Figure 5.27c. The maximum angular frequency in this frequency sweeps is 100 rad/s (i.e. 16 Hz). Different from the behaviors of PAN solutions in amplitude sweeps, the loss factors of solutions in frequency sweeps are closely dependent on angular frequency. With the increasing of angular frequency, the loss factors firstly increase and then decrease. This is because both over-low and over-high frequencies did not cause serious hysteresis in the PAN solutions. Only at medium frequency sections, the segments of polymer chains can keep pace, but not totally, with the shear rate. Therefore, serious internal friction happens. The appearance of internal friction peak [63] is a character of viscoelasticity.

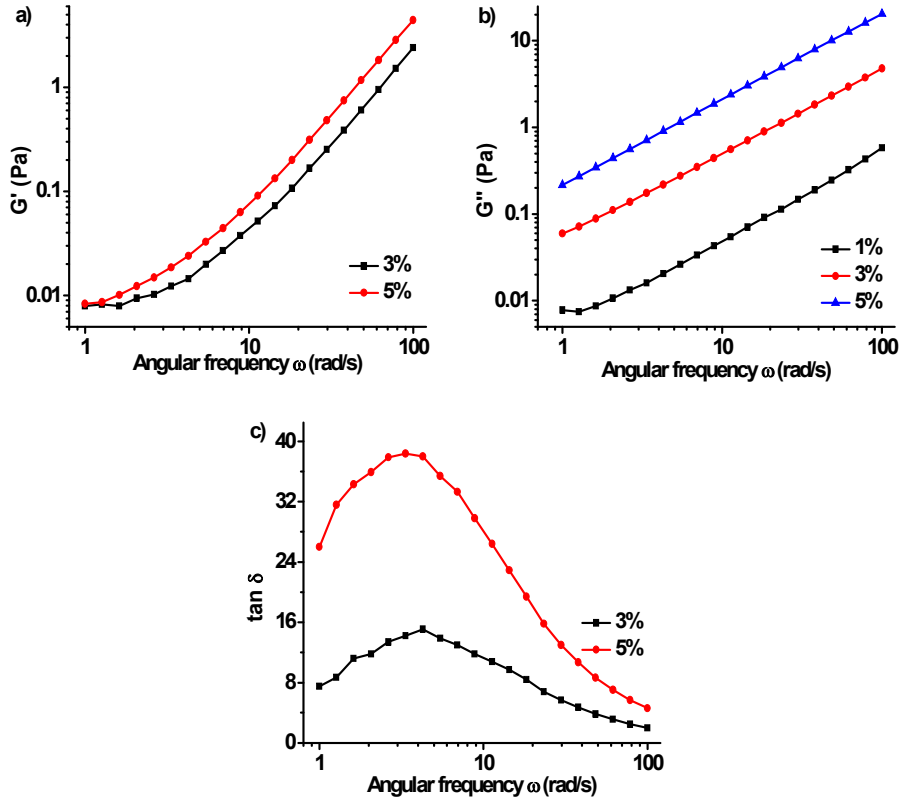

Figure 5.27 Frequency sweeps of PAN 200 solutions. amplitude strain: 10%; temperature: 25°C; a) storage modulus (G') and angular frequency; b) loss modulus (G'') and angular frequency; c) loss factor (tan δ) and angular frequency.

The actual frequency in shaping microdroplets is far higher than 16 Hz. It can be imagined that with the increasing of shaping frequency, the energy dissipated by internal friction also decreases and thus the initial kinetic energy of microdroplets can be increased. Moreover, decreasing the concentration of PAN solutions can also decrease the internal friction in solution.

The temperature sweeps of PAN 200 solutions are shown in Figure 5.28. Due to the same reason as explained in strain amplitude sweeps, the G' values of 1% solution are not shown here.

The liquid in shaping head can be heated up to 130°C. Both G' and G'' values of PAN 200 solutions decrease as the temperature increases within the section presented, which means both energy storing and dissipating in solution decrease. In Figure 5.28a, with the increasing of temperature, the G' values of 5% solution decrease deeper than those of 3% solution. At a specific temperature, G'' values increase as the concentration of PAN solution increases as shown in Figure 5.28b.

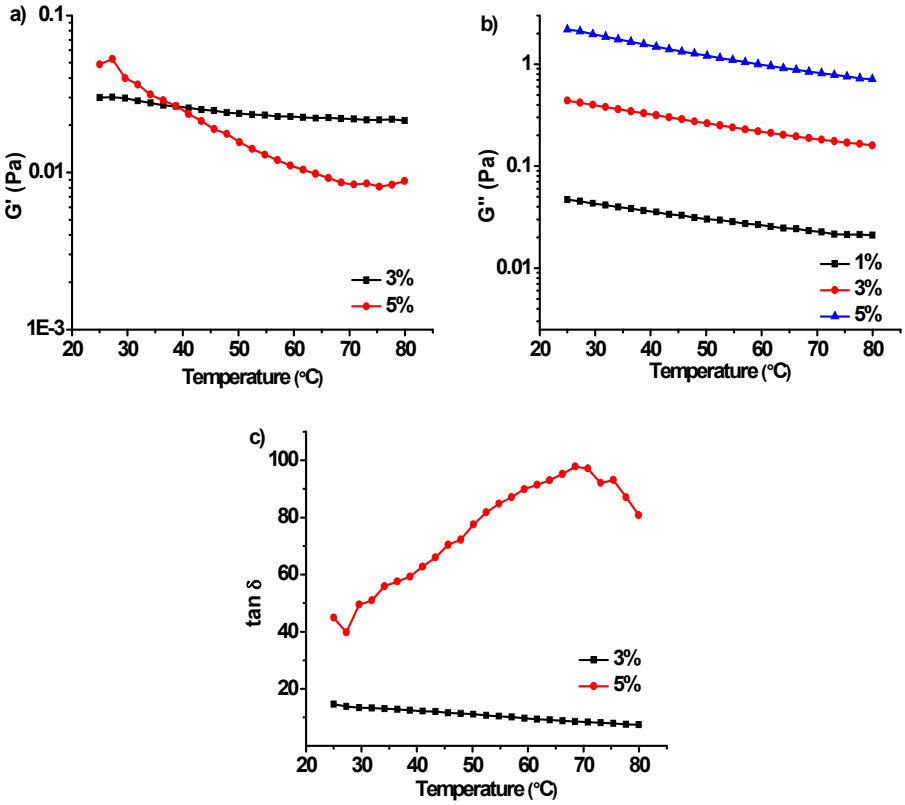

Figure 5.28 Temperature-dependent behaviors of PAN 200 solutions. amplitude strain: 10%; angular frequency: 10 rad/s; a) storage modulus (G') and temperature; b) loss modulus (G'') and temperature; c) loss factor (tan δ) and temperature.

The composite effect of energy storing and dissipating in PAN 200 solution is shown in Figure 5.28c. The loss factors of PAN solution in temperature sweeps are closely dependent on heating temperature. With the increasing of temperature, solution of 5% shows an internal friction peak; however, the loss factor of 3% solution continuously decreases. It can be inferred that with the increasing of concentration, internal friction peaks in temperature sweeps become more and more obvious.

The temperature used in the work ranged from 50 to 120°C. It can be inferred that with the shaping temperature over 80°C, the energy dissipated by internal friction also decreases and thus the initial kinetic energy of microdroplets can be increased. Moreover, decreasing the concentration of PAN solutions can also decrease the internal friction in solution.

5.3.2 Preparation of PAN microspheres

With the micrometer-sized hydrogel microspheres successfully prepared (see section 5.2.3), the work turned to the preparation of PAN microspheres in the range of micrometer. One of the most common phenomena encountered in shaping PAN solutions with high molecular weight was the blocking of shaping orifice. With many trials and errors, two kinds of blocking often happened during the shaping process. The first blocking was the formation of polymer gel in the capillary tube, which is called "real blocking". The solving method to this problem is to submerge the shaping orifice below the surface of DMF solvent, with the shaping and heating function of the equipment operating. Fortunately, this kind of blocking

did not occur very often. The second one was the formation of polymer crust at the orifice [75], which is called “pseudo blocking”. This blocking can be easily solved by cleaning the orifice with a fine tissue for several times. With the shaping process proceeding, “pseudo blocking” can not be avoided and the orifice should be cleaned from time to time to make sure that the shaping is ongoing.

Based on the results of rotational and oscillatory tests, it can be inferred that decreasing either the molecular weight of polymer in solution or the concentration of polymer solution is beneficial to shape microdroplets. In the process of shaping large PAN spheres, however, over-low concentration of PAN solution was disadvantageous for acquiring perfect spherical spheres. Therefore, the concentration of PAN solution should not be too low. In order to shape microdroplets from PAN solutions with high concentration, high driving voltage, high shaping frequency, and high shaping temperature are needed. The shaping and gelling results of a series of PAN microdroplets are shown in Figure 5.29. Before intact and perfect PAN microspheres were acquired, the size of microspheres was temporarily not considered.

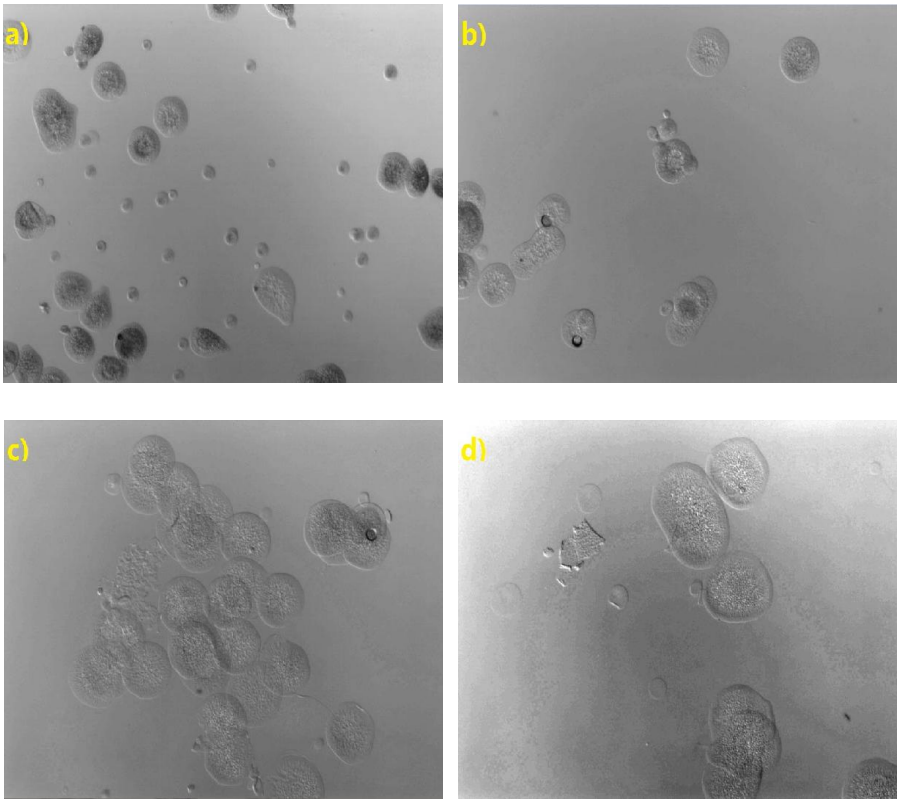

Figure 5.29 Photographs of “microspheres” from various PAN solutions. common shaping conditions: 250 V, 25 μs, 400 Hz; falling distance: 7 cm; gelation conditions: water bath at 20°C; a) X-PAN with a concentration of 9%, temperature of shaping head: 120°C; b) L-PAN with a concentration of 8%, temperature of shaping head: 120°C; C) PAN 150 with a concentration of 5%, temperature of shaping head: 85°C; d) PAN 200 with a concentration of 3%, temperature of shaping head: 80°C.

In Figure 5.29a (i.e. X-PAN), except for some smaller microspheres, the shape of rest microspheres is “disk-like”. According to the results of shaping SA hydrogel microspheres, the flattening (i.e. deformation and breakup) of PAN microspheres was due to the impact of

microdroplets with coagulant surface. Microspheres in Figure 5.29b (L-PAN), 5.29c (PAN 150), and 5.29d (PAN 200) are all "disk-like". For various PAN solutions, their initial shaping concentrations all started from 10%. If no droplets came out of the orifice, then decreasing the concentration of PAN solution was needed. By this way, the permissible highest shaping concentrations of various PAN solutions are 9% (for X-PAN), 8% (for L-PAN), 5% (for PAN 150), and 3% (for PAN 200).

With the PAN microdroplets successfully shaped, the work turned to acquire perfect and spherical microspheres. For simplicity, X-PAN solution is taken for an example, which has the highest shaping concentration because of the lowest M_w in all four PAN solutions. The reason, i.e. solution's low concentration, can be excluded for the deformation and breakup of microspheres by using an X-PAN solution of 8%.

For the deformation and breakup of PAN microspheres, the most immediate cause is the impact of microdroplets with coagulant surface, which is related to impact velocity (i.e. terminal velocity). According to the principle of droplets' deformation in 2.2.4, the impact velocity can be analyzed from direction and speed. The direction of impact velocity is affected by the direction of initial velocity of microdroplets and can not be predicted precisely. Impact speed is related to falling distance and initial speed of microdroplets. Furthermore, initial speed of microdroplets is again related to driving voltage and shaping frequency. Correspondingly, the modulation of driving voltage and shaping frequency is limited by the concentration of PAN solution.

The direction of initial velocity of microdroplets is shown in Scheme 5.3. The angle between the axis of shaping head and the normal line of coagulant surface is defined as θ. The default value of θ is 0°. The intention of changing the position of shaping head is to decrease the vertical component of initial velocity. The larger the angle θ is, the smaller is the vertical component of initial velocity.

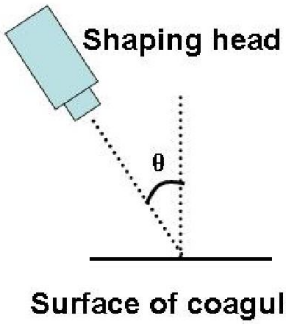

Scheme 5.3 The angle between axis of shaping head and normal line of coagulant surface.

The effect of initial velocity's direction on the shape of microspheres is shown in Figure 5.30. As shown in Figure 5.30a, the broken morphology (i.e. "disk-like") of microspheres, which is common in Figure 5.29a, has disappeared. The central part of microspheres, however, is still deformed and crinkled due to impact. As θ increases from 30° to 60°, the crinkled surface of microspheres still exists as shown in Figure 5.30b. Changing the position of shaping head is effective to improve the shape of microspheres; however, further increasing the θ (i.e. larger than 60°) resulted in less microdroplets falling into the coagulation bath within the same period. In conclusion, the actual effect of changing the position of shaping head on the shape

of microspheres is finite.

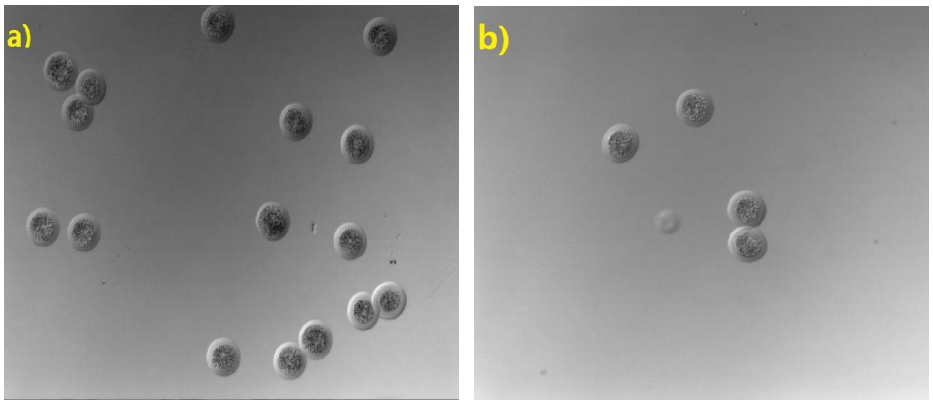

Figure 5.30 Photographs of microspheres shaped from different angles. 8% X-PAN solution; common shaping conditions: 250 V, 25 µs, 100 Hz; falling distance: 7.5 cm; temperature of shaping head: 85°C; gelation conditions: water bath at 20°C; a) θ: 30°; b) θ: 60°.

The effect of falling distance of microdroplets on the shape of microspheres is shown in Figure 5.31.

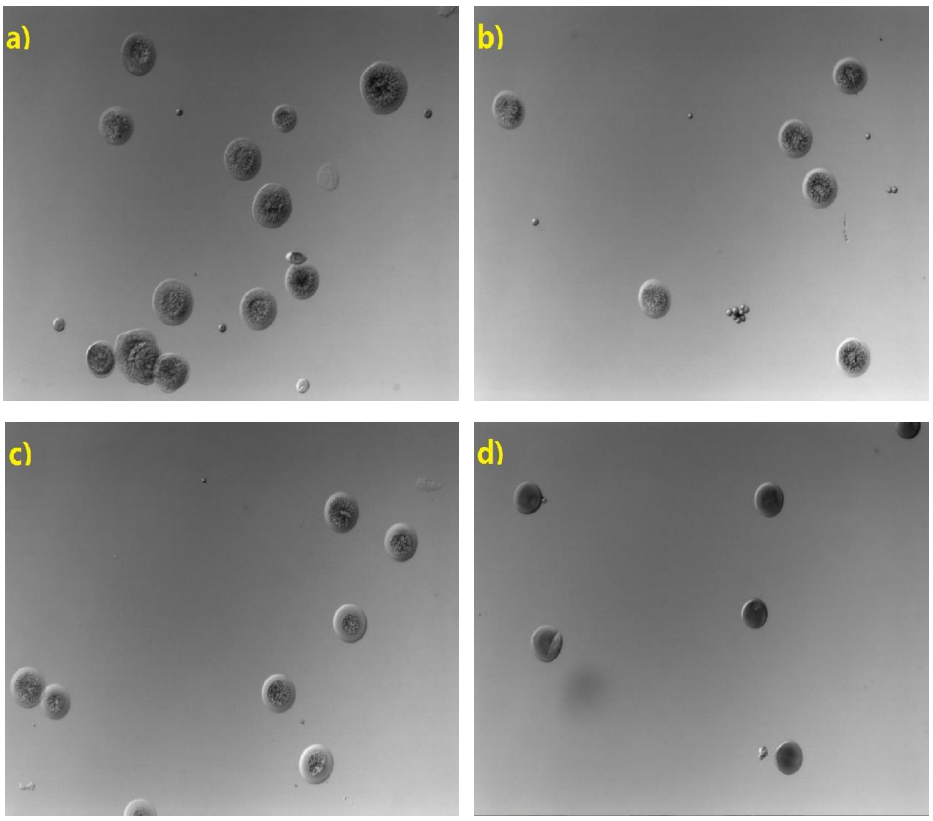

Figure 5.31 Photographs of microspheres from various falling distances. 8% X-PAN solution; common shaping conditions: 250 V, 25 µs, and 100 Hz; temperature of shaping head: 85°C; gelation conditions: water bath at 20°C; falling distance of microdroplets: a) 5 cm, b) 7 cm, c) 10 cm, and d) 14 cm.

As shown in Figure 5.31a, most microspheres broke up and displayed “disk-like” shape due

to the over-low falling distance. As the falling distance increases up to 7 cm and 10 cm, the phenomenon of breakup disappears. Only the central part of these microspheres is deformed and crinkled. With the falling distance further increased to 14 cm, crinkled surface of microspheres disappears. At the same time, however, the number of microspheres collected in the coagulation bath of Figure 5.31d was smaller within the same period. In conclusion, increasing the falling distance of microdroplets is beneficial to acquire perfect and spherical microspheres. The reason is given below.

When the polymer microdroplets were ejected from the orifice, their initial velocity is rather high (e.g. as high as 10 m/s). During the falling process, the principle aerodynamic force of air to microdroplets is Strokes drag [65], which is proportional to the first power of the velocity of microdroplets. According to the force analysis of microdroplets, even though the microdroplets were just jetted from the orifice, the influencing of aerodynamic drag was obvious. Due to the small mass of micrometer-sized droplets (i.e. small inertia and gravity), the actual decelerating effect of aerodynamic drag is large. With the increasing of falling distance, the deformation of microdroplets upon impact with liquid surface decreases. For large PAN droplets and PAN microdroplets, the lower the mass of droplets is, the more obvious is the decelerating effect of aerodynamic drag.

The effect of driving voltage and shaping frequency on the shape of microspheres is shown in Figure 5.32.

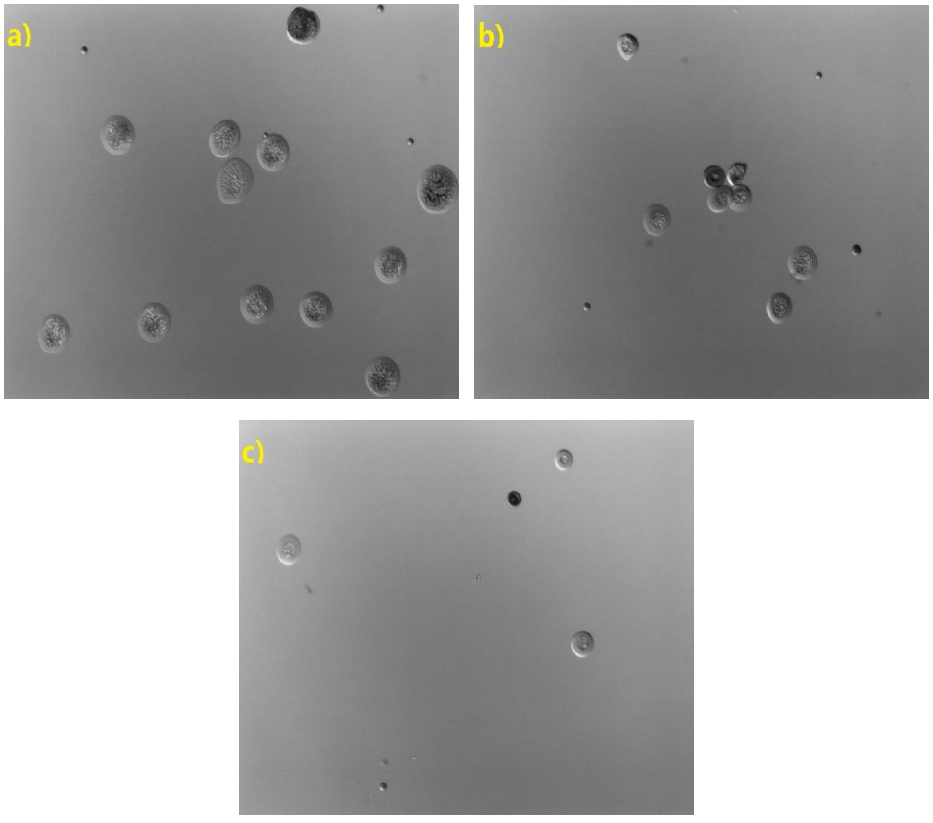

Figure 5.32 Photographs of microspheres from 8% X-PAN solution. shaping conditions: 25 μs; falling distance: 9 cm; gelation conditions: water bath at 20°C; other shaping conditions: a) 220 V, 220 Hz, temperature of shaping head: 85°C; b) 200 V, 200 Hz, temperature of shaping head: 100°C; c) 180 V, 190 Hz, temperature of shaping head: 120°C.

With the falling distance too short, the impact speed of microdroplets can not be effectively decreased. Instead, with the falling distance too long, only a few microdroplets came into the coagulation bath within the same period. With many trials and errors, a compromise for the falling distance was set at 9 cm in this series of experiments.

As shown in Figure 5.32, the central part of all microspheres are all deformed and crinkled. With the decreasing of driving voltage and shaping frequency (from 5.32a to 5.32c), however, the areas of central crinkled surface of microspheres decrease. In conclusion, the higher the driving voltage and shaping frequency are, the higher is the initial speed of microdroplets. Higher initial speed of microdroplets leads to larger deformation of microspheres.

A disadvantage of this strategy, however, existed. For microspheres from Figure 5.32c, their actual number collected in the coagulation bath was much smaller within the same period. Since driving voltage and shaping frequency are two driving factors to facilitate the jetting of microdroplets, excessively decreasing these two factors damages the shaping durability thus the frequency of cleaning orifice is increased. Therefore, the modulation of these two factors is rather finite.

In order to acquire microspheres as many and spherical as possible within a specific period, the following strategy is proposed.

Given a certain concentration of polymer solution and a falling distance (9 cm), the strategy to acquire microspheres as many and spherical as possible within a specific period is to increase the shaping temperature while to decrease the driving voltage and shaping frequency. For simplicity, the temperature of shaping head is set at 120°C. If the driving voltage and shaping frequency are decreased to specific values (below these values, no microdroplets will come out) and the quality and number of microspheres are still not satisfying, then further decreasing the concentration of polymer solution is needed.

In this way, satisfactory microspheres were acquired in terms of number and quality from 6.5% X-PAN solution, 6% X-PAN solution, and 6% L-PAN solution as shown in Figure 5.33. As shown in Figure 5.33a, although there are still some larger microspheres which means they are deformed, the rest smaller microspheres are quite intact. The mean diameter of microspheres from 6.5% X-PAN solution is 31 μm according to the scale. With the concentration of X-PAN solution further decreased to 6%, the deformation of microspheres decreases. Similarly, microspheres from 6% L-PAN were also acquired as shown in Figure 5.33c. The shape of microspheres is similar to that of microspheres from 6.5% and 6% X-PAN solution. The shaping strategy was again confirmed by using L-PAN solution.

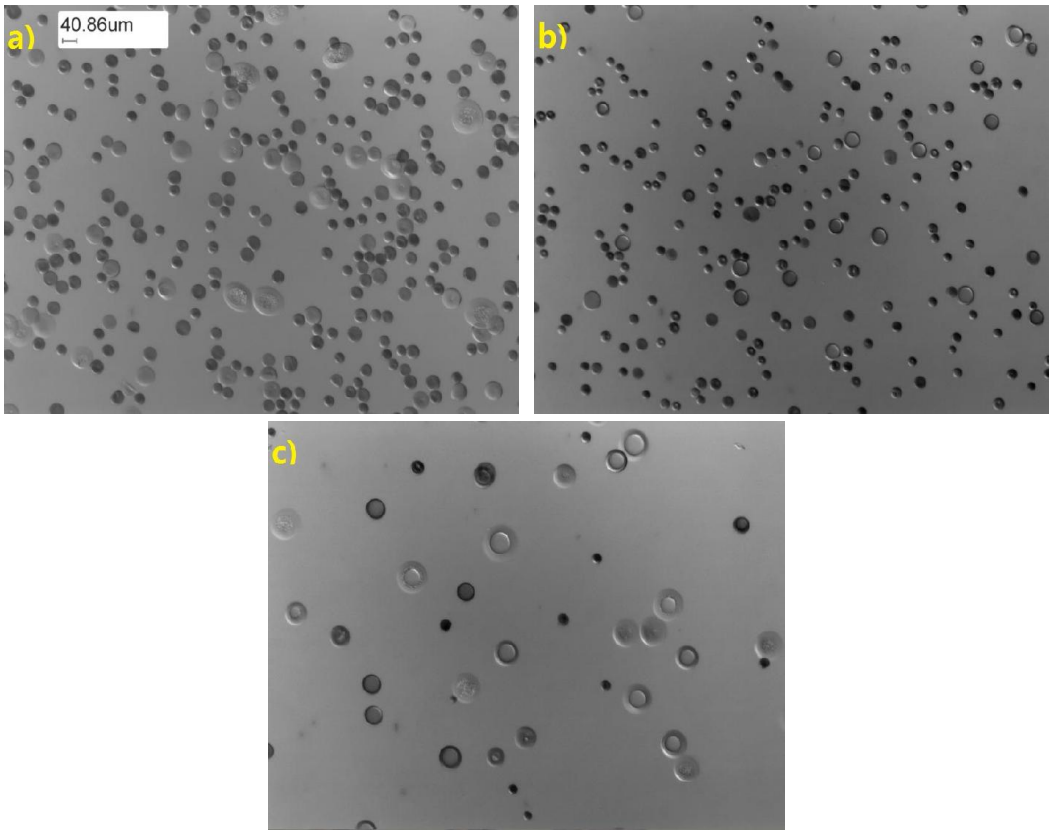

Figure 5.33 Photographs of microspheres from X- and L-PAN solutions. common shaping conditions: 25 μs; temperature of shaping head: 120°C; falling distance: 9 cm; gelation conditions: water bath at 20°C; other shaping conditions: a) 6.5% X-PAN, 140 V, and 105 Hz; b) 6% X-PAN, 145 V, and 95 Hz; c) 6% L-PAN, 185 V, and 125 Hz.

Although a number of microspheres can be collected within a long period, the shaping rate is still unsatisfying and should be further increased for pragmatic purpose. Increasing driving voltage and shaping frequency can be seen as two driving factors to increase the shaping rate. Over-high voltage and shaping frequency, however, will render the microdroplets deformed and broken. To overcome this disadvantage, the falling distance of microdroplets should be increased at the same time. Higher shaping temperature leads to easier blocking of the nozzle; therefore, the shaping temperature should be suppressed as low as possible.

For 6.5% X-PAN solution, the results of increasing shaping rate by increasing voltage are shown in Figure 5.34. One notice should be mentioned here that the number of microspheres captured by photographs did not represent the shaping rate of microdroplets. The determination of shaping rate was qualitative and was done by visual observation to measure the time of coagulant becoming opaque and turbid.

Compared with the microspheres in Figure 5.33a, although the shaping rate of microspheres in Figure 5.34a was increased, the deformation and breakup of microspheres also increase. Fortunately, with the increasing of falling distance of microdroplets from 9 cm to 15 cm, the deformation and breakup of microspheres are suppressed and the number of deformed and broken microspheres decreases. As shown in Figure 5.34c, when the falling distance reaches 13 cm, almost no broken microspheres can be found. When the falling distance reaches 15 cm,

almost no deformed microspheres can be found.

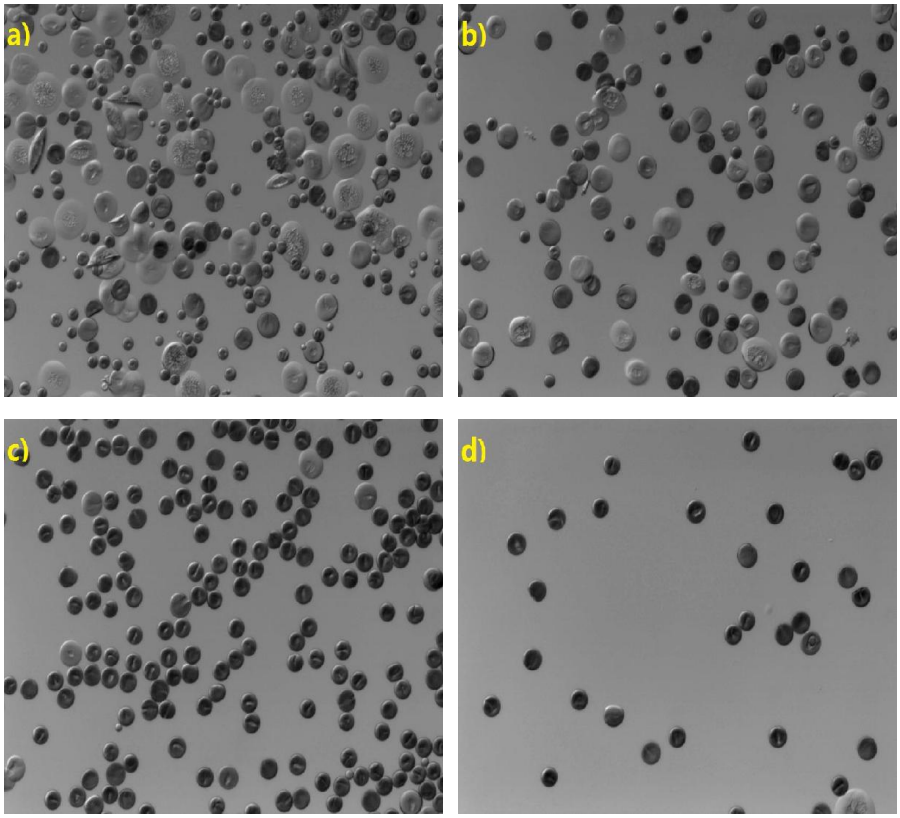

Figure 5.34 Photographs of microspheres from higher driving voltage. 6.5% X-PAN solution; shaping conditions: 160 V, 25 μs, and 100 Hz; temperature of shaping head: 100°C; gelation conditions: water bath at 20°C; falling distance: a) 9 cm, b) 11 cm, c) 13 cm, and d) 15 cm.

Due to the low mass of microdroplets and disturbance of air flow, the trajectory of microdroplets was random after being jetted a short distance from the orifice. With the increasing of falling distance, fewer microdroplets fell into the coagulation bath.

Based on the results of Figure 5.34, for 6.5% X-PAN solution, the shaping frequency was further increased from 100 Hz to 300 Hz, as shown in Figure 5.35.

For the shaping of Newtonian liquid at low frequency, such as 10 Hz, the shaping frequency equals numerically to the shaping rate, i.e. 10 Hz means 10 microdroplets per second. For the shaping of viscoelastic liquid at high frequency, however, this relation does not hold any more, i.e. 100 Hz is not 100 microdroplets per second.

Compared with the microspheres in Figure 5.33a, although the shaping rate of microspheres in Figure 5.35a was increased, the deformation and breakup of microspheres also increase. Fortunately, with the increasing of falling distance of microdroplets from 10 cm to 22 cm, the deformation and breakup of microspheres are suppressed and the number of deformed and broken microspheres decreases. As shown in Figure 5.35c and 5.35d, when the falling distance reaches 18 cm and 22 cm, almost no deformed and broken microspheres can be found.

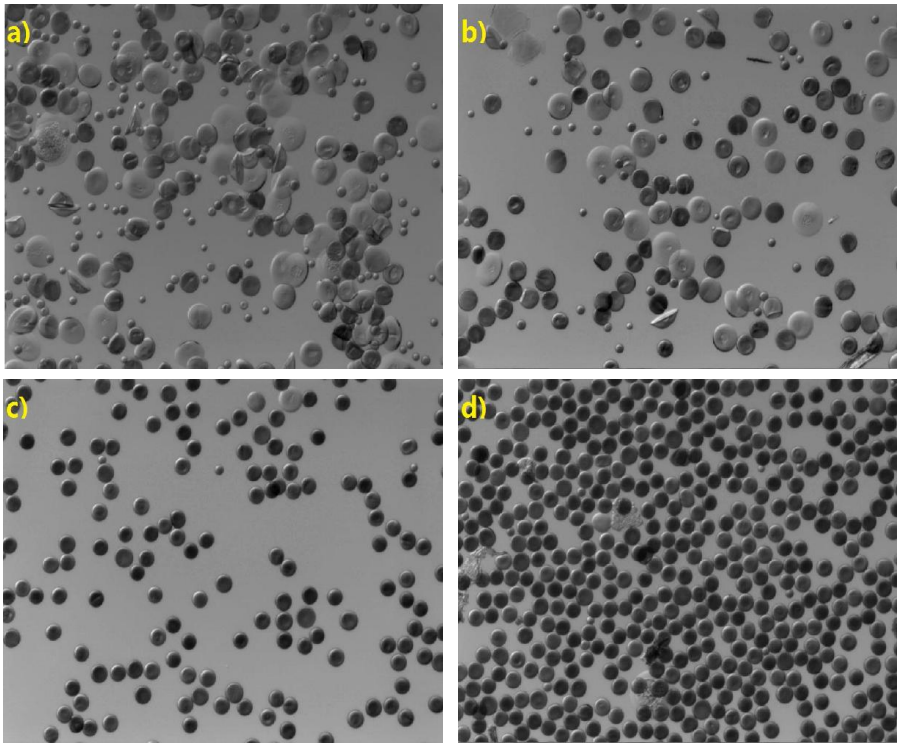

Figure 5.35 Photographs of microspheres from higher shaping frequency. 6.5% X-PAN solution; shaping conditions: 160 V, 25 μs, and 300 Hz; temperature of shaping head: 100°C; gelation conditions: water bath at 20°C; falling distance: a) 10 cm, b) 14 cm, c) 18 cm, and d) 22 cm.

With the increasing of falling distance, fewer microdroplets fell into the coagulation bath. In this case, the collection of microdroplets was still a problem. To solve the problem of collecting microdroplets, a paper cylinder was put between the shaping head and coagulation bath as shown in Figure 5.36.

Figure 5.36 A photograph of the shaping equipment with a paper cylinder to protect the falling routes of microdroplets.

By this, most microdroplets whose trajectories are vertical to the coagulant surface will come into the coagulation bath. In this way, about 250 mg dry microspheres were acquired in one week from the coagulant of DMF/water mixture.
The shape of microspheres (from 6.5% X-PAN solution) gelled in water was again observed by SEM as shown in Figure 5.37.

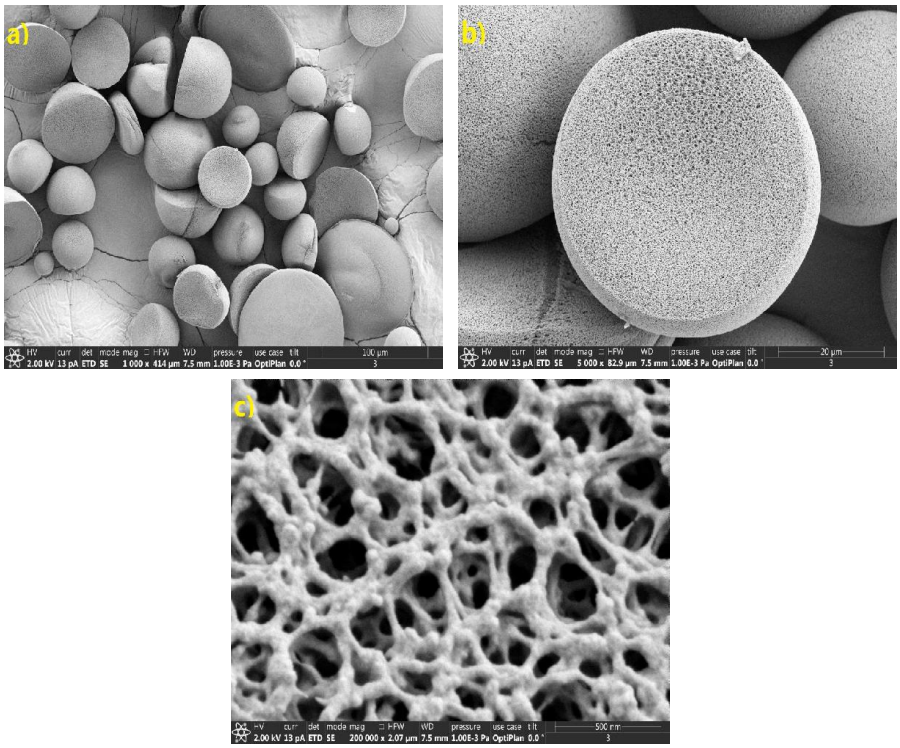

Figure 5.37 SEM photographs of microspheres gelled in water. 6.5% X-PAN solution; shaping conditions: 140 V, 25 µs, and 105 Hz; temperature of shaping head: 120°C; falling distance: 9 cm; gelation conditions: water bath at 20°C; scales of a-c): 100 µm, 20 µm, and 500 nm.

Although the shape of microspheres observed by optical microscope (Figure 5.33a) is round, the shape of some microspheres observed by SEM is not spherical as shown in Figure 5.37a. Because of the impact of microdroplets with water surface, the shape of deformed microspheres consists of a plane and 1/2 to 3/4 of spherical surfaces. By SEM inspection, it is confirmed that some microspheres with oversize areas observed by optical microscope were actually serious deformed. One notice should be mentioned that the plane of the microsphere in Figure 5.37b is not a cross-section. As shown in Figure 5.37c, the surface of X-PAN microspheres is highly porous.

Up to here, all PAN microdroplets gelled in water bath. The shape of microspheres (from 6.5% X-PAN solution) gelled in DMF/water mixture is shown in Figure 5.38.

The morphology of microspheres observed by optical microscope is shown in Figure 5.38a. Microspheres in this figure are highly homogeneous and the mean diameter of these microspheres is 44 µm (see scale in 5.38c). Some microspheres with serious deformation or flattening, however, can not be avoided as shown in Figure 5.38b by SEM inspection. The shape of microspheres in Figure 5.38c, however, is more spherical than that of microspheres in Figure 5.37a. Due to the increasing of falling distance, the deformation of microspheres has decreased in Figure 5.38c. This means increasing falling distance did help to alleviate the impact between microdroplets and coagulant surface. As shown in Figure 5.38d, the surface of microspheres is highly porous.

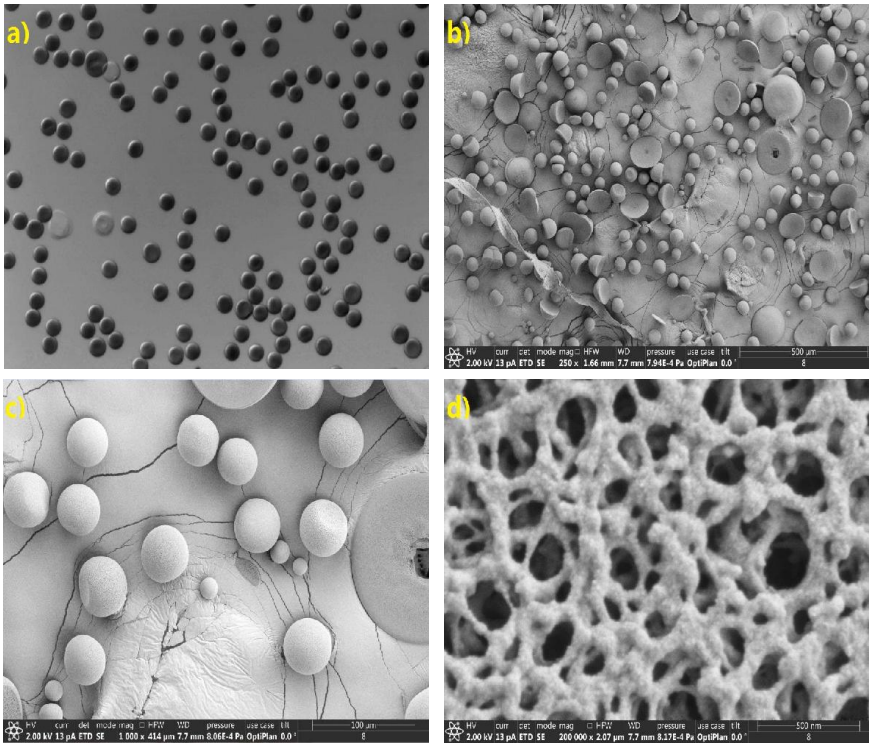

Figure 5.38 Photographs of microspheres gelled in DMF/water mixture. 6.5% X-PAN solution; shaping conditions: 160 V, 25 µs, and 300 Hz; temperature of shaping head: 100°C; falling distance: 26 cm; gelation conditions: 65% DMF in DMF/water mixture at 20°C; a) a photograph captured by optical microscope; b-d): photographs captured by SEM; scale: b) 500 µm, c) 100 µm, and d) 500 nm.

The internal structure of X-PAN microspheres was analyzed in terms of specific surface areas and specific pore volumes. With the volume fractions of DMF increased from 0% to 65%, both specific surface areas and specific pore volumes of microspheres increase as shown in Figure 5.39.

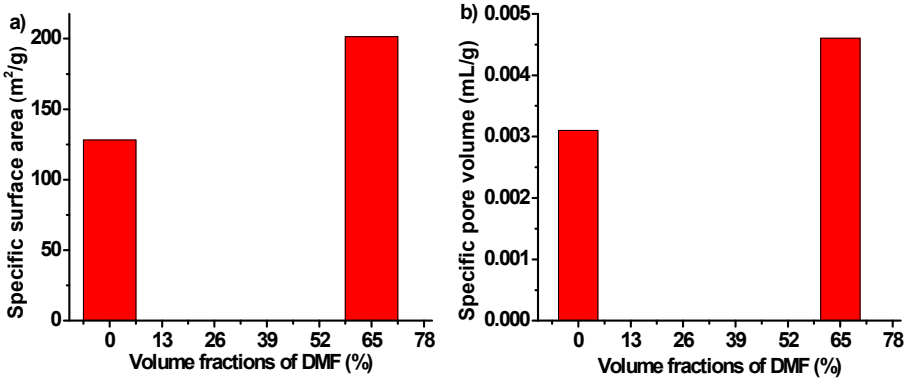

Figure 5.39 Pore characterizations of X-PAN microspheres. 6.5% X-APN solution; "0/100" microspheres: gelation conditions: 0% DMF in coagulant at 20°C; "65/35" microspheres: gelation conditions: 65% DMF in coagulant at 20°C; a) specific surface area; b) specific pore volume.

The higher the volume fractions of DMF in coagulant are, the lower is the gelation rate of microdroplets in coagulant. Lower gelation rate results in microspheres with more characters

of delayed phase separation, which renders the number of inner pores more and the mean diameter of inner pores smaller.
Moreover, with the same shaping conditions, higher concentration of polymer solution will result in microspheres with better shape. This conclusion can be confirmed by the results shown in Figure 5.40.

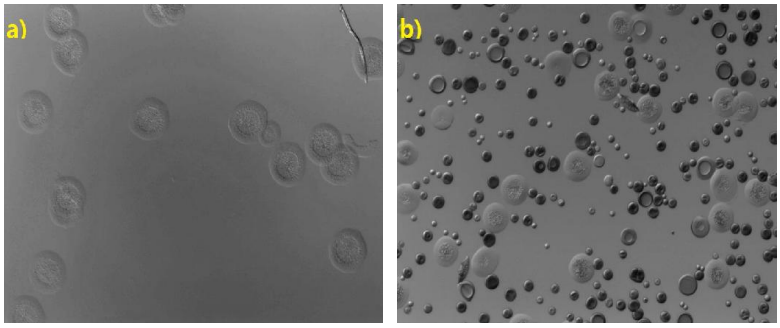

Figure 5.40 Effect of polymer concentration on the shape of microspheres. common shaping conditions: 160 V, 25 μs, and 100 Hz; falling distance: 7 cm; gelation conditions: water bath at 20°C; a) microspheres from 5% X-PAN solution, temperature of shaping head: 50°C; b) microspheres from 6.5% X-PAN solution, temperature of shaping head: 100°C.

As shown in Figure 5.40a, the shapes of all microspheres are "disk-like", which means they have broken. When the concentration of X-PAN solution increases to 6.5%, intact microspheres appear though deformed and broken microspheres still exist as shown in Figure 5.40b. The effect of volume fractions of DMF in coagulant on the shape of X-PAN microspheres is shown in Figure 5.41.

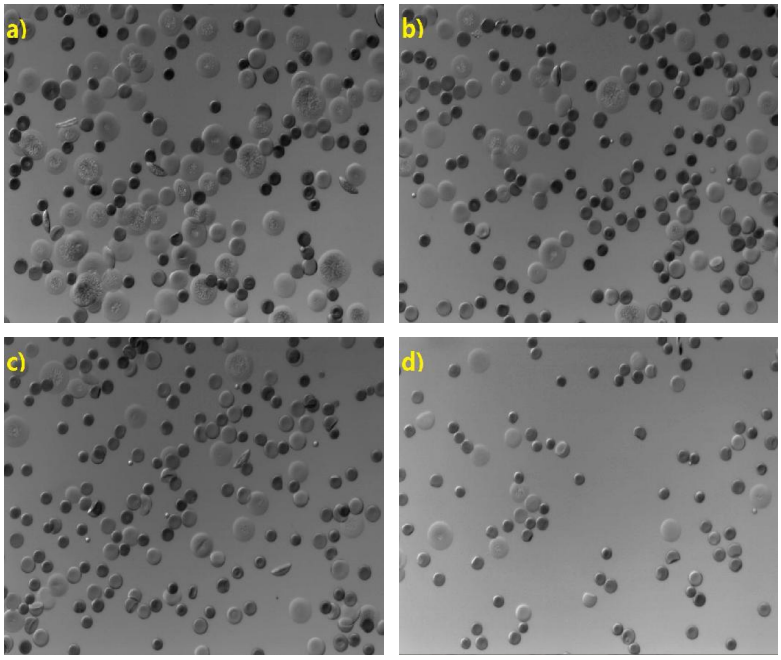

Figure 5.41 Effect of gelation rate on the shape of microspheres with a falling height of 22 cm. shaping conditions: 6.5% X-PAN solution, 160 V, 25 μs, and 300 Hz; temperature of shaping head: 100°C; volume fractions of DMF in coagulant: a) 15%, b) 25%, c) 30%, and d) 45%.

With the increasing volume fractions of DMF in coagulation bath, the number of deformed and broken microspheres seems to decrease from Figure 5.41a to 5.41d. The ratio of these microspheres in all microspheres, however, is still large as shown in Figure 5.41d.
With the same shaping conditions as shown in Figure 5.42, when the falling distance of microdroplets increased from 22 cm to 26 cm, deformed and broken microspheres are seldom seen in all coagulation bath as shown in Figure 5.42a-d.

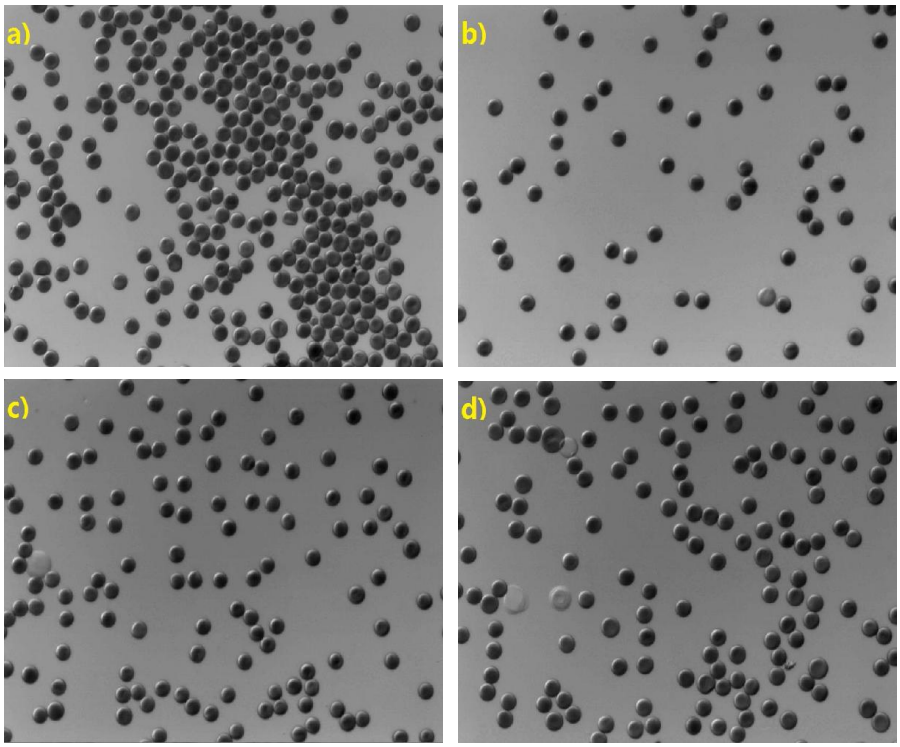

Figure 5.42 Effect of gelation rate on the shape of microspheres with a falling height of 26 cm. shaping conditions: 6.5% X-PAN solution, 160 V, 25 μs, and 300 Hz; temperature of shaping head: 100°C; volume fractions of DMF in coagulant: a) 5%, b) 25%, c) 45%, and d) 65%.

5.3.3 Summary

1. For a specific polymer which is to be shaped into microspheres by DOD ink-jetting *cum* gelation, its molecular weight and concentration in solution are the first two factors to be considered. Decreasing the concentration of this polymer is definitely beneficial to the shaping of microdroplets; however, the results of gelation may be not ideal. Medium polymer concentration is suggested for first trails.
2. High driving voltage, high shaping frequency, and high shaping temperature are three promoting factors to shape microdroplets. Over-high driving voltage and shaping frequency lead to over-high initial velocity of microdroplets, which aggravates the deformation and breakup of microspheres. Over-high shaping temperature results in the higher probability of orifice's blocking.
3. The deformation and breakup of microspheres mainly results from high initial velocity and low falling distance of microdroplets. To shape intact microspheres, high driving voltage and high shaping frequency should be matched with high falling distance of microdroplets. At the

same time, the shaping temperature should be as low as possible.
4. Compared with M_w, polymer concentration, driving voltage, shaping frequency and temperature, and falling distance, the effects of gelation rate and surface tension on shaping intact microspheres are not so important.
5. The shaping conditions of X-PAN solution can be used as references for the shaping of other polymer solutions.

5.4 Carbonization of large polymer spheres

5.4.1 Thermo analysis of PAN 200

The thermo behaviors of PAN 200 polymer in terms of mass loss are shown in Figure 5.43. In Figure 5.43a, the decomposition temperature (i.e. T_d, mass loss of 5%) of PAN 200 within oxygen atmosphere is 272°C while the total decomposition temperature (i.e. mass loss of 100%) is 638°C. For the rate of mass loss, the maximum rate occurred at 271°C in oxygen as shown in Figure 5.43b. Although this rate of mass loss is high, the actual mass loss at this temperature was rather low within short time.

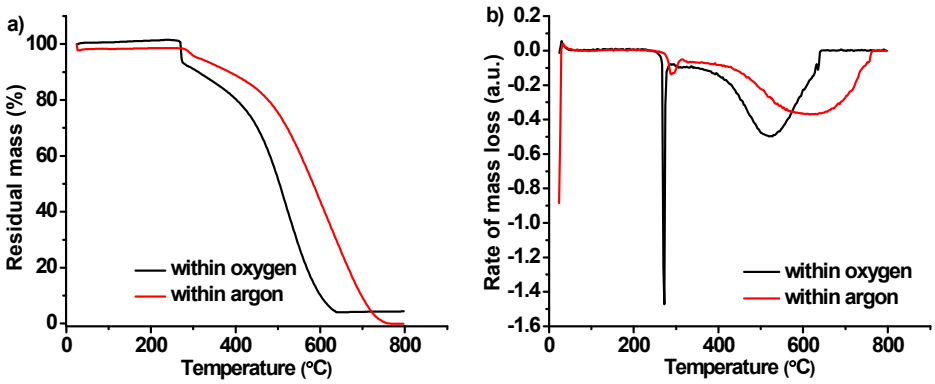

Figure 5.43 TGA and DTG curves of PAN 200. heating rate: 5 K/min; a) TGA curves; b) the first derivative of TGA curves (i.e. DTG).

By contrast, the T_d of PAN 200 in argon atmosphere is 310°C and total decomposition temperature is 754°C. The decomposition temperature of homo-PAN was reported to be 317°C [77] within inert atmosphere. Due to the absence of oxygen, the T_d of PAN 200 increased in inert atmosphere. Correspondingly, the maximum rate of mass loss occurred at 612°C. There is also one maximal point of loss rate, which occurred at 290°C.
The thermo behaviors of PAN 200 in terms of temperature difference are shown in Figure 5.44. The downward direction of signals means the incidents are exothermic.
Within oxygen atmosphere, there were mainly two exothermic incidents. The first incident peaked at 273°C. When the atmosphere was changed from oxygen to argon, this exothermic peak is shifted from 273°C to 297°C. The cyclization reaction is assumed to happen below 300°C [77] for PAN polymer. So this exothermic peak is assumed to be related to the cyclization reaction of PAN 200 chains.
Both original PAN and ladder PAN products can undergo dehydrogenation reaction [78]. The dehydrogenation reaction of ladder PAN 200 and original PAN 200 is assumed to happen

above 300°C [77, 78]. Since PAN 200 has 0.5% methyl acrylate (MA), the dehydrogenation reaction of PAN 200 can not be avoided above 300°C even within argon atmosphere.

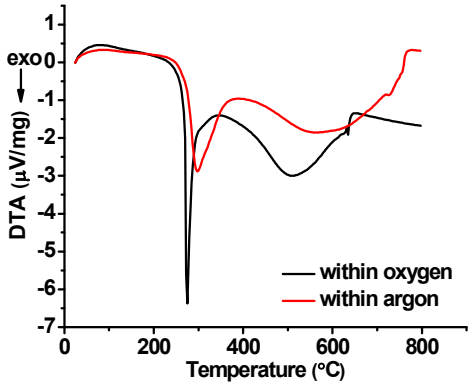

Figure 5.44 DTA curves of PAN 200. heating rate: 5 K/min.

The thermo behaviors of PAN 200 in terms of enthalpy change are shown in Figure 5.45. Within argon atmosphere, the only exothermic signal peaks at about 300°C. Similarly, this exothermic peak is also assumed to be related to cyclization reaction.

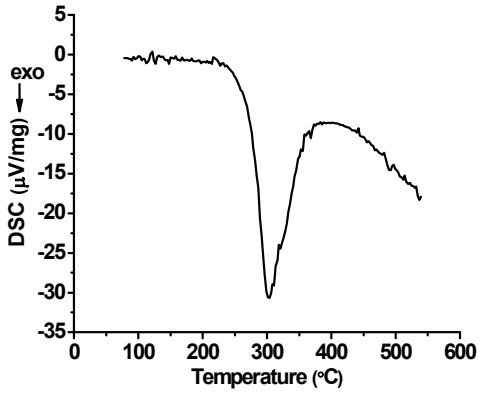

Figure 5.45 DSC curves of PAN 200. heating rate: 5 K/min; atmosphere: argon.

For the pre-oxidation of polymer spheres made of PAN 200, over low temperature leads to the incomplete oxidation of polymer spheres while over high temperature results in excessive mass loss. Since the heating rate was set at 5 K/min in both TGA and DTA analysis, the effect of retention time on pre-oxidation was not clear. To be prudent, four pre-oxidation temperatures were selected, which are 240°C, 270°C, 300°C, and 330°C.

5.4.2 Pre-oxidation of polymer spheres

Theoretically, the stabilization of precursors can be done in inert atmosphere. For PAN 200, however, the involving of oxygen can render the products after oxidation higher stability to resist the heat treatment of pyrolysis than those after stabilization in inert atmosphere [79]. The ratios of residual mass and mean size of carbon spheres after pre-oxidation are shown in Figure 5.46.

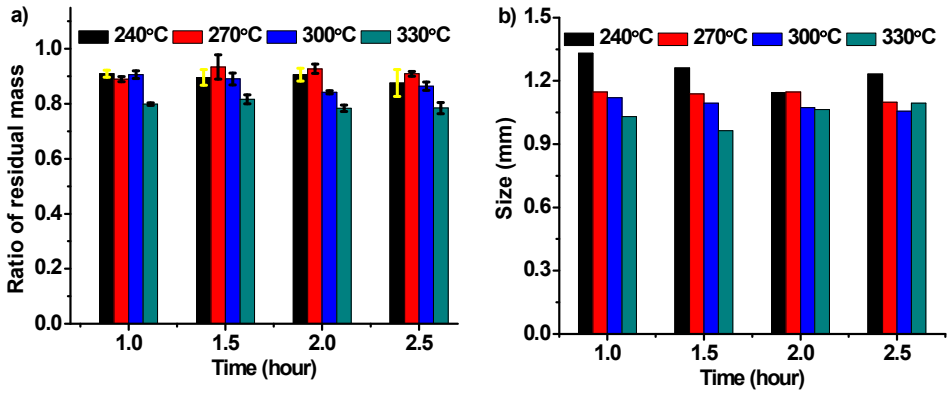

Figure 5.46 Carbon spheres after pre-oxidation. a) ratio of residual mass; b) mean size.

As shown in Figure 5.46a, with the retention time increasing from 1 hour to 2.5 hours, the mass loss almost keeps the same within carbon spheres of "240°C". Carbon spheres of "270°C", "300°C", and "330°C" also have the similar results.

With the oxidation temperature increasing from 240°C to 300°C, the mass loss almost keeps the same, i.e.10%, within carbon spheres of "1 hour". Carbon spheres of "1.5 hour", "2 hour", and "2.5 hour" also have the similar results. With the oxidation temperature below 300°C, the fluctuation of mass loss is little. It can be inferred that the mass loss of carbon spheres oxidized below 300°C was related to cyclization reaction.

As the oxidation temperature increased to 330°C, a higher mass loss of 20% happened in carbon spheres of "1 hour", "1.5 hour", "2 hour", and "2.5 hour". Likewise, the mass loss of carbon spheres at 330°C has no dependence on retention time. As discussed in Figure 5.44, the higher mass loss of carbon spheres at 330°C was inferred to be related to dehydrogenation reaction.

The mean minor axis of "8%, 65/35" polymer spheres is 2.6 mm. In Figure 5.46b, the mean size of carbon spheres after pre-oxidation is below 1.2 mm except for three samples. Therefore, polymer spheres shrank after oxidation. With the oxidation temperature increasing from 240°C to 330°C, the mean size of carbon spheres "1 hour" decreases. Carbon spheres of "1.5 hour", "2 hour", and "2.5 hour" also have the same trend. With the retention time increasing from 1 hour to 2.5 hours, the mean size of carbon spheres "240°C" almost keeps the same. Carbon spheres of "270°C", "300°C", and "330°C" also have the same feature.

The specific surface areas and specific pore volumes of carbon spheres after pre-oxidation are shown in Figure 5.47. The specific surface areas of "8%, 65/35" polymer spheres are 269 m^2/g while its specific pore volumes are 1.12 mL/g. As shown in Figure 5.47a, the specific surface areas of carbon spheres are all below 15 m^2/g. In addition, the specific pore volumes of carbon spheres are all below 0.05 mL/g.

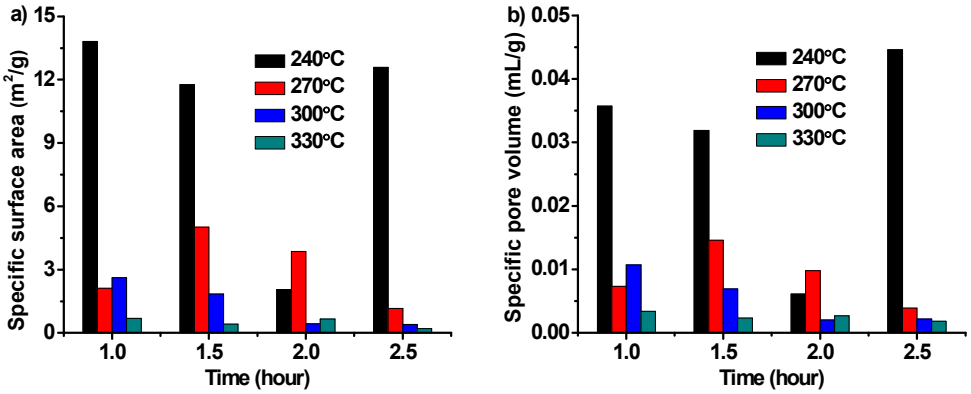

Figure 5.47 Pore characterizations of carbon spheres after pre-oxidation. a) specific surface area; b) specific pore volume.

In order to exclude the occasionality of results, some more carbon spheres were inspected by nitrogen adsorption and the results are shown in Figure 5.48. The specific surface areas of four carbon samples did not increase much even after three times' repetition.

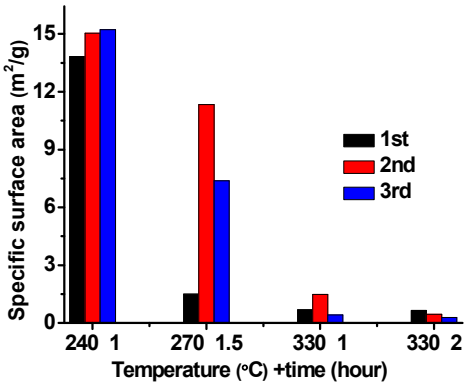

Figure 5.48 Specific surface areas of carbons spheres after pre-oxidation from repeated experiments. "240 1" means carbon spheres oxidized at 240°C for 1 hour.

Therefore, it can be inferred that much porous structures of PAN 200 polymer spheres were "lost" after pre-oxidation process. Two possible reasons can be proposed. The first reason is that the inner porous structure of polymer spheres is really destroyed during the oxidation process. The second one is that the surface pores of carbon spheres are temporarily blocked after oxidation.

The photographs of carbon spheres after pre-oxidation captured by SEM are shown in Figure 5.49. As shown in Figure 5.49a, the inner porous structure of carbon spheres did not change compared with the structure shown in Figure 5.7d. In Figure 5.49b, the boundary between skin layer and support layer is also clear. Therefore, the inner porous structure was kept after pre-oxidation process. Compared with the surface morphology of polymer spheres in Figure 5.11d, the number of surface pores in Figure 5.49c is much less. Up to here, it is plausible that the surface pores of carbon spheres were blocked, which resulted in the loss of surface areas and pore volumes.

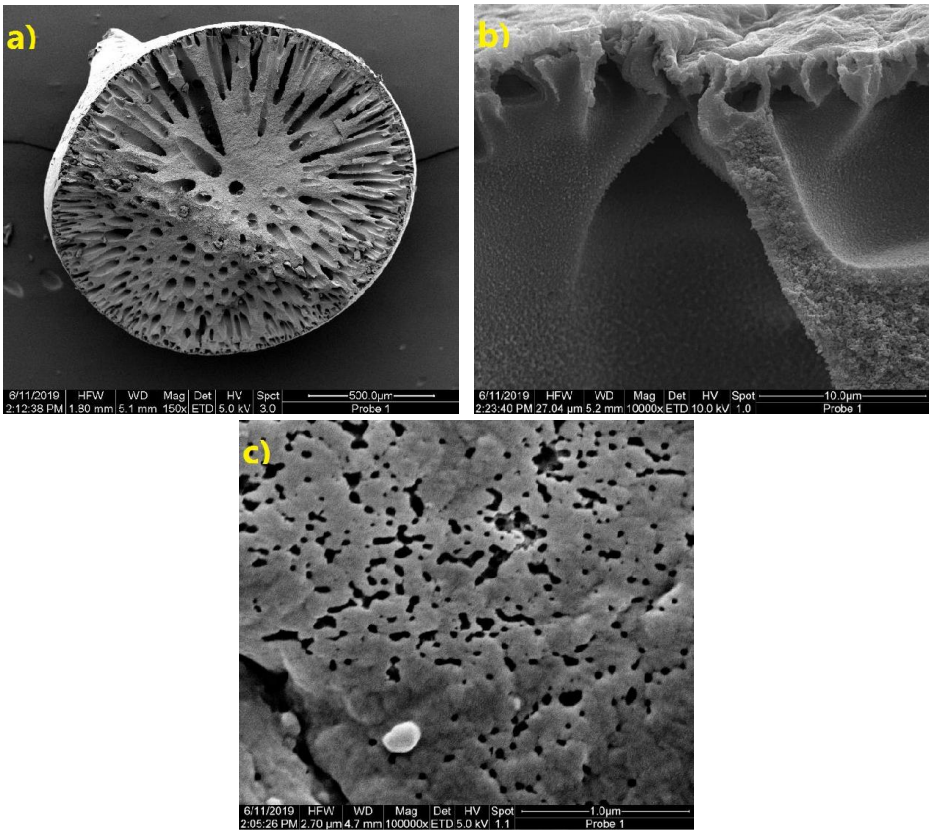

Figure 5.49 Carbon spheres oxidized at 240°C for 1 hour. flow rate of air: static; heating mode: "one-step" heating; a) cross section; b) skin layer; c) surface morphology.

To further confirm this claim, the porosity of carbon spheres needs to be determined. The porosity of carbon spheres after pre-oxidation by uptake of *n*-heptane is shown in Figure 5.50. Before the determination of porosity, the effective solid density of carbon spheres needs to be calculated as shown in Figure 5.50a. During the measurement, *n*-heptane can wet carbon spheres finely and all carbon spheres precipitated to the bottom of pycnometer within short time. The effective solid density of "8%, 65/35" polymer spheres by uptake of *n*-heptane is 0.995 g/cm^3. The effective solid density of all carbon spheres is below 1 g/cm^3.

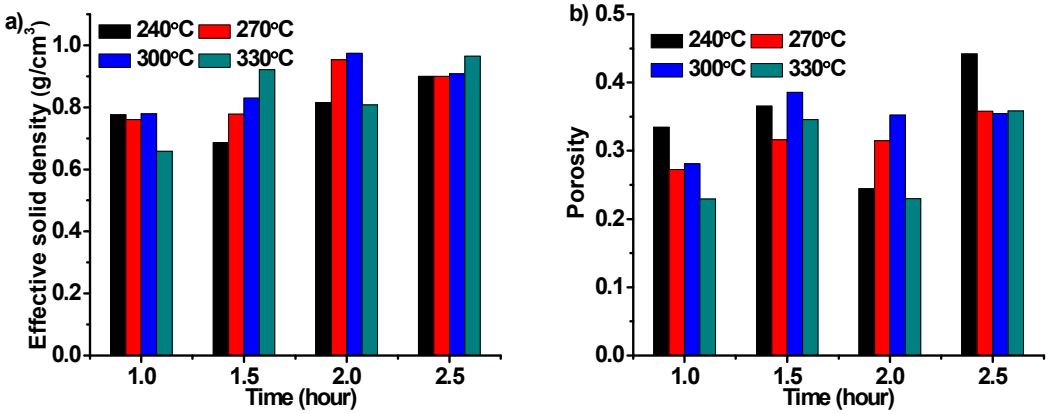

Figure 5.50 The porosity of carbon spheres after pre-oxidation by uptake of *n*-heptane. temperature: 21°C; density of *n*-heptane at 21°C: 0.68217 g/cm^3; a) effective solid density; b) porosity.

The porosity of all carbon spheres is below 50% as shown in Figure 5.50b. By contrast, the porosity of "8%, 65/35" precursor by uptake of *n*-heptane is 87%, and by water, it is 89%. Up to here, it can be concluded that with the most surface pores of carbon spheres blocked, nitrogen molecules can not detect the inner structure of these carbon spheres during nitrogen adsorption. During the pre-oxidation process, small gaseous molecules evolved and yellow tar formed on the inner wall of quartz tube. It can be inferred that the surface pores of carbon spheres were blocked by these substances. Therefore, using flowing air may be helpful to alleviate the sedimentation of these waste substances.
The effect of flow rate of air and heating mode on the specific surface areas and specific pore volumes of carbon spheres after pre-oxidation is shown in Figure 5.51.

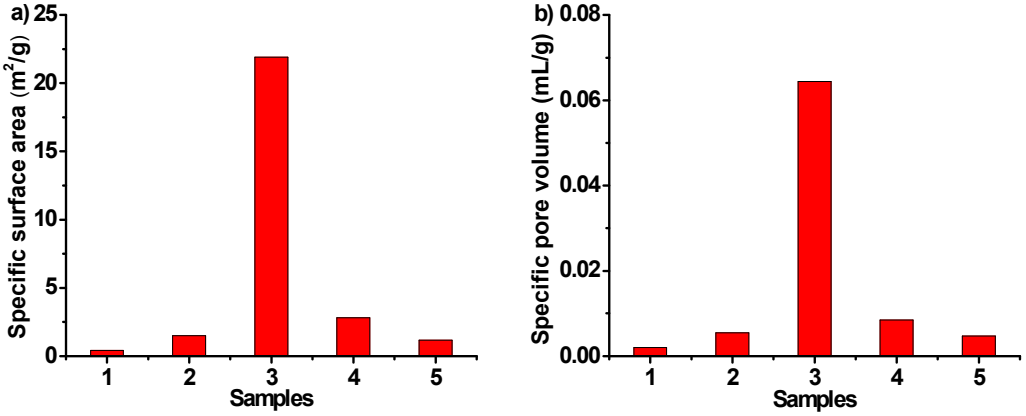

Figure 5.51 The impact of flow rate of air and heating mode. retention time: 2 hours; oxidation temperature: 300°C; atmosphere: air; a) specific surface area; b) specific pore volume; sample 1: static air; "one-step" heating; sample 2: static air; "stepwise" heating (increment: 50°C)； sample 3: air with high flow rate; "one-step" heating; sample 4: flow rate of air: 1 bubble per second; "one-step" heating; sample 5: flow rate of air: 1 bubble per second; "stepwise" heating (increment: 50°C).

With the increasing of flow rate of air (sample 1→4→3), both specific surface areas and specific pore volumes increase. One disadvantage of over-high flow rate is that sample 3 was found to be partially white, which was due to incomplete oxidation. During the oxidation process, although flow air can remove small gaseous molecules and tar from the samples, over-high flow rate can also effectively take away the heat, which is detrimental to the oxidation of samples. The higher the flow rate of gas is, the lower is the actual temperature of quartz tube. With the heating mode changed (sample 1→2 and sample 4→5), the fluctuation of both specific surface areas and specific pore volumes is little.
The IR spectrum of PAN 200 is shown in Figure 5.52. PAN 200 shows strong absorption at the position of 2,250 cm^{-1}, which indicates the existence of –CN group. The second feature of PAN 200 is the existence of even stronger absorption, i.e. bending vibration of -CH_2-, at about 1,450 cm^{-1}. In addition, the absorption at 1,750 cm^{-1} is very low due to the very low content of methyl acrylate (MA) in this polymer, which indicates the existence of C=O group. Absorption peak at nearly 3,000 cm^{-1} indicates a mixture characteristic of asymmetric and symmetric stretching vibration of -CH_2- and stretching vibration of C-H.

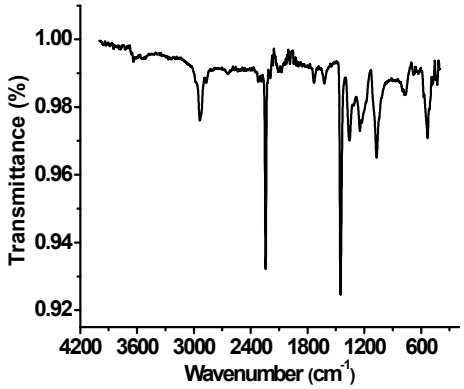

Figure 5.52 IR spectrum of PAN 200.

The IR spectra of some carbon spheres after oxidation are shown in Figure 5.53.

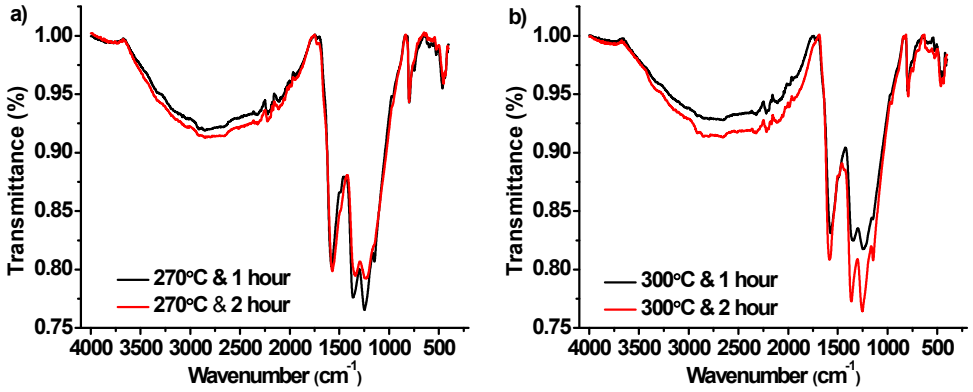

Figure 5.53 IR spectra of carbon spheres after pre-oxidation. a) oxidized at 270°C; b) oxidized at 300°C.

According to the former thermal analysis and some references [77, 80], two representative temperatures of pre-oxidation were selected which are 270°C and 300°C. In the oxidation process of PAN, cyclization reaction is the main reaction to form heat-resistant ladder structure. Although the desired ladder structure of carbon spheres after oxidation can not be fully determined by IR spectroscopy, the disappearance of –CN groups partially indicates the finish of cyclization reaction. As shown in Figure 5.53, the –CN groups at 2,250 cm^{-1} in all samples disappear. Moreover, there is no essential difference between these IR spectra. In terms of time and energy saving, the conditions of pre-oxidation, i.e. "270°C & 1 hour", were selected for the later oxidation operation.

5.4.3 Pyrolysis without activation

Compared with the narrow temperature range of pre-oxidation, the temperature range of pyrolysis is even wider. Some researches [77] proposed low temperature pyrolysis (300-1,000°C) and high temperature pyrolysis (1,100-1,600°C). In addition, the selection of pyrolysis temperature is always according to actual scenarios of application. The higher the pyrolysis temperature is, the lower is the content of non-carbon elements in final carbon product. In terms of energy saving, low pyrolysis temperatures were firstly selected, which are 500°C, 550°C, 600°C, and 650°C. In order to improve the yield of final products, the

retention time of pyrolysis is usually less than that of pre-oxidation [77]. In this section, the longest retention time is 90 min. The ratios of residual mass and mean size of carbon spheres after pyrolysis without activation are shown in Figure 5.54.

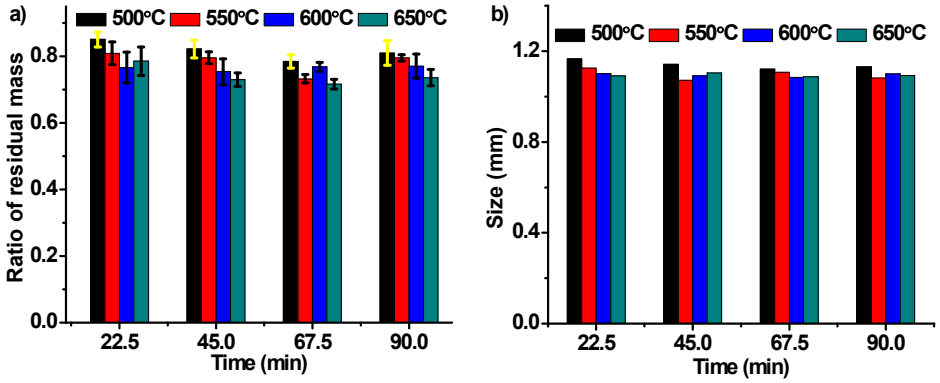

Figure 5.54 Carbon spheres after pyrolysis without activation. a) ratio of residual mass; b) mean size.

As shown in Figure 5.54a, with the increasing of pyrolysis temperature from 500°C to 650°C, the mass loss of carbon spheres "22.5 min" increases. Carbon spheres of "45 min", "67.5 min", and "90 min" also have the same trend. As the retention time increases from 22.5 min to 90 min, the mass loss almost keeps the same within carbon spheres of "500°C". Carbon spheres of "550°C", "600°C", and "650°C" also have the same trend. In conclusion, the effect of pyrolysis temperature on mass loss is larger than that of retention time within the scope of temperature and time presented.

In Figure 5.54b, the mean size of all carbon spheres after pre-oxidation is below 1.2 mm. Compared with the mean size of carbon spheres in Figure 5.46b, the mean size of carbon spheres after pyrolysis changed little. The mean size of all 16 carbon spheres also changed little within the scope of temperature and time presented.

The specific surface areas and specific pore volumes of carbon spheres after pyrolysis are shown in Figure 5.55.

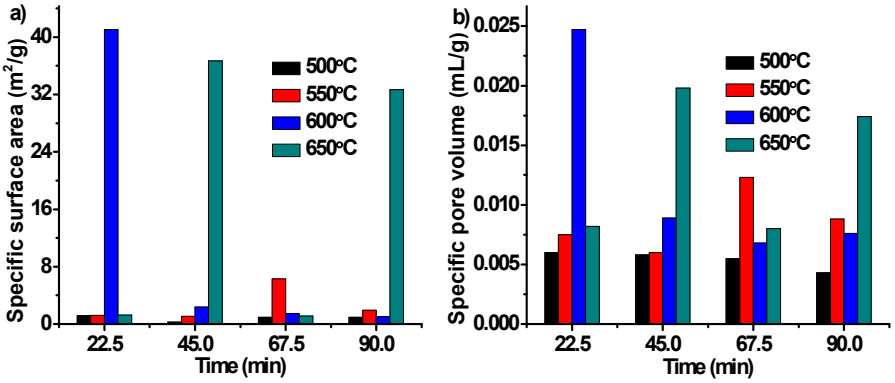

Figure 5.55 Pore characterizations of carbon spheres after pyrolysis without activation. a) specific surface area; b) specific pore volume.

As shown in Figure 5.55a, the specific surface areas of carbon spheres are all below 50 m^2/g.

In addition, the specific pore volumes of carbon spheres are all below 0.025 mL/g. Compared with the specific surface areas and specific pore volumes of carbon spheres after oxidation, the specific surface areas and specific pore volumes of carbon spheres after pyrolysis did not increase much.

In order to exclude the occasionality of results, some more carbon spheres were inspected by nitrogen adsorption and the results are shown in Figure 5.56. The specific surface areas of three carbon samples did not increase much even after three times' repetition. Especially for carbon spheres of "600°C & 22.5 min", the specific surface areas happened in the first test did not repeat itself in the following second, third, and forth test.

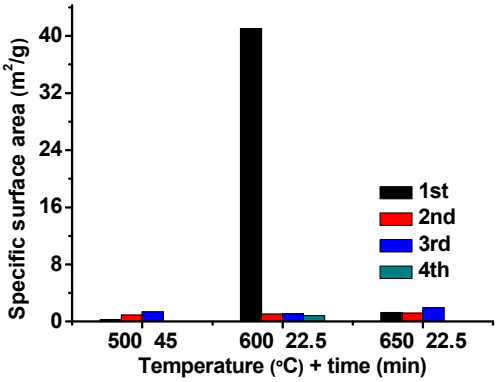

Figure 5.56 Specific surface areas of carbons spheres after pyrolysis without activation from repeated experiments. "500 45" means carbon spheres pyrolyzed at 500°C for 45 min.

Two possible reasons can be proposed to explain the low surface areas. The first reason is that the inner porous structure of carbon spheres after oxidation is destroyed during the pyrolysis process. The second one is that the surface pores of carbon spheres are still blocked after pyrolysis.

The photographs of carbon spheres after pyrolysis captured by SEM are shown in Figure 5.57. As shown in Figure 5.57a, the inner porous structure collapsed and shrank to some extent, compared with the inner structure of carbon spheres shown in Figure 5.49a. In Figure 5.57b, the boundary between skin layer and support layer is still clear; however, the skin layer seems denser. In summary, the inner porous structure was destroyed to some extent after pyrolysis. Compared with the surface morphology of carbon spheres in Figure 5.49c, the number of surface pores in Figure 5.57c is much less. Although the inner porous structure was destroyed after pyrolysis, it is still plausible that the loss of surface areas and pore volumes are mainly due to the blockage of surface pores. To confirm this claim, the porosity of carbon spheres after pyrolysis needs to be determined.

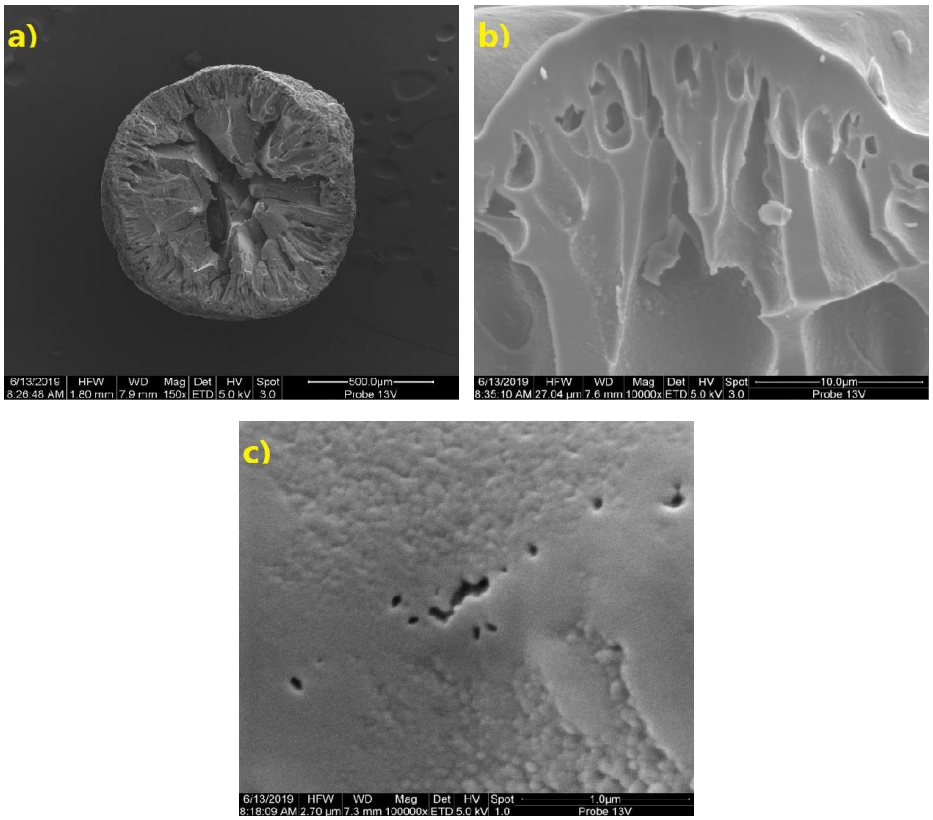

Figure 5.57 Carbon spheres pyrolyzed at 600°C for 23 min. flow rate of nitrogen: 1 bubble per second; heating mode: "step-wise" heating; a) cross section; b) skin layer; c) surface morphology.

The porosity of carbon spheres after pyrolysis by uptake of *n*-heptane is shown in Figure 5.58. Before the determination of porosity, the effective solid density of carbon spheres needs to be calculated as shown in Figure 5.58a. During the measurement, *n*-heptane can wet carbon spheres finely and all carbon spheres precipitated to the bottom of pycnometer within short time. The effective solid density of some carbon spheres is over 1 g/cm^3 while the effective solid density of rest carbon spheres is below 1 g/cm^3. The porosity of all carbon spheres after pyrolysis is still below 50% as shown in Figure 5.58b.

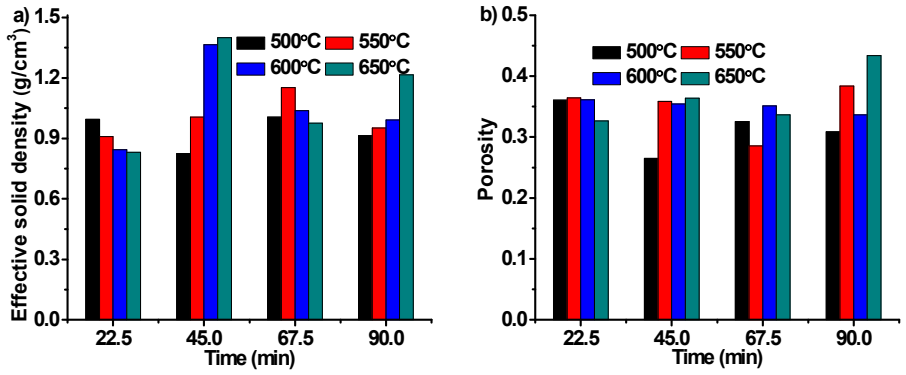

Figure 5.58 The porosity of carbon spheres after pyrolysis without activation by uptake of *n*-heptane. temperature: 21°C; density of *n*-heptane at 21°C: 0.68217 g/cm^3; a) effective solid density; b) porosity.

Up to here, it can be concluded that with the most surface pores of carbon spheres blocked, nitrogen molecules can not detect the inner structure of these carbon spheres during nitrogen adsorption. During the pyrolysis process, small gaseous molecules further evolved and yellow tar further formed on the inner wall of quartz tube. Denser skin layer of carbon spheres indicates the further blockage of surface pores. It can be inferred that the surface pores of carbon spheres were further blocked by these substances. Since the destroyed inner porous structure can not be totally restored, it is necessary to reopen the surface pores of carbon spheres after pyrolysis before pragmatic application.

5.4.4 Pyrolysis with activation

Several methods can be used to reopen the surface pores of carbon spheres in pyrolysis process, which are the increasing flow rate of nitrogen, increasing pyrolysis temperature, increasing retention time, and activation. The effect of two former factors is shown in Figure 5.59.

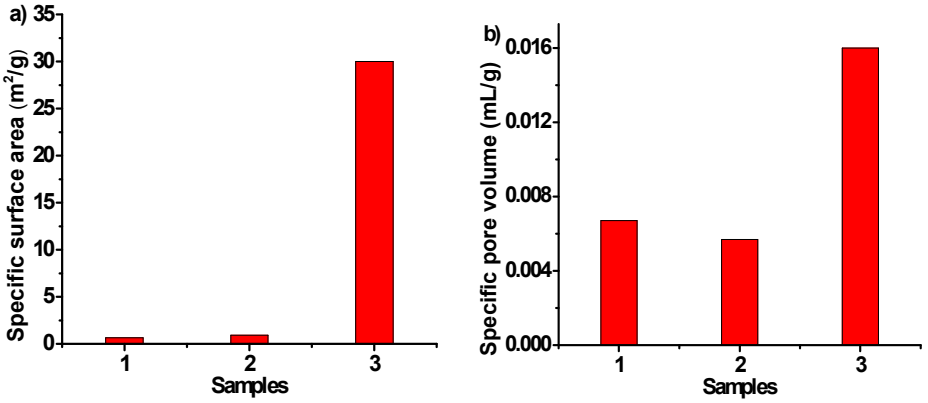

Figure 5.59 The impact of flow rate of nitrogen and pyrolysis temperature. sample 1: 600°C; 1 hour; flow rate of nitrogen: 1 bubble per second; sample 2: 600°C; 1 hour; flow rate of nitrogen: high; sample 3: 1,000°C; 1 hour; flow rate of nitrogen: 5 bubbles per second; a) specific surface area; b) specific pore volume.

As discussed in section 5.4.3, increasing the retention time from 22.5 min to 90 min did not increase the specific surface areas and specific pore volumes of carbon spheres. It can be inferred that the effect of further increasing retention time on reopening surface pores is little. As shown in Figure 5.59a, with the increasing of flow rate of nitrogen from low to high, the specific surface areas of sample 2 does not improve much. With the pyrolysis temperature increasing from 600°C to 1,000°C, both surface areas and pore volumes are improved. Nevertheless, the result of such high temperature is unsatisfactory. The last and hopeful method is activation.

In this work, carbon dioxide (CO_2) was selected as the gaseous activator. In addition, pyrolysis and activation were done at the same time for simplicity. According to literature [81], the activation method is adding the stream of carbon dioxide into that of nitrogen. The effect of activation by CO_2 on carbon spheres is shown in Figure 5.60.

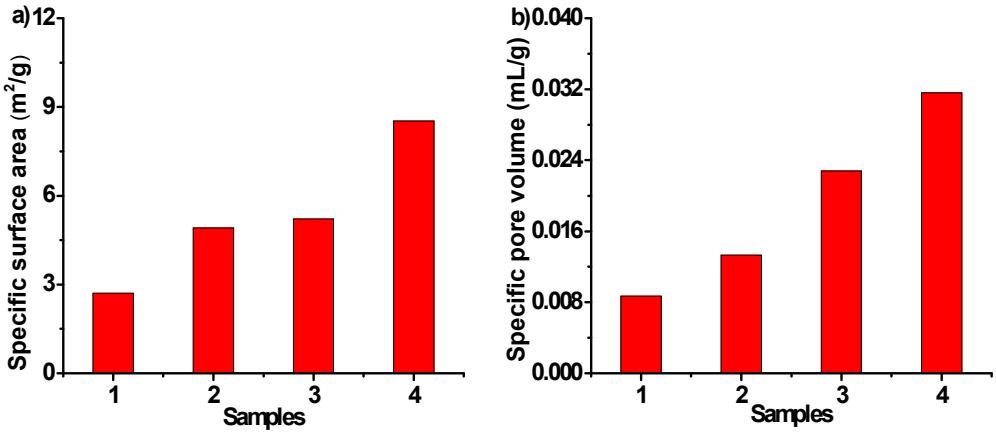

Figure 5.60 The impact of CO_2 activation on pore structures. flow rate of N_2+CO_2: (1+1) bubbles per second; sample 1: 600°C; 1 hour; sample 2: 600°C; 2 hours; sample 3: 800°C; 1 hour; sample 4: 800°C; 2 hours; a) specific surface area; b) specific pore volume.

With the help of CO_2, both increasing pyrolysis temperature (sample 1→3 and sample 2→4) and increasing retention time (sample 1→2 and sample 3→4) can increase the specific surface areas and specific pore volumes of carbon spheres. The functions of nitrogen stream in the pyrolysis process are inflaming retarding, blowing away volatile wastes, and diluting activation gas. Since only CO_2 can achieve these functions, CO_2 was used as the only atmosphere in latter activation experiments.

Although adding CO_2 into the pyrolysis process is effective on reopening surface pores, the match between flow rate of CO_2 and pyrolysis temperature is still a problem to improve the effect of activation. These results are shown in Figure 5.61.

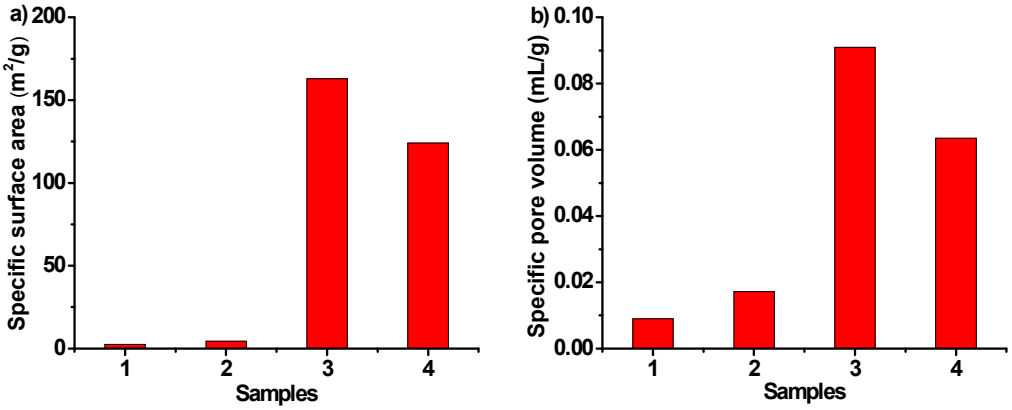

Figure 5.61 The match between flow rate of CO_2 and pyrolysis temperature. sample 1: 600°C; 1 hour; flow rate of CO_2: 1 bubble per second; sample 2: 600°C; 1 hour; flow rate of CO_2: high; sample 3: 800°C; 1 hour; flow rate of CO_2: 5 bubbles per second; sample 4: 800°C; 2 hours; flow rate of CO_2: moderate rate larger than 5 bubbles per second; a) specific surface area; b) specific pore volume.

At 600°C, with the increasing of flow rate of CO_2 (sample 1→2), both specific surface areas and specific pore volumes of carbon spheres almost keep the same. Compared with the specific surface areas of sample 1, the specific surface areas of sample 3 increase much. It

can be inferred that there is no obvious effect of activation with pyrolysis temperature below 800°C.
Compared with the specific surface areas of sample 3 and 4 in Figure 5.61, the sum flow rate of N_2 and CO_2 of sample 3 and 4 in Figure 5.60 was not enough. In Figure 5.61a, although the retention time of sample 4 was twice as long as that of sample 3, the specific surface areas of sample 4 is lower than that of sample 3. This is due to the over-high flow rate of CO_2 when preparing sample 4. In addition, too fast flow rate of CO_2 is also a waste. It can be inferred that even though the pyrolysis temperature is enough, good effect of activation can not be acquired with over-low or over-high flow rate of CO_2.
Finally, the activation conditions for carbon spheres were determined. The flow rate of CO_2 was set at 5 bubbles per second and the pyrolysis temperature was at least 800°C. Based on these conditions, the results of further increasing pyrolysis temperature are shown in Figure 5.62.

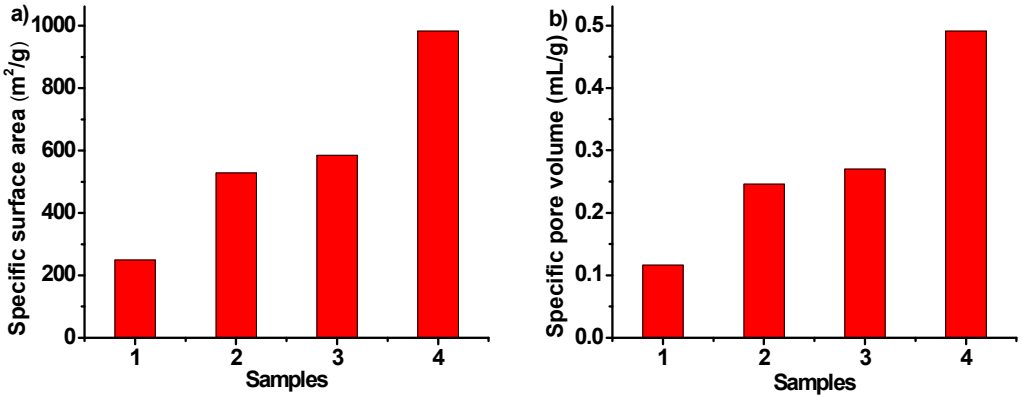

Figure 5.62 Verification of the flow rate of CO_2. atmosphere: flow rate of CO_2: 5 bubbles per second; sample 1: 900°C; 1 hour; sample 2: 900°C; 2 hours; sample 3: 1,000°C; 30 min; sample 4: 1,000°C; 1 hour; a) specific surface area; b) specific pore volume.

As shown in Figure 5.62a, with the increasing of retention time (sample 1→2 and 3→4), the specific surface areas of carbon spheres increase. Increasing the pyrolysis temperature also has the same effect (sample 1→4). Up to here, the specific surface areas of carbon spheres prepared in this work are close to that of commercial activated carbon (e.g. 1,000 m^2/g) [6].
Until here, the polymer precursors of all carbon spheres are polymer spheres of "8%, 65/35". As an alternative, polymer spheres of "8%, 0/100" were also used. There are two reasons. The first one is that polymer spheres of "8%, 0/100" gelled in pure water without using DMF. Secondly, the blockage of surface pores of carbon spheres after pre-oxidation process can not be avoided; therefore, the selection of polymer precursors is relatively free. The results of activation of carbon spheres derived from "8%, 0/100" precursors are shown in Figure 5.63. Although the precursors of carbon sphere were changed, large specific surface areas and specific pore volumes of carbon spheres after pyrolysis and activation were still acquired.

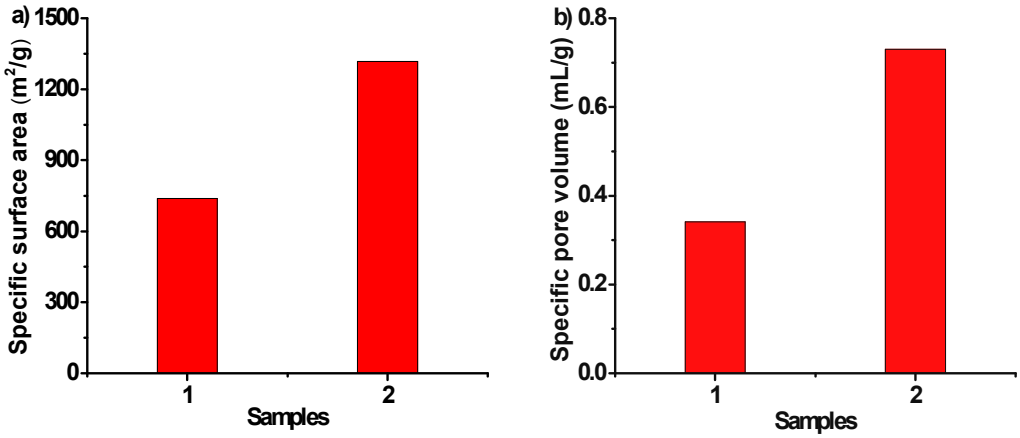

Figure 5.63 Pore characterizations of carbon spheres after pyrolysis with activation. flow rate of CO_2: 5 bubbles per second; sample 1: 1,000°C; 30 min; sample 2: 1,000°C; 1 hour; a) specific surface area; b) specific pore volume.

The photographs of two carbon spheres mentioned in Figure 5.63 are shown in Figure 5.64. These two kinds of carbon spheres are named "1,000°C, 30 min" and "1,000°C, 1 hour", respectively. They have similar appearance and diameter (about 1 mm). For carbon spheres of "1,000°C, 30 min", the yield after the pyrolysis process is 37.6%. For carbon spheres of "1,000°C, 1 hour", the yield is 24.8%.

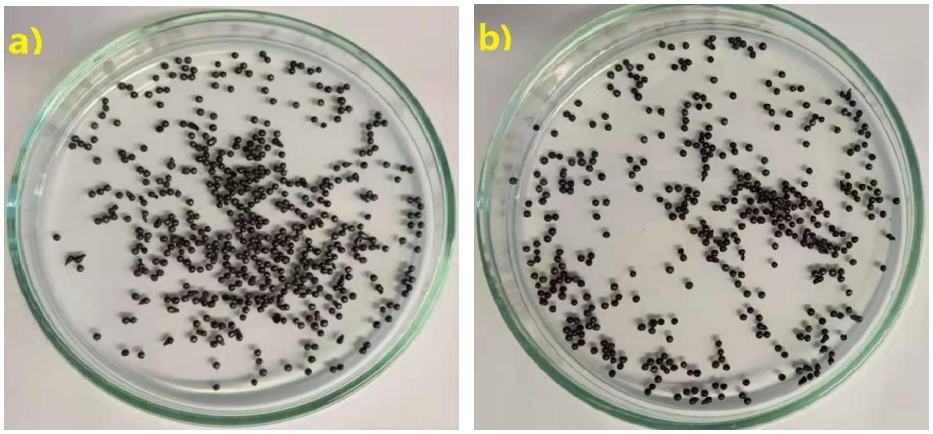

Figure 5.64 Photographs of carbon sphere after pyrolysis with activation. flow rate of CO_2: 5 bubbles per second; a) "1,000°C; 30 min"; b) "1,000°C; 1 hour".

The photographs of carbon spheres "1,000°C, 30 min" and "1,000°C, 1 hour" captured by SEM are shown in Figure 5.65 and 5.66, respectively. After activation, macropores are almost not found in Figure 5.65a and b. In Figure 5.65c and d, however, large numbers of mesopores can still be observed. Limited by the resolution of photographs, micropores (less than 2 nm) can not be spotted in Figure 5.65d.

After activation, some macropores can be found in Figure 5.66a and b. In Figure 5.66c and d, the number of mesopores is little. Limited by the resolution of photographs, micropores (less than 2 nm) can not be spotted in Figure 5.66d.

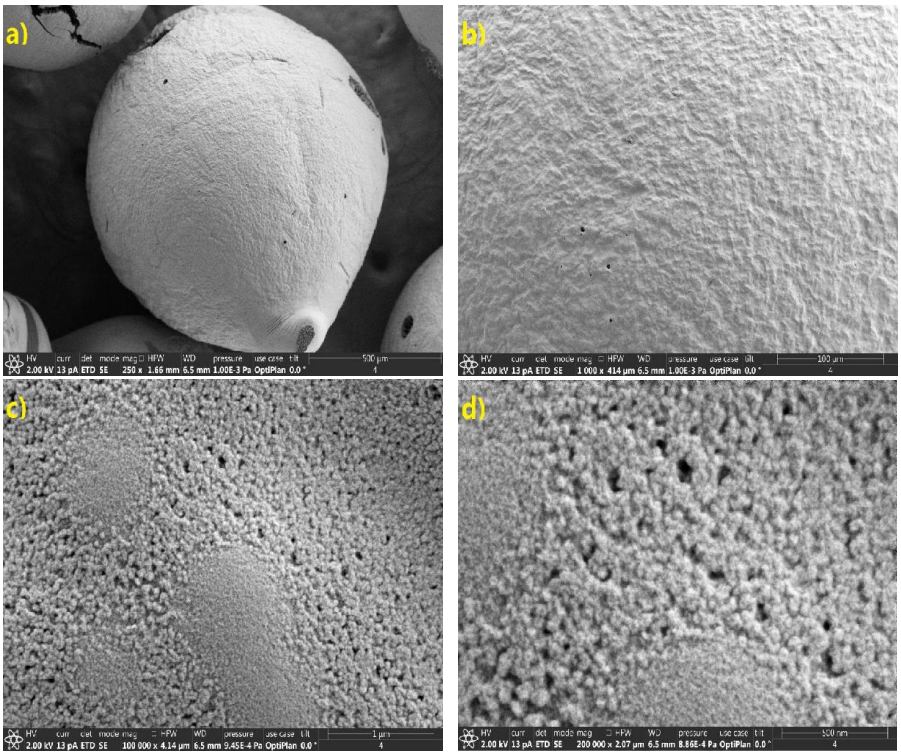

Figure 5.65 SEM photographs of "1,000°C, 30 min" spheres after pyrolysis with activation. conditions of pyrolysis: 1,000°C; 30 min; flow rate of CO_2: 5 bubbles per second; scales: a) 500 µm; b) 100 µm; c) 1 µm; d) 500 nm.

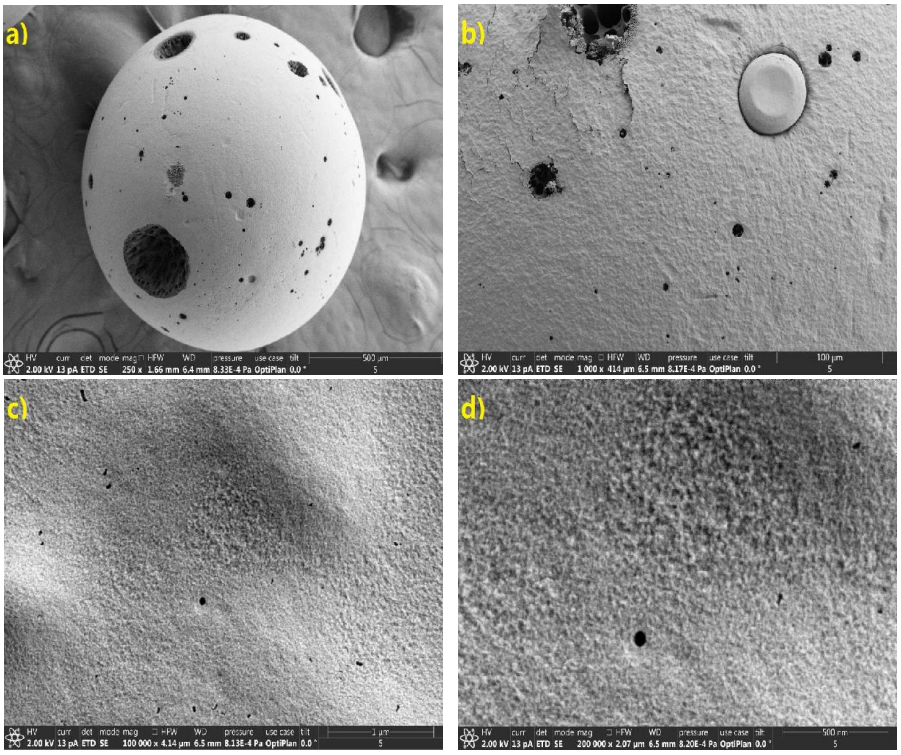

Figure 5.66 SEM photographs of "1,000°C, 1 hour" spheres after pyrolysis with activation. conditions of pyrolysis: 1,000°C; 1 hour; flow rate of CO_2: 5 bubbles per second; scales: a) 500 µm; b) 100 µm; c) 1 µm; d) 500 nm.

Undoubtedly, large surface pores of polymer spheres are easy to be spotted as shown in Figure 5.11d. After pre-oxidation as well as pyrolysis without activation, large surface pores can still be observed as shown in Figure 5.49c and 5.57c though their number decreases. After pyrolysis with activation, large surface pores are seldom spotted, which are supposed to be replaced by smaller micropores as shown in Figure 5.65 and 5.66.

5.4.5 Elemental and structural characterizations of carbon samples

Three carbon samples were used in the ORR tests (section 5.8), which are "900°C, 30 min", "1,000°C, 30 min", and "1,000°C, 1 hour". The mass fractions of various elements in these carbon spheres by combustion analyzer are shown in Table 5.5. As shown in Table 5.5, with the increasing of retention time or pyrolysis temperature in carbonization, the content of carbon increases while the contents of non-carbon elements decrease. This phenomenon is normal in general carbonization process featured by the elimination of non-carbon elements and the increasing of carbon content.

Table 5.5 Mass fractions of various elements in carbon samples by combustion analyzer.

Carbon samples	Carbon (%)	Hydrogen (%)	Nitrogen (%)	Oxygen (%)
"900°C, 30 min"	72.2	1.775	10.8	6.775
"1,000°C, 30 min"	81.6	0.451	6.66	4.81
"1,000°C, 1 hour"	86.4	0.39	5.28	2.205

Fractions of amount of substance for various elements in carbon samples are shown in Table 5.6. As shown in Table 5.6, with the increasing of retention time or pyrolysis temperature in carbonization, the content of carbon increases while the contents of non-carbon elements decrease.

Table 5.6 Fractions of amount of substance for elements in carbon samples by XPS analysis.

Carbon samples	Carbon (%)	Oxygen (%)	Nitrogen (%)
"900°C, 30 min"	87.5	5.1	7.4
"1,000°C, 30 min"	90.6	4.9	4.5
"1,000°C, 1 hour"	92.9	4.1	3.0

For the elemental characterization by XPS, the scanning of all elements in samples is not shown here. The high-resolution spectra of elements in "900°C, 30 min" carbon spheres are shown in Figure 5.67. The photoelectron lines of carbon, oxygen, and nitrogen are C 1s, O 1s, and N 1s, respectively.

The high-solution spectrum of C 1s is shown in Figure 5.67a. The various species containing carbon element (i.e. various valences of carbon element) are also fitted. The content of C-C is the highest among all species. The existence of C-O/C-N, C=O, and COOH also confirms the oxidative features of this sample.

The high-solution spectrum of O 1s is shown in Figure 5.67b. The various species containing oxygen element are also fitted. The content of C-O is the higher than that of -OH.

The high-solution spectrum of N 1s is shown in Figure 5.67c. The various species containing nitrogen element are also fitted. Only two species of nitrogen are found, which are quaternary

N (i.e. N-Q, 400.8 eV) and pyridinic N (i.e. N-6, 398.2 eV). The binding energies of these nitrogen species are close to the values of some reported researches [43, 46].
The intensity of O 1s and N 1s is much lower than that of C 1s, which means the contents of oxygen and nitrogen in "900°C, 30 min" spheres are lower than that of carbon.

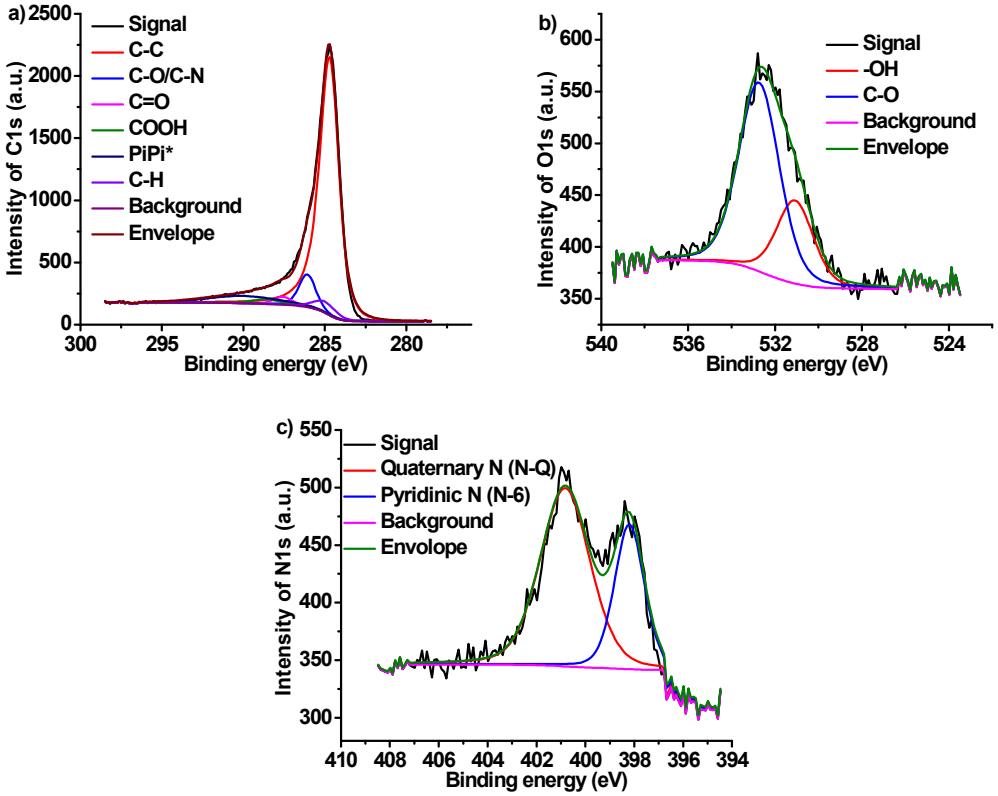

Figure 5.67 High-resolution XPS spectra of "900°C, 30 min" spheres. a) C 1s; b) O 1s; c) N 1s.

The high-resolution spectra of elements in "1,000°C, 30 min" carbon spheres are shown in Figure 5.68. The photoelectron lines of carbon, oxygen, and nitrogen are C 1s, O 1s, and N 1s, respectively.
The high-solution spectrum of C 1s is shown in Figure 5.68a. The various species containing carbon element are also fitted. The content of C-C is the highest among all species. The existence of C-O/C-N, C=O, and COOH also confirms the oxidative features of this sample.
The high-solution spectrum of O 1s is shown in Figure 5.68b. The various species containing oxygen element are also fitted. The content of C-O is the higher than that of -OH.
The high-solution spectrum of N 1s is shown in Figure 5.68c. The various species containing nitrogen element are also fitted. Only two species of nitrogen are found, which are quaternary N (i.e. N-Q, 401.0 eV) and pyridinic N (i.e. N-6, 398.4 eV). The binding energies of these nitrogen species are close to the values of some reported researches [43, 46].
The intensity of O 1s and N 1s is much lower than that of C 1s, which means the contents of oxygen and nitrogen in "1,000°C, 30 min" carbon spheres are lower than that of carbon.

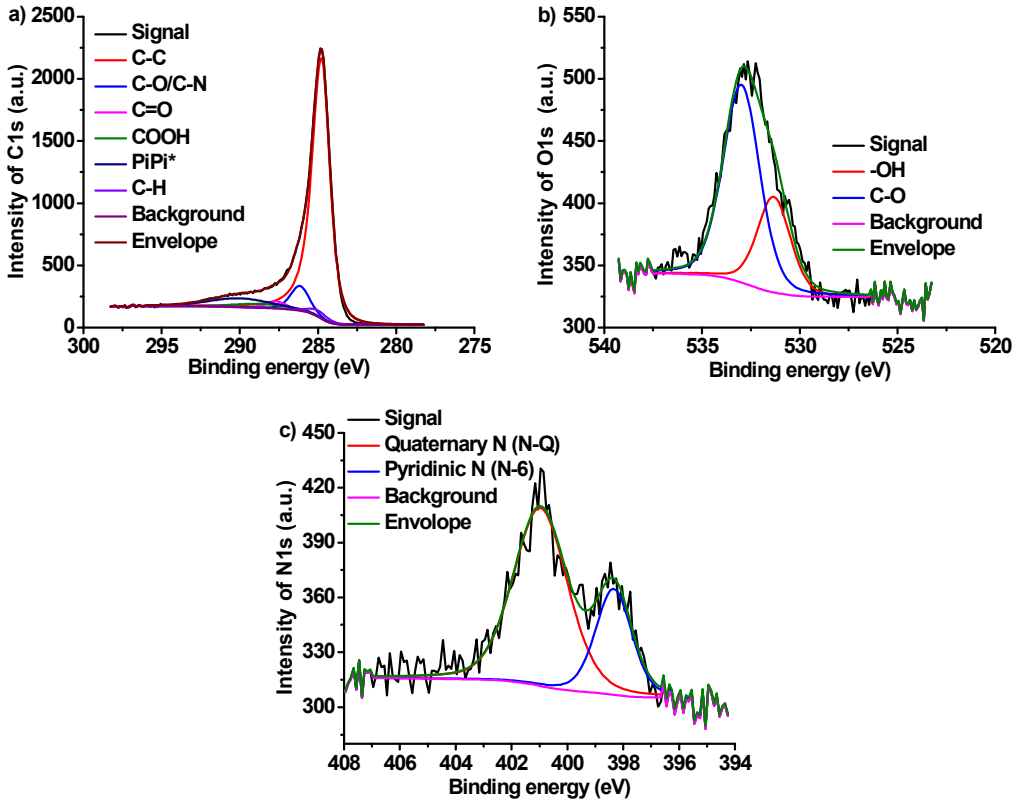

Figure 5.68 High-resolution XPS spectra of "1,000°C, 30 min" spheres. a) C 1s; b) O 1s; c) N 1s.

The high-resolution spectra of some elements in "1,000°C, 1 hour" carbon spheres are shown in Figure 5.69. The photoelectron lines of carbon, oxygen, and nitrogen are C 1s, O 1s, and N 1s, respectively.

The high-solution spectrum of C 1s is shown in Figure 5.69a. The various species containing carbon element are also fitted. The content of C-C is the highest among all species. The existence of C-O/C-N, C=O, and COOH also confirms the oxidative features of this sample.

The high-solution spectrum of O 1s is shown in Figure 5.69b. The various species containing oxygen element are also fitted. The content of C-O is the higher than that of -OH.

The high-solution spectrum of N 1s is shown in Figure 5.69c. The various species containing nitrogen element are also fitted. Only two species of nitrogen are found, which are quaternary N (i.e. N-Q, 400.9 eV) and pyridinic N (i.e. N-6, 398.3 eV). The binding energies of these nitrogen species are close to the values of some reported researches [43, 46].

The intensity of O 1s and N 1s is much lower than that of C 1s, which means the contents of oxygen and nitrogen in "1,000°C, 1 hour" carbon spheres are lower than that of carbon.

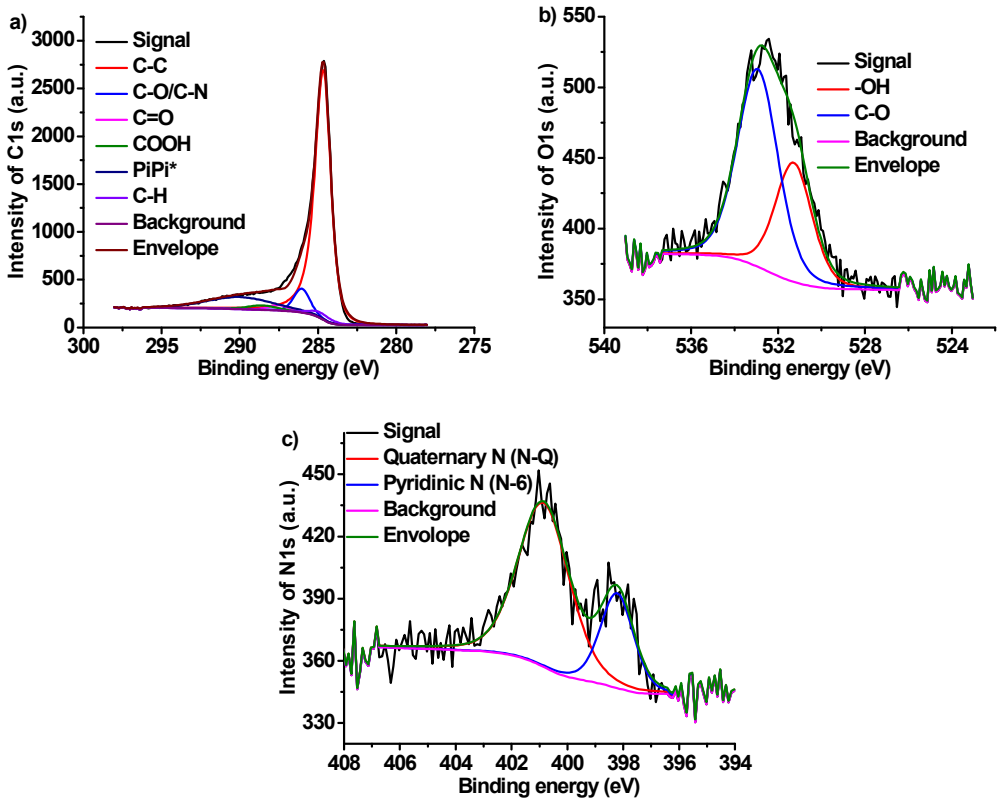

Figure 5.69 High-resolution XPS spectra of "1,000°C, 1 hour" spheres. a) C 1s; b) O 1s; c) N 1s.

According to already published researches, the active sites for ORR in N-doped carbon can be attributed to quaternary N [47] or pyridinic N [48]. The relative contents (i.e. fractions of amount of substance) of quaternary N (N-Q) and pyridinic N (N-6) in carbon samples are shown in Table 5.7. With the increasing of retention time or pyrolysis temperature in carbonization, the content of quaternary N increases while the content of pyridinic N decreases.

Table 5.7 Relative content of nitrogen species in various carbon samples by XPS analysis.

Nitrogen species	"900°C, 30 min"	"1,000°C, 30 min"	"1,000°C, 1 hour"
N-Q (%)	67.3	71.4	72.6
N-6 (%)	32.7	28.6	27.4

The XRD spectra of carbon spheres "900°C, 30 min", "1,000°C, 30 min" and "1,000°C, 1 hour" are shown in Figure 5.70. Figure 5.70c shows the XRD spectrum of single crystalline graphite [82]. The diffraction signals at 26.7°, 42.4°, and 44.6° are assigned to the (002) face, (100) face, and (101) face, respectively. As shown in Figure 5.70b, the diffraction signal at about 25° is assigned to the (002) face while the signals between 40° and 45° could be assigned to the (100) face and (101) face. Since the diffraction intensity of these signals is low, it can be inferred that the degree of graphitization and crystallinity of these carbon spheres are low. In conclusion, these three carbon materials show characters of amorphous carbon.

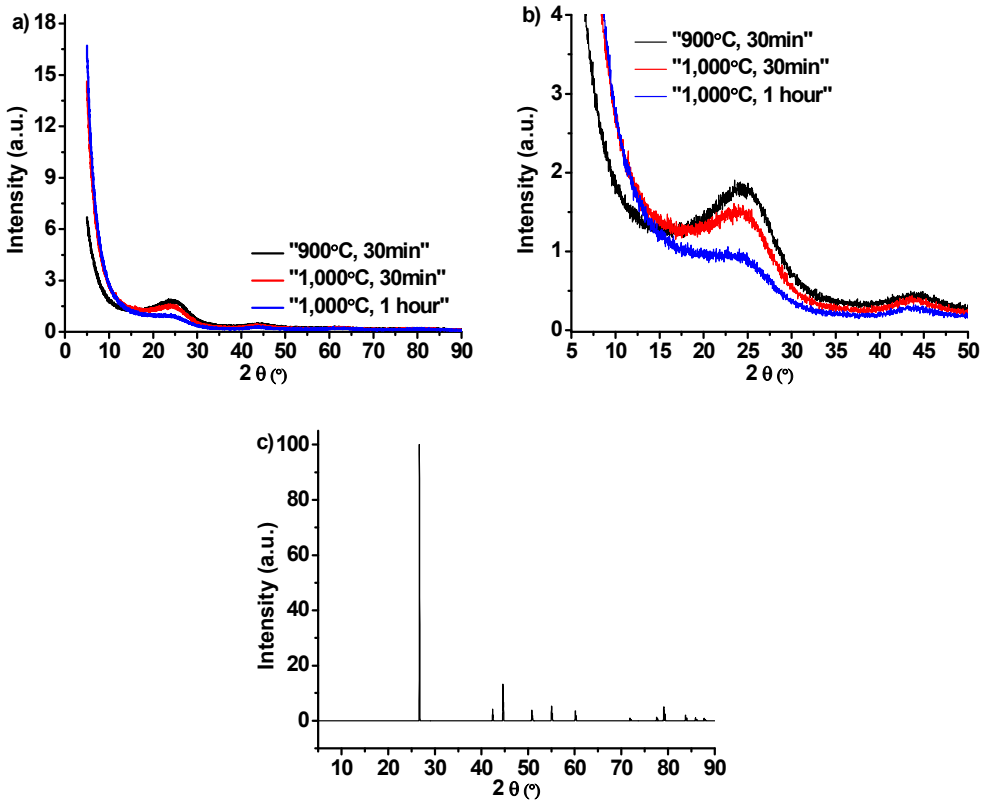

Figure 5.70 XRD spectra of carbon spheres. a) XRD spectra of carbon spheres; b) zoom in between 5° and 50° of 5.70a; c) XRD spectrum of single crystalline graphite [82].

The Raman spectra of carbon spheres "900°C, 30 min", "1,000°C, 30 min" and "1,000°C, 1 hour" are shown in Figure 5.71.

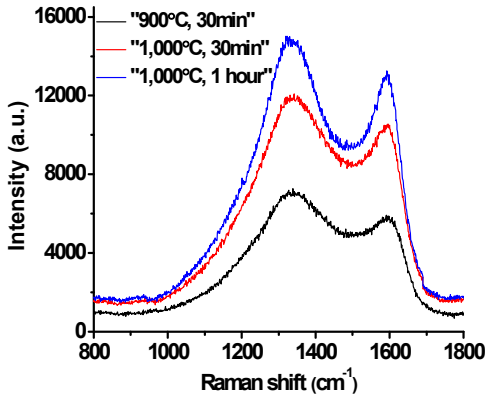

Figure 5.71 Raman spectra of carbon spheres. exciting wavelength: 633 nm.

These three carbon materials show two signals around 1,341 and 1,596 cm^{-1} [83], respectively. One signal at 1,596 cm^{-1} (i.e. G-band) represents the graphitic sheets of carbon materials. The other one is at 1,341 cm^{-1}, which is the D-band and indicates the presence of defects. The intensity ratio of D- and G-band ($I_{D\text{-}band}/I_{G\text{-}band}$) indicates the degree of graphitization. The intensity ratios of D- and G-band in "900°C, 30 min", "1,000°C, 30 min" and "1,000°C, 1 hour" spheres are 1.18, 1.13, and 1.14, respectively. High intensity ratio of

D- and G-band means these carbon materials are amorphous, which is accordance with the results of XRD measurement. Compared with the Raman spectrum of graphite crystals (G-band: 1,575 cm^{-1}) [84], the wavenumber of G-band shifts to higher wavenumber, which indicates some structural deficits of these carbon materials.

5.5 Preparation and characterization of nanocomposites

5.5.1 Preparation of polymer and carbon nanocomposites

Five TiO_2 nanoparticles were used in this work and all of them are mainly made of anatase phase. The detailed information is shown in Table 5.8. P90 (416), P25, P90 (315), and T805 are prepared by AEROSIL® process from Evonik company. Modified from P25, T805 has an organosilicone shell offering the possibility of dispersion in organic solvents.

Table 5.8 Information of TiO_2 nanoparticles used.

Type of TiO_2	Size (nm)	Specific surface area (m^2/g)	Content of anatase (%)
P90 (416)	10-15	70-100	≥90 [28]
P90 (315)	10-15	70-100	≥90 [28]
P25	20-25	35-65	≥90 [28]
T805	25-30	35-55	≥90
Anatase	≤ 25	45-55	99.7

The photocatalytic activity of various TiO_2 nanoparticles is shown in Figure 5.72. For comparison, a controlled trial was also done without adding any photocatalyst. Since TiO_2 T805 can not be dispersed in aqueous solution, its photocatalytic results are not shown here. The photocatalytic rates of various nanoparticles can be read qualitatively from Figure 5.72. Photocatalyst of P90 (416) shows the highest photocatalytic rate according to the slope of regressive line.

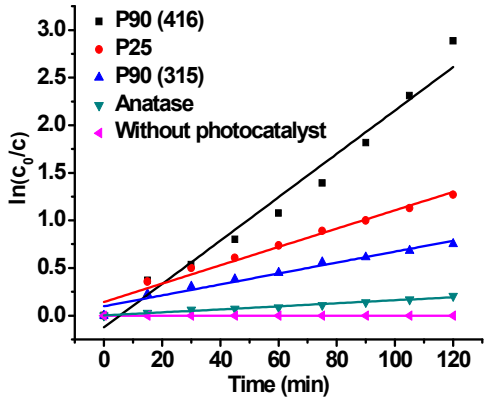

Figure 5.72 Photocatalytic activities of various TiO_2 nanoparticles. dosage: 10 mg.

The regressive results of photocatalytic rates are shown in Table 5.9. Photocatalyst of P90 (416) has the highest photocatalytic rate among all photocatalysts, which is accordance with the qualitative analysis. Anatase TiO_2 shows the lowest photocatalytic rate among all photocatalysts.

Table 5.9 Photocatalytic rates of various nanoparticles of TiO_2.

Rate of photocatalysis	No photocatalyst	P90 (416)	P90 (315)	P25	Anatase
k (min^{-1})	0	0.0228	0.00574	0.00964	0.0016

Since all photocatalysts were put into the dye solution directly without ultrasonic treatment, the aggregation of nanoparticles is assumed to have some influence on the photocatalytic rates. Although all photocatalysts are mainly made of anatase phase, there is still some rutile phase in P90 (416), P25, and P90 (315). The wavelength of UV light is 365 nm (i.e. 3.4 eV), which can excite the electrons of valence band of both anatase phase (band gap: 3.2 eV) and rutile phase (band gap: 3.0 eV). For the photocatalysis of rhodamine B, however, there is no evidence to demonstrate that anatase phase is superior to rutile phase [30, 31].

The dispersion results of various TiO_2 nanoparticles in DMF are shown in Figure 5.73. P90 (416), P25, and P90 (315) can be dispersed in DMF while T805 can not be wetted and dispersed in DMF. For pure anatase, some of them were still not dispersed after ultrasonic treatment. Empirically, mean intensity diameter (MI) and mean volume diameter (MV) are significantly influenced by larger particles, which will lead to a larger dispersion size. The dispersion size (by mean number diameter) of P25 nanoparticles is larger than those of P90 (416) and P90 (315).

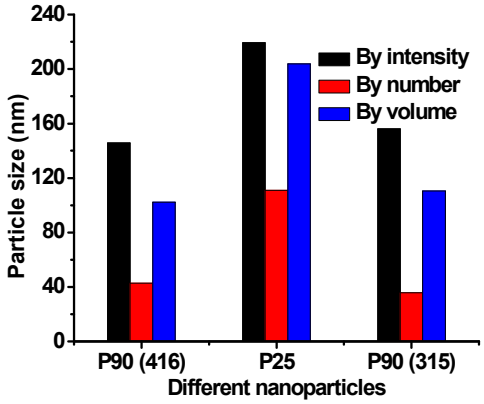

Figure 5.73 Dispersion results of various nanoparticles of TiO_2 in DMF. mass fraction of nanoparticles: 1.3%.

According to the photocatalytic performance and dispersion results of nanoparticles, P90 (416) was chosen to prepare nanocomposites and named as P90.

The dispersion results of various mass fractions of P90 in DMF are show in Figure 5.74. With the increasing of mass fractions of P90 from 0.5% to 1%, the dispersion diameter of P90 also increases. The mean number diameter of three samples is about 60 nm.

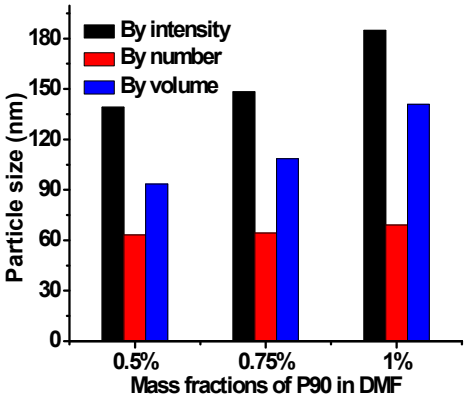

Figure 5.74 Dispersion results of P90 in DMF.

The pore characterizations of both polymer and carbon nanocomposites are shown in Figure 5.75. For comparison, samples of "5% PAN spheres" and "5% carbon spheres" are also added.

When P90 were introduced into PAN and carbon spheres, the specific surface areas of both polymer and carbon nanocomposites increase compared with pure polymer and carbon spheres as shown in Figure 5.75a. From pure polymer and carbon spheres to polymer and carbon nanocomposites, the change of specific pore volumes also have the same trend, except for the case of 20% Carbon+P90.

With the nominal content of P90 increasing from 10% to 20%, the specific surface areas of polymer-based nanocomposites almost keep the same, i.e. 200 m^2/g. For carbon-based nanocomposites, however, their specific surface areas decrease from 650 m^2/g to 400 m^2/g.

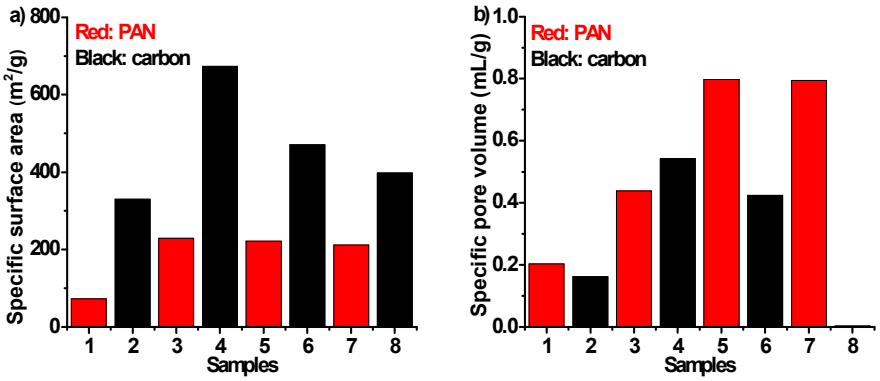

Figure 5.75 Pore characterizations of nanocomposites. sample 1: 5% PAN spheres; sample 2: 5% carbon spheres; sample 3: 10% PAN+P90; sample 4: 10% Carbon+P90; sample 5: 15% PAN+P90; sample 6: 15% Carbon+P90; sample 7: 20% PAN+P90; sample 8: 20% Carbon+P90; a) specific surface area; b) specific pore volume.

5.5.2 Elemental analysis of polymer and carbon nanocomposites

Two nanocomposites, i.e. 10% PAN+P90 and 10% Carbon+P90, were selected for related characterization.

As 10% PAN+P90 is composited by mechanical blending of polyacrylonitrile (i.e. PAN 200) and P90, its elemental analysis is not shown here. The mass fractions of elements in 10%

Carbon+P90 by combustion analyzer are shown in Table 5.10.

Table 5.10 Mass fractions of elements in 10% Carbon+P90 by combustion analyzer. N/A: not applicable.

Nanocomposites	Carbon (%)	Hydrogen (%)	Nitrogen (%)	Oxygen (%)
10% Carbon+P90	50.6	0.227	4.81	N/A

Since the equipment can not distinguish organic oxygen and inorganic oxygen, the content of oxygen can not be shown here. In addition, this equipment can not analyze titanium so the content of titanium is also not shown here. Due to the adding of nanoparticles, the carbon content in 10% Carbon+P90 is low.
Fractions of amount of substance for elements in 10% Carbon+P90 by XPS analysis are shown in Table 5.11.

Table 5.11 Fractions of amount of substance for elements in 10% Carbon+P90 by XPS analysis.

Nanocomposites	Carbon (%)	Titanium (%)	Nitrogen (%)	Oxygen (%)
10% Carbon+P90	81.2	3.3	4.3	11.2

The surface morphology of 10% PAN+P90 and 10% Carbon+P90 by SEM inspection is shown in Figure 5.76. There are many macropores on the surface of 10% PAN+P90 as shown in Figure 5.76a. This feature is accordance with that of PAN 200 spheres. Moreover, nanoparticles disperse on the surface of this nanocomposite. After carbonization process, the surface macropores disappear as shown in Figure 5.76b. The increasing of specific surface areas of 10% Carbon+P90 is due to the increasing number of micropores and capillary pores. At the same time, the nanoparticles on the surface also disappear, which may be entrapped in the carbon matrix.

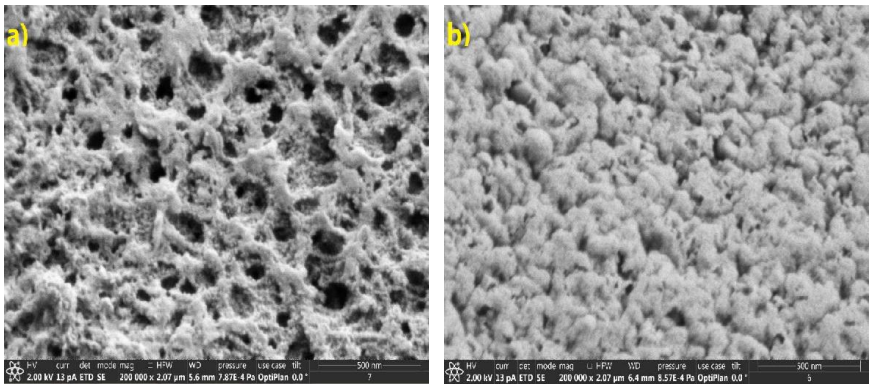

Figure 5.76 Surface morphologies of nanocomposites. a) 10% PAN+P90; b) 10% Carbon+P90.

The elemental mapping of 10% PAN+P90 by EDS inspection is shown in Figure 5.77. According to the mapping of titanium, it can be inferred that the distribution of TiO_2 is homogeneous.

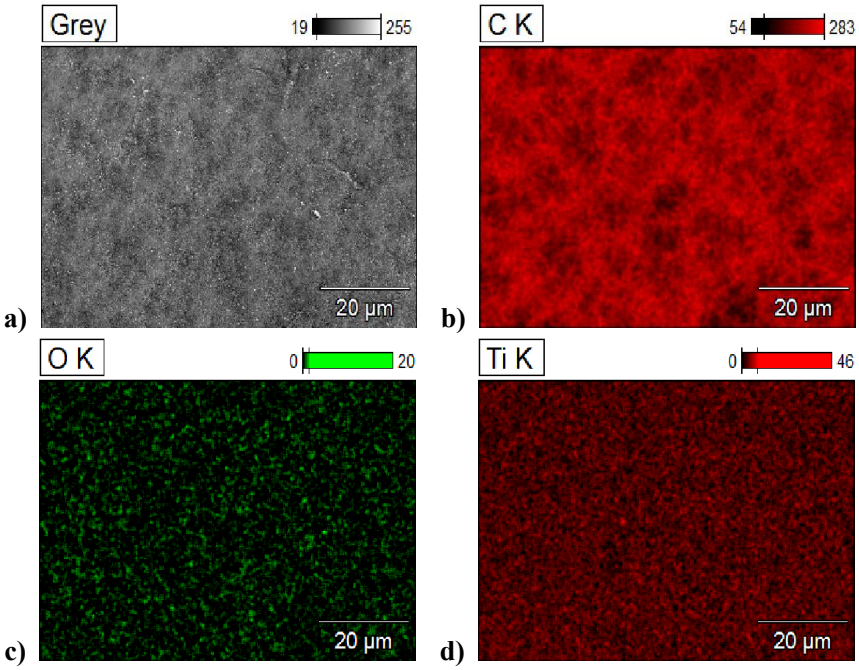

a) b) c) d)

Figure 5.77 Elemental mapping of 10% PAN+P90. a) the region for inspection; b) mapping of carbon; c) mapping of oxygen; d) mapping of titanium.

The elemental mapping of 10% Carbon+P90 by EDS inspection is shown in Figure 5.78. According to mapping of titanium, it can be inferred that the distribution of titanium is homogeneous. In addition, the distribution of oxygen in carbon nanocomposites is less homogeneous than that in polymer nanocomposites.

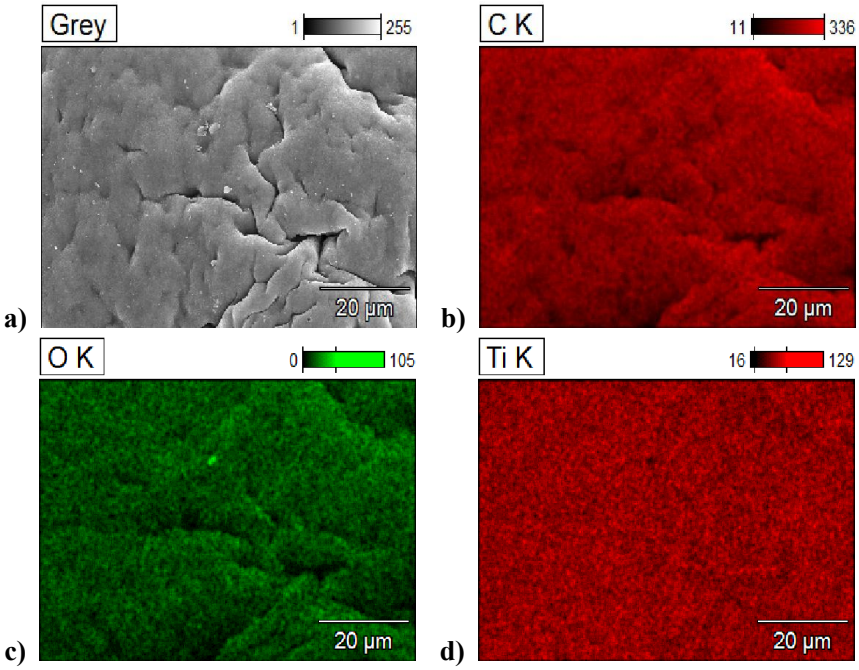

a) b) c) d)

Figure 5.78 Elemental mapping of 10% Carbon+P90. a) the region for inspection; b) mapping of carbon; c) mapping of oxygen; d) mapping of titanium.

As 10% PAN+P90 is composited by mechanical blending of polyacrylonitrile (i.e. PAN 200)

and P90, its XPS analysis is not shown here.
The high-resolution spectra of elements in "5% carbon spheres" (i.e. "900°C, 30 min") has been discussed in section 5.4.5, which are used as references here.
The high-resolution XPS spectra of oxygen and titanium in P90 are shown in Figure 5.79, which are used as references here. The photoelectron lines of oxygen and titanium in P90 are O 1s and Ti 2p, respectively.

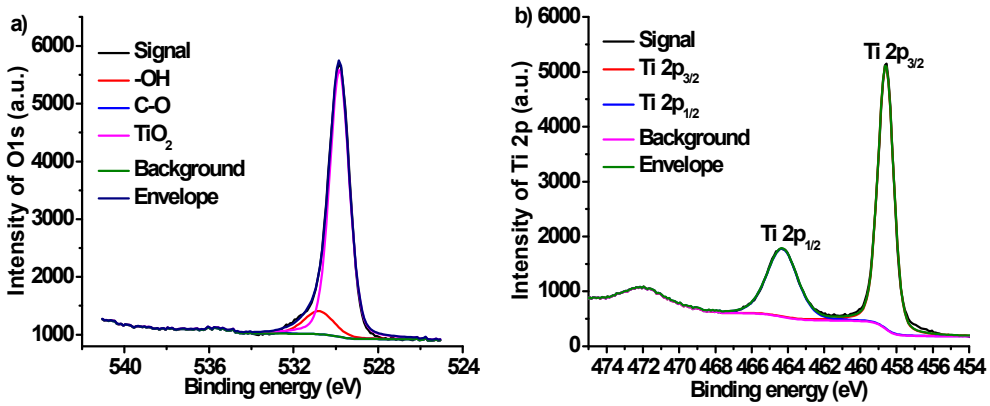

Figure 5.79 High-resolution XPS spectra of P90. a) O 1s; c) Ti 2p.

The high-solution spectrum of O 1s is shown in Figure 5.79a. The various species containing oxygen element are also fitted. The existence of carbon (i.e. C-O signal) from O1s spectrum is due to the calibration by carbon element. The content of TiO_2 is the highest among all species.
The high-solution spectrum of Ti 2p is shown in Figure 5.79b. The various species containing titanium element are also fitted. Because of spin-orbit splitting (i.e. SOS) [51], the Ti 2p signal is split into Ti $2p_{3/2}$ (458.6 eV) and Ti $2p_{1/2}$ (464.4 eV). The binding energies of Ti 2p are close to the values of some reported researches [51].
As 10% PAN+P90 is composited by mechanical blending of polyacrylonitrile (PAN 200) and P90, its XPS spectra are not shown here. The high-resolution XPS spectra of some elements in 10% Carbon+P90 are shown in Figure 5.80. The photoelectron lines of carbon, oxygen, nitrogen, and titanium in 10% Carbon+P90 are C 1s, O 1s, N 1s, and Ti 2p, respectively.
The high-solution spectrum of C 1s is shown in Figure 5.80a. The various species containing carbon element are also fitted. The content of C-C is the highest among all species. The signal of Ti-C (C 1s, 281.6 eV, [51]) is not found in this high-solution spectrum, which means there is no interaction between carbon and titanium.
The high-solution spectrum of O 1s is shown in Figure 5.80b. The various species containing oxygen element are also fitted. The content of TiO_2 is the highest among all species. The content of C-O is the lower than that of -OH.
The high-solution spectrum of N 1s is shown in Figure 5.80c. The various species containing nitrogen element are also fitted. Only two species of nitrogen are found, which are pyrrolic N (i.e. N-5, 400.2 eV) and pyridinic N (i.e. N-6, 397.6 eV). The binding energies of these nitrogen species are close to the values of some reported researches [43, 46]. The signal of Ti-N (N 1s, 396.9 eV, [51]) is not found in this high-solution spectrum, which means there is no interaction between nitrogen and titanium.

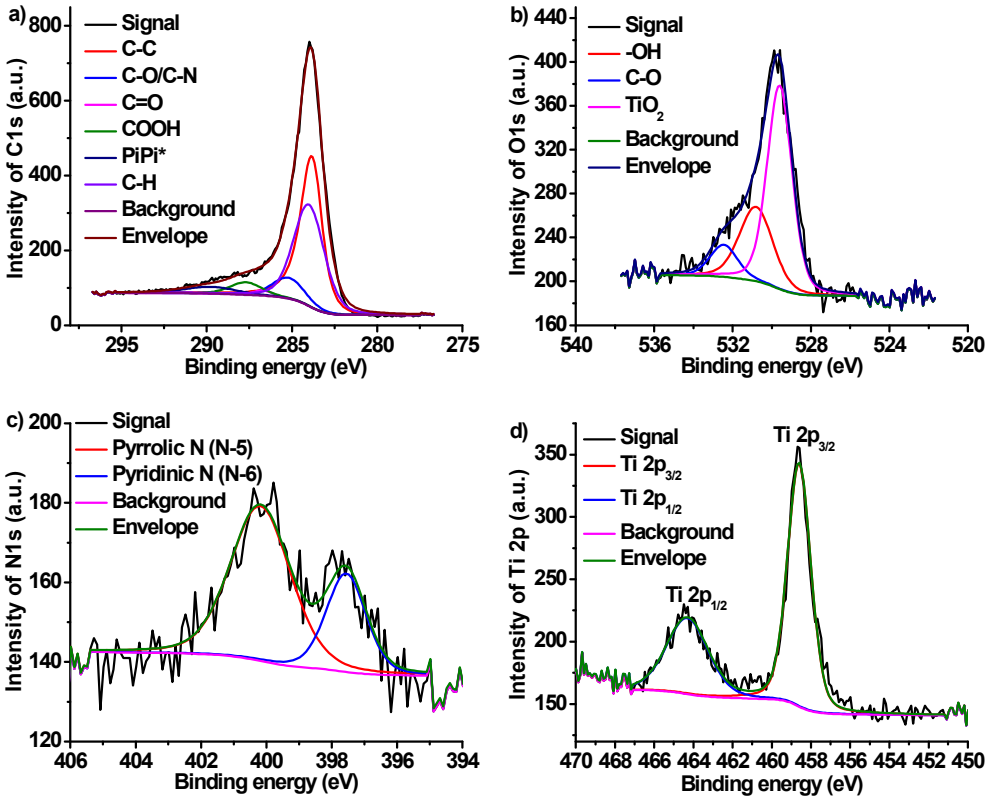

Figure 5.80 High-resolution XPS spectra of 10% Carbon+P90 nanocomposites. a) C 1s; b) O 1s; c) N 1s; d) Ti 2p.

The high-solution spectrum of Ti 2p is shown in Figure 5.80d. After being blended with P90, the high-solution spectrum of Ti 2p did not change. The various species containing titanium element are also fitted. Because of spin-orbit splitting, the Ti 2p signal is split into Ti $2p_{3/2}$ (458.6 eV) and Ti $2p_{1/2}$ (464.4 eV). The binding energies of Ti 2p in nanocomposites did not change compared with those in P90. Both Ti-C (Ti 2p, 454.9 eV) and Ti-N (Ti 2p, 455.8 eV, [51]) are not found in this high-solution spectrum, which means there is no interaction between carbon (and nitrogen) and titanium.

5.5.3 Structural analysis of polymer and carbon nanocomposites

Two nanocomposites, i.e. 10% PAN+P90 and 10% Carbon+P90, were selected for related characterization.

As 10% PAN+P90 is composited by mechanical blending of polyacrylonitrile (i.e. PAN 200) and P90, its XRD analysis is not shown here. The XRD characterization of 10% Carbon+P90 is shown in Figure 5.81. The XRD spectrum of commercial P90 can be easily found in the research [28]. Both anatase phase and rutile phase coexisted in commercial P90 though the content of rutile phase is much lower than that of anatase phase. It can be inferred that the content of anatase phase in commercial P90 is about 90%.

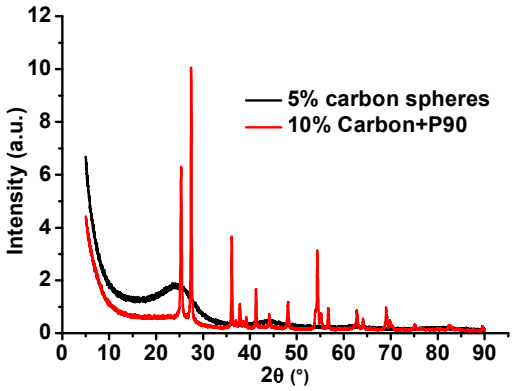

Figure 5.81 XRD spectra of 10% Carbon+P90 nanocomposites.

In 10% Carbon+P90, the diffraction signals corresponding to (002), (100) and (101) faces of graphite are submerged by P90's diffraction signals. Compared with the XRD spectrum of commercial P90 [28], the XRD spectrum of 10% Carbon+P90 changes much. The phase analysis of nanoparticles in 10% Carbon+P90 is shown in Figure 5.82.

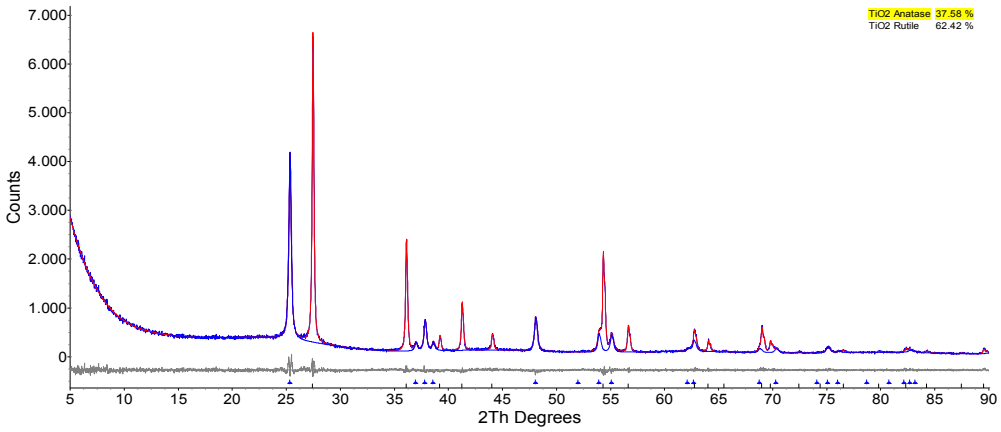

Figure 5.82 Phase analysis of nanoparticles in 10% Carbon+P90.

After professional polycrystalline phase analysis of these signals in 10% Carbon+P90, the content of anatase phase is 37.58% (blue line, volume fractions) while the content of rutile phase is 62.42% (red line, volume fractions). In conclusion, part of anatase phase was transformed into rutile phase in 10% Carbon+P90 after carbonization.

As 10% PAN+P90 is composited by mechanical blending of polyacrylonitrile (PAN 200) and P90, its Raman analysis is not shown here. The Raman characterization of 10% Carbon+P90 is shown in Figure 5.83.

Both "5% carbon spheres" and 10% Carbon+P90 show two signals around 1,341 and 1,596 cm^{-1} [83]. The signal at 1,596 cm^{-1} (i.e. G-band) is characteristic for graphitic layers. The D-band at around 1,341 cm^{-1} is attributed to the presence of defects within graphitic layers. The intensity ratio of D- and G-band ($I_{D\text{-}band}/I_{G\text{-}band}$) indicates the degree of graphitization. The intensity ratio of D- and G-band in "5% carbon spheres" is 1.18 while the intensity ratio of D- and G-band in 10% Carbon+P90 is 1.16. The high intensity ratio of D- and G-band means low degree of graphitization. Compared to the Raman spectrum of graphite crystals

(G-band: 1575 cm^{-1}) [84], the wavenumber of G-band shifts to higher wavenumber in all carbon containing samples.

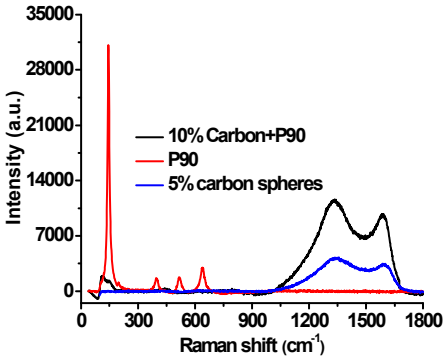

Figure 5.83 Raman spectra of 10% Carbon+P90 nanocomposites.

According to the symmetry group, TiO_2 of anatase phase has 15 optical modes in Raman spectrum (i.e. irreducible representation $1A_{1g}+1A_{2u}+2B_{1g}+1B_{2u}+3E_g+2E_u$) [83]. Modes A_{1g} (519 cm^{-1}), B_{1g} (399 and 519 cm^{-1}), and E_g (144, 197, and 639 cm^{-1}) are Raman active modes of anatase phase [85, 86]. Meanwhile, four modes A_{1g} (612 cm^{-1}), B_{1g} (143 cm^{-1}), B_{2g} (826 cm^{-1}), and E_g (447 cm^{-1}) are Raman active modes of rutile phase [87, 88]. Although P90 shows the characteristic Raman modes of anatase phase, the 10% Carbon+P90 only shows a non-sharp peak at 150 cm^{-1}.
As 10% PAN+P90 is composited by mechanical blending of polyacrylonitrile (PAN 200) and P90, its IR analysis is not shown here. The IR characterization of 10% Carbon+P90 is shown in Figure 5.84.

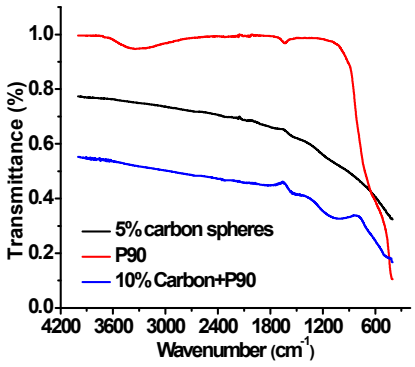

Figure 5.84 IR spectra of 10% Carbon+P90 nanocomposites.

No direct evidence can be read from Figure 5.93 to confirm the interaction between nanoparticles and carbon substrate.

5.6 Adsorption tests on large polymer spheres and carbon spheres

5.6.1 The polarity of adsorbents

As mentioned in 2.6.3 and 4.5.1, all the adsorption tests happened in dilute and aqueous solutions. Solution adsorption process refers to the transfer of solute from solution to the surface of adsorbent.

There are mainly two factors influencing static adsorption capacity. The first factor is the affinity of single adsorption site. The second one is the number of these adsorption sites. In solid solution adsorption (SSA) system as shown in Scheme 5.4 [40], there are three sets of affinities: solute and adsorbent (affinity A), solute and solvent (affinity B), solvent and adsorbent (affinity C). In order to have a good adsorption performance, affinity A should be enhanced while affinity B and C should be suppressed.

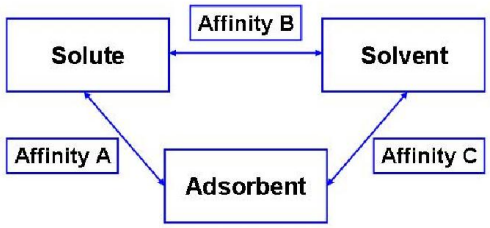

Scheme 5.4 Principles of solid solute adsorption (SSA) in dilute solution [40].

In terms of adsorbent, the primary factors influencing the adsorption process are the polarity and porous structure [3]. Moreover, surface chemistry of adsorbent, e.g. surface functional groups, pH_{IEP} (i.e. isoelectric point, a pH at which the external surface charge is zero), and pH_{PZC} (i.e. point of zero charge, a pH at which the total surface charge is zero), are also important in some specific cases.

For the solvent (or solution), the primary factor is the polarity of solvent. Both pH and temperature of solution should be also considered. As to solute, the polarity and size of solute should be firstly taken into account [3]. Other important factors such as pKa and solubility of solute are also important in some cases.

There are several physical adsorption mechanisms, such as dispersion interaction, dipole-dipole interaction, electrostatic interaction, and hydrogen bond. The dispersion interaction is represented by the adsorption on non-polar or low polarity adsorbents, like activated carbon while the dipole-dipole interaction is represented by the adsorption on polar adsorbents, like zeolite, molecular sieve, and Al_2O_3. More than one adsorption mechanism can coexist in an adsorption system.

The polarity of single molecule is described by the dipole moment of this molecule [89]. For macroscopic and impure matter, however, dipole moment is no longer applicable to describe its polarity. Water molecule is a representative in molecules with strong polarity. The affinity between matter and water can be seen as a representative of the polarity of matter, i.e. hydrophilicity and hydrophobicity of matter. The hydrophobicity of matter means low polarity while the hydrophilicity of matter means high polarity, which derives from the polar groups in matter.

As is widely known, activated carbon is an amphoteric material [3], which derives from the acid and basic functional groups, especially oxygen-containing groups. These functional groups, undoubtedly, are hydrophilic. At the same time, the graphitic structure in activated

carbon also renders this material hydrophobicity. In classical adsorption, although activated carbon is always regarded as a low polarity adsorbent (compared with the polarity of zeolite, molecular sieve, and Al_2O_3), it is indeed an amphiphilic material. In adsorption process, low polar solutes are merely preferred to be adsorbed on activated carbon. The carbon spheres ("1,000°C, 30 min" and "1,000°C, 1 hour") used in this study are amphoteric and amphiphilic.

For polymer spheres used in this study ("8%, 0/100" and "8%, 65/35"), their polarity is just opposite. In aqueous solution, the zeta potential (ζ) of PAN based nanoparticles [90] and PAN based membranes [91] is below zero within a wide pH range. In literature [90], the PAN based nanoparticles carried negative charges within the pH between 2.5 and 12. For the adsorption of phenols on polymer spheres, it can be inferred that these PAN nanoparticles also carried negative charges at pH of two according to the tendency of the titration curve. For the adsorption of dyes on polymer spheres, the pH of solutions was always between 2.5 and 12 (see appendix 8.7). Therefore, these polymer spheres carry negative charges in aqueous solutions and they are polar adsorbents. This polarity derives from the -CN groups, which are polar and hydrophilic.

5.6.2 Adsorption of phenols on polymer spheres

The adsorption isotherms of various phenols on polymer spheres are shown in Figure 5.85. All the phenols are not charged at pH of two and they have lower polarity compared with the polarity of water. Since PAN 200 spheres are polar adsorbents as argued in 5.6.1, the initial parts of adsorption isotherms of various phenols shown in Figure 5.85 are assumed to be S isotherm according to Giles' classification.

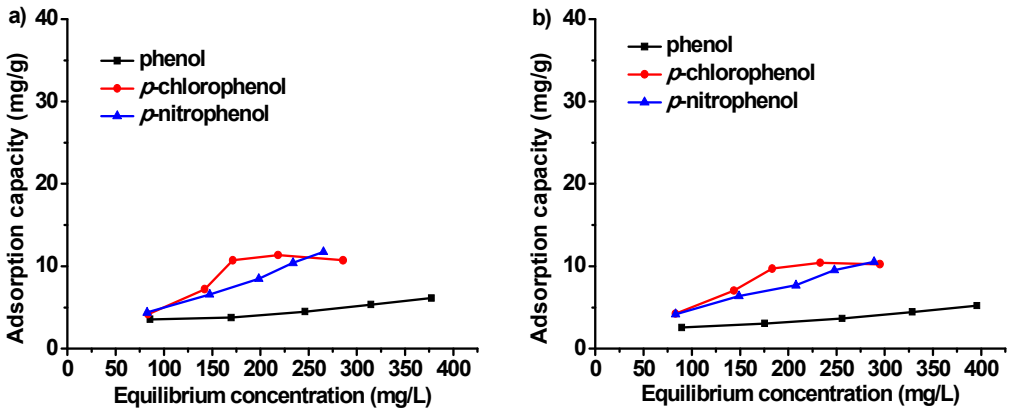

Figure 5.85 Adsorption isotherms of phenols on polymer spheres. temperature: 20°C; pH of the solution: two. a) "8%, 0/100" polymer spheres; b) "8%, 65/35" polymer spheres.

The affinity reflected by adsorption isotherms changes as the equilibrium concentration varies. The equilibrium concentration section should be firstly indicated in order to discuss the affinity of isotherms. For a selected concentration section, the affinity of isotherm can be determined qualitatively or quantitatively. As to qualitative method, the mean affinity of this segment can be estimated by the mean steepness of this segment. The steeper the mean steepness is, the higher is the mean affinity. For quantitative method, the affinity at one

concentration point is determined by calculating the slope of this point, which needs fine regression results of the isotherm. The larger the slope is, the higher is the affinity.
Although isotherms within low concentration section (below 100 mg/L) are not plotted here, it can be inferred that the mean affinities in this section are low. This conclusion fits the feature of S isotherm.
The regression results of these isotherms by adsorption models are shown in Table 5.12 and 5.13.

Table 5.12 Linear regression results of isotherms of phenols on "8%, 0/100" polymer spheres. unit of q_{mono}: mg/g; unit of b: L/mg; unit of K_F: (mg/g)(L/mg)$^{1/n}$.

Solutions	Langmuir model				Freundlich model			
	q_{mono}	b	r	R^2	K_F	$1/n$	r	R^2
phenol	8	0.0064	0.94	0.88	0.65	0.36	0.93	0.86
p-chlorophenol	33	0.002	0.59	0.35	0.11	0.86	0.92	0.85
p-nitrophenol	53	0.001	0.77	0.59	0.10	0.84	0.99	0.98

Table 5.13 Linear regression results of isotherms of phenols on "8%, 65/35" polymer spheres. unit of q_{mono}: mg/g; unit of b: L/mg; unit of K_F: (mg/g)(L/mg)$^{1/n}$.

Solutions	Langmuir model				Freundlich model			
	q_{mono}	b	r	R^2	K_F	$1/n$	r	R^2
phenol	8	0.0043	0.94	0.88	0.29	0.47	0.97	0.94
p-chlorophenol	25	0.0028	0.83	0.69	0.17	0.75	0.95	0.90
p-nitrophenol	28	0.0021	0.93	0.86	0.16	0.74	0.996	0.99

As shown in Table 5.12 and 5.13, the K_F values of phenol are larger than those of *p*-chlorophenol and *p*-nitrophenol and the $1/n$ values of phenol is smaller than those of *p*-chlorophenol and *p*-nitrophenol. Thus, the affinity of phenol on PAN 200 spheres is higher than those of *p*-chlorophenol and *p*-nitrophenol within middle and high concentration section. The affinity tendency reflected by b values from Langmuir model is the same as that by K_F values and $1/n$ values from Freundlich model.
Theoretically, the $1/n$ value of S isotherm in low concentration section should be above one. The concentration section presented belongs to middle and high section of concentration; therefore, it is reasonable that the $1/n$ value from Freundlich model is below one.
The higher affinity of phenol derives from its larger polarity. Compared with the dipole moments of *p*-chlorophenol and *p*-nitrophenol, the dipole moment of phenol is larger according to the molecular structure. This can also be confirmed by the higher solubility of phenol in water (see Table 5.14).

Table 5.14 Properties of phenols used for adsorption [8].

Phenols	Area (nm^2)	Size (nm)	M_W (g/mol)	Solubility (g/100g water, 20°C)	pKa (25°C)
phenol	0.44	0.66*0.66	94	8.0	9.89
p-chlorophenol	0.48	0.69*0.69	128.5	2.7	9.37
p-nitrophenol	0.53	0.72*0.72	139	1.2	7.15

Overall, the adsorption affinities of three phenols on PAN 200 spheres are low even within middle and high concentration section. The adsorption mechanism is dipole-dipole interaction between phenols and PAN 200 spheres. There is intense competition for the adsorption sites between water and phenols. After water molecule desorbed from the adsorbents, the adsorption of phenols on adsorbents happened. Compared with the affinity between phenols and adsorbents, the affinity between water and adsorbents is larger.

Compared with the affinities (i.e. K_F and $1/n$ values) between phenols and "8%, 0/100" spheres, the affinities between phenols and "8%, 65/35" spheres do not change much. Both specific surface areas and specific pore volumes of "8%, 65/35" spheres are higher than those of "8%, 0/100" spheres (see Table 5.15), which means that "8%, 65/35" spheres can provide more adsorption sites; however, the adsorption capacity in middle and high concentration section does not improve. This implies that these extra adsorption sites in "8%, 65/35" spheres are not effective for phenols.

Table 5.15 Pore characterizations of polymer spheres used for adsorption.

PAN 200 spheres	Specific surface area (m^2/g)	Specific pore volume (mL/g)	Porosity (%)
"8%, 0/100"	190	0.583	91
"8%, 65/35"	269	1.12	89

The adsorption isotherms of phenol on two polymer spheres in low concentration section are shown in Figure 5.86. These two isotherms present low affinity in low concentration section, which fits the features of S isotherm. During the adsorption, the intense competition between water and phenol was again demonstrated.

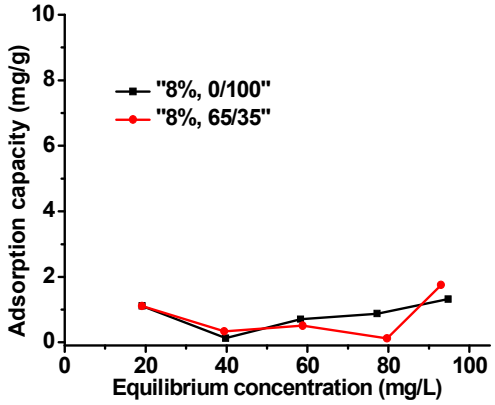

Figure 5.86 Adsorption isotherms of phenol on PAN 200 polymer spheres. temperature: 20°C; pH of the solution: two.

The pore size distribution of two polymer spheres is shown in Figure 5.87. It is clear that the pore volumes (less than 6 nm) in both "8%, 0/100" and "8%, 65/35" polymer spheres are small. Mesopores (2-50 nm) and macropores (over 50 nm) are predominant among all pores.

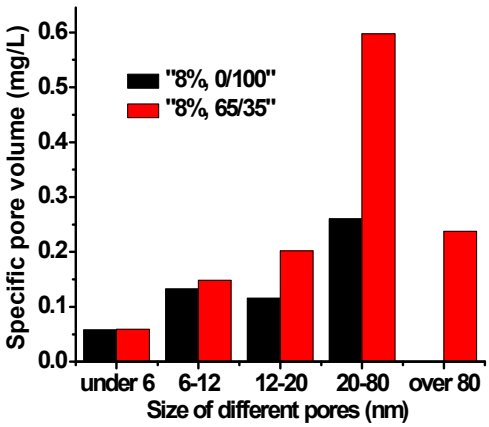

Figure 5.87 Pore size distributions of PAN 200 spheres used in adsorption tests.

5.6.3 Adsorption of dyes on polymer spheres

The adsorption isotherms of various dyes on PAN 200 spheres are shown in Figure 5.88. No methyl orange (MO) molecules were adsorbed on these spheres; as a result, the adsorption isotherm of methyl orange is not shown here.

In aqueous solutions, both methylene blue (MB) and rhodamine B (Rh B) were positively charged. Although the polarity of water molecule is strong, it is still not charged. Since PAN 200 spheres are negatively charged adsorbents in solution as argued in 5.6.1, the initial parts of adsorption isotherms of various dyes shown in Figure 5.88 belong to L isotherm according to Giles' classification.

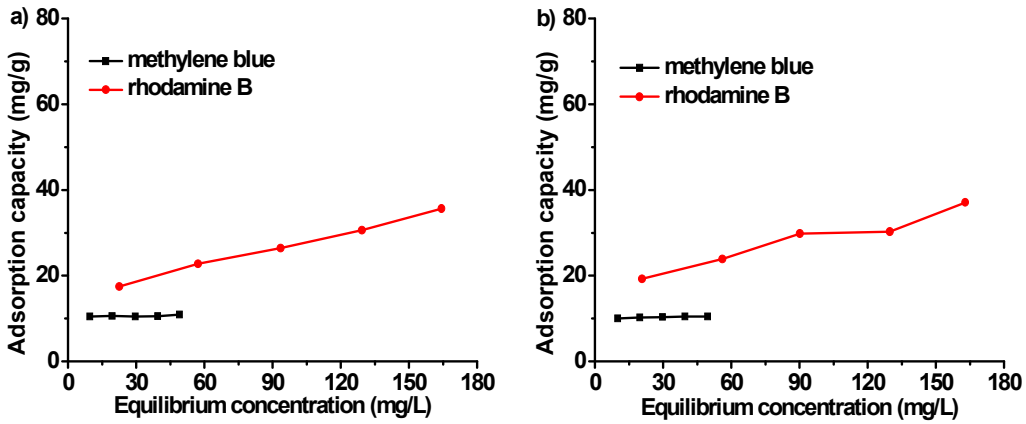

Figure 5.88 Adsorption isotherms of dyes on PAN 200 spheres. temperature: 20°C; a) "8%, 0/100" polymer spheres; b) "8%, 65/35" polymer spheres.

In low concentration section (below 100 mg/L), isotherms show moderate affinity between dye cations and adsorbents. This conclusion fits the feature of L isotherm. The regression results of these isotherms by adsorption models are shown in Table 5.16 and 5.17.

For MB and Rh B, the regression results from Langmuir model are much better than those from Freundlich model. Given that all the isotherms can be described by Langmuir model, then the affinity between dyes and polymer spheres in selected concentration section can be analyzed.

Table 5.16 Linear regression results of isotherms of dyes on "8%, 0/100" polymer spheres. unit of q_{mono}: mg/g; unit of b: L/mg; unit of K_F: (mg/g)(L/mg)$^{1/n}$.

Solutions	Langmuir model				Freundlich model			
	q_{mono}	b	r	R^2	K_F	$1/n$	r	R^2
MB	11	1.24	0.999	0.998	10	0.016	0.54	0.29
Rh B	43	0.022	0.98	0.96	6	0.35	0.99	0.98

Table 5.17 Linear regression results of isotherms of dyes on "8%, 65/35" polymer spheres. unit of q_{mono}: mg/g; unit of b: L/mg; unit of K_F: (mg/g)(L/mg)$^{1/n}$.

Solutions	Langmuir model				Freundlich model			
	q_{mono}	b	r	R^2	K_F	$1/n$	r	R^2
MB	11	1.7	0.99999	0.99998	9	0.027	0.98	0.96
Rh B	42	0.029	0.98	0.96	8	0.30	0.97	0.94

As shown in Table 5.16 and 5.17, the b values of MB are larger than those of Rh B. Thus, the affinity of MB on PAN 200 spheres is higher than that of Rh B in low concentration section. It can be inferred that the higher affinity of MB derives from its smaller molecular size, which can make itself come into the interior of polymer spheres further (see Table 5.18). The affinity tendency reflected by K_F values and $1/n$ values from Freundlich model is the same as that by b values from Langmuir model.

Table 5.18 Properties of dyes used for adsorption.

Dyes	Area (nm^2)	Size (nm)	M_W (g/mol)	Solubility (g/100 g water, 20°C)	pKa (25°C)
methylene blue (MB)	0.87	1.43*0.61 [92]	320	4	3.14
methyl orange (MO)	0.79	1.46*0.54 [93]	327	0.5	3.46
rhodamine B (Rh B)	1.57	1.44*1.09 [94]	479	1.5	4.2

The specific surface areas of "8%, 0/100" spheres can also be estimated by the adsorption of methylene blue. The "plateaus capacity" is 10.46 mg/g when the C_e reaches 9.54 mg/L. Langmuir model gives the value of q_{mono} as 10.92 mg/g, which is close to the "plateaus capacity". Even though the MB molecule spreads horizontally on the surface of PAN spheres, the specific surface areas of "8%, 0/100" spheres calculated by MB are only 17.2 m^2/g, compared with the specific surface areas of 190 m^2/g (Table 5.15) by nitrogen adsorption.
Overall, the adsorption affinities of MB and Rh B on "8%, 0/100" spheres are moderate within low equilibrium concentration section. Different from the adsorption of phenols on PAN 200 spheres, the adsorption mechanism of dyes on PAN 200 spheres is electrostatic attraction. The magnitude of electrostatic interaction is larger than that of Van der Waals' force. After ionization, a MB or Rh B molecule became a cation while a MO molecule became an anion. There is competition for the adsorption sites between water and dye cations. With the adsorbents negatively charged, the MB or Rh B cations can easily come into the interior of PAN 200 spheres while no MO anions can be adsorbed on PAN 200 spheres due to electrostatic repulsion. Compared with the affinity between water and adsorbents, the

affinity between dye cations and adsorbents is larger.
Compared with the affinities (i.e. *b* values) between dyes and "8%, 0/100" spheres, the affinities between dyes and "8%, 65/35" spheres do not change much. Both specific surface areas and specific pore volumes of "8%, 65/35" spheres are higher than those of "8%, 0/100" spheres (see Table 5.15), which means that "8%, 65/35" spheres can provide more adsorption sites; however, the adsorption capacity in low and middle concentration section does not improve. This implies that these extra adsorption sites in "8%, 65/35" spheres are not effective for dyes.
The Freundlich adsorption parameters of phenols and dyes on PAN 200 polymer spheres are shown in Table 5.19 and 5.20, respectively. Although the adsorption isotherms of dyes belong to L isotherm, these isotherms can also be analyzed by Freundlich model.

Table 5.19 Summary of Freundlich parameters of phenols and dyes on "8%, 0/100" spheres. unit of K_F: mg/g)(L/mg)$^{1/n}$.

	phenol	*p*-chlorophenol	*p*-nitrophenol	MB	Rh B
K_F	0.65	0.11	0.10	10	6
1/n	0.36	0.86	0.84	0.016	0.35

Table 5.20 Summary of Freundlich parameters of phenols and dyes on "8%, 65/35" spheres. unit of K_F: (mg/g)(L/mg)$^{1/n}$.

	phenol	*p*-chlorophenol	*p*-nitrophenol	MB	Rh B
K_F	0.29	0.17	0.16	9	8
1/n	0.47	0.75	0.74	0.027	0.30

Dye cations were adsorbed on polymer spheres by electrostatic attraction. The adsorption mechanism between phenols and polymer spheres is dipole-dipole interaction, which is a weakened form of electrostatic interaction. When the electroneutral phenols were replaced by dye cations, the K_F values of solutes increase while the *1/n* values decrease. This implies the affinity between solutes and adsorbents increases and the competitiveness of solutes to adsorption sites increases. At the same time, from MB to Rh B, the excessive size of dyes cations can weaken the affinity of solutes to adsorbents.

5.6.4 Adsorption of phenols on carbon spheres

The adsorption isotherms of various phenols on carbon spheres are shown in Figure 5.89. All the phenols are not charged at pH of two and they have lower polarity compared with the polarity of water. Since carbon spheres are low polar adsorbents as argued in 5.6.1, the initial parts of adsorption isotherms of various phenols shown in Figure 5.89 belong to H isotherm according to Giles' classification.

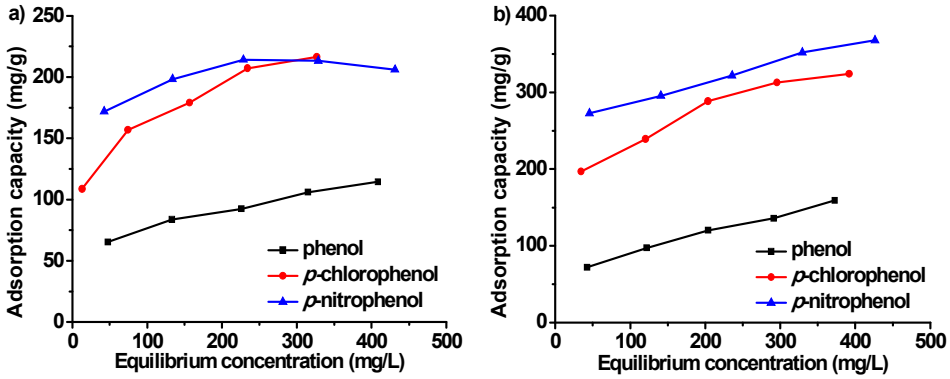

Figure 5.89 Adsorption isotherms of phenols on carbon spheres. temperature: 20°C; pH of the solution: two; a) "1,000°C, 30 min" carbon spheres; b) "1,000°C, 1 hour" carbon spheres.

Within low concentration section (below 100 mg/L), although isotherms are not plotted in detail, it can be inferred that they show high affinity between phenols and adsorbents. This conclusion fits the feature of H isotherm. The regression results of these isotherms by adsorption models are shown in Table 5.21 and 5.22.

For isotherms of all phenols, the regression results from Langmuir model are better than those from Freundlich model. Given that all the isotherms can be described by Langmuir model, then the affinity between phenols and carbon spheres within selected concentration section can be analyzed.

Table 5.21 Linear regression results of isotherms of phenols on "1,000°C, 30 min" carbon spheres. unit of q_{mono}: mg/g; unit of b: L/mg; unit of K_F: (mg/g)(L/mg)$^{1/n}$.

Solutions	Langmuir model				Freundlich model			
	q_{mono}	b	r	R^2	K_F	$1/n$	r	R^2
phenol	128	0.016	0.99	0.98	24	0.26	0.99	0.98
p-chlorophenol	230	0.035	0.996	0.99	62	0.22	0.997	0.99
p-nitrophenol	213	0.15	0.999	0.998	125	0.09	0.91	0.83

Table 5.22 Linear regression results of isotherms of phenols on "1,000°C, 1 hour" carbon spheres. unit of q_{mono}: mg/g; unit of b: L/mg; unit of K_F: mg/g)(L/mg)$^{1/n}$.

Solutions	Langmuir model				Freundlich model			
	q_{mono}	b	r	R^2	K_F	$1/n$	r	R^2
phenol	189	0.01	0.98	0.96	18	0.36	0.99	0.98
p-chlorophenol	355	0.024	0.997	0.99	90	0.21	0.99	0.98
p-nitrophenol	389	0.029	0.996	0.99	159	0.13	0.96	0.92

As shown in Table 5.21 (and 5.22), the b value of phenol is smaller than that of *p*-chlorophenol and the b value of *p*-chlorophenol is smaller than that of *p*-nitrophenol. Thus, the affinity of *p*-nitrophenol on carbon spheres is the highest among three phenols in low concentration section. The lower affinity of phenol derives from its larger polarity. Compared with the dipole moments of *p*-chlorophenol and *p*-nitrophenol, the dipole moment of phenol is larger according to the molecular structure. This can also be confirmed by the higher

solubility of phenol in water (see Table 5.14). The affinity tendency reflected by K_F values and *1/n* values from Freundlich model is the same as that by *b* values from Langmuir model. Overall, the adsorption affinities of three phenols on carbon spheres are high within low concentration section. The adsorption mechanism is dispersion interaction between phenols and carbon spheres. With the help of CO_2, activation process rendered carbon spheres more and thinner micropores and capillary pores, which show high affinity towards phenols. At the same time, the number of these micropores and capillary pores is vast as confirmed by the large specific surface areas and specific pore volumes after activation.

Compared with the affinities (i.e. *b* values) between phenols and "1,000°C, 30 min" carbon spheres, the affinities between phenols and "1,000°C, 1 hour" spheres do not change much. Both specific surface areas and specific pore volumes of "1,000°C, 1 hour" spheres are higher than those of "1,000°C, 30 min" spheres (see Table 5.23), which means that "1,000°C, 1 hour" spheres can provide more adsorption sites. By virtue of more micropores and capillary pores, the adsorption capacity of phenols on "1,000°C, 1 hour" carbon spheres is higher than that of phenols on "1,000°C, 30 min" carbon spheres when the equilibrium concentration is the same.

Table 5.23 Pore characterizations of carbon spheres used for adsorption.

Carbon spheres	Specific surface area (m^2/g)	Specific pore volume (mL/g)
"1,000°C, 30 min"	739	0.341
"1,000°C, 1 hour"	1318	0.730

The pore size distribution of two carbon spheres is shown in Figure 5.90. It is clear that the pore volumes (less than 6 nm) in both "1,000°C, 30 min" and "1,000°C, 1 hour" carbon spheres are the largest. Moreover, all kinds of pores further developed as demonstrated by larger pore volumes in "1,000°C, 1 hour" spheres than those in "1,000°C, 30 min" spheres.

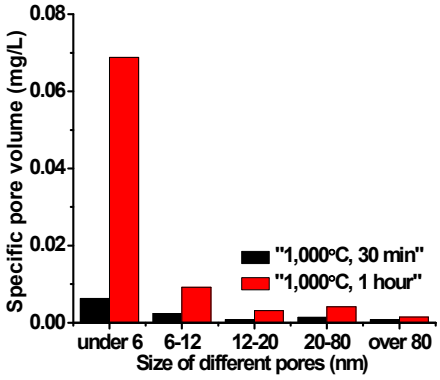

Figure 5.90 Pore size distributions of carbon spheres used in adsorption tests.

5.6.5 Adsorption of dyes on carbon spheres

The adsorption isotherms of various dyes on carbon spheres are shown in Figure 5.91. Since both cations (MB^+, Rh B^+) and anions (MO^-) can be adsorbed on the same carbon spheres, the surface of these carbon spheres is charged with both positive and negative charges. Therefore, the effect of electrostatic interaction on the adsorption of dye ions on carbon

spheres can be neglected. The electroneutral part of dye ions has lower polarity compared with the polarity of water. Since carbon spheres are low polar adsorbents as argued in 5.6.1, the initial parts of adsorption isotherms of various dyes shown in Figure 5.91 belong to H (or L) isotherm according to Giles' classification.

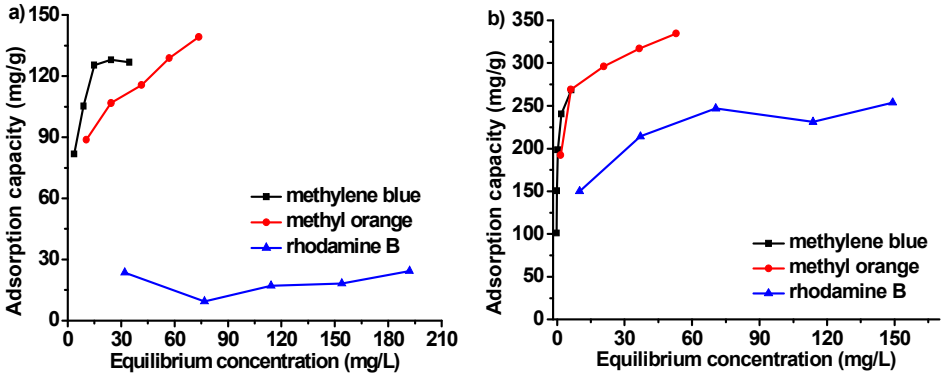

Figure 5.91 Adsorption isotherms of dyes on carbon spheres. temperature: 20°C; a) "1,000°C, 30 min" carbon spheres; b) "1,000°C, 1 hour" carbon spheres.

In low concentration section (below 100 mg/L), isotherms (except for the isotherm Rh B in Figure 5.91a) show high affinity between dye ions and carbon spheres. This conclusion fits the feature of H isotherm. The regression results of these isotherms by adsorption models are shown in Table 5.24 and 5.25.

Table 5.24 Linear regression results of isotherms of dyes on "1,000°C, 30 min" carbon spheres. unit of q_{mono}: mg/g; unit of b: L/mg; unit of K_F: (mg/g)(L/mg)$^{1/n}$.

Solutions	Langmuir model				Freundlich model			
	q_{mono}	b	r	R^2	K_F	$1/n$	r	R^2
MB	137	0.46	0.999	0.998	66	0.21	0.94	0.88
MO	154	0.099	0.995	0.995	52	0.22	0.99	0.98
Rh B	29	0.013	0.73	0.53	15	0.028	0.052	0.0027

Table 5.25 Linear regression results of isotherms of dyes on "1,000°C, 1 hour" carbon spheres. unit of q_{mono}: mg/g; unit of b: L/mg; unit of K_F: (mg/g)(L/mg)$^{1/n}$.

Solutions	Langmuir model				Freundlich model			
	q_{mono}	b	r	R^2	K_F	$1/n$	r	R^2
MB	262	-16	0.997	0.99	225	0.099	0.9997	0.999
MO	341	0.51	0.999	0.998	189	0.15	0.97	0.94
Rh B	260	0.13	0.997	0.99	102	0.19	0.95	0.90

For isotherms of all dyes, the regression results from Langmuir model are better than those from Freundlich model. Given that all the isotherms can be described by Langmuir model, then the affinity between dye ions and carbon spheres within selected concentration section can be analyzed.

As shown in Table 5.24 and 5.25, the b values of MB and MO are larger than that of Rh B

(except for the case of MB in Table 5.25). Thus, the affinities of MB and MO on carbon spheres are higher than that of Rh B in low concentration section. It can be inferred that the higher affinities of MB and MO derive from their smaller molecular size, which can make themselves come into the interior of carbon spheres further. The affinity tendency reflected by K_F values and *1/n* values (except for the case of Rh B in Table 5.24) from Freundlich model is the same as that by *b* values from Langmuir model.

Overall, the adsorption affinities of dyes on carbon spheres are high within low concentration section except for the case of Rh B on "1,000°C, 30 min" carbon spheres. The adsorption mechanism is dispersion interaction between the electroneutral part of dye ions and carbon spheres. With the help of CO_2, activation process rendered carbon spheres more and thinner micropores and capillary pores, which show high affinity towards dye ions. At the same time, the number of these micropores and capillary pores is vast as confirmed by the large specific surface areas and specific pore volumes after activation

Compared with the affinities (i.e. *b* values) between dyes and "1,000°C, 30 min" carbon spheres, the affinities between dyes and "1,000°C, 1 hour" spheres do not change much. Both specific surface areas and specific pore volumes of "1,000°C, 1 hour" spheres are higher than those of "1,000°C, 30 min" spheres (see Table 5.23), which means that "1,000°C, 1 hour" spheres can provide more adsorption sites. By virtue of more micropores and capillary pores, the adsorption capacity of dyes on "1,000°C, 1 hour" carbon spheres is higher than that of dyes on "1,000°C, 30 min" carbon spheres when the equilibrium concentration is the same.

The Freundlich adsorption parameters of phenols and dyes on carbon spheres are shown in Table 5.26 and 5.27, respectively. Although the adsorption isotherms of phenols and dyes belong to H isotherm, these isotherms can also be analyzed by Freundlich model.

Table 5.26 Summary of Freundlich parameters of phenols and dyes on "1,000°C, 30 min" spheres. unit of K_F: $(mg/g)(L/mg)^{1/n}$.

	phenol	*p*-chlorophenol	*p*-nitrophenol	MB	MO	Rh B
K_F	24	62	125	66	52	15
1/n	0.26	0.22	0.09	0.21	0.22	0.028

Table 5.27 Summary of Freundlich parameters of phenols and dyes on "1,000°C, 1 hour" spheres. unit of K_F: $(mg/g)(L/mg)^{1/n}$.

	phenol	*p*-chlorophenol	*p*-nitrophenol	MB	MO	Rh B
K_F	18	90	159	225	189	102
1/n	0.36	0.21	0.13	0.099	0.15	0.19

The affinity between phenols and carbon spheres derives from dispersion interaction. This interaction also applies to the adsorption of dye ions on carbon spheres. From the low polar phenols to the electroneutral part of dye ions which has larger hydrophobicity, the K_F values of solutes firstly increase and then decrease while the *1/n* values firstly decrease and then increase. This implies the affinity between solutes and adsorbents firstly increases and then decreases. Among dye ions, the excessive size of solutes can weaken the affinity of solutes to adsorbents.

5.7 Photocatalytic tests

5.7.1 Photocatalytic tests of polymer nanocomposites

The photocatalytic results of polymer nanocomposites are shown in Figure 5.92.

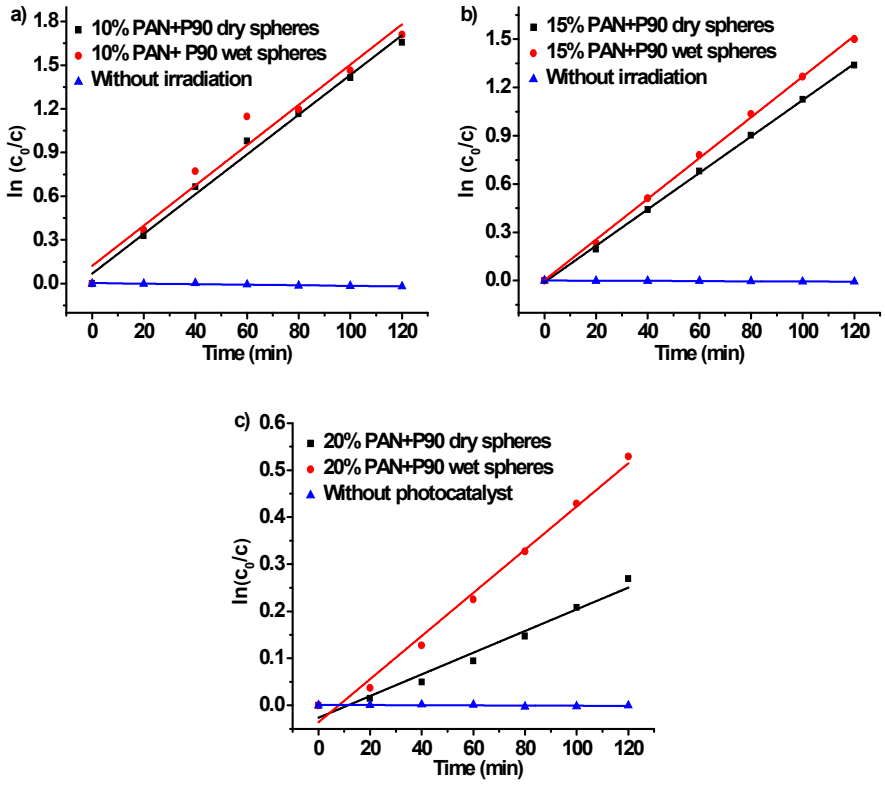

Figure 5.92 Results of photocatalysis by polymer nanocomposites. nominal dosage of P90: 10 mg; temperature: 20°C; a) 10% PAN+P90; b) 15% PAN+P90; c) 20% PAN+P90.

The related data are summarized in Table 5.28. Compared with the photocatalytic rate of P90, the photocatalytic rates of both wet and dry polymer nanocomposites decrease a half or more. The controlled trials of these nanocomposites in dark environment did not show adsorption. This implies that the adsorption of rhodamine B on polymer nanocomposites reached equilibrium before photocatalysis.

Table 5.28 Summary of photocatalytic rates of polymer nanocomposites.

Nanocomposites	Loading of P90 (mg/g)	k (min^{-1}) (dry spheres)	k (min^{-1}) (wet spheres)	k (min^{-1}) (no irradiation)
10% PAN+P90	100	0.014	0.014	0
15% PAN+P90	150	0.011	0.013	0
20% PAN+P90	200	0.0023	0.0046	0

The total dosage of P90 in each of polymer nanocomposites is controlled as 10 mg. In terms of dosage of P90, the photocatalytic rate of all nanocomposites should be the same theoretically. With the nominal content of P90 increasing from 10% to 20%, the nominal

loading of P90 in nanocomposites per unit mass also increases as shown in Table 5.28. The order of photocatalytic rate, however, follows the opposite trend.

There is some relation between nominal content of P90 and actual content of P90 in polymer nanocomposites. The actual content of P90 in polymer nanocomposites by TGA analysis is shown in Table 5.29. Except for 20% PAN+P90, the actual contents of P90 in 10% PAN+P90 and 15% PAN+P90 are higher than the nominal contents of P90 in these nanocomposites.

Table 5.29 Actual content of P90 in dry polymer nanocomposites by TGA.

Nanocomposites	10% PAN+P90	15% PAN+P90	20% PAN+P90
Dosage of nanocomposites (mg)	100	67	50
Actual mass of P90 (mg)	15.88	15.85	10.1
Actual content of P90 (%)	15.88	23.65	20.19

The specific surface areas of all polymer nanocomposites are almost the same (i.e.200 m^2/g) as shown in Figure 5.75a. The higher photocatalytic rates of 10% and 15% PAN+P90 could be due to the higher actual mass of P90. Moreover, similar actual mass of P90 leads to similar photocatalytic rate. At the same time, the actual content of P90 in polymer nanocomposites is hard to be precisely controlled.

5.7.2 Photocatalytic tests of carbon nanocomposites

The photocatalytic results of carbon nanocomposites are shown in Figure 5.93.

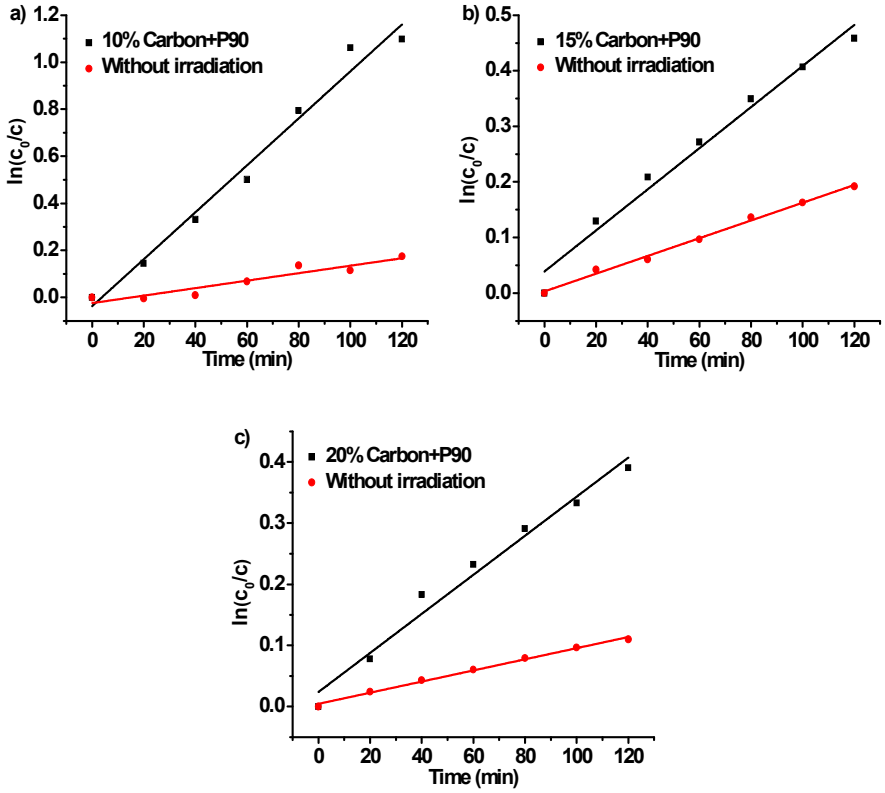

Figure 5.93 Results of photocatalysis by carbon nanocomposites. nominal dosage of P90: 10 mg; temperature: 20°C; a) 10% Carbon+P90; b) 15% Carbon+P90; c) 20% Carbon+P90.

The related data are summarized in Table 5.30. Compared with the photocatalytic rate of P90, the photocatalytic rates of carbon nanocomposites decrease a half or more. The controlled trials of these nanocomposites in dark environment did show adsorption. This implies that the adsorption of rhodamine B on carbon nanocomposites did not reach equilibrium before photocatalysis. The adsorption rates are lower than photocatalytic rates in carbon nanocomposites.

The net photocatalytic rates of carbon nanocomposites decreased further, compared with those of polymer nanocomposites. One reason is that the black carbon in carbon nanocomposites did absorb the 365 nm light greatly, which should have been used to excite the electrons of nanoparticles.

Table 5.30 Summary of photocatalytic rates of carbon nanocomposites.

Nanocomposites	Loading of P90 (mg/g)	k (min^{-1}) (photocatalysis)	k (min^{-1}) (no irradiation)	k (min^{-1}) (net rate)
10% Carbon+P90	435	0.010	0.0016	0.0084
15% Carbon+P90	625	0.0037	0.0016	0.0021
20% Carbon+P90	833	0.0032	0.00091	0.0023

The total dosage of P90 in each carbon nanocomposite is controlled as 10 mg. In terms of dosage of P90, the photocatalytic rates of all nanocomposites should be the same theoretically. Due to the elimination of carbon element in activation process, the nominal content of P90 in carbon nanocomposites (e.g. 10% Carbon+P90) is “pseudo”, which is used just as the naming of carbon nanocomposites. There is no necessary relation between nominal content of P90 and actual content of P90 in carbon nanocomposites. Similarly, the nominal loading of P90 in carbon nanocomposites is also “pseudo”.

With the nominal content of P90 increasing from 10% to 20%, the nominal loading of P90 in photocatalysts per unit mass also increases as shown in Table 5.30. The order of net photocatalytic rate, however, follows the opposite trend.

The actual contents of nanoparticles in carbon nanocomposites by TGA analysis are shown in Table 5.31. The actual contents of nanoparticles in all carbon nanocomposites are higher than nominal contents of P90 in these nanocomposites.

Table 5.31 Actual content of nanoparticles (NPs) in carbon nanocomposites determined by TGA.

Nanocomposites	10% Carbon+P90	15% Carbon+P90	20% Carbon+P90
Dosage of nanocomposites (mg)	23	16	12
Actual mass of NPs (mg)	8.76	7.32	8.24
Actual content of NPs (%)	38.07	45.73	68.65

Due to the elimination of carbon element in activation process, the actual contents of nanoparticles in all carbon nanocomposites increased. It should be mentioned that the properties of P90 for photocatalysis may be changed after carbonization process. The higher photocatalytic rates of 10% Carbon+P90 could be due to the higher actual mass of nanoparticles. Another possible reason is that the higher specific surface areas and specific

pore volumes of 10% Carbon+P90 allow higher transport rates of dye-input and product-output as shown in Figure 5.75.

5.8 ORR characterizations of N-doped carbon materials

5.8.1 The ORR activity of various N-doped carbon materials

The polarization curves of various N-doped carbon materials are shown in Figure 5.94.

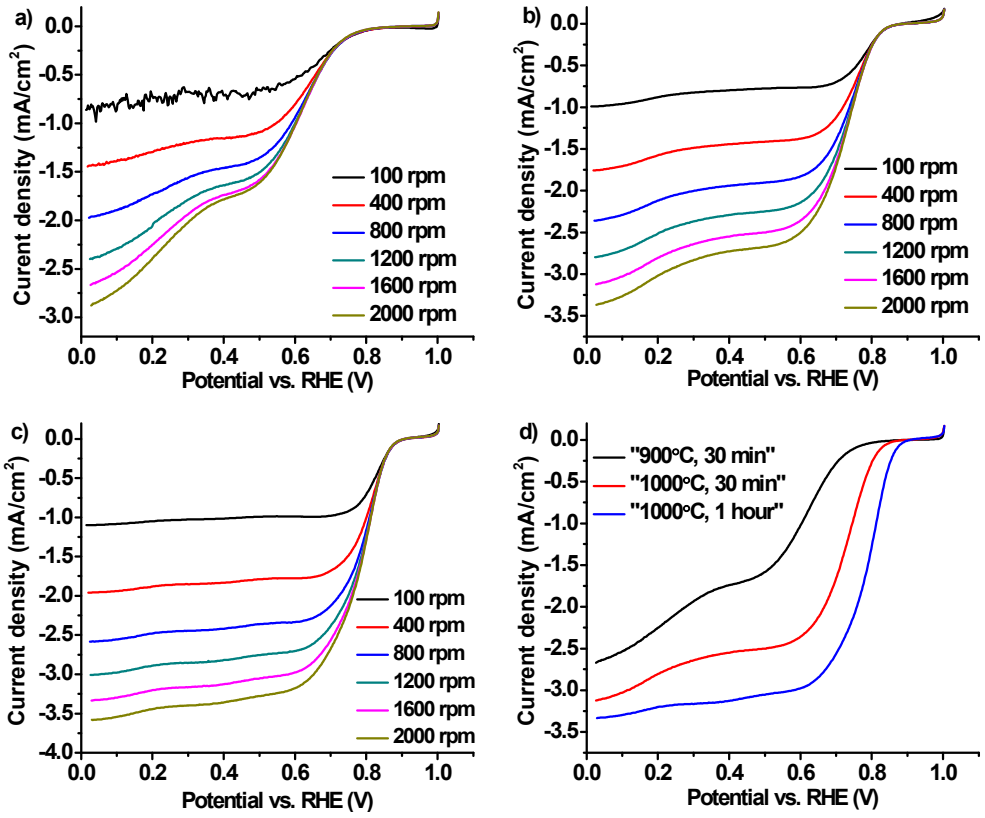

Figure 5.94 Polarization curves of N-doped carbon materials at various rotating speeds recorded in O_2 saturated 0.1 M KOH solution with a scan rate of 5 mV/s. loading of catalyst: 0.2 mg/cm^2; a) "900°C, 30 min"; b) "1,000°C, 30 min"; c) "1,000°C, 1 hour"; d) comparison at 1,600 rpm.

As shown in Figure 5.94a, with the increasing of over-potential, the polarization current densities also increase at various rotating speeds. This implies that catalyst of "900°C, 30 min" has some effect on the catalytic reduction of oxygen. At a specific potential, the current density also increases as the rotating speed of electrode increases. This is because higher rotating speed of electrode leads to higher rate of mass transfer by diffusion and thus higher current density on the electrode. The higher the rate of mass transfer by diffusion is, the higher is the rate of ORR. This indicates the rate of ORR is strongly limited by the rate of mass transfer by diffusion. The same trend can also be seen in Figure 5.94b and 5.94c.

The polarization curves of three carbon materials at 1,600 rpm are compared in Figure 5.94d. At a specific potential, the current density increases as the pyrolysis temperature or retention time of carbon materials under pyrolysis conditions increases. The higher pyrolysis temperature (or longer retention time) of carbon material is, the higher is the electrocatalytic

activity of this carbon material. The potential (vs. RHE) at which a current density of -1 mA/cm^2 is generated and half-wave potential (vs. RHE) from Figure 5.94d are summarized in Table 5.32.

Table 5.32 Potential (vs. RHE) at -1 mA/cm^2 and half-wave potential (vs. RHE) for various carbon materials. rotating speed: 1,600 rpm; N/A: not applicable.

	"900°C, 30 min"	"1,000°C, 30 min"	"1,000°C, 1 hour"
Potential at -1 mA/cm^2 (V)	0.60	0.74	0.81
half-wave potential (V)	N/A	N/A	0.78

As shown in Table 5.32, the potential at -1 mA/cm^2 also increases as the pyrolysis temperature or retention time of carbon materials increases. The increasing of both current density and potential at -1 mA/cm^2 indicates the improvement of catalytic activity of carbon materials.

The pore characterizations of these carbon materials are shown in Table 5.33. With the increasing of pyrolysis temperature or retention time, both specific surface areas and specific pore volumes increase. Advanced pore structures undoubtedly promote the mass transfer on the electrode and thus contribute to the high catalytic performance.

Table 5.33 Pore characterizations of carbon materials used in ORR.

Carbon spheres	Specific surface area (m^2/g)	Specific pore volume (mL/g)
"900°C, 30 min"	330	0.162
"1,000°C, 30 min"	739	0.341
"1,000°C, 1 hour"	1318	0.730

As discussed in section 2.7, the increasing of graphitization degree of carbon materials is beneficial to the increasing of conductivity, which also contributes to the catalytic performance of carbon materials. The indicator of the increasing of graphitization degree is the decreasing of the content of non-carbon elements, which can be demonstrated by the trend reflected in Table 5.5 and 5.6. The contents of nitrogen, oxygen, and hydrogen decrease as the pyrolysis temperature or retention time of carbon materials increases. The over-high content of nitrogen in carbon materials seems to be harmful to the ORR activity [44].

As demonstrated in section 5.4.5, in terms of nitrogen species, only quaternary N and pyridinic N were found in these carbon materials. According to the current opinions [47, 48], the activity centers of ORR derive from quaternary N or pyridinic N. The authors in research [43] regarded quaternary N as conductive center while pyridinic N as defects in the process of electron transportation. In Table 5.7, with the increasing of pyrolysis temperature or retention time, the relative content of quaternary N increases while that of pyridinic N decreases. This trend obviously contributes to the conductivity of carbon materials according to the opinions of research [43].

According to the research [95], the higher the content of quaternary N is, the larger is the diffusion-limited current density. The higher the content of pyridinic N is, the lower is the ORR over-potential. The trend of current density reflected in Figure 5.94d is in accordance with conclusion on quaternary N in research [95]. The trend of over-potential reflected in

Figure 5.94d, however, contradicts the conclusion on pyridinic N made by research [95].
The best ORR performance was acquired from sample of "1,000°C, 1 hour", with potential at -1 mA/cm^2 being 0.81 V (vs. RHE) and the half-wave potential being 0.78 V (vs. RHE). Compared with the commercial Pt/C catalyst [11] (potential at -1 mA/cm^2 being 0.9 V (vs. RHE) and the half-wave potential being 0.82-0.88 V (vs. RHE)), this performance is lower. However, these values are still among the highest values ever reported so far for metal-free carbon ORR catalysts.
The electron transfer number plotted against potential is shown in Figure 5.95. The related K-L plots are shown in appendix 8.8.

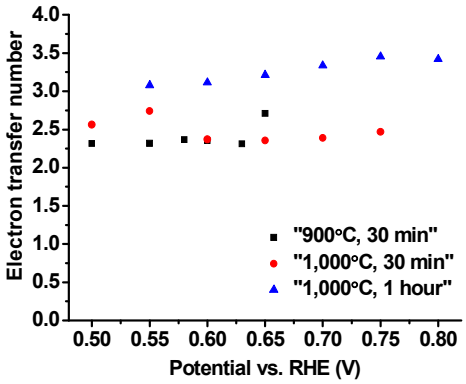

Figure 5.95 Electron transfer number of various carbon materials. loading of catalyst: 0.2 mg/cm^2.

With the increasing of potential, the electron transfer numbers of both "900°C, 30 min" and "1,000°C, 30 min" does not show specific trend. For sample of "1,000°C, 1 hour", however, its electron transfer number slowly increases as the potential increases. In addition, the electron transfer number of sample "1,000°C, 1 hour" is higher than those of "900°C, 30 min" and "1,000°C, 30 min" within the whole potential presented. The electron transfer number (n) at 0.6 V (vs. RHE) is summarized in Table 5.34.

Table 5.34 Electron transfer number (n) at 0.6 V (vs. RHE) for various carbon materials.

	"900°C, 30 min"	"1,000°C, 30 min"	"1,000°C, 1 hour"
n	2.4	2.4	3.1

Different from the order of catalytic activity reflected by Figure 5.94d, both "900°C, 30 min" and "1,000°C, 30 min" show the same electron transfer numbers at 0.6 V (vs. RHE), which are 2.4. The electron transfer number at 0.6 V (vs. RHE) of sample "1,000°C, 1 hour" is 3.1.
Apart from the RDE tests, RRDE tests were also performed to determine the yield of hydrogen peroxide and electron transfer number. The polarization curves acquired by RRDE tests are shown in Figure 5.96.

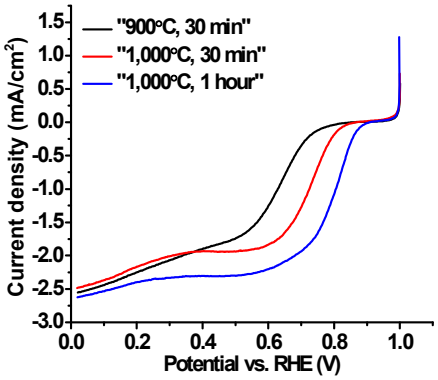

Figure 5.96 Polarization curves of various carbon materials recorded in O_2 saturated 0.1 M KOH solution with a scan rate of 5 mV/s. rotating speed: 1,600 rpm; loading of catalyst: 0.2 mg/cm^2.

At a specific potential (over 0.4 V vs. RHE), the current density increases as the pyrolysis temperature or retention time of carbon materials increases. The same order of catalytic activity repeats again in RRDE tests. The potential (vs. RHE) at which a current density of -1 mA/cm^2 is generated from Figure 5.96 is summarized in Table 5.35.

Table 5.35 Potential (vs. RHE) at -1 mA/cm^2 for various carbon materials. rotating speed: 1600 rpm.

	"900°C, 30 min"	"1,000°C, 30 min"	"1,000°C, 1 hour"
Potential (V)	0.63	0.72	0.80

As shown in Table 5.35, the potentials (vs. RHE) at -1 mA/cm^2 are almost the same as those shown in Table 5.32, which indicates a good reproducibility of the experiments. The yield of hydrogen peroxide and electron transfer number are shown in Figure 5.97.

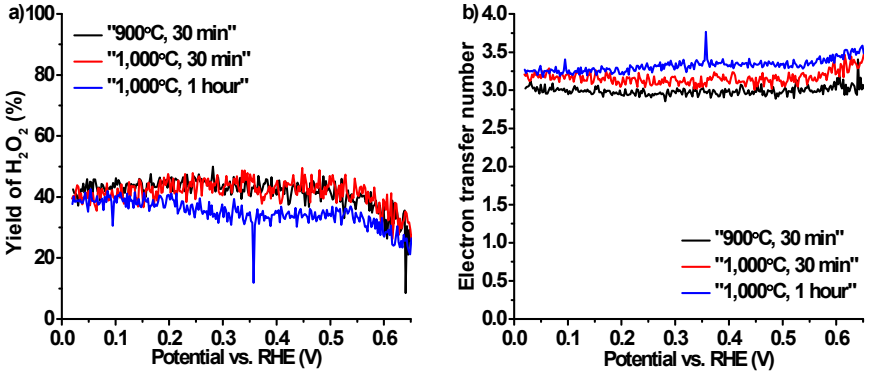

Figure 5.97 Yield of hydrogen peroxide a) and electron transfer number b) of various carbon materials. loading of catalyst: 0.2 mg/cm^2.

As shown in Figure 5.97a, the yield of hydrogen peroxide of both "900°C, 30 min" and "1,000°C, 30 min" is about 40% while that of "1,000°C, 1 hour" is lower than 40%. In Figure 5.97b, at a specific potential, the electron transfer number increases as the pyrolysis temperature or retention time of carbon samples increases. This order of catalytic activity is in accordance with those reflected by Figure 5.94d and 5.96. The yield of hydrogen peroxide

and electron transfer number at 0.6 V (vs. RHE) are summarized in Table 5.36.

Table 5.36 Yield of hydrogen peroxide and electron transfer number at 0.6 V (vs. RHE) for various carbon materials. loading of catalyst: 0.2 mg/cm^2.

	"900°C, 30 min"	"1,000°C, 30 min"	"1,000°C, 1 hour"
Yield of H_2O_2 (%)	37	38	27
n	3.1	3.2	3.5

As shown in Table 5.36, sample "1,000°C, 1 hour" has the lowest yield of hydrogen peroxide (27%) while the highest electron transfer number (3.5) at 0.6 V (vs. RHE) among the three carbon materials. Moreover, the electron transfer number calculated by RRDE tests is higher than that calculated by RDE tests and K-L regression. In conclusion, the ORR process on these carbon materials is a mixed process of four-electron transfer and two-electron transfer.

5.8.2 The effect of N-doped carbon materials' loading on the ORR performance

The polarization curves of sample "1,000°C, 1 hour" at different loadings are shown in Figure 5.98.

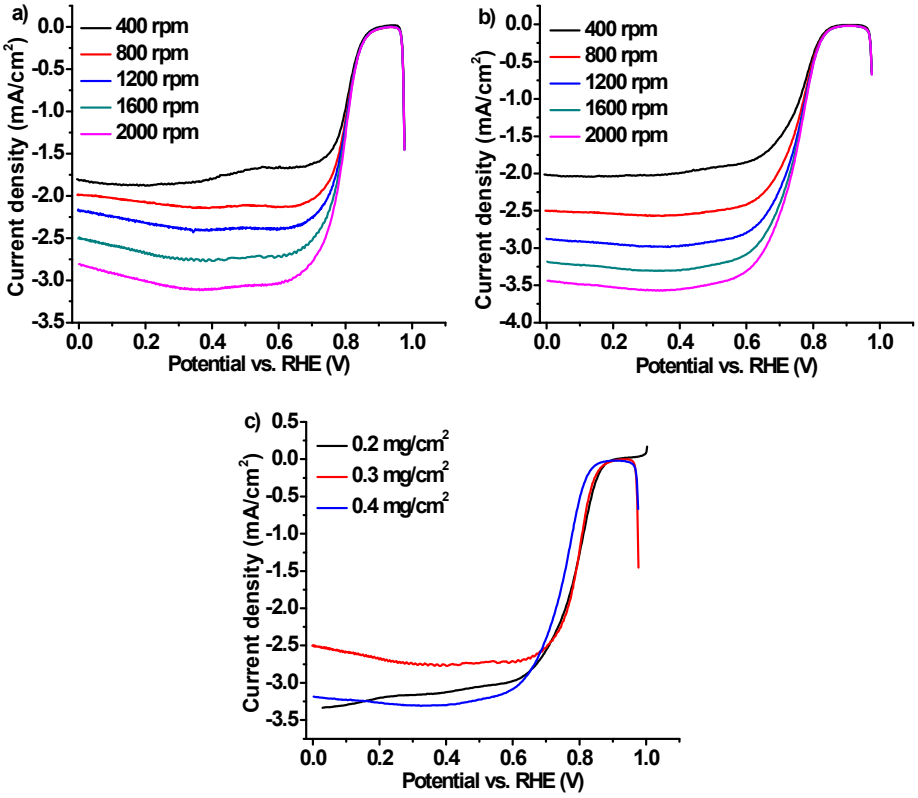

Figure 5.98 Polarization curves of sample "1,000°C, 1 hour" at various rotating speeds recorded in O_2 saturated 0.1 M KOH solution with a scan rate of 5 mV/s. a) loading of catalyst: 0.3 mg/cm^2; b) loading of catalyst: 0.4 mg/cm^2; c) comparison at 1,600 rpm.

Inspired by the superior ORR performance of sample "1,000°C, 1 hour", the effect of its catalyst loading on the ORR performance was studied. As shown in Figure 5.98a and 5.98b,

with the increasing of over-potential, the polarization current densities at various rotating speeds also increase. At a specific potential, the current density also increases as the rotating speed of electrode increases.

The polarization curves of sample "1,000°C, 1 hour" with various catalyst loadings are compared in Figure 5.98c. Within a specific potential section (0.2-0.6 V vs. RHE), the current density firstly decreases and then increases as the loading of catalyst on the electrode increases. The potential (vs. RHE) at which a current density of -1 mA/cm^2 is generated and half-wave potential (vs. RHE) from Figure 5.98c are summarized in Table 5.37.

Table 5.37 Potential (vs. RHE) at -1 mA/cm^2 and half-wave potential (vs. RHE) for various loadings of sample "1,000°C, 1 hour". rotating speed: 1,600 rpm.

Loadings (mg/cm^2)	0.2	0.3	0.4
Potential at -1 mA/cm^2 (V)	0.81	0.81	0.78
half-wave potential (V)	0.78	0.79	0.75

For the potentials at -1 mA/cm^2, they have no essential difference when the catalyst loading varies from 0.2 to 0.4 mg/cm^2. This conclusion also applies to the case of half-wave potential. For the carbon materials in section 5.8, increasing the catalyst loading may not result in the increasing of catalytic activity for ORR.

The electron transfer number plotted against potential is shown in Figure 5.99. The related K-L plots are shown in appendix 8.8.

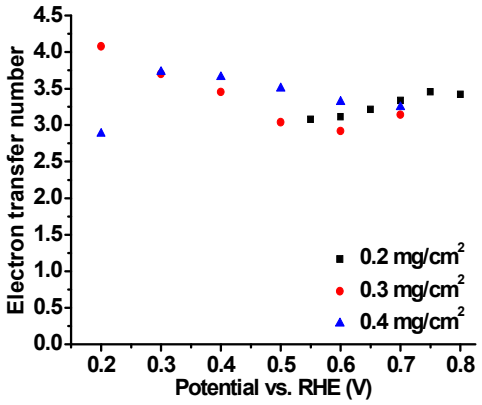

Figure 5.99 Electron transfer number of sample "1,000°C, 1 hour" with various loadings.

As shown in Figure 5.99, with the increasing of potential, there is no specific trend of electron transfer number whether the catalyst loading is 0.3 or 0.4 mg/cm^2. The electron transfer number (n) at 0.6 V (vs. RHE) is summarized in Table 5.38.

Table 5.38 Electron transfer number (n) at 0.6 V (vs. RHE) for various loadings of sample "1,000°C, 1 hour".

Loadings (mg/cm^2)	0.2	0.3	0.4
n	3.1	2.9	3.3

There is no essential difference between the three electron transfer numbers when the catalyst

loading increases from 0.2 to 0.4 mg/cm^2.

In the end, it can be inferred that with the further increasing of pyrolysis temperature or retention time in pyrolysis process, the ORR performance of carbon materials derived from PAN by carbonization and activation could be further increased.

6 Conclusions and Outlook

Shape of large PAN spheres

Large (i.e. millimeter-sized) PAN spheres have been successfully prepared by droplet shaping (i.e. syringe pump) *cum* phase separation. The average size of large PAN 200 spheres is 2.5 mm when the shaping orifice is 1.2 mm. There was no loss of PAN solutions during the shaping and gelation process.

PAN 200 solution with a concentration of 8% was selected to shape perfect spheres. Pure water as coagulant renders PAN droplets the highest gelation rate. With a shaping orifice of 1.2 mm, a falling distance of 5 cm was chosen to acquire wet PAN 200 spheres with an average aspect ratio of 1.05. Moreover, the circularity of polymer spheres increases after drying process.

The surface tension coefficients of PAN 200 solutions (concentration up to 10%) are 35 mJ/m^2. The current theoretical model describing the spreading of a droplet on another different liquid can not be readily put into practice. Compared with gelation rate, polymer concentration, and falling distance, the effect of surface tension on the deformation of PAN spheres can be neglected.

Inner structure of large PAN spheres

With DMF/water mixture (volume ratio: 65/35) as coagulant, the specific surface areas and specific pore volumes of PAN 200 spheres gelled in this coagulant are 269 m^2/g and 1.12 mL/g, respectively. These spheres are rich in larger numbers of sponge-like pores. Gelation rate almost has no effect of the porosity of PAN 200 spheres, which is about 90%.

The impacts of polymer concentration, gelation temperature, and gelation rate on the porous structures of PAN 200 spheres were analyzed by orthogonal tests and intuitive analysis. In terms of specific surface areas and specific pore volumes, the impacts of all three factors on these two indexes are significant while the impacts of interactions between any two factors are not significant. For porosity, however, only the impact of polymer concentration on this index is significant.

Preparation of SA hydrogel microspheres

The mean size of most SA microdroplets is below 100 μm. Both increasing the driving voltage and pulse width can increase the mean size of SA microdroplets. The 2D contours of shaping SA microdroplets by DOD ink-jetting were also plotted. These contours meet the shaping requirements of monodispersity, stability, and reproducibility statistically. It is suggested that a specific polymer-solvent system has its own specific 2D shaping contour.

For the durability of shaping, it is advisable to take the strategy that the numerical value of pulse width should be far lower than that of driving voltage. A narrow pulse width of 25 μs was chosen for all shaping experiments. By qualitative observation, the higher the concentration of SA solution is, the shorter is the shaping durability of SA microdroplets.

For hydrogel microspheres shaped from 1% SA solution, two acceptable shapes were found,

which are “tear-like” and spherical. SA hydrogel microspheres with oversize top-view areas are due to breakup of microdroplets when hitting the coagulant surface. Other deformation of SA hydrogel microspheres was not found.
SA hydrogel microspheres (i.e. micrometer-sized) have been successfully prepared by droplet shaping (i.e. DOD ink-jetting) *cum* crosslinking. The mean size of most SA hydrogel microspheres is below 100 μm. After gelation process, the volume of SA microdroplets shrinks. With the increasing of concentration of SA solutions, the initial shaping voltages of microdroplets also need to be increased. As the driving voltage increases, the mean size of hydrogel microspheres from same SA solution also increases.
Compared with driving voltage, concentration of SA solution, and falling distance, the effect of surface tension on the shape of SA hydrogel microspheres can be neglected.

Preparation of PAN microspheres

The shaping of PAN microspheres is closely related to the concentration of PAN solution, especially the molecular weight of PAN.
The viscoelasticity of PAN solutions was characterized by oscillatory tests. Shear strain amplitude sweeps indicate PAN solutions are viscoelastic liquid. The effect of increasing shear strain amplitude is similar to that of increasing driving voltage in DOD shaping, which is beneficial to form PAN microdroplets. Both increasing shaping frequency and temperature can decrease the energy dissipated by internal friction, which can be seen as two promoting factors for shaping PAN microdroplets.
Two kinds of blocking to shaping orifice were found, which are “real blocking” and “pseudo blocking”. The permissible highest shaping concentrations of various PAN solutions are 9% (X-PAN), 8% (L-PAN), 5% (PAN 150), and 3% (PAN 200).
The adjustment of any one of the three factors, i.e. angle of shaping head, falling distance of microdroplets, and shaping voltage and frequency, can not totally solve the problems of shaping microspheres, i.e. deformation, breakup, and collection.
In order to acquire microspheres as many and spherical as possible, one preparation strategy was proposed. With the falling distance and shaping temperature fixed, intact microspheres are acquired by decreasing the driving voltage and shaping frequency. If this way does not work, then the concentration of PAN solution should be further deceased. In this way, large numbers of round PAN microspheres were prepared from 6.5% X-PAN, the mean size of which is 31 μm.
Both increasing the driving voltage and shaping frequency were used to further increase the shaping rate of X-PAN microspheres. The problems of deformation and breakup of microspheres were solved by increasing the falling distance of microdroplets. The falling routes of X-PAN microdroplets were protected from air disturbance to collect X-PAN microspheres as many as possible within a specific period. In this way, about 250 mg dry X-PAN microspheres were acquired in one week.
The surface of X-APN microspheres is highly porous. By SEM inspection, the over-size areas of X-PAN microspheres from top-view by optical microscope did mean deformation or even breakup (i.e. “disk-like” shape). The effect of increasing falling distance on alleviating deformation and breakup of X-PAN microspheres was confirmed by SEM inspection;

however, deformation and breakup are difficult to be totally eliminated.
Increasing the concentration of X-PAN solution did alleviate the deformation and breakup of X-PAN microspheres. Compared with falling distance, driving voltage, and shaping frequency, the effects of both gelation rate of microdroplets and surface tension on the deformation and breakup of PAN microspheres can be neglected.
To shape a polymer with known M_w into microdroplets, the shaping conditions of X-PAN solution can be used as references.
In conclusion, PAN microspheres (i.e. micrometer-sized) have been successfully prepared by droplet shaping (i.e. DOD ink-jetting) *cum* phase separation. The mean sizes of X-PAN microspheres are 31 μm (gelled in water) and 44 μm (gelled in DMF/water mixture), respectively. The specific surface areas of X-PAN microspheres are 128 m^2/g (gelled in water) and 202 m^2/g (gelled in DMF/water mixture), respectively.

Carbonization of large PAN spheres

After pre-oxidation, both mass and mean size of carbon spheres decreased compared with those of polymer precursors. The mean size of all these carbon spheres is less than 1.4 mm. Both specific surface areas and specific pore volumes of carbon spheres decreased compared with those of polymer precursors. The highest specific surface areas recorded among these carbon spheres are only 14 m^2/g. The inner pores of polymer precursors were kept during oxidation process; however, the surface pores were blocked after pre-oxidation process. The porosity of all these carbon spheres is less than 50%.
The disappearance of –CN groups in polymer precursors partially indicates the finish of cyclization reaction according to the IR spectra.
After pyrolysis without activation, the mass of carbon spheres further decreased; however, the mean size of all carbon spheres changed little, which is less than 1.2 mm. The specific surface areas and specific pore volumes of carbon spheres did not increase after pyrolysis, compared with those of carbon spheres after pre-oxidation. The highest specific surface areas recorded among these carbon spheres are only 41 m^2/g. The inner pores of carbon spheres were destroyed to some extent and the surface pores were further blocked reflected by the denser skin layer. The porosity of all these carbon spheres is less than 45%.
Some measures should be done to reopen the surface pores rather than restoring the inner porous structure.
Carbon dioxide (CO_2) was chosen as the activator and pyrolysis and activation of carbon spheres were done at the same time. The functions of flow CO_2 are inflaming retarding, blowing away volatile wastes, and activation. With the activation of CO_2, the flow rate of CO_2 and pyrolysis temperature should be matched wisely. The final flow rate of CO_2 was set at 5 bubbles per second. After optimization of pyrolysis temperature, the specific surface areas of some carbon spheres can be over 1,000 m^2/g, which is close to those of commercial activated carbon. The usage of CO_2 during pyrolysis process can be further optimized by using a gas flow meter.
After pyrolysis and activation, the size of carbon spheres is about 1 mm and the yields of two representative carbon spheres are 38% and 25%, respectively. The large and easily recognizable surface pores on polymer spheres were replaced by smaller surface pores, not

easy to identify, on carbon spheres after activation.
With the increasing of pyrolysis temperature or retention time in pyrolysis, the content of carbon increased while the contents of non-carbon elements decreased as reflected in samples "900°C, 30 min", "1,000°C, 30 min", and "1,000°C, 1 hour" spheres. In these carbon spheres, both quaternary N (N-Q) and pyridinic N (N-6) were found by XPS inspection. With the increasing of retention time or pyrolysis temperature in pyrolysis, the content of quaternary N increased while the content of pyridinic N decreased. The results of XRD and Raman inspection indicate that these carbon spheres are amorphous carbon.

Preparation and characterization of nanocomposites

The specific surface areas of polymer nanocomposites (200 m^2/g) are lower than those of carbon nanocomposites (400-650 m^2/g).
On the surface of 10% PAN+P90, nanoparticles of TiO_2 can be spotted by SEM inspection; after carbonization process, these nanoparticles merged with carbon matrix. The results of EDS inspection indicate that the distribution of titanium is homogeneous on the surface of both 10% PAN+P90 and 10% Carbon+P90 nanocomposites.
In "5% carbon spheres", both quaternary N (N-Q) and pyridinic N (N-6) were found by XPS inspection while nitrogen species of pyrrolic N (N-5) and pyridinic N (N-6) were found in 10% Carbon+P90. In the high-resolution XPS spectra of carbon and nitrogen elements from 10% Carbon+P90, both Ti-C (C 1s, 281.6 eV) and Ti-N (N 1s, 396.9 eV) were not found. In terms of titanium, both Ti-C (Ti 2p, 454.9 eV) and Ti-N (Ti 2p, 455.8 eV) were also not found in 10% Carbon+P90. It can be inferred that carbon nanocomposites of 10% Carbon+P90 are simply a mixture of carbon materials and P90.
According to the results of XRD inspection, the content of anatase phase in 10% Carbon+P90 is 37.58% while that of rutile phase is 62.42%. Therefore, part of anatase phase in P90 was transformed into rutile phase after carbonization process. The results of both Raman and IR inspection can not confirm the interaction between nanoparticles and carbon substrate in 10% Carbon+P90.
For the forming of new bonds between nanoparticles and carbon matrix, generating nanoparticles by *in situ* synthesis *cum* carbonization is more effective than adding nanoparticles into polymer matrix directly *cum* carbonization.

Adsorption on large polymer and carbon spheres

Two kinds of large PAN spheres were used as polar adsorbents, which carried negative charges during the range of pH used. Two kinds of carbon spheres were used as low polar adsorbents, which are essentially amphiphilic.
The adsorption mechanism between phenols and PAN spheres is dipole-dipole interaction. Due to the lower polarity of phenols, their adsorption isotherms within low concentration section belong to S isotherm (i.e. low affinity). In terms of adsorption capacity for phenols, PAN spheres of "8%, 65/35" did not show improvement to PAN spheres of "8%, 0/100".
The adsorption mechanism between dyes and PAN spheres is electrostatic attraction. Due to the higher polarity of dye cations, their adsorption isotherms within low concentration section

belong to L isotherm (i.e. moderate affinity). In terms of adsorption capacity for dyes, PAN spheres of "8%, 65/35" did not show improvement to PAN spheres of "8%, 0/100".
For the same PAN adsorbents, when the solutes were changed from phenols to dyes, the affinities between solutes and adsorbents increased according to the regression results of Freundlich model. The excessive molecular size of dye cations can weaken their affinity to polymer adsorbents.
The adsorption mechanism between phenols and carbon spheres is dispersion interaction. Due to the lower polarity of phenols, their adsorption isotherms within low concentration section belong to H isotherm (i.e. high affinity). In terms of adsorption capacity for phenols, carbon spheres of "1,000°C, 1 hour" did show improvement to carbon spheres of "1,000°C, 30 min". For example, the adsorption capacity of *p*-nitrophenol increased from 172 mg/g (on "1,000°C, 30 min") to 272.5 mg/g (on "1,000°C, 1 hour"), when the equilibrium concentration reaches 45 mg/L.
The adsorption mechanism between dyes and carbon spheres is dispersion interaction. Due to the lower polarity of electroneutral part of dye ions, their adsorption isotherms within low concentration section belong to H isotherm (i.e. high affinity). In terms of adsorption capacity for dyes, carbon spheres of "1,000°C, 1 hour" did show improvement to carbon spheres of "1,000°C, 30 min". For example, the adsorption capacity of methyl orange increased from 107 mg/g (on "1,000°C, 30 min") to 296 mg/g (on "1,000°C, 1 hour"), when the equilibrium concentration reaches 24 mg/L.
For the same carbon adsorbents, when the solutes were changed from phenols to dyes, the affinities between solutes and adsorbents firstly increased and then decreased according to the regression results of Freundlich model. The excessive molecular size of dye ions can weaken their affinity to carbon adsorbents.
For the same phenols (or dyes), when the adsorbents were changed from PAN spheres to carbon spheres, the affinities between phenols and adsorbents increased according to the regression results of Freundlich model. At the same time, the adsorption capacity of phenols (or dyes) on carbon spheres was higher at specific equilibrium concentrations compared with that on polymer spheres. This means for the adsorption of phenols (or dyes), carbon spheres are superior to PAN spheres.

Photocatalysis of polymer and carbon nanocomposites

The photocatalytic rate of polymer nanocomposites was analyzed in terms of the content of P90 in nanocomposites. The highest photocatalytic rate among three polymer nanocomposites is 0.014 min^{-1}, which belongs to 10% PAN+P90. Compared with the photocatalytic rate of P90, the photocatalytic rates of polymer nanocomposites decreased a half or more. Photocatalytic rates of polymer nanocomposites are found to be related to the actual mass of P90 in nanocomposites while they have no relation to the nominal content, nominal loading, and actual content of P90. In addition, the actual content of P90 in polymer nanocomposites is hard to be precisely controlled.
The photocatalytic rate of carbon nanocomposites was analyzed in terms of the content of nanoparticles in nanocomposites. The highest (net) photocatalytic rate among three carbon nanocomposites is 0.0084 min^{-1}, which belongs to 10% Carbon+P90. Compared with the

photocatalytic rate of P90, the photocatalytic rates of carbon nanocomposites decreased a half or more. The photocatalytic rates of carbon nanocomposites were also lower than those of polymer nanocomposites. Net photocatalytic rates of carbon nanocomposites are assumed to be related to the actual mass of nanoparticles and specific surface areas of nanocomposites; however, the photocatalytic rates have no relation to the actual content of nanoparticles. Two possible reasons resulted in the lower photocatalytic rates of carbon nanocomposites, which are the change of properties of P90 after carbonization and the absorption of black carbon to UV light.

Oxygen reduction reaction of carbon materials

The ORR activity of three carbon materials was firstly analyzed by polarization curves. At a specific potential, the current density increases as the pyrolysis temperature or retention time of carbon materials increases. At the same time, the potential (vs. RHE) at which a current density of -1 mA/cm^2 is generated also follows this trend. The possible reasons are that with the increasing of pyrolysis temperature or retention time of carbon materials, more advanced pore structures, higher degree of graphitization, and higher content of quaternary N, all of them contribute to the improvement of ORR activity.

The best ORR performance was acquired from sample of "1,000°C, 1 hour", with potential at -1 mA/cm^2 being 0.81 V (vs. RHE) and the half-wave potential being 0.78 V (vs. RHE). Moreover, the electron transfer number of sample "1,000°C, 1 hour" at 0.6 V (vs. RHE) is 3.1 by K-L regression. The results of RRDE tests show that sample "1,000°C, 1 hour" has the lowest yield of H_2O_2 (i.e. 27%) and highest electron transfer number (i.e. 3.5) at 0.6 V (vs. RHE) among three carbon materials. In conclusion, the ORR process on these carbon materials is a mixed process of four-electron transfer and two-electron transfer.

For sample "1,000°C, 1 hour", the results of RDE tests indicate that increasing the catalyst loading may not result in the increasing of catalytic activity to ORR.

All in all, it can be inferred that with the further increasing of pyrolysis temperature or retention time (based on sample "1,000°C, 1 hour"), the ORR performance of carbon materials derived from PAN by carbonization and activation could be further increased.

7 References

[1] G. Li, C. Fang, and et al.: The effect of economic growth, urbanization, and industrialization on fine particulate matter ($PM_{2.5}$) concentrations in China. Environ. Sci. Technol., 2016, 50, 11452-11459.
[2] J. R. Elliott and S. Frickel: The historical nature of cities: a study of urbanization and hazardous waste accumulation. American Sociological Review, 2013, 78 (4), 521 -543.
[3] C. Moreno-Castilla: Adsorption of organic molecules from aqueous solutions on carbon materials. Carbon, 2004, 42, 83-94.
[4] M. Ulbricht: Advanced functional polymer membranes. Polymer, 2006, 47, 2217-2262.
[5] D. Bahnemann: Photocatalytic water treatment: solar energy applications. Solar Energy, 2004, 77, 445-459.
[6] Y. Chen: Preparation and characterization of porous materials. Monograph, Press of University of Science and Technology of China, 2010.
[7] O. Mechling: Poröse Polymer- und Kohlenstoff-basierte TiO_2 Nanokomposite. Dissertation, Universität Duisburg-Essen, 2015.
[8] H. Thierfeld: Herstellung poröser Polymer- und Kohlenstoff- basierter Hybridmaterialien zur Adsorption und Photokatalyse. Dissertation, Universität Duisburg-Essen, 2018.
[9] M. Inagaki and F. Kang: Materials science and engineering of carbon: fundamentals. Monograph, Butterworth-Heinemann, 2014.
[10] M.S.A. Rahaman, A.F. Ismail and et al.: A review of heat treatment on polyacrylonitrile fiber. Polymer Degradation and Stability, 2007, 92, 1421-1432.
[11] A. Wütscher, T. Eckhard, and et al.: Nitrogen-doped metal-free carbon materials derived from cellulose as electrocatalysts for the oxygen reduction reaction. ChemElectroChem, 2019, 6, 514-521.
[12] A. Fujishima and K. Honda: Electrochemical photolysis of water at a semiconductor electrode. Nature, 1972, 238, 37-38.
[13] F. Pellegrino, L. Pellutiè and et al.: Influence of agglomeration and aggregation on the photocatalytic activity of TiO_2 nanoparticles. Applied Catalysis B: Environmental, 2017, 216, 80-87.
[14] W. Liu, X. Yang, and et al.: Catalytic properties of carboxylic acid functionalized polymer microsphere-stabilized gold metallic colloids. Journal of Colloid and Interface Science, 2006, 304, 160-165.
[15] H. Kawaguchi: Functional polymer microspheres. Prog. Polym. Sci., 2000, 25, 1171-1210.
[16] J. Fan, C. Huang, and et al.: Nanoporous microspheres: from controllable synthesis to healthcare applications. J. Mater. Chem. B, 2013, 1, 2222-2235.
[17] O. Okay: Macroporous copolymer networks. Prog. Polym. Sci., 2000, 25, 711-779.
[18] M. Talha Gokmen and F. Du Prez: Porous polymer particles-A comprehensive guide to synthesis, characterization, functionalization and applications. Progress in Polymer Science, 2012, 37, 365- 405.
[19] R. Arshady: Suspension, emulsion, and dispersion polymerization: A methodological survey. Colloid Polym Sci, 1992, 270, 717-732.
[20] D. Horak：Uniform polymer beads of micrometer size. Acta Polymer., 1996，47, 20-28.

[21] M. Gericke, J. Trygg, and et al.: Functional cellulose beads: preparation, characterization, and applications. Chem. Rev., 2013, 113, 4812-4836.
[22] H. Strathmann, K. Kock, and et al.: The formation mechanism of asymmetric membranes. Desalination, 1975, 16, 179-203.
[23] H. Strathmann and K. Kock: The formation mechanism of phase inversion membranes. Desalination, 1977, 21, 241-255.
[24] P.S.T. Machado, A.C. Habert, and et al.: Membrane formation mechanism based on precipitation kinetics and membrane morphology: flat and hollow fiber polysulfone membranes. Journal of Membrane Science, 1999, 155, 171-183.
[25] Microdrop Technologies GmbH: The hand book of microdrop dosing system MD-E-3011-130. https://www.microdrop.de.
[26] X. Fu, W. Shen and et al.: Physical chemistry. Monograph, Higher Education Press, 2006.
[27] D. J. Donahue and F. E. Bartell: The boundary tension at water-organic liquid interfaces. The Journal of Physical Chemistry, 1952, 56(4), 480-484.
[28] S. Banerjee, A. Zangiabadi, and et al.: Quantitative structural characterization of catalytically active TiO_2 nanoparticles. ACS Appl. Nano Mater., 2019, 2, 6268-6276.
[29] R. Leary and A. Westwood: Carbonaceous nanomaterials for the enhancement of TiO_2 photocatalysis. Carbon, 2011, 49, 741-772.
[30] W. Kim, T, Tachikawa, and et al.: Molecular-level understanding of the photocatalytic activity difference between anatase and rutile nanoparticles. Angew. Chem. Int. Ed., 2014, 53, 14036 -14041.
[31] T. Luttrell, S. Halpegamage, and et al.: Why is anatase a better photocatalyst than rutile? - Model studies on epitaxial TiO_2 films. Scientific reports, 2014, 4 (1), 1-8.
[32] F. Qi, A. Moiseev, and et al.: Synthesis and characterization of highly reactive and thermostable anatase titania nanoparticles for photocatalytic applications. Chemie Ingenieur Technik, 2014, 86, 1-9.
[33] D. A. H. Hanaor and C. C. Sorrell: Review of the anatase to rutile phase transformation. Journal of Materials Science, 2011, 46, 855-874.
[34] I. Slowing, B. G. Trewyn, and et al.: Effect of surface functionalization of MCM-41-Type mesoporous silica nanoparticles on the endocytosis by human cancer cells. J. Am. Chem. Soc., 2006, 128, 14792-14793.
[35] M. Qhobosheane, S. Santra, and et al.: Biochemically functionalized silica nanoparticles. Analyst, 2001, 126, 1274-1278.
[36] S. Brunauer, L. S. Deming, and et al.: On a theory of the van der Waals adsorption of gases. J. Am. Chem. Soc., 1940, 62 (7), 1723-1732.
[37] S. J. Gregg and K. S. W. Sing: Adsorption, surface area and porosity. Monograph, Academic press, 1982.
[38] S. Brunauer, P. H. Emmett, and et al.: Adsorption of gases in multimolecular layers. J. Am. Chem. Soc., 1938, 60 (2), 309-319.
[39] E. P. Barrett, L. G. Joyner, and et al.: The determination of pore volume and area distributions in porous substances. I. computations from nitrogen isotherms. J. Am. Chem. Soc., 1951, 73 (1), 373-380.
[40] S. Kondo, T. Ishikawa, and et al.: Adsorption science. Monograph, Press of Chemical

Industry, 2005.
[41] C. H. Giles and D. Smith: A general treatment and classification of the solute adsorption isotherm I. theoretical. Journal of Colloid and Interface Science, 1974, 47 (3), 755-765.
[42] Z. Jia, C. Dai, and et al.: Electrochemical measurement methods. Monograph, Chemical Industry Press, 2006.
[43] M. Einert, C. Wessel, and et al.: Nitrogen-doped carbon electrodes: influence of microstructure and nitrogen configuration on the electrical conductivity of carbonized polyacrylonitrile and poly(ionic liquid) blends. Macromol. Chem. Phys., 2015, 216, 1930-1944.
[44] Z. R. Ismagilov, A. E. Shalaginaa and et al.: Structure and electrical conductivity of nitrogen-doped carbon nanofibers. Carbon, 2009, 47 (8), 1922-1929.
[45] C. Kim, C. Zhu, and et al.: Exothermically efficient exfoliation of biomass cellulose to value added N‑doped hierarchical porous carbon for oxygen reduction electrocatalyst. Ind. Eng. Chem. Res. 2019, 58, 3047-3059.
[46] D. Yu, L. Zhou, and et al.: Nitrogen-doped porous carbon nanosheets derived from coal tar pitch as an efficient oxygen-reduction catalyst. Ind. Eng. Chem. Res. 2017, 56, 8880-8887.
[47] Y. Wang, H. Liu, and et al.: 3D interconnected hierarchically porous N-doped carbon with NH_3 activation for efficient oxygen reduction reaction. Applied Catalysis B: Environmental, 2017, 210 (5), 57-66.
[48] D. Guo, R. Shibuya, and et al.: Active sites of nitrogen-doped carbon materials for oxygen reduction reaction clarified using model catalysts. Science, 2016, 351, 361-365.
[49] M. D. Abramoff, P. J. Magalhaes, and et al.: Image processing with Image J. Biophotonics International, 2004, 11, 36-42.
[50] E. Olson: Particle shape factors and their use in image analysis-part 1: theory. Journal of GXP compliance, 2011, 15 (3), 85-96.
[51] J. F. Moulder, W. F. Stickle, and et al.: Handbook of X-ray photoelectron spectroscopy. Monograph, Perkin-Elmer Corporation, 1992.
[52] T. G. Mezger: The rheology handbook: for users of rotational and oscillatory rheometers. Monograph, Vincentz Network, 2006.
[53] M. Zenkiewicz: Methods for the calculation of surface free energy of solids. Journal of achievements in materials and manufacturing engineering, 2007, 24 (1), 137-145.
[54] R. Ober, L. Paz, and et al.: Study of the surface tension of polymer solutions: theory and experiments. 1. Good solvent conditions. Macromolecules, 1983, 16 (1), 50-55.
[55] G. Zhou, Z. Yan, and et al.: Fluid mechanics. Monograph, Higher Education Press, 2003.
[56] J. J. Cooper-White, J.E. Fagan, and et al.: Drop formation dynamics of constant low-viscosity, elastic fluids. J. Non-Newtonian Fluid Mech., 2002, 106, 29-59.
[57] C. J. Van Oss: Interfacial forces in aqueous media. Monograph, CRC Press, 2006.
[58] KRÜSS GmbH: The handbook of force tensiometer-K6. https://www.kruss.de.
[59] K. Fang and C. Ma: Orthogonal and uniform design. Monograph, Science Press, 2001.
[60] H. Dong, W. W. Carr, and et al.: An experimental study of drop-on-demand drop formation. Physics of fluids, 2006, 18, 072102.
[61] P. Shin, S. Lee, and et al.: Operability diagram of drop formation and its response to

temperature variation in a piezoelectric inkjet nozzle. Microelectronics Reliability, 2011, 51, 437-444.
[62] A. S. M. Wittmar and M. Ulbricht: Ionic liquid-based route for the preparation of catalytically active cellulose-TiO_2 porous films and spheres. Ind. Eng. Chem. Res., 2017, 56, 2967-297.
[63] M. He, H. Zhang, and et al.: Polymer physics. Monograph, Fudan University Press, 2007.
[64] P. Bowen: Particle size distribution measurement from millimeters to nanometers and from rods to platelets. Journal of Dispersion Science and Technology, 2002, 23 (5), 631-622.
[65] E. R. Lee: Microdrop generation. Monograph, CRC PRESS, 2003.
[66] H. J. Shore and G. M. Harrison: The effect of added polymers on the formation of drops ejected from a nozzle. Physics of fluids, 2005, 17, 033104.
[67] J. Yang, D. Katagiri, and et al.: Generation of controlled monodisperse porous polymer particles by dipped inkjet injection. RSC Adv., 2015, 5, 7297-7303.
[68] N. Reis, C. Ainsley, and et al.: Ink-jet delivery of particle suspensions by piezoelectric droplet ejectors. Journal of applied physics, 2005, 97, 094903.
[69] E. Tekin, E. Holder, and et al.: Controlled pattern formation of poly [2-methoxy-5-(2'-ethylhexyloxyl)-1,4-phenylenevinylene] (MEH-PPV) by ink-jet printing. Adv. Funct. Mater., 2007, 17, 277-284.
[70] D. Xu, V. Sanchez-Romaguera, and et al.: Inkjet printing of polymer solutions and the role of chain entanglement. J. Mater. Chem., 2007, 17, 4902-4907.
[71] B. J. de Gans, L. Xue, and et al.: Ink-jet printing of linear and star polymers. Macromol. Rapid Commun., 2005, 26, 310-314.
[72] Y. Christanti, and L. M. Walker: Surface tension driven jet break up of strain-hardening polymer solutions. J. Non-Newtonian Fluid Mech., 2001, 100, 9-26.
[73] X. Yan, W. W. Carr, and et al.: Drop-on-demand drop formation of polyethylene oxide solutions. Physics of fluids, 2011, 23, 107101.
[74] R. P. Mun, J. A. Byars, and et al.: The effects of polymer concentration and molecular weight on the breakup of laminar capillary jets. J. Non-Newtonian Fluid Mech., 1998, 74, 285- 297.
[75] B. J. de Gans, E. Kazancioglu, and et al.: Ink-jet printing polymers and polymer libraries using micropipettes. Macromol. Rapid Commun., 2004, 25, 292-296.
[76] S. D. Hoath, I. M. Hutchings, and et al.: Links between ink rheology, drop-on-demand jet formation, and printability. Journal of Imaging Science and Technology, 2009, 53(4), 041208.
[77] F. He: Carbon fiber and its application technology. Monograph, Chemical Industry Press, 2004.
[78] E. Fitzer and D. J. Müller: The Influence of oxygen on the chemical reaction during stabilization of PAN as carbon fiber precursor. Carbon, 1975, 13 (1), 63-69.
[79] P. Rangarajan, V. A. Bhanu, and et al.: Dynamic oscillatory shear properties of potentially melt processable high acrylonitrile terpolymers. Polymer, 2002, 43 (9), 2699-2709.
[80] N. Yusof and A. F. Ismail: Post spinning and pyrolysis processes of polyacrylonitrile (PAN)-based carbon fiber and activated carbon fiber: A review. Journal of Analytical and

Applied Pyrolysis, 2012, 93, 1-13.
[81] M. Nandi, K. Okada, and et al.: Unprecedented CO_2 uptake over highly porous N-doped activated carbon monoliths prepared by physical activation. Chem. Commun., 2012, 48, 10283-10285.
[82] Information from RRUFF™ Project: https://rruff.info.
[83] L. Zhang, H. Fu, and et al.: Efficient TiO_2 photocatalysts from surface hybridization of TiO_2 particles with graphite-like carbon. Adv. Funct. Mater., 2008, 18, 2180-2189.
[84] F. Tuinstra and J. L. Koenig: Raman spectrum of graphite. J. Chem. Phys., 1970, 53 (3), 1126-1130.
[85] T. Oksaka, F. Izumi, and et al.: Raman Spectrum of Anatase, TiO_2. Journal of Raman Spectroscopy, 1978, 7 (6), 321-324.
[86] H. Berger, H. Tang, and et al.: Growth and Raman spectroscopic characterization of TiO_2 anatase single crystals. Journal of Crystal Growth, 1993, 130, 108-112.
[87] S. P. S. Porto, P. A. Fleury, and et al.: Raman spectra of TiO_2, MgF_2, ZnF_2, FeF_2, and MnF_2. Physical Review, 1967,154 (2), 522-526.
[88] Y. Hara and M. Nicol: Raman spectra and the structure of rutile at high pressures. Phys. Stat. Sol. (b), 1979, 94, 317-322.
[89] X. Cao, T. Song, and et al.: Monograph, Inorganic chemistry. Higher Education Press, 1994.
[90] L. Boguslavsky, S. Baruch, and et al.: Synthesis and characterization of polyacrylonitrile nanoparticles by dispersion/emulsion polymerization process. Journal of Colloid and Interface Science, 2005, 289, 71-85.
[91] W. Bao, Z. Xu, and et al.: Electrokinetic and permeation characterization of hydrolyzed polyacrylonitrile (PAN) hollow fiber ultrafiltration membrane. Sci China Ser B-Chem, 2009, 52 (5), 683-689.
[92] Nitric acid modification of activated carbon produced from waste tea and adsorption of methylene blue and phenol. Applied Surface Science, 2014, 313 (15), 352-359.
[93] Á. Sánchez-Sánchez, F. Suárez-García and et al.: Synthesis, characterization and dye removal capacities of N-doped mesoporous Carbons. Journal of Colloid and Interface Science, 2015, 450 (15), 91-100.
[94] J. Huang, K. Huang, and et al.: Adsorption of rhodamine B and methyl orange on a hypercrosslinked polymeric adsorbent in aqueous solution. Colloids and Surfaces A: Physicochem. Eng. Aspects, 2008, 330, 55-61.
[95] X. Liu and L. Dai: Carbon-based metal-free catalysts. Nat. Rev. Mater., 2016, 1, 16064.

8 Appendix

8.1 List of chemicals used

Table 8.1 List of chemicals used. N/A: not applicable.

Chemicals	Purity (%)	Manufacturer
Calcium chloride·$2H_2O$	99.5	AppliChem, Germany
Carbon dioxide	99.995	Air Liquide, France
p-chlorophenol	≥ 99	Sigma Aldrich, USA
N, N-dimethylformamide (DMF)	99.9	VWR International, USA
n-heptane	≥ 99	Alfa Aesar, USA
Hydrogen chloride (0.1 M)	N/A	Bernd Kraft, Germany
Hydrogen chloride (concentrated)	N/A	Bernd Kraft, Germany
Methylene blue (MB)	≥ 95	Fluka, USA
Methyl orange (MO)	≥ 90	Fluka, USA
Nitrogen	99.8	Air Liquide, France
p-nitrophenol	≥ 99	Sigma Aldrich, USA
Phenol	≥ 99	Alfa Aesar, USA
Polyacrylonitrile (L-PAN)	93	Sigma Aldrich, USA
Polyacrylonitrile (PAN 150)	N/A	Polysciences, Inc., USA
Polyacrylonitrile (PAN 200)	99.5	Dolan, Germany
Polyacrylonitrile (X-PAN)	93	Sigma Aldrich, USA
Rhodamine B (Rh B)	≥ 99	Alfa Aesar, USA
Sodium alginate (SA)	≥ 90	Fluka, USA
Titanium dioxide (Anatase)	99.7	Sigma Aldrich, USA
Titanium dioxide (P25)	≥ 99.5	Evonik, Germany
Titanium dioxide (P90 315)	≥ 99.5	Evonik, Germany
Titanium dioxide (P90 416)	≥ 99.5	Evonik, Germany
Titanium dioxide (T805)	97	Evonik, Germany
Water (Milli-Q)	N/A	Merck Millipore, Germany

8.2 Major axis, minor axis, aspect ratio, and circularity

The illustration of an ellipse is shown in Scheme 8.1.

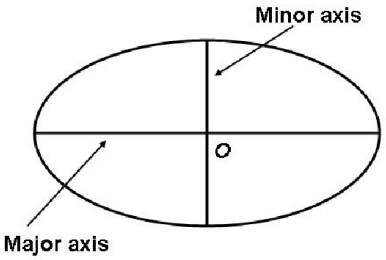

Scheme 8.1. Illustration of an ellipse.

The aspect ratio (AR) is defined as the ratio of major axis and minor axis as shown in Formula 8.1.

$$AR = \text{major axis/minor axis}$$

Formula 8.1

The circularity is shown in Formula 8.2.

$$C = \sqrt{\frac{4\pi A}{P^2}}$$

Formula 8.2

P: the perimeter of the ellipse;
A: the area of the ellipse.

8.3 The molecular structure of polymers used

The structural formula of sodium alginate (SA) is shown in Scheme 8.2.

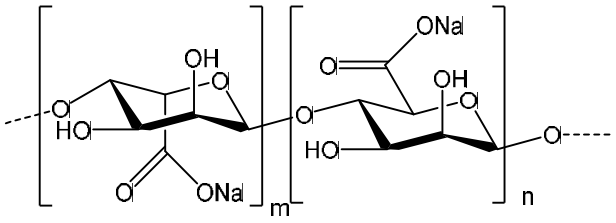

Scheme 8.2 Structural formula of sodium alginate.

PAN 200 (i.e. H-PAN)
This polymer is composed of 99.5% polyacrylonitrile and 0.5% methyl acrylate (MA) as shown in Scheme 8.3.

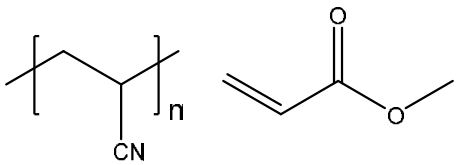

Scheme 8.3 Structural formula of PAN 200.

X-PAN
This polymer is composed of 93% polyacrylonitrile, 6% methyl acrylate (MA), and 1% sodium methylallyl sulfonate as shown in Scheme 8.4.

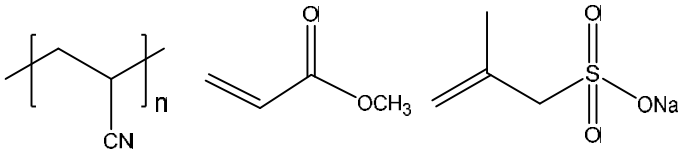

Scheme 8.4 Structural formula of X-PAN.

L-PAN

This polymer is composed of 93% polyacrylonitrile and 7% vinyl acetate as shown in Scheme 8.5.

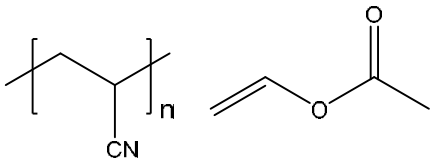

Scheme 8.5 Structural formula of L-PAN.

PAN 150

This polymer has the same structural formula as that of PAN 200 but with a lower M_w.

8.4 Standard curves of phenols and dyes used in adsorption tests

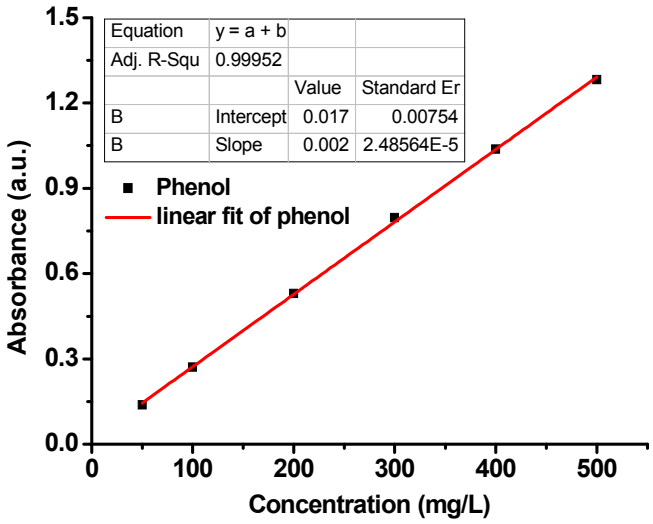

Figure 8.1 The standard curve of phenol solution for the adsorption on both PAN 200 and carbon spheres. wavelength of absorbance: 250 nm; pH: two; regulator: concentrated HCl solution.

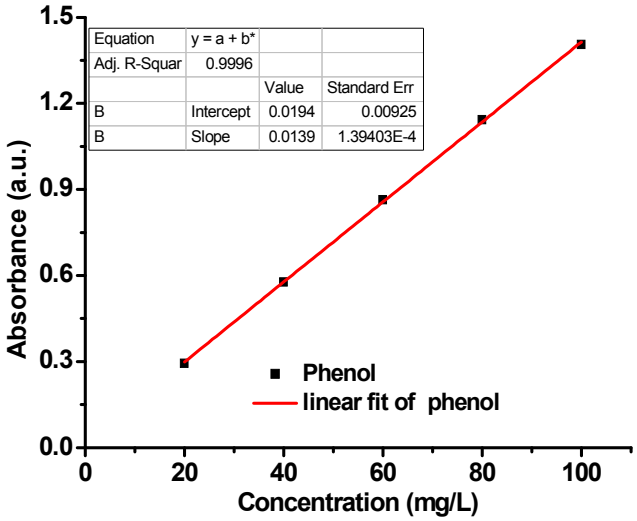

Figure 8.2 The standard curve of phenol solution for the adsorption on PAN 200 spheres. wavelength of absorbance: 270 nm; pH: two; regulator: 0.1 M HCl solution.

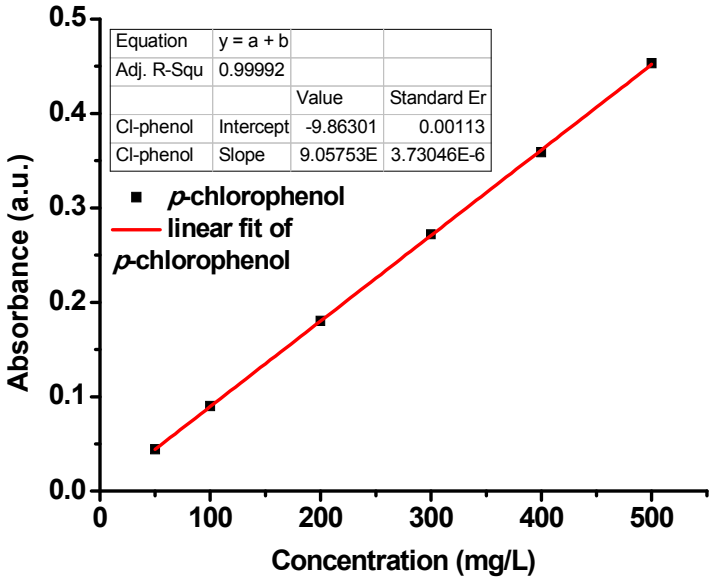

Figure 8.3 The standard curve of *p*-chlorophenol solution for the adsorption on PAN 200 spheres. wavelength of absorbance: 250 nm; pH: two; regulator: 0.1 M HCl solution.

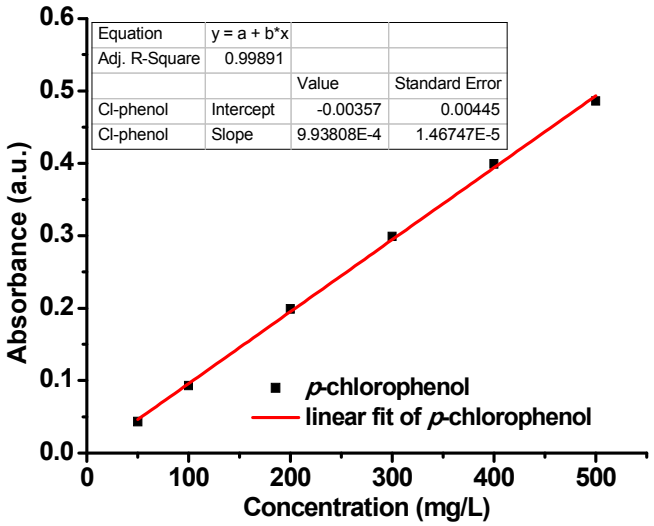

Figure 8.4 The standard curve of *p*-chlorophenol solution for the adsorption on carbon spheres. wavelength of absorbance: 250 nm; pH: two; regulator: concentrated HCl solution.

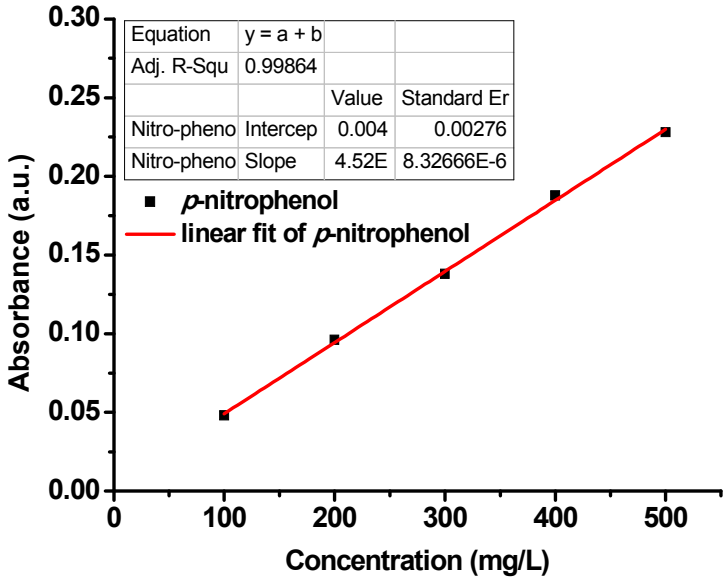

Figure 8.5 The standard curve of *p*-nitrophenol solution for the adsorption on PAN 200 spheres. wavelength of absorbance: 402 nm; pH: two; regulator: 0.1 M HCl solution.

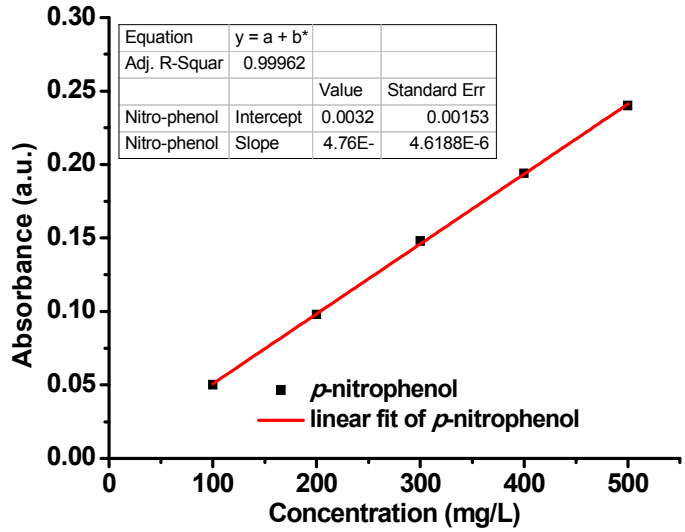

Figure 8.6 The standard curve of *p*-nitrophenol solution for the adsorption on carbon spheres. wavelength of absorbance: 402 nm; pH: two; regulator: concentrated HCl solution.

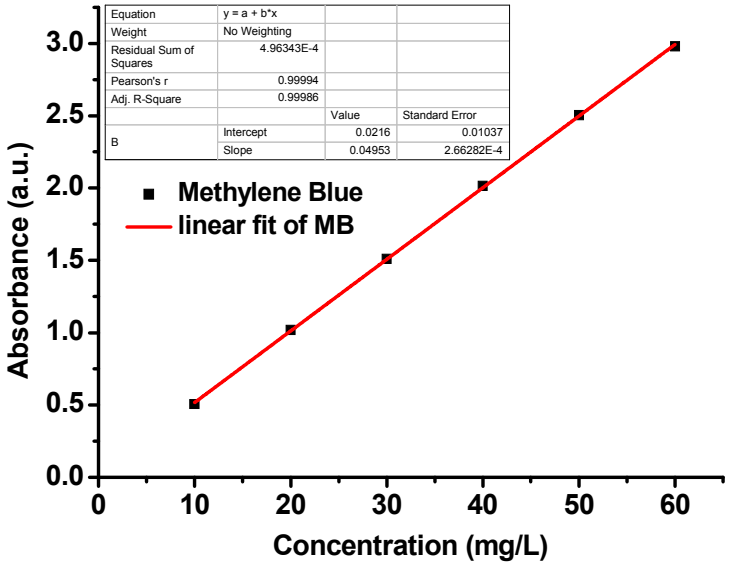

Figure 8.7 The standard curve of MB solution for the adsorption on both PAN 200 and carbon spheres. wavelength of absorbance: 247 nm.

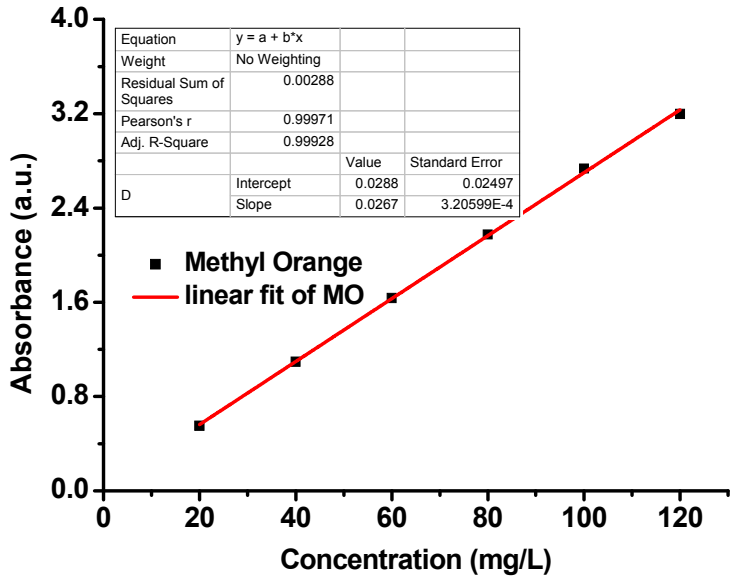

Figure 8.8 The standard curve of MO solution for the adsorption on carbon spheres. wavelength of absorbance: 272 nm.

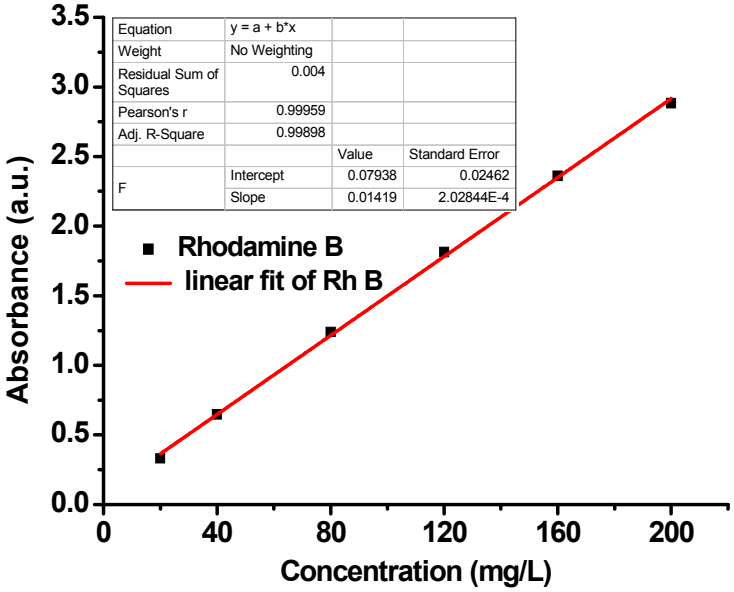

Figure 8.9 The standard curve of Rh B solution for the adsorption on both PAN 200 and carbon spheres. wavelength of absorbance: 354 nm.

8.5 Process of intuitive analysis

Table 8.2 Process of intuitive analysis for specific surface areas.

Order	A	B	A*B	C	A*C	B*C	Blank	Specific surface area (m^2/g)
1	1	1	1	1	1	1	1	164.72
2	1	1	1	2	2	2	2	191.61
3	1	2	2	1	1	2	2	117.21

4	1	2	2	2	2	1	1	144.41
5	2	1	2	1	2	1	2	190.08
6	2	1	2	2	1	2	1	216.06
7	2	2	1	1	2	2	1	139.85
8	2	2	1	2	1	1	2	155.22
K1	618.0	762.5	651.4	611.9	653.2	654.4	665.0	
K2	701.2	556.7	667.8	707.3	666.0	664.7	654.1	
Ave. K1	154.5	190.6	162.9	153.0	163.3	163.6	166.3	
Ave. K2	175.3	139.2	167.0	176.8	166.5	166.2	163.5	
Range	20.82	51.45	4.09	23.86	3.19	2.58	2.73	

Table 8.3 Process of intuitive analysis for specific pore volumes.

Order	A	B	A*B	C	A*C	B*C	Blank	Specific pore volume (mL/g)
1	1	1	1	1	1	1	1	0.478
2	1	1	1	2	2	2	2	0.646
3	1	2	2	1	1	2	2	0.394
4	1	2	2	2	2	1	1	0.500
5	2	1	2	1	2	1	2	0.58
6	2	1	2	2	1	2	1	0.786
7	2	2	1	1	2	2	1	0.486
8	2	2	1	2	1	1	2	0.604
K1	2.018	2.493	2.214	1.941	2.262	2.165	2.249	
K2	2.459	1.984	2.262	2.536	2.215	2.312	2.228	
Ave. K1	0.504	0.623	0.554	0.485	0.565	0.541	0.562	
Ave. K2	0.615	0.496	0.566	0.634	0.554	0.578	0.557	
Range	0.110	0.127	0.012	0.149	0.012	0.037	0.005	

Table 8.4 Process of intuitive analysis for porosity.

Order	A	B	A*B	C	A*C	B*C	Blank	Porosity
1	1	1	1	1	1	1	1	0.942
2	1	1	1	2	2	2	2	0.938
3	1	2	2	1	1	2	2	0.945
4	1	2	2	2	2	1	1	0.935
5	2	1	2	1	2	1	2	0.906
6	2	1	2	2	1	2	1	0.898
7	2	2	1	1	2	2	1	0.897
8	2	2	1	2	1	1	2	0.889
K1	3.761	3.685	3.666	3.690	3.674	3.672	3.673	
K2	3.590	3.666	3.684	3.660	3.677	3.678	3.677	
Ave. K1	0.940	0.921	0.917	0.922	0.918	0.918	0.918	
Ave. K2	0.897	0.916	0.921	0.915	0.919	0.920	0.919	
Range	0.043	0.005	0.004	0.007	0.001	0.001	0.001	

8.6 Combined shaping conditions of SA solutions

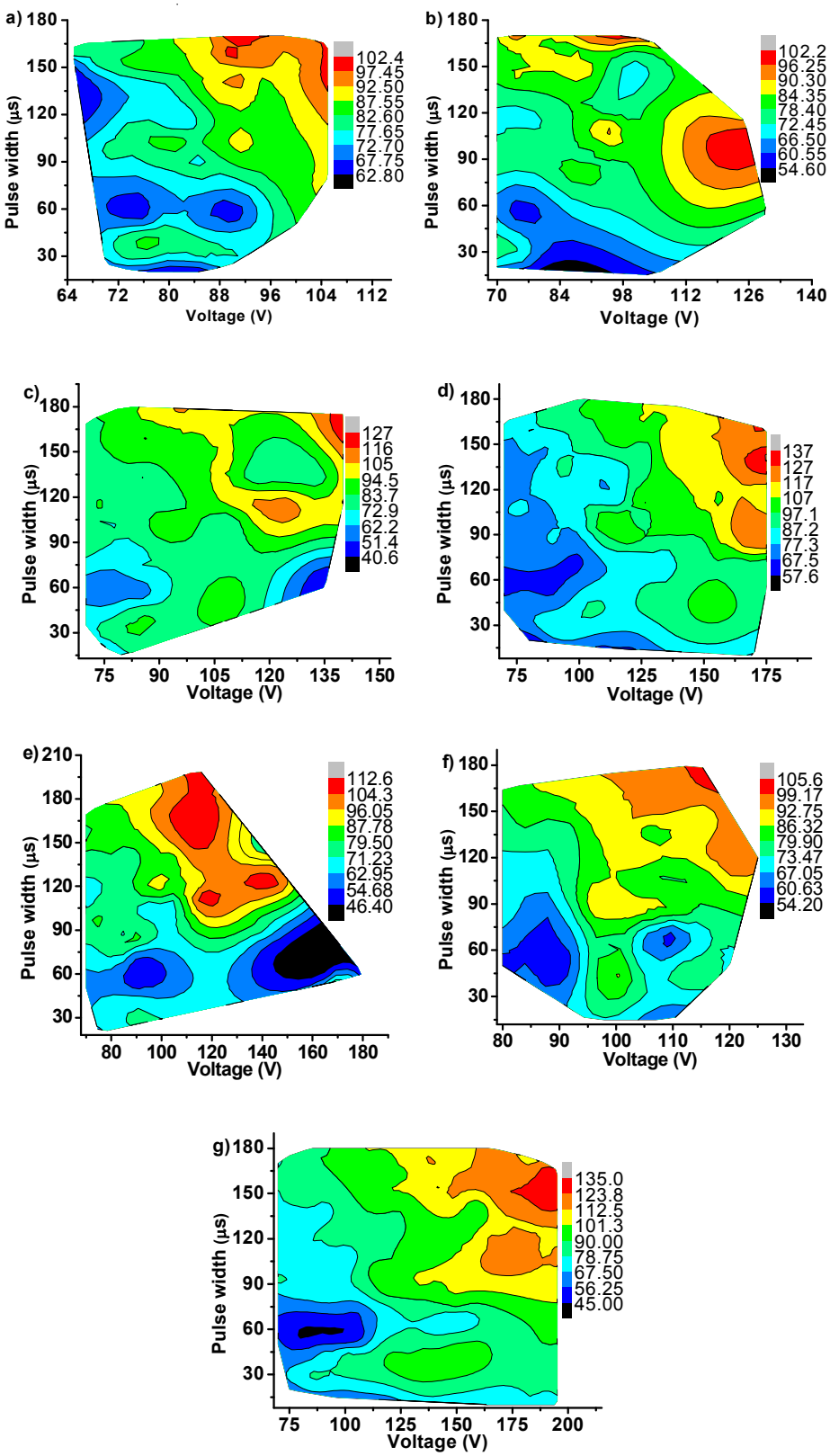

Figure 8.10 Combined conditions of shaping SA microdroplets. concentrations of SA solutions a-g): 0.1%, 0.8%, 1%, 1.5%, 1.6%, 1.7%, and 1.8%; unit of droplet size: µm.

8.7 The pH values of dyes' solution

Table 8.5 pH of MB solutions. "before": before the adsorption test; "after": after the adsorption test with "1,000°C, 1hour"carbon spheres.

pH at 20°C	Concentration (mg/L)					
	10	20	30	40	50	60
"before"	5.14	6.09	5.62	6.13	6.11	5.59
"after"	N/A	6.45	6.12	5.89	5.19	5.2

Table 8.6 pH of MO solutions. "before": before the adsorption test; "after": after the adsorption test with "1,000°C, 1hour"carbon spheres.

pH at 20°C	Concentration (mg/L)					
	20	40	60	80	100	120
"before"	6.7	6.72	6.91	6.65	6.78	6.99
"after"	N/A	6.79	8.43	6.89	6.38	7.06

Table 8.7 pH of Rh B solutions. "before": before the adsorption test; "after": after the adsorption test with "1,000°C, 1hour"carbon spheres.

pH at 20°C	Concentration (mg/L)					
	20	40	80	120	160	200
"before"	5.27	4.62	4.2	3.79	4.01	3.84
"after"	N/A	5.14	4.59	4.28	4.04	3.71

8.8 K-L plots of various carbon materials

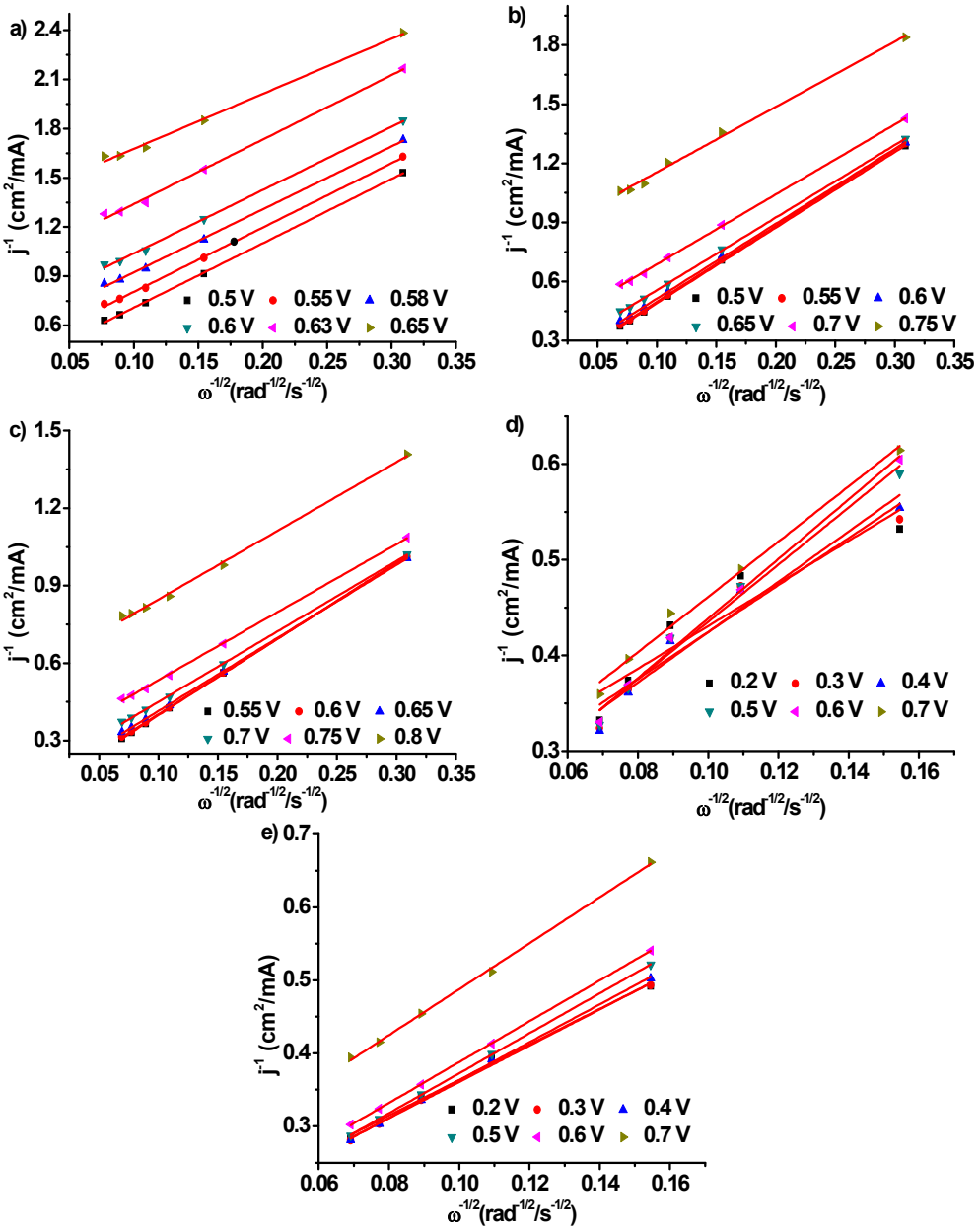

Figure 8.11 K-L plots of various carbon materials with different loadings. a) "900°C, 30 min", 0.2 mg/cm^2; b) "1,000°C, 30 min", 0.2 mg/cm^2; c) "1,000°C, 1 hour", 0.2 mg/cm^2; d) "1,000°C, 1 hour", 0.3 mg/cm^2; e) "1,000°C, 1 hour", 0.4 mg/cm^2.

Declaration

I hereby explain that I have written this dissertation independently and only used specified sources and aids. Furthermore, this dissertation or similar form of it has not been submitted to any other university.

Essen, 20, 09, 2022